

Copyright  
by  
Benjamin Charles Treweek  
2019

**Acoustic Radiation Force Due to Sound Beams Incident  
on Spherical Scatterers in Soft Tissue-Like Media**

by

**Benjamin Charles Treweek**

**DISSERTATION**

Presented to the Faculty of the Graduate School of  
The University of Texas at Austin  
in Partial Fulfillment  
of the Requirements  
for the Degree of

**DOCTOR OF PHILOSOPHY**

THE UNIVERSITY OF TEXAS AT AUSTIN

May 2019

The Dissertation Committee for Benjamin Charles Treweek  
certifies that this is the approved version of the following dissertation:

**Acoustic Radiation Force Due to Sound Beams Incident  
on Spherical Scatterers in Soft Tissue-Like Media**

Committee:

---

Mark F. Hamilton, Supervisor

---

Michael R. Haberman

---

Yurii A. Ilinskii

---

Loukas F. Kallivokas

---

Preston S. Wilson

In loving memory of my mother

Linda Sue Kole

## Acknowledgments

First, I would like to thank my advisor Dr. Mark Hamilton for overseeing my work on this topic. His honest, responsive feedback was invaluable as I worked through this difficult research, and his unparalleled instruction in physical acoustics, nonlinear acoustics, and wave phenomena provided me with a solid background in physical intuition and mathematical analysis that I will draw upon heavily as I progress in my career. I also wish to thank dissertation committee member Dr. Yurii Ilinskii, who not only served as the driving force behind the theory I investigated but also helped immensely as I sought to better understand its finer points.

I would also like to thank dissertation committee member Dr. Michael Haberman for providing me with the opportunity to work on other funded projects in 2018 and 2019, as well as Dr. Mohsen Ahmadian for funding me in the Fall 2017 semester. Both of these research opportunities were pivotal to the continuation of my studies, and they exposed me to different applications of acoustics from those with which I had previously worked, helping me gain important experience so I could better aim my job search after graduating. For evaluating my work in this dissertation, I am also grateful to my other dissertation committee members: Dr. Preston Wilson, whose notes were useful in the transducers course I took when I began my graduate studies, and Dr. Loukas

Kallivokas, whose course introduced me to the finite element method.

I extend warm thanks to my friends at The University of Texas at Austin, both in the Graduate Program in Acoustics and in the Texas Running Club. They helped me retain my sanity during my time in graduate school by providing me with advice, solidarity, and all-too-necessary release valves for pent-up energy. In particular, fellow Acoustics students Anthony Bonomo and Ben Goldsberry were knowledgeable resources when my research demanded the use of the finite element method, and they were great companions with whom to share weekly gatherings at the Flying Saucer to unwind. I thank Kyle Spratt for helpful discussions as I finished writing, and I thank Mustafa Abbasi for indulging my venting during our weekly rock climbing sessions. Also, fellow graduate student and Texas Running Club member Kyle Higdon, in his diligent organization of track workouts for the club, helped train me to run a personal best in the 1500-meter run, my favorite race. It was my first personal best in seven years, and I had feared that I was past my athletic prime, but he helped me prove myself wrong.

Finally, I must thank my family for reminding me of what is truly important, especially my mother Linda Kole and my father Steven Treweek. Their unwavering support as they raised me, their encouragement to challenge myself both intellectually and physically, and their prudent money management ensuring me a rewarding undergraduate experience without any financial worry—all of these have built me into the person I am. My mother's untimely passing on August 9, 2010 due to breast cancer was what ultimately led me

to pursue the particular project I selected for my Ph.D., and in moments of difficulty, I have found the resolve to continue by remembering that she would be proud of the path I have chosen.

This work was supported primarily by the Applied Research Laboratories Chester M. McKinney Graduate Fellowship in Acoustics. Additional funding was provided by a recruitment fellowship from the Cockrell School of Engineering and the Thrust 2000—Richard J. Lee Endowed Graduate Fellowship in Engineering.

# **Acoustic Radiation Force Due to Sound Beams Incident on Spherical Scatterers in Soft Tissue-Like Media**

Publication No. \_\_\_\_\_

Benjamin Charles Treweek, Ph.D.  
The University of Texas at Austin, 2019

Supervisor: Mark F. Hamilton

This dissertation presents a theory for acoustic radiation force on a spherical scatterer embedded in a soft elastic medium that supports the propagation of shear waves. Existing theories for acoustic radiation force on a sphere are restricted to a fluid surrounding the sphere. Potential applications reside in biology and medicine. For example, the mechanical properties of soft tissue, in particular its shear stiffness, are a useful proxy for tissue health and can be used for non-invasive tissue characterization. The present work investigates the effect that shear elasticity in the surrounding medium has on the radiation force on an embedded spherical scatterer. The theory is developed in Lagrangian coordinates, instead of Eulerian coordinates that are traditionally used for a fluid surrounding the sphere. It is assumed that a compressional wave is incident on the sphere. Coefficients in the spherical harmonic expansions describing the incident compressional wave field, and the scattered compressional and shear wave fields, are examined in detail. The radiation force is separated into two

contributions, one that corresponds to the scattered compressional waves and the other to the scattered shear waves, both of which displace the sphere from its initial position. The compressional wave contribution can be determined analytically, and a variety of material properties for the sphere and incident beam patterns are examined for this contribution. The shear wave contribution has yet to be determined analytically, and is investigated numerically. A third contribution, corresponding to the static deformation of the surrounding medium due to the scattered shear wave, is also investigated numerically. A finite element method is used to determine the full effect of the scattered shear wave on the sphere displacement, and it is found that effects due to the scattered shear wave may be of the same order as those due to the scattered compressional wave.

# Table of Contents

<b>Acknowledgments</b>	<b>v</b>
<b>Abstract</b>	<b>viii</b>
<b>List of Tables</b>	<b>xiii</b>
<b>List of Figures</b>	<b>xiv</b>
<b>Chapter 1. Introduction</b>	<b>1</b>
1.1 Brief History of Radiation Force Theory . . . . .	2
1.2 Applications of Acoustic Radiation Force . . . . .	11
1.3 Dissertation Overview . . . . .	18
<b>Chapter 2. Theoretical Framework for Acoustic Radiation Force on an Elastic Sphere in a Soft Elastic Medium</b>	<b>21</b>
2.1 Elastodynamic Equations . . . . .	23
2.1.1 Stress Tensor and Body Force . . . . .	25
2.1.2 Displacement Field Equations . . . . .	28
2.2 Acoustic Radiation Force Terms . . . . .	31
2.3 Eulerian Description of Acoustic Radiation Force . . . . .	35
2.4 Radiation Force Due to Compressional Wave Fields . . . . .	37
2.5 Comparison with Existing Theory . . . . .	41
2.6 Radiation Force Associated with the Scattered Shear Wave . . . . .	48
2.7 Summary . . . . .	51
<b>Chapter 3. Incident and Scattered Fields</b>	<b>52</b>
3.1 Incident Field Coefficients . . . . .	53
3.1.1 Non-axisymmetric Incident Field . . . . .	53

3.1.2	Axisymmetric Incident Field . . . . .	57
3.1.3	Off-Origin Field Expansion . . . . .	58
3.1.4	Incident Field Coefficients for Transverse Radiation Forces	59
3.2	Modeling the Incident Beam . . . . .	61
3.2.1	Simple Focused Beam . . . . .	61
3.2.2	Focused Gaussian Beam . . . . .	66
3.2.3	Focused Circular Transducer . . . . .	69
3.3	Elastic Scattering Coefficients . . . . .	72
3.3.1	Elastic Sphere in Elastic Medium . . . . .	74
3.3.2	Elastic Sphere in Fluid Medium . . . . .	75
3.3.3	Fluid Sphere in Elastic Medium . . . . .	76
3.3.4	Fluid Sphere in Fluid Medium . . . . .	78
3.3.5	Spherical Void or Rigid Sphere in Elastic Medium . . . . .	78
3.4	Discussion of Scattering Coefficients . . . . .	80
3.4.1	Compressional Wave Scattering Coefficients . . . . .	80
3.4.2	Shear Wave Scattering Coefficients . . . . .	87
3.5	Summary . . . . .	92
<b>Chapter 4. Radiation Force Due to Compressional Wave Fields</b>		<b>94</b>
4.1	Numerical Convergence . . . . .	97
4.2	Scatterer Position . . . . .	100
4.2.1	Scatterer Located On Axis . . . . .	100
4.2.2	Scatterer Located Off Axis . . . . .	110
4.3	Scatterer Size . . . . .	113
4.4	Elasticity in Surrounding Medium . . . . .	120
4.5	Summary . . . . .	125
<b>Chapter 5. Acoustic Radiation Force Associated with the Scattered Shear Wave</b>		<b>127</b>
5.1	Comparison of $F_n$ and $G_n^B$ . . . . .	129
5.2	Approximation of $G_n^P$ . . . . .	132
5.3	Numerical Solution for $G_z^P$ . . . . .	141
5.3.1	Description of Numerical Helmholtz Decomposition . . . . .	142

5.3.2	Results for $G_z^P$ . . . . .	145
5.4	Full Solution for $u_n^{(2)}$ with Finite Element Method . . . . .	148
5.4.1	Weak Form and Simplifications . . . . .	149
5.4.2	Displacement Results . . . . .	154
5.5	Summary . . . . .	158
<b>Chapter 6.</b>	<b>Conclusions and Future Work</b>	<b>160</b>
<b>Appendices</b>		<b>166</b>
<b>Appendix A.</b>	<b>Mathematical Conventions</b>	<b>167</b>
<b>Appendix B.</b>	<b>Acoustic Radiation Force Integrals</b>	<b>170</b>
B.1	Radiation Force Due to Compressional Wave Fields . . . . .	170
B.2	Radiation Force Associated with the Scattered Shear Wave . . . . .	173
<b>Bibliography</b>		<b>175</b>
<b>Vita</b>		<b>195</b>

## List of Tables

2.1	Medium and scatterer properties for comparison with Hasegawa and Yosioka [5, 6]. . . . .	46
3.1	Medium and scatterer properties for rigid/void comparisons . . . . .	81
4.1	Medium and spherical scatterer properties for radiation force comparisons. . . . .	95

## List of Figures

1.1	Experimental confirmation of King’s predictions for radiation force on spheres that are rigid compared with the surrounding air. (a) Measured acoustic pressure (plus signs) and acoustic radiation force divided by cork sphere weight (filled circles) compared with curves from King’s theory (from Rudnick [41]). (b) Acoustic force per weight of a polyethylene sphere for several sound pressure levels (from Leung et al. [42]). . . . .	6
1.2	Schematic of shear wave elasticity imaging with multiple imaging transducers and detection sensors (from Sarvazyan et al. [23]). . . . .	13
1.3	Diagram of supersonic shear imaging with the source being moved along the beam axis three times as fast as the shear waves propagating away from the region (from Bercoff et al. [25]).	15
1.4	Experimental setup (left, from Karpouk et al. [89]) and results (right, from Aglyamov et al. [90]) for examining transient displacement of a sphere in a viscoelastic gel phantom due a short pulses of various durations. On the right, (a) shows the theoretical prediction of sphere displacement and (b) shows experimental measurement. . . . .	16
2.1	Comparison of Eq. (2.68) with results of Hasegawa and Yosioka [5] for the acoustic radiation force function $Y_p$ versus dimensionless sphere size $kR$ for various spheres in water. Note that the two curves, calculated with different equations, lie directly on top of each other. . . . .	47
3.1	Diagram of a focused transducer (left) projecting a sound beam with a focus at the origin and the scatterer located away from the focus. Scattered waves are illustrated departing the scatterer.	58
3.2	Beam amplitude profiles for $\Psi(\theta_k)$ defined as in Eq. (3.28) for various confinement angles $\theta_0$ at frequency $f = 1$ MHz. For $\theta_0 = 30^\circ$ , a focal profile (where dashed lines indicate the half-power beamwidth) is shown in (d) and an axial profile is shown in (e). The colors in (a), (b), and (c) correspond to the vertical axes in (d) and (e), with yellow equal to unity and dark blue equal to zero. . . . .	62

3.3	Plots of beam amplitude for a focused Gaussian beam and circular transducer with $a = 1$ cm and $d = 4$ cm ( $G = 5.2$ ) at $f = 1$ MHz. The first row shows color plots of the beam amplitude in the $z$ - $x$ plane, and the second and third rows show focal and axial profiles, respectively. The colors in the first row correspond to the vertical axes in the second and third rows, with yellow equal to the maximum value and dark blue equal to zero. . . . .	71
3.4	Compressional wave scattering coefficients for a steel sphere and a rigid movable sphere of equivalent density in water. . . . .	82
3.5	Compressional wave scattering coefficients for an air bubble and a spherical void in water. . . . .	83
3.6	Compressional wave scattering coefficients in water and soft tissue ( $\mu = 100$ kPa) for a steel sphere. . . . .	84
3.7	Compressional wave scattering coefficients in water and soft tissue for a steel sphere. . . . .	85
3.8	Monopole scattering coefficient magnitude for an air bubble in water and soft tissue-like media. . . . .	86
3.9	Scattering coefficients for the shear wave in a soft tissue-like medium ( $\mu = 4$ kPa) surrounding a steel sphere and a rigid movable sphere of equivalent density. . . . .	87
3.10	Scattering coefficients for the shear wave in a soft tissue-like medium ( $\mu = 4$ kPa) surrounding an air bubble and a spherical void. . . . .	89
3.11	Scattering coefficients for the shear wave versus shear modulus for an air bubble (left column) and a steel sphere (right column). . . . .	90
4.1	Axial profile of a plane standing wave at frequency $f = 1$ MHz in a medium with compressional wave speed $c_l = 1500$ m/s. The filled red circle marks an example sphere positioned at $z = z_0$ . . . . .	96
4.2	Number of terms $N$ required for convergence of radiation force $F_z$ given by Eq. (2.68) due to a traveling plane wave incident on spheres of various sizes $kR$ in water. . . . .	98
4.3	Terms required for convergence of axial ( $F_z$ ) and transverse ( $F_x$ ) radiation force due to a simple focused beam incident on spheres of various sizes $kR$ in water. Both $F_z$ and $F_x$ are calculated using Eq. (2.67) with respective incident field coefficients. The sphere is located at $(z_0, x_0) = (0, 0.5$ mm). . . . .	99
4.4	Acoustic radiation force function $Y_{p,z}$ versus axial position $z_0$ of a stainless steel sphere embedded in various media with a plane standing wave incident on the sphere. A dashed line is included at $Y_{p,z} = 0$ for visual clarity. . . . .	102

4.5	Force on a bubble in a standing wave at two different moments in the cycle. . . . .	103
4.6	Acoustic radiation force function $Y_{p,z}$ versus axial position $z_0$ of an air bubble embedded in various media with a plane standing wave incident on the bubble. A dashed line is included at $Y_{p,z} = 0$ for visual clarity. . . . .	104
4.7	Acoustic radiation force function $Y_{p,z}$ versus axial position $z_0$ of an aluminum sphere embedded in various media with a simple focused beam incident on the sphere. Solid lines indicate $Y_{p,z} > 0$ and dashed lines indicate $Y_{p,z} < 0$ . . . . .	106
4.8	Acoustic radiation force function $Y_{p,z}$ versus axial position $z_0$ of an aluminum sphere ( $kR = 1$ ) embedded in various media with a simple focused beam incident on the sphere. . . . .	107
4.9	Acoustic radiation force function $Y_{p,z}$ versus axial position $z_0$ of an air bubble embedded in various media with a simple focused beam incident on the sphere. Solid lines indicate $Y_{p,z} > 0$ and dashed lines indicate $Y_{p,z} < 0$ . . . . .	108
4.10	Acoustic radiation force function $Y_{p,z}$ versus transverse position $x_0$ of a stainless steel sphere and a gas bubble embedded in various media with a simple focused beam incident on the sphere. Compare with Fig. 3.2(d), which shows that the first null is approximately 2 mm from the axis in the focal plane. . . . .	109
4.11	Acoustic radiation force function $Y_{p,x}$ versus transverse position $x_0$ of a stainless steel sphere embedded in various media with a simple focused beam incident on the sphere. Solid lines indicate $Y_{p,x} > 0$ and dashed lines indicate $Y_{p,x} < 0$ . . . . .	111
4.12	Acoustic radiation force function $Y_{p,x}$ versus transverse position $x_0$ of an aluminum sphere embedded in various media with a simple focused beam incident on the sphere. A dashed line is included at $Y_{p,x} = 0$ for visual clarity. . . . .	112
4.13	Acoustic radiation force function $Y_{p,x}$ versus transverse position $x_0$ of an air bubble embedded in various media with a simple focused beam incident on the bubble. Solid lines indicate $Y_{p,x} > 0$ and dashed lines indicate $Y_{p,x} < 0$ . . . . .	114
4.14	Acoustic radiation force function $Y_{p,z}$ versus scatterer size $kR$ of a stainless steel sphere embedded in various media with a plane traveling wave incident on the sphere. . . . .	115
4.15	Acoustic radiation force function $Y_{p,x}$ versus scatterer size $kR$ of a stainless steel sphere and an aluminum sphere embedded in various media with a simple focused beam incident on the sphere, located at $x_0 = 0.5$ mm in the focal plane. Solid lines indicate $Y_{p,x} > 0$ and dashed lines indicate $Y_{p,x} < 0$ . . . . .	117

4.16	Acoustic radiation force function $Y_{p,z}$ versus scatterer size $kR$ of an air bubble embedded in various media with a plane traveling wave incident on the bubble. . . . .	118
4.17	Acoustic radiation force function $Y_{p,x}$ versus scatterer size $kR$ of an air bubble embedded in various media with a simple focused beam incident on the sphere, located at $x_0 = 0.5$ mm in the focal plane. Solid lines indicate $Y_{p,x} > 0$ and dashed lines indicate $Y_{p,x} < 0$ . . . . .	119
4.18	Ratio of axial radiation force in various media to that in inviscid water for air bubbles of various sizes located at $(z_0, x_0) = (0.2$ mm, 0.5 mm) off the focus of a beam incident on the bubble. 120	
4.19	Ratio of transverse radiation force in various media to that in inviscid water versus shear modulus $\mu$ or shear viscosity $\eta$ for air bubbles of various sizes located at $(z_0, x_0) = (0.2$ mm, 0.5 mm) off the focus of a beam incident on the bubble. A solid line indicates a positive ratio and a dashed line indicates a negative ratio. . . . .	121
4.20	Ratio of axial radiation force in various media to that in inviscid water for aluminum spheres of various sizes located at $(z_0, x_0) = (0.2$ mm, 0.5 mm) off the focus of a beam incident on the sphere. 122	
4.21	Ratio of transverse radiation force in various media to that in inviscid water versus shear modulus $\mu$ or shear viscosity $\eta$ for aluminum spheres of various sizes located at $(z_0, x_0) = (0.2$ mm, 0.5 mm) off the focus of a beam incident on the sphere. A solid line indicates a positive ratio and a dashed line indicates a negative ratio. . . . .	123
4.22	Ratio of transverse radiation force in various media to that in inviscid water versus scatterer size $kR$ and shear modulus $\mu$ or shear viscosity $\eta$ for air bubbles and aluminum spheres in a simple focused beam, located at $(z_0, x_0) = (0, 0.5$ mm). Black lines have been added as visual aids to identify direction reversals [127]. . . . .	124
5.1	Ratio of force terms $G_n^B/F_n$ for various spheres embedded in soft tissue-like media subject to a simple focused beam with confinement angle $\theta_0 = 30^\circ$ located off the beam axis at $(z_0, x_0) = (0, 0.5$ mm). A positive ratio is indicated with solid lines, and a negative ratio is indicated with dashed lines. . . . .	130
5.2	Plots of the two force terms $F_z^B$ and $F_z^P$ due to compressional wave fields for a traveling plane wave incident on various spheres in a soft tissue-like medium ( $\mu = 100$ kPa). A dashed line is included at $F_z = 0$ for visual clarity. . . . .	133

5.3	Ratio of terms $ g_n^S / g_n^Q $ in Eqs. (5.21)–(5.22) for various spheres in a soft tissue-like medium ( $\mu = 100$ kPa) subject to a simple focused beam with confinement angle $\theta_0 = 30^\circ$ . Small ratio is indicated with blue shading, large ratio with red shading. . . .	139
5.4	Ratio of terms $ g_n^S / g_n^Q $ in Eqs. (5.21)–(5.22) for a spherical mass of castor oil in a soft tissue-like medium ( $\mu = 100$ kPa) subject to a simple focused beam with confinement angle $\theta_0 = 30^\circ$ . Small ratio is indicated with blue shading, large ratio with red shading. . . . .	140
5.5	Synthesized test field comprised of irrotational and solenoidal parts. Red dots mark a source of strength 0.9 at $(-1/2, -3/4)$ , a sink of strength 0.5 at $(-1/2, 0)$ , and two rotations of strength 0.7 and 1 centered at $(-1/4, -1/2)$ and $(1/2, 0)$ , respectively. Note that the deviation between the red dots and <i>apparent</i> centers of source, sink, and rotation is due to their being spatially near each other and of different strengths. . . . .	144
5.6	Irrotational potential for synthesized test field in Fig. 5.5 (left) and computed from numerical Helmholtz decomposition (right). . . . .	144
5.7	Acoustic radiation force function $Y_{p,z}$ on various spheres embedded in soft tissue-like media due to a simple focused beam with confinement angle $\theta_0 = 30^\circ$ . Solid lines indicate that both $F_z$ and $G_z$ force terms are included, whereas dashed lines show only $F_z$ . . . . .	147
5.8	Plots of the body force $g_n$ due to shear wave fields versus $kr$ at various angles outside a steel scatterer ( $kR = 1$ ) in a soft tissue-like medium with shear wave speed $c_t = 100$ m/s. The incident field is a simple focused beam with confinement angle $\theta_0 = 30^\circ$ . Note the logarithmic $x$ -axis so that oscillatory properties of $g_n$ may be seen for $kr$ just outside the sphere. . . . .	153
5.9	Displacement of a steel sphere ( $kR = 1$ ) versus domain size in a soft tissue-like medium with shear wave speed $c_t = 100$ m/s. The incident field is a simple focused beam with confinement angle $\theta_0 = 30^\circ$ . . . . .	155
5.10	FEM calculation of the displacement (blue dots) of a steel sphere embedded in a soft tissue-like medium ( $c_t = 100$ m/s) due to the body force $f_n + g_n$ . The incident field is a simple focused beam with confinement angle $\theta_0 = 30^\circ$ . . . . .	156

# Chapter 1

## Introduction

This dissertation presents a theory for acoustic radiation force on an elastic sphere surrounded by an infinite fluid to include the effects of shear forces exerted by a soft elastic medium surrounding the sphere. While for many years radiation force has been investigated for scatterers in ideal fluid media [1–10], viscous fluids [3, 11–16], and heat-conducting fluids [14, 17–19], until recently [20] a theory had not been developed for the case of scatterers embedded in soft elastic media that support the propagation of shear waves, which has important applications in biology and medicine. Improving the theoretical understanding of this last case is the main focus of this dissertation.

The primary application of acoustic radiation force on scatterers in soft elastic media is remote assessment of soft tissue health. Soft tissues have acoustic properties (density  $\rho$  and bulk modulus  $K$ ) very similar to those of water, but they also have a nonzero shear modulus  $\mu$  that is many orders of magnitude smaller than the bulk modulus [21]. The shear modulus correlates with tissue health and may be dramatically different for normal and abnormal tissues [22]. Since tissue health is frequently assessed through invasive surgical techniques such as biopsy, the past few decades have seen a strong push to

improve measurements of shear modulus in soft tissue through non-invasive means [23–25]. These methods typically make use of acoustic radiation force produced by the absorption of an incident beam in, and momentum transfer into, the surrounding soft tissue medium, then measuring the resulting displacements at a number of different locations within the tissue. Another goal of this dissertation is therefore to examine the practicality of investigating soft tissue health with acoustic radiation force due to scattering from a spherical inhomogeneity embedded within the tissue instead of that due to absorption of the incident beam. By determining the radiation force from a focused beam and measuring the resulting displacement of the scatterer within the tissue, one may expect to evaluate the shear stiffness of the tissue and draw conclusions about its health.

## 1.1 Brief History of Radiation Force Theory

Originally referred to as radiation pressure when proposed by Leonhard Euler in 1746 to explain why the tail of a comet points away from the sun [26], radiation force enjoys a long history that is often confusing and controversial in its subtler principles [9]. In his 1978 review, Beyer writes the following [27]: “It might be said that radiation pressure is a phenomenon that the observer thinks he understands—for short intervals, and only every now and then.” Bearing this propensity for confusion in mind, we shall begin by discussing the history of the theory of radiation force in fluids to prepare the reader for the extension to soft elastic media described in this dissertation. Several

equations are provided where necessary to facilitate the discussion of certain key concepts, but for the most part this section is meant to provide a physical overview.

As with many topics that are investigated in acoustics, a description of radiation pressure first appeared in optics. In 1874, James Clerk Maxwell published his treatise on electromagnetism [28] where he claimed that electromagnetic waves carry momentum and that they can exert a directional force on a scatterer. This claim was confirmed experimentally in 1901 by Lebedev [29] and in 1903 by Nichols and Hull [30]. Applications of optical radiation force have exploded in number since that time, and while they are far too numerous to list in detail here, it is worth mentioning that Arthur Ashkin received the 2018 Nobel Prize in Physics “for the optical tweezers and their application to biological systems” [31–33]. Optical tweezers were also used by Steven Chu, Claude Cohen-Tannoudji, and William D. Phillips in their work on laser cooling of neutral atoms, for which they received the 1997 Nobel Prize in Physics. Even over a hundred years after its initial mathematical description and experimental confirmation, radiation force remains relevant in applied physics.

Lord Rayleigh was the first to propose an analogous phenomenon in acoustics [34, 35], and an alternative definition was proposed by Langevin [36, 37], both of which were described for sound waves normally incident on a plane interface. According to Lee and Wang [9], the difference between the two can be described (and generalized to two and three dimensions) as follows:

the radiation force is of the Langevin type if it depends only on the waves themselves, and it is of the Rayleigh type if it depends on both the waves and a constraint. For example, the force due to reflection from the interior of the end of a closed tube, where the fluid in the tube is not allowed to interact with the fluid outside the tube, is of the Rayleigh type, whereas the force on a spherical scatterer surrounded by an infinite medium—the focus of this dissertation—is of the Langevin type because the infinite medium does not impose any additional constraints. In practice, Langevin radiation force is usually the more relevant quantity.

Another description of the radiation force, which was developed by Brillouin, is especially useful to mathematically describe the radiation force in an arbitrary volume or on an arbitrary scatterer. Brillouin first defined a quantity called the acoustic radiation stress tensor as [38]

$$S_{ij} = \langle \tilde{\sigma}_{ij} \rangle - \langle \rho v_i v_j \rangle , \quad (1.1)$$

where  $\rho$  represents density,  $v_i$  denotes particle velocity,  $\tilde{\sigma}_{ij}$  is the Cauchy stress tensor—equal to  $P\delta_{ij}$  in an ideal fluid, where  $P$  is the total pressure and  $\delta_{ij}$  is the Kronecker delta—and angled brackets indicate a time average. From this quantity, the force per unit volume in a fluid is found to be

$$F_i^V = \frac{\partial S_{ij}}{\partial \tilde{x}_j} , \quad (1.2)$$

where  $\tilde{x}_j$  denotes Eulerian position, and the force per unit area is found to be

$$F_i^S = S_{ij} \tilde{n}_j , \quad (1.3)$$

where  $\tilde{n}_j$  denotes the outward unit vector normal to an Eulerian surface. Whether explicitly or through less direct means, historical descriptions of radiation force on a scatterer in a fluid medium make use of the quantity in Eq. (1.1).

The first such calculation of radiation force on a scatterer, though not making explicit use of Brillouin’s reasoning, was performed by King, who examined radiation force on rigid spheres [1]. King noted that the force tends to push rigid spheres toward pressure nodes or antinodes depending on their size and density. He also noted that for spheres much smaller than an acoustic wavelength ( $kR \ll 1$ , where  $k$  is the compressional wavenumber and  $R$  is the sphere radius), the force is proportional to  $(kR)^6$  in plane traveling waves and proportional to  $(kR)^3$  in plane standing waves, indicating dramatic differences depending on the incident field and suggesting a much higher force on small particles in a standing wave. (Ergo, it is little wonder that in 1874, Kundt and Lehmann first experimentally demonstrated acoustic radiation force acting on particles in a standing wave [39], before any mathematical description of the phenomenon.) Gor’kov extended the analysis to arbitrary (but small) particles through a simpler method based in fluid dynamics, corroborating King’s conclusions for traveling and standing waves [7]. King’s results have been confirmed experimentally in a number of works [5, 40–42], two examples of which are shown in Fig. 1.1.

Westervelt applied Brillouin’s reasoning to scatterers of arbitrary size and shape [2, 3], though he did not analytically evaluate the force on non-

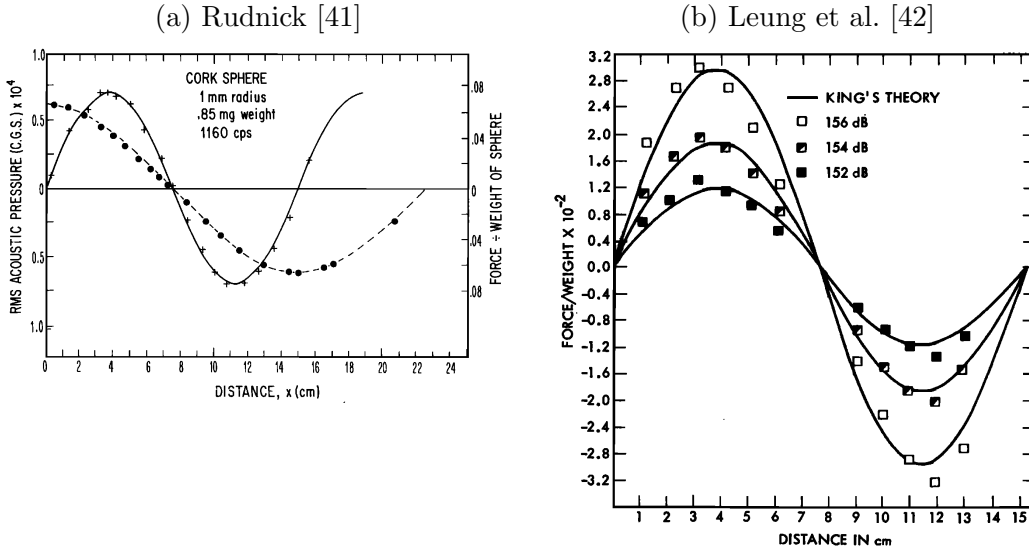


Figure 1.1: Experimental confirmation of King’s predictions for radiation force on spheres that are rigid compared with the surrounding air. (a) Measured acoustic pressure (plus signs) and acoustic radiation force divided by cork sphere weight (filled circles) compared with curves from King’s theory (from Rudnick [41]). (b) Acoustic force per weight of a polyethylene sphere for several sound pressure levels (from Leung et al. [42]).

spherical scatterers. Of particular importance is his recognition that in order to calculate the radiation force on the scatterer, it is not necessary to integrate the acoustic radiation stress tensor over the surface of the scatterer itself. Instead, a more convenient surface enclosing the scatterer can be chosen to yield a mathematically equivalent result. The process, as summarized by Lee and Wang [8, 9], is as follows. In Eulerian coordinates, conservation of momentum, which is written as

$$\rho \left( \frac{\partial v_n}{\partial t} + v_k \frac{\partial v_n}{\partial x_k} \right) = \frac{\partial \tilde{\sigma}_{nk}}{\partial x_k}, \quad (1.4)$$

and conservation of mass, which is written as

$$\frac{\partial \rho}{\partial t} + \frac{\partial(\rho v_k)}{\partial \tilde{x}_k} = 0, \quad (1.5)$$

can be combined to obtain

$$\frac{\partial(\rho v_n)}{\partial t} = \frac{\partial \tilde{\sigma}_{nk}}{\partial x_k} - \frac{\partial(\rho v_n v_k)}{\partial \tilde{x}_k}. \quad (1.6)$$

For time-harmonic quantities, time averaging Eq. (1.6) eliminates the time derivative term and gives, in terms of the acoustic radiation stress tensor defined in Eq. (1.1),

$$\frac{\partial S_{nk}}{\partial \tilde{x}_k} = 0, \quad (1.7)$$

which describes that force per unit volume due to the radiation stress tensor is zero in the region surrounding the sphere. By integrating over a volume surrounding the sphere and using the divergence theorem, we can find the radiation force  $F_n$  to be

$$\begin{aligned} F_n &= - \int_{\tilde{S}} (\langle \tilde{\sigma}_{nk} \rangle - \langle \rho v_n v_k \rangle) \tilde{n}_k d\tilde{S} \\ &= \int_{\tilde{S}_0} (\langle \tilde{\sigma}_{nk} \rangle - \langle \rho v_n v_k \rangle) \tilde{n}_k d\tilde{S}_0, \end{aligned} \quad (1.8)$$

where  $\tilde{S}$  is the surface of the sphere and  $\tilde{S}_0$  is a (possibly much larger) surface that encloses the sphere. (The difference in sign occurs because  $\tilde{n}_k$  points away from the volume bounded by  $\tilde{S}$  and  $\tilde{S}_0$ , meaning it points inward from  $\tilde{S}$  and outward from  $\tilde{S}_0$ .) Though not often used in early derivations of the radiation force on spherical scatterers, this technique allows for the use of far-field expressions of pressure and particle velocity, which simplifies the analysis

compared with integrating at the scatterer surface itself. This same property will be noted in Chapter 2 in the derivation of the radiation force due to compressional wave fields, and its implications for the force associated with shear wave fields are briefly discussed in Chapter 5.

For spherical scatterers of arbitrary size, Yosioka and Kawasima integrated the acoustic radiation stress tensor over the equilibrium sphere radius to provide relations for the force on compressible spheres subject to plane waves [4]. In addition to confirming several of King's results, they noted several interesting effects for gas bubbles. First, they observed that the magnitude of the radiation force increases rapidly near the bubble resonance, and second, for standing wave fields, they observed that the bubble is pushed toward either pressure nodes or antinodes depending on whether the frequency is above or below the bubble resonance, respectively; both of these effects are discussed further in Chapter 4. The results obtained by Yosioka and Kawasima have repeatedly been verified experimentally [43, 44].

Hasegawa and Yosioka extended the analysis of Yosioka and Kawasima to solid elastic spheres of arbitrary size [5] and found several interesting results when comparing with King's theory. In particular, they found that there are noticeable deviations from King's theory around resonances associated with normal modes of the free vibration of the sphere. As with the results presented by Yosioka and Kawasima for compressible spheres [4], Hasegawa and Yosioka noted that the elastic properties of a hard scatterer have a significant effect on the radiation force on the scatterer. Since Hasegawa and Yosioka

were investigating the use of radiation force for measuring acoustic intensity in a wave, they concluded that these sphere resonances must be considered for accurate determination of the intensity—and that they should be avoided, if possible, so as to not confound the measurement. The analytical results obtained by Hasegawa and Yosioka were experimentally confirmed in the same work [5] as well as by a number of other works [6, 45–48], and as their theory allows for spheres with arbitrary material properties, it has become an important benchmark, and it will be used as such in Chapter 2.

While most early works focused their discussions on simple plane waves or converging/diverging spherical waves [49] incident on the sphere, there have since been many investigations of sound beams incident on spheres. For reasons of analytical simplicity, axisymmetric beams were considered first [50–52], but advances in computing and numerical techniques have recently allowed for simulations of radiation force due to more complicated beam geometries [10, 53–56]. Several peculiar results can arise from more complicated incident fields, including direction reversal of the force such that the scatterer is pushed in a direction opposite the propagation direction of the beam [52–54], so incident sound beams have received greater attention as of late. The present work therefore considers arbitrary fields incident on the sphere and compares the resulting changes in amplitude and direction of the predicted radiation force for several different cases.

In addition to the work cited above describing the force on a sphere in an ideal fluid, there have been a number of discussions of the effects of viscosity

in the fluid. Westervelt first noted [2] that for spheres that are small compared to a wavelength ( $kR \ll 1$ ), viscous forces at the sphere surface can cause the radiation force to be several orders of magnitude higher than predicted by King. The effect of viscosity on the radiation force on small spheres was further examined by Doinikov to include effects related to acoustic streaming [11–14], and he noted several interesting effects depending on the viscous wave penetration depth  $\delta$ , written as [57]

$$\delta = \sqrt{\frac{2\eta}{\omega\rho}} \quad (1.9)$$

where  $\eta$  is the dynamic viscosity and  $\omega$  is angular frequency. In particular, for  $R/\delta \ll 1$ , the force on the sphere may be opposite the direction of propagation of the incident wave, and he posited that good theoretical agreement with inviscid fluid predictions in previous experiments could be attributed to large  $R/\delta$ . For example, Rudnick’s experiments use spheres with  $R/\delta$  between 9.2 and 69.4 and show good agreement with King’s theory [41]. However, as noted by Danilov and Mironov [15], even for  $R/\delta \gg 1$  the magnitude of the force can be much greater in viscous fluid than in inviscid fluid for small spheres ( $kR \ll 1$ ) in traveling waves. Danilov and Mironov also consider more general incident fields and simplify the analysis, and later work by Settnes and Bruus [16] contains a discussion of the more experimentally relevant parameter range characterized by  $R/\delta = O(1)$ , which is useful for microchannel acoustophoresis of compressible particles in liquids.

Still, to the present author’s knowledge, previous analyses related to viscosity have only addressed sphere sizes much smaller than an acoustic wave-

length. Additionally, while there are several authors who discuss radiation force in elastic solids due to traveling waves [58, 59] and perform experiments confirming the resulting predictions of acoustic-radiation induced static strain [60], in existing literature there are few analyses of acoustic radiation force on scatterers embedded in elastic media. This dissertation will therefore address effects related to shear modulus in soft elastic media. The choice of “soft” elastic media allows for several useful approximations to be made to the Piola-Kirchhoff stress tensor (discussed in Chapter 2) and is especially applicable to soft tissue surrounding a scatterer. Also, though effects due to heat conduction and streaming will be ignored as a result of the aforementioned approximation, effects related to viscosity will be examined as well so as to both compare with effects due to shear modulus and also offer qualitative comparisons with the results mentioned previously.

## 1.2 Applications of Acoustic Radiation Force

In order to appreciate the relevance of acoustic radiation force on scatterers in soft elastic media, it is useful to discuss existing applications of acoustic radiation force. The phenomenon has a wide variety of applications in biology and medicine [61], including acoustic tweezers [50], cell trapping [62] and nonintrusive manipulation of microparticles [63], acoustomicrofluidics for particle sorting [64], repositioning kidney stones [65], targeting nanodroplets and microbubbles for imaging and therapy [66, 67], etc. These are just a few of the many applications, so in this section there will only be a discussion of

those most relevant to soft tissue elastography.

While the primary focus of this dissertation is acoustic radiation force on a sphere, many existing applications of acoustic radiation force in soft tissue elastography make use of a different physical mechanism: absorption in the medium. The force per unit volume due to absorption of an incident acoustic field is described by the relation [68, 69]

$$F^V = \frac{2\alpha\langle I \rangle}{c_l}, \quad (1.10)$$

where  $\alpha$  is the attenuation coefficient in the medium [Np/m],  $I$  is the intensity of the incident field, and  $c_l$  is the compressional (longitudinal) wave speed in the medium. This mechanism differs from that discussed in the remainder of this dissertation, but it is important to discuss as a comparison because of its existing clinical applications and because in a medium without scatterers of contrasting material properties, absorption is the primary mechanism of attenuation instead of scattering [70]. In particular, the techniques that will be discussed in the present section are shear wave elasticity imaging, acoustic radiation force impulse imaging, supersonic shear imaging, and harmonic motion imaging.

In shear wave elasticity imaging (SWEI) [23], an ultrasound transducer is used to produce a beam focused in a localized region of excitation (ROE) within the tissue. The higher acoustic intensity in this focused region causes a higher radiation force due to absorption per Eq. (1.10), and this radiation force causes the region to displace. This displacement results in the propagation

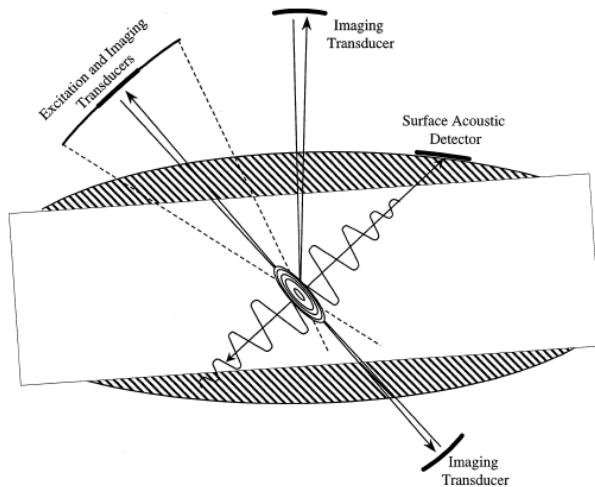


Figure 1.2: Schematic of shear wave elasticity imaging with multiple imaging transducers and detection sensors (from Sarvazyan et al. [23]).

of shear waves from the ROE through the surrounding tissue. These shear waves are then detected by a variety of possible techniques, including the use of the same excitation transducer or other ultrasound pulse-echo imaging transducers, magnetic resonance imaging, or detection of shear waves at the surface of the tissue. (See Fig. 1.2 for a diagram of such a setup, reproduced from Sarvazyan et al. [23].) SWEI has been used extensively since its inception because it allows for quantitative analysis of the tissue (e.g., evaluating liver tissue [71]), and it plays a central role in supersonic shear imaging [25]. Axial elasticity (i.e., stiffness in the direction of propagation of the incident field) in the ROE itself is not assessed in this method.

In acoustic radiation force impulse (ARFI) imaging [24, 72, 73], the mechanism of inducing displacement in the tissue is the same, but the mea-

surement is different. With ARFI imaging, the axial displacement of the tissue is tracked in the focal region itself. By probing multiple locations and tracking the axial displacement at each, a two-dimensional B-mode type image can be constructed, giving a comprehensive relational map of shear stiffness in different parts of the tissue. Axial elasticity is assessed in this modality, and the spatial resolution is typically higher than in SWEI [73], but the effect of the propagating shear waves is not considered and the analysis is of the *relative* shear stiffness in the medium as opposed to the *absolute* shear stiffness. The ARFI imaging method is therefore a more qualitative method of tissue assessment.

Supersonic shear imaging (SSI) [25, 74, 75] makes use of SWEI to create a real-time map of tissue stiffness. This technique involves focusing a beam at different depths in rapid succession, such that the movement of the focus is faster than the shear wave speed in the medium to be imaged. An example of this process is shown in Fig. 1.3 (from Bercoff et al. [25]). The resulting displacements are imaged through the use of an ultrafast imaging system to capture results at several thousand frames per second, giving a real-time look at a relatively large region even in strongly viscous media. The shear elasticity in the medium can then be determined quantitatively through inversion and comparison with the wave propagation data. This approach has been demonstrated to be clinically useful for a number of different tissues, including breast [76, 77], muscle [78], thyroid [79, 80], and liver tissues [81, 82], as well as thermally induced lesions [83].

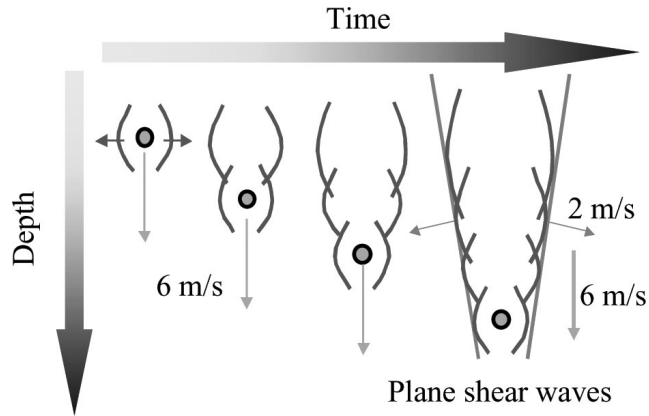


Figure 1.3: Diagram of supersonic shear imaging with the source being moved along the beam axis three times as fast as the shear waves propagating away from the region (from Bercoff et al. [25]).

Finally, harmonic motion imaging (HMI) [84] creates an oscillating acoustic radiation force in the tissue through the use of focused, amplitude-modulated incident wave fields. This oscillating force results in an oscillating displacement within the tissue, and unlike the other methods described above, HMI involves tracking the displacement during the excitation instead of after. Displacements produced via HMI have been shown to correlate with Young’s modulus in tissue-mimicking gel phantoms [85], and since the imaging occurs during excitation, Suomi et al. have also identified it as a useful candidate for real-time monitoring of high intensity focused ultrasound (HIFU) and other such therapies [86–88].

For acoustic radiation force due to scattering—the mechanism of interest in this dissertation—instead of absorption, there have also been several recent attempts at quantifying shear modulus of a soft elastic medium. Based

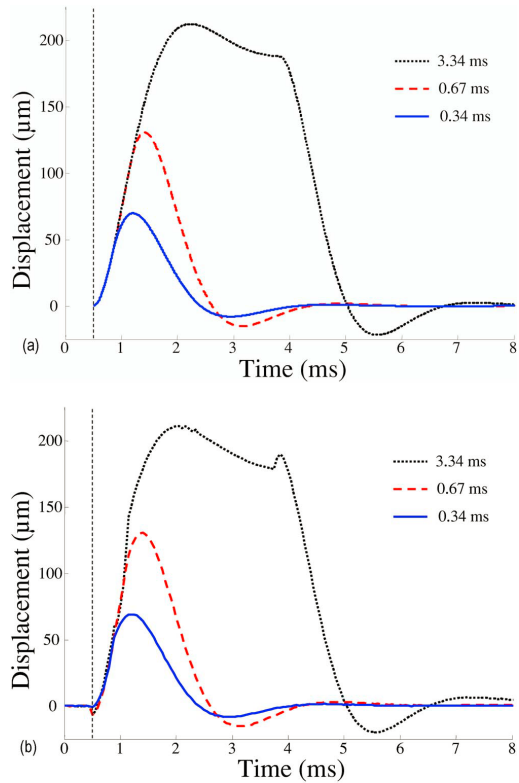
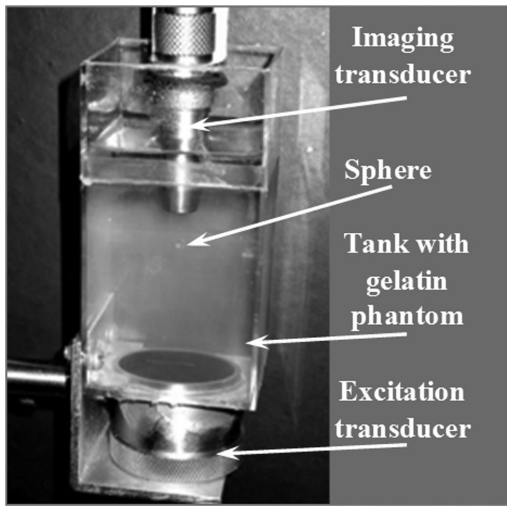


Figure 1.4: Experimental setup (left, from Karpouk et al. [89]) and results (right, from Aglyamov et al. [90]) for examining transient displacement of a sphere in a viscoelastic gel phantom due a short pulses of various durations. On the right, (a) shows the theoretical prediction of sphere displacement and (b) shows experimental measurement.

on theory by Ilinskii et al. [91] for displacement of gas bubbles and solid spheres in soft elastic media, Aglyamov et al. [90] and Karpouk et al. [89] studied transient sphere motion as a result of radiation force due to a short burst of ultrasound. As shown in Fig. 1.4, they found excellent agreement between theory and experiment in the temporal characteristics of the displacement curve for various spheres, and they noted that the shape of the displacement waveform

was only dependent on shear modulus and pulse length, not on the intensity of the incident field (or, correspondingly, the magnitude of the radiation force). While they did not know the magnitude of the radiation force that would be induced on the sphere beforehand, they were still able to determine shear modulus in the gel phantom and later determine the magnitude of the radiation force by matching their measured transient responses with theoretical predictions of the time waveforms.

The method of determining shear modulus from sphere displacement due to radiation force has also been used in *ex vivo* tissue measurements as well, such as by Yoon et al. [92, 93], who created a microbubble by focusing a laser in various animal crystalline lenses and then pushed the bubble with compressional waves radiated by an ultrasound transducer, finding similarly strong agreement between experiment and theory. The method may also be useful in other tissues where microbubbles can be delivered via the blood stream. Since microbubbles are often used as contrast agents to enhance reflectivity in regions of interest within the tissue or as mechanisms for drug delivery [66, 94–96], they might also be useful as scattering targets for acoustic radiation force measurements. Furthermore, to assist magnetic resonance imaging of tissue for the purpose of identifying a region, metallic markers are often placed in the tissue [97–100], so these could also be used as scattering targets to probe with a focused ultrasound beam.

However, in determining soft tissue characteristics from the acoustic radiation force on a sphere and its resulting displacement, there is an im-

portant missing piece of information that currently limits the utility of this method *in vivo*: the actual radiation force on the scatterer. As discussed in Sec. 1.1, existing literature has examined spheres in fluid media, and while the radiation force in soft tissue might reasonably be expected to be similar to that in water due to its similar density and compressional wave speed, we will see in this dissertation that even weak shear effects can cause the predicted force to deviate noticeably from what would be expected in water. Furthermore, while absorption is the dominant mechanism for attenuation of an incident beam in tissue due to the similarity with water, there are useful applications where scatterers are added intentionally to the tissue. For scatterers that are sufficiently large and that have mechanical properties that are sufficiently different from those of the surrounding tissue, the scattering mechanism of radiation force becomes dominant, and is therefore useful to investigate further. Improved understanding of the radiation force in soft elastic media due to this scattering mechanism is the primary goal of this dissertation.

### **1.3 Dissertation Overview**

The dissertation proceeds as follows. In Chapter 2, a theoretical framework is presented for modeling acoustic radiation force on a sphere in a soft elastic medium. The relevant elastodynamic equations, stress tensors, body forces, and displacement field equations are defined, and instead of Eulerian coordinates, the analysis is performed in Lagrangian coordinates, which are more often used in elasticity. The expressions for radiation force obtained in

Chapter 2 are found to recover existing analytical results for the special case of radiation force on a sphere in fluid, and they are used throughout the dissertation.

In Chapter 3, mathematical descriptions of the incident and scattered wave fields are presented in greater detail. Since the incident field is described by a spherical harmonic expansion, a process for finding the coefficients in this expansion is described. Instead of the usual two-dimensional angular spectrum method used in acoustics [101], a three-dimensional angular spectrum description is used because a) it lends itself to a convenient expression for the coefficients of a focused sound beam, and b) a two-dimensional angular spectrum description can be reformulated in three dimensions without tremendous difficulty [102]. The scattered field coefficients are examined for a variety of different scatterers and soft tissue-like medium properties, with special emphasis on scattering resonances and the effects of elasticity that become important for the calculation of the acoustic radiation force.

Results for acoustic radiation force due to incident and scattered compressional wave fields in a soft elastic medium are presented in Chapter 4. While this does not present a complete description of the radiation force on a scatterer in a soft tissue-like medium, which is the subject of Chapter 5, it is useful as a preliminary investigation of the types of phenomena that we may expect to be important when shear wave effects must be taken into account. In particular, results associated with shifting resonance frequencies and reversals in the direction of the force provide specific parameter ranges that might be

interesting to investigate experimentally. Though the main focus of Chapter 4 is the effect of shear modulus, since that is the parameter of interest in actual soft tissue, effects due to viscosity are also considered to compare quantitatively with shear modulus and qualitatively with existing work on radiation force in viscous fluids.

Results for acoustic radiation force associated with the scattered shear wave are presented in Chapter 5. As this contribution to the radiation force does not appear to lend itself to a purely analytical approach, several alternative methods are explored: an approximation to the body force due to shear wave fields in the surrounding medium that may allow for an analytical result for some special cases, a semi-analytical description involving a numerical Helmholtz decomposition of this body force and integration of the resulting irrotational potential, and a fully numerical finite element method (FEM) result to compare expected displacements of a hard sphere in an elastic medium.

Finally, in Chapter 6, the key results of the dissertation are summarized and possible avenues for future work are recommended.

## Chapter 2

# Theoretical Framework for Acoustic Radiation Force on an Elastic Sphere in a Soft Elastic Medium

The purpose of this chapter is to develop the general theoretical framework for acoustic radiation force on a spherical scatterer in a soft elastic medium. As this is meant to introduce the reader to the concept of radiation force on a spherical scatterer, it includes a discussion of the basic physical principles and mathematics required, but it does not include exhaustive treatment of the mathematical steps. The expressions for radiation force obtained herein are used throughout the dissertation. The main results presented in this chapter appear in a recently published paper [20], with several of the results also appearing in prior conference proceedings [103, 104]. The present chapter provides additional details and discussion.

Several assumptions are made to simplify the analysis. First, the incident field is assumed to be represented via purely compressional waves in an

---

Yu. A. Ilinskii, E. A. Zabolotskaya, B. C. Treweek, and M. F. Hamilton, “Acoustic radiation force on an elastic sphere in a soft elastic medium,” *J. Acoust. Soc. Am.*, vol. 144, no. 2, pp. 568–576, 2018. The author of the present work verified the force  $F_n$  due to compressional wave fields by analytical comparison with Sapozhnikov and Bailey [10], elaborated on the force  $G_n$  due to the scattered shear wave and its physical significance, and discussed the Wigner D-matrix transformation of incident field coefficients  $a_n^m$ .

infinite medium. Radiation force due to incident shear waves may be found using comparable analysis, but due to the prevalent use of compressional wave transducers in assessment of soft tissue, incident shear waves are not considered here. Shear waves only arise due to mode conversion from the incident compressional wave field to the fields scattered from, and transmitted into, the scatterer. Second, the wave amplitudes are assumed to be such that nonlinear propagation effects (e.g., waveform steepening and the formation of shocks) can be ignored. Third, momentum transfer from the incident beam to the medium via absorption is assumed to be negligible. If this were included, then the deformation of the medium due to absorption of the incident field would need to be taken into account, which causes both radiation of shear waves from the compressional wave beam prior to interaction with the sphere, and displacement of the sphere due to deformation of the medium associated with absorption. Neither of these effects is addressed here. Fourth, effects related to acoustic streaming (addressed in Refs. [11, 12]) and heat conduction (addressed in Refs. [17–19]) are also ignored here.

Finally, to exploit basic symmetry, the scattering target embedded in the medium is assumed to be spherical with radius  $R$ . Therefore, much of the analysis is performed in spherical coordinates  $(r, \theta, \phi)$ , where  $r$  is the distance from the origin,  $\theta$  is the polar angle, and  $\phi$  is the azimuthal angle. A brief discussion of relevant definitions and notation conventions is included in Appendix A.

Section 2.1 begins with an introduction of the relevant elastodynamic

equations and radiation force terms. The distinct contributions to the radiation force on a sphere are described in Sec. 2.2, and the use of Lagrangian coordinates instead of the more classical Eulerian coordinates is explained and justified in Sec. 2.3. Then in Sec. 2.4 an expression for radiation force on a sphere due to compressional wave fields, which is complete for a sphere in fluid, is obtained. In Sec. 2.5 this expression is compared with previously obtained results to demonstrate its validity. Finally, in Sec. 2.6, the analytic portion of the radiation force due to scattered shear wave fields is obtained.

## 2.1 Elastodynamic Equations

Though much of the analysis in this chapter will be performed in Lagrangian coordinates, classical derivations of acoustic radiation force on a scatterer in a fluid usually employ Eulerian coordinates [4, 5]; see also the review by Wang and Lee [105]. In Eulerian coordinates, the elastodynamic equations of motion are [106]

$$\rho \left( \frac{\partial v_n}{\partial t} + v_k \frac{\partial v_n}{\partial \tilde{x}_k} \right) = \frac{\partial \tilde{\sigma}_{nk}}{\partial \tilde{x}_k}, \quad (2.1)$$

$$\frac{\partial \rho}{\partial t} + \frac{\partial(\rho v_k)}{\partial \tilde{x}_k} = 0, \quad (2.2)$$

where  $\tilde{x}_k$  denotes Eulerian position,  $\rho$  is the density in the deformed configuration,  $v_n$  denotes particle velocity, and  $\tilde{\sigma}_{nk}$  represents the Cauchy stress tensor. For a fluid, the Cauchy stress tensor is  $\tilde{\sigma}_{nk} = -P\delta_{nk}$ , where  $P$  is the pressure and  $\delta_{nk}$  is the Kronecker delta. In Lagrangian coordinates, the equations of

motion are [106]

$$\rho_0 \frac{\partial^2 u_n}{\partial t^2} = \frac{\partial \sigma_{nm}}{\partial x_m}, \quad (2.3)$$

where  $x_m$  denotes Lagrangian position,  $\rho_0$  is the density in the reference configuration,  $u_n = \tilde{x}_n - x_n$  denotes particle displacement, and  $\sigma_{nm}$  is the first Piola-Kirchhoff pseudostress tensor. Here,  $\sigma_{nm}$  is not symmetric, and the quantity  $\sigma_{nm} n_m$  represents the force in the deformed configuration acting on a unit area with normal  $n_m$  in the reference configuration.

The Eulerian and Lagrangian descriptions are equivalent because the Cauchy stress tensor and Piola-Kirchhoff pseudostress tensor are connected via

$$\rho \sigma_{nm} = \rho_0 \tilde{\sigma}_{nk} \frac{\partial x_m}{\partial \tilde{x}_k}, \quad (2.4)$$

$$\rho_0 \tilde{\sigma}_{nk} = \rho \sigma_{nm} \frac{\partial \tilde{x}_k}{\partial x_m}, \quad (2.5)$$

where  $\partial \tilde{x}_k / \partial x_m$  is the deformation gradient, which ultimately allows for either formulation to be used. However, for calculation of the acoustic radiation force on a scatterer in a soft elastic medium, Eq. (2.3) is more convenient for several reasons. First, the position of the scatterer is fixed in the reference frame of interest—that is, the integration of the first Piola-Kirchhoff pseudostress tensor can be performed over fixed Lagrangian coordinates—which is especially useful in problems pertaining to elasticity. Second, nonlinearity arises only in  $\sigma_{nm}$ , which simplifies the analysis. Except for a brief comparison with results in Eulerian coordinates in Sec. 2.3, the remainder of the analysis is therefore performed in Lagrangian coordinates.

### 2.1.1 Stress Tensor and Body Force

The first Piola-Kirchhoff pseudostress tensor (hereafter referred to as simply the “stress tensor” for convenience) can be expressed through the strain energy density  $\mathcal{E}$  as

$$\sigma_{nm} = \frac{\partial \mathcal{E}}{\partial (\partial u_n / \partial x_m)}. \quad (2.6)$$

To third order in the particle displacement, the energy density is, based on the expansion of Landau and Lifshitz [107],

$$\begin{aligned} \mathcal{E} = & \frac{\mu}{4} \left( \frac{\partial u_i}{\partial x_k} + \frac{\partial u_k}{\partial x_i} \right)^2 + \frac{1}{2} \left( K - \frac{2\mu}{3} \right) \left( \frac{\partial u_l}{\partial x_l} \right)^2 \\ & + \left( \mu + \frac{A}{4} \right) \frac{\partial u_i}{\partial x_k} \frac{\partial u_l}{\partial x_i} \frac{\partial u_l}{\partial x_k} + \frac{1}{2} \left( K + B - \frac{2\mu}{3} \right) \frac{\partial u_l}{\partial x_l} \left( \frac{\partial u_i}{\partial x_k} \right)^2 \\ & + \frac{A}{12} \frac{\partial u_i}{\partial x_k} \frac{\partial u_k}{\partial x_l} \frac{\partial u_l}{\partial x_i} + \frac{B}{2} \frac{\partial u_i}{\partial x_k} \frac{\partial u_k}{\partial x_i} \frac{\partial u_l}{\partial x_l} + \frac{C}{3} \left( \frac{\partial u_l}{\partial x_l} \right)^3, \end{aligned} \quad (2.7)$$

where  $K$  is bulk modulus,  $\mu$  is shear modulus, and  $A$ ,  $B$ , and  $C$  are nonlinear elastic constants (also referred to as the third-order elastic constants). The stress tensor can be written to second order as

$$\sigma = \sigma_{nm}^{(1)} + \sigma_{nm}^{(2)}, \quad (2.8)$$

where  $\sigma_{nm}^{(1)}$  and  $\sigma_{nm}^{(2)}$  are linear and nonlinear parts of the tensor, respectively.

From Eqs. (2.6)–(2.7), these are found to be

$$\sigma_{nm}^{(1)} = \mu \left( \frac{\partial u_n}{\partial x_m} + \frac{\partial u_m}{\partial x_n} \right) + \left( K - \frac{2\mu}{3} \right) \left( \frac{\partial u_l}{\partial x_l} \right) \delta_{nm}, \quad (2.9)$$

and

$$\begin{aligned}
\sigma_{nm}^{(2)} = & \left( \mu + \frac{A}{4} \right) \left( \frac{\partial u_l}{\partial x_n} \frac{\partial u_l}{\partial x_m} + \frac{\partial u_m}{\partial x_l} \frac{\partial u_n}{\partial x_l} + \frac{\partial u_l}{\partial x_m} \frac{\partial u_n}{\partial x_l} \right) \\
& + \frac{1}{2} \left( K + B - \frac{2\mu}{3} \right) \left[ \left( \frac{\partial u_i}{\partial x_k} \right)^2 \delta_{nm} + 2 \frac{\partial u_l}{\partial x_l} \frac{\partial u_n}{\partial x_m} \right] \\
& + \frac{A}{4} \frac{\partial u_m}{\partial x_l} \frac{\partial u_l}{\partial x_n} + B \left( \frac{\partial u_l}{\partial x_l} \frac{\partial u_m}{\partial x_n} + \frac{1}{2} \frac{\partial u_i}{\partial x_k} \frac{\partial u_k}{\partial x_i} \delta_{nm} \right) + C \left( \frac{\partial u_l}{\partial x_l} \right)^2 \delta_{nm}.
\end{aligned} \tag{2.10}$$

When calculating the radiation force on a sphere, the first step will be to directly integrate the stress tensor  $\sigma_{nm}^{(2)}$  over the surface of the sphere.

The stress tensor also gives rise to the body force

$$f_n = f_n^{(1)} + f_n^{(2)} = \frac{\partial \sigma_{nm}^{(1)}}{\partial x_m} + \frac{\partial \sigma_{nm}^{(2)}}{\partial x_m}, \tag{2.11}$$

and from Helmholtz's theorem, this force can be separated into conservative (or potential) and non-conservative parts as

$$\mathbf{f} = \nabla \Phi + \nabla \times \mathbf{A}, \tag{2.12}$$

where  $\Phi$  is a scalar and  $\mathbf{A}$  is a vector. Potential forces produced by the time-averaged stress tensor do not contribute to the net radiation force acting on the sphere and are instead offset by equal and opposite reaction forces due to the static deformation of the medium. Mathematically, this manifests as an additional stress tensor,

$$\sigma_{nm}^P = -\Phi \delta_{nm}, \tag{2.13}$$

where superscript  $P$  indicates that this involves purely potential forces. When calculating the radiation force on a sphere, the second step will be to integrate this derived stress tensor over the surface of the sphere.

According to measurements by Catheline et al. [21], the elastic constants  $\mu$ ,  $A$ , and the combination  $(K + B)$  are several orders of magnitude less than  $K$ ,  $B$ , and  $C$  for soft elastic media like tissue. Hamilton et al. [108] subsequently proved that the first term in Eq. (2.9) and the first three terms in Eq. (2.10) can be ignored, and that since  $K + B = O(\mu/K)$ , we can replace  $B$  with  $-K$ . Also note that when the body force is calculated from Eq. (2.11), all terms including  $\delta_{nm}$  will be potential, and may therefore be removed. This removes the second term in Eq. (2.9) and all but one term in Eq. (2.10),

$$\sigma_{nm}^B = -K \frac{\partial u_l}{\partial x_l} \frac{\partial u_m}{\partial x_n}, \quad (2.14)$$

with corresponding body force

$$f_n^B = -K \frac{\partial}{\partial x_m} \left( \frac{\partial u_l}{\partial x_l} \frac{\partial u_m}{\partial x_n} \right). \quad (2.15)$$

The superscript  $B$  indicates the relevant third-order elastic constant in the full stress tensor that remains after simplification. This is the only term that must be considered in the Lagrangian description of radiation force on a sphere in a soft elastic medium.

The additional stress tensor in Eq. (2.13) and the removal of terms in  $\sigma_{nm}^{(2)}$  that are proportional to  $\delta_{nm}$  follow from the lack of constraints on the medium. In the case of, say, a medium enclosed by a tube, then terms proportional to  $\delta_{nm}$  may need to be retained due to external forces imposed by the tube walls. This may result in a dependence of the radiation force on third-order elastic constant  $C$  as well, but this case is not treated here.

As a result, Eqs. (2.14) and (2.15) are independent of any third-order elastic constants.

### 2.1.2 Displacement Field Equations

Next, in order to evaluate the stress tensor, it is necessary to calculate the particle displacement  $\mathbf{u}$ . This vector can be decomposed in several ways. First, it can be separated into compressional and shear components, which are assigned superscripts  $l$  for “longitudinal” and  $t$  for “transverse”, respectively, after Landau and Lifshitz [107]:

$$\mathbf{u} = \mathbf{u}^l + \mathbf{u}^t. \quad (2.16)$$

Second, each of these components can be decomposed into linear (first order) and nonlinear (second order) parts as

$$\mathbf{u}^l = \mathbf{u}^{l1} + \mathbf{u}^{l2}, \quad (2.17)$$

$$\mathbf{u}^t = \mathbf{u}^{t1} + \mathbf{u}^{t2}. \quad (2.18)$$

Substitution of  $u_n$  into  $\sigma_{nm}$ , both into Eq. (2.3), and subsequent manipulation yield linear equations for  $\mathbf{u}^{l1}$  and  $\mathbf{u}^{t1}$ ,

$$\nabla^2 \mathbf{u}^{l1} - \frac{1}{c_l^2} \frac{\partial^2 \mathbf{u}^{l1}}{\partial t^2} = 0, \quad (2.19)$$

$$\nabla^2 \mathbf{u}^{t1} - \frac{1}{c_t^2} \frac{\partial^2 \mathbf{u}^{t1}}{\partial t^2} = 0, \quad (2.20)$$

and linear equations for  $\mathbf{u}^{l2}$  and  $\mathbf{u}^{t2}$ ,

$$\nabla^2 \mathbf{u}^{l2} - \frac{1}{c_l^2} \frac{\partial^2 \mathbf{u}^{l2}}{\partial t^2} = \nabla \cdot \boldsymbol{\sigma}|_{\mathbf{u}^{t1}}, \quad (2.21)$$

$$\nabla^2 \mathbf{u}^{t2} - \frac{1}{c_t^2} \frac{\partial^2 \mathbf{u}^{t2}}{\partial t^2} = \nabla \cdot \boldsymbol{\sigma}|_{\mathbf{u}^{t1}}. \quad (2.22)$$

The linear parts are now defined in terms of displacement potentials  $\varphi$  and  $\Theta$  as [109]

$$\mathbf{u}^{l1} = \nabla \varphi, \quad (2.23)$$

$$\mathbf{u}^{t1} = \nabla \times \nabla \times (\mathbf{r}\Theta), \quad (2.24)$$

which obey the same wave equations as their respective displacements. For time-harmonic particle displacement with angular frequency  $\omega$ , Eqs. (2.19) and (2.20) can be written as Helmholtz equations in terms of the displacement potentials,

$$\nabla^2 \varphi + k^2 \varphi = 0, \quad (2.25)$$

$$\nabla^2 \Theta + \kappa^2 \Theta = 0, \quad (2.26)$$

where  $k = \omega/c_l$  is the compressional wavenumber and  $\kappa = \omega/c_t$  is the shear wavenumber.

The displacement potentials can be expressed as

$$\varphi = \frac{1}{2} (\psi e^{-i\omega t} + \psi^* e^{i\omega t}) = \frac{1}{2} \psi e^{-i\omega t} + \text{c.c.}, \quad (2.27)$$

$$\Theta = \frac{1}{2} (\Pi e^{-i\omega t} + \Pi^* e^{i\omega t}) = \frac{1}{2} \Pi e^{-i\omega t} + \text{c.c.}, \quad (2.28)$$

where c.c. denotes complex conjugate. Spatial dependence of  $\varphi$  and  $\Theta$  appears only in the functions  $\psi$  and  $\Pi$ , which are described through spherical harmonic expansions. The function  $\psi$  contains incident, scattered, and transmitted compressional fields  $\psi_i$ ,  $\psi_s$ , and  $\psi_t$ , respectively, and the function  $\Pi$  contains scattered and transmitted shear fields  $\Pi_s$  and  $\Pi_t$ , respectively. For an arbitrary incident compressional wave, the expansions are

$$\psi_i = \sum_{n=0}^{\infty} \sum_{m=-n}^n a_n^m j_n(kr) P_n^m(\cos \theta) e^{im\phi}, \quad (2.29)$$

$$\psi_s = \sum_{n=0}^{\infty} \sum_{m=-n}^n A_n a_n^m h_n^{(1)}(kr) P_n^m(\cos \theta) e^{im\phi}, \quad (2.30)$$

$$\psi_t = \sum_{n=0}^{\infty} \sum_{m=-n}^n C_n a_n^m j_n(k_p r) P_n^m(\cos \theta) e^{im\phi}, \quad (2.31)$$

$$\Pi_s = \sum_{n=1}^{\infty} \sum_{m=-n}^n B_n a_n^m h_n^{(1)}(\kappa r) P_n^m(\cos \theta) e^{im\phi}, \quad (2.32)$$

$$\Pi_t = \sum_{n=1}^{\infty} \sum_{m=-n}^n D_n a_n^m j_n(\kappa_p r) P_n^m(\cos \theta) e^{im\phi}. \quad (2.33)$$

The incident compressional wave field is characterized by coefficients  $a_n^m$ , and scattered and transmitted field coefficients are respectively described by  $A_n$  and  $C_n$  for compressional waves and by  $B_n$  and  $D_n$  for shear waves. (Note that due to the spherical symmetry of the scatterer, the scattered and transmitted field coefficients have no dependence on  $m$ . The computation of these coefficients is discussed in Sec. 3.3.) The medium has compressional wavenumber  $k$  and shear wavenumber  $\kappa$ , and the sphere has compressional wavenumber  $k_t$  and shear wavenumber  $\kappa_t$ . Finally,  $P_n^m(\cos \theta)$  are the associated Legendre functions,  $j_n(z)$  are the spherical Bessel functions, and  $h_n^{(1)}(z)$  are the spherical

Hankel functions of the first kind corresponding to outgoing waves. Hereafter  $h_n^{(1)}(z)$  will be written  $h_n(z)$  with no superscript for notational convenience. The special case of an axisymmetric incident field is represented by setting  $m = 0$ .

Another simplification involving the stress tensor that proves useful is obtained by noting that since  $\mathbf{u}^l$  is irrotational and  $\mathbf{u}^t$  is solenoidal, then

$$\nabla \cdot \mathbf{u} = \nabla \cdot \mathbf{u}^l = \nabla^2 \varphi = -k^2 \varphi, \quad (2.34)$$

substitution of which into Eq. (2.14) yields

$$\sigma_{nm}^B = K k^2 \varphi \frac{\partial u_m}{\partial x_n}. \quad (2.35)$$

## 2.2 Acoustic Radiation Force Terms

The total acoustic radiation force  $F_n^{\text{total}}$  will be discussed as a sum of four distinct terms:

$$F_n^{\text{total}} = F_n^B + F_n^P + G_n^B + G_n^P, \quad (2.36)$$

where  $F_n^B$  and  $F_n^P$  correspond to the scattered compressional wave, and  $G_n^B$  and  $G_n^P$  correspond to the scattered shear wave. The subscript  $n$  here identifies the vector component (i.e., the  $x$ -,  $y$ -, or  $z$ -component). For example, we will frequently be interested in the axial force  $F_z^{\text{total}}$  in the direction of the incident field. The meaning of each of these terms is now discussed in detail.

The terms  $F_n^B$  and  $G_n^B$  are considered first. Both terms are calculated via direct integration of the stress tensor over the surface of the sphere. We

begin with Eq. (2.35) by separating the displacement into its compressional and shear components,

$$\sigma_{nm}^B = \sigma_{nm}^l + \sigma_{nm}^{lt}, \quad (2.37)$$

where

$$\sigma_{nm}^l = Kk^2\varphi \frac{\partial u_m^l}{\partial x_n}, \quad (2.38)$$

$$\sigma_{nm}^{lt} = Kk^2\varphi \frac{\partial u_m^t}{\partial x_n}. \quad (2.39)$$

Note that the superscript  $l$  is used in the first term because it involves only the compressional field, whereas  $lt$  is used in the second term because it involves both the compressional field and the shear field. Each of these is time averaged and integrated over the surface of the sphere to obtain two of the terms in the radiation force,

$$F_n^B = \int_S \langle \sigma_{nm}^l \rangle \frac{x_m}{R} dS, \quad (2.40)$$

$$G_n^B = \int_S \langle \sigma_{nm}^{lt} \rangle \frac{x_m}{R} dS, \quad (2.41)$$

where  $R$  is the radius of the sphere and  $S$  is its surface. As shown in Secs. 2.4 and 2.6, and in greater depth in Appendix B, both terms can be calculated analytically.

Next, the terms  $F_n^P$  and  $G_n^P$  are addressed. These arise from the reaction force in the medium due to the body force  $f_n^B$ . As with the stress tensor, this body force can be separated as

$$f_n^B = f_n + g_n, \quad (2.42)$$

where

$$f_n = \frac{\partial \sigma_{nm}^l}{\partial x_m}, \quad (2.43)$$

$$g_n = \frac{\partial \sigma_{nm}^{lt}}{\partial x_m}. \quad (2.44)$$

From Helmholtz's theorem, both  $f_n$  and  $g_n$  can be written as a sum of irrotational and solenoidal parts, expressed here for brevity in vector (rather than index) form,

$$\mathbf{f} = \nabla P + \nabla \times \mathbf{R}, \quad (2.45)$$

$$\mathbf{g} = \nabla Q + \nabla \times \mathbf{S}, \quad (2.46)$$

where  $P$  and  $Q$  are scalar potentials, and  $\mathbf{R}$  and  $\mathbf{S}$  are vector potentials.

Finally,  $F_n^P$  and  $G_n^P$  are written as

$$F_n^P = - \int_S \langle P \rangle \frac{x_n}{R} dS, \quad (2.47)$$

$$G_n^P = - \int_S \langle Q \rangle \frac{x_n}{R} dS. \quad (2.48)$$

To better understand why Eqs. (2.47) and (2.48) are necessary, consider a simple analog: the uniform body force due to gravity acting on a volume of fluid that is not allowed to accelerate (e.g., a large body of water such as a lake). In order for the fluid to remain in place despite the body force, the fluid must deform to produce a compensating force. This deformation manifests as a pressure that increases with depth below the surface of the fluid, resulting in the well-known buoyancy force. While the body force  $f_n^B$  is not spatially

uniform and is considerably more complicated, it can be thought of in similar terms.

The force  $F_n^P$  in Eq. (2.47) can be calculated analytically, but this is not generally true for  $G_n^P$  in Eq. (2.48). To calculate the former, we can substitute the relation from Eq. (2.23) into Eq. (2.45) and manipulate to obtain

$$\begin{aligned}
\frac{f_n}{Kk^2} &= \frac{\partial}{\partial x_m} \left( \varphi \frac{\partial^2 \varphi}{\partial x_m \partial x_n} \right) = \frac{\partial \varphi}{\partial x_m} \frac{\partial^2 \varphi}{\partial x_m \partial x_n} + \varphi \frac{\partial^3 \varphi}{\partial x_m^2 \partial x_n} \\
&= \frac{\partial \varphi}{\partial x_m} \frac{\partial^2 \varphi}{\partial x_m \partial x_n} - k^2 \varphi \frac{\partial \varphi}{\partial x_n} = \frac{1}{2} \left[ \frac{\partial}{\partial x_n} \left( \frac{\partial \varphi}{\partial x_m} \right)^2 - k^2 \frac{\partial \varphi^2}{\partial x_n} \right] \\
&= \frac{1}{2} \frac{\partial}{\partial x_n} \left[ \left( \frac{\partial \varphi}{\partial x_m} \right)^2 - k^2 \varphi^2 \right]. \tag{2.49}
\end{aligned}$$

The final form of the expression is clearly a gradient of a scalar function, which is therefore expressed as

$$f_n = \frac{\partial P}{\partial x_n}, \tag{2.50}$$

where

$$P = \frac{Kk^2}{2} \left[ \left( \frac{\partial \varphi}{\partial x_m} \right)^2 - k^2 \varphi^2 \right] \tag{2.51}$$

is an effective pressure and the vector potential  $\mathbf{A}$  in Eq. (2.45) is zero. However, no such simplification appears to be possible for  $g_n$  in Eq. (2.46). Both its gradient component and its curl component must be retained, and these components may not be analytically separable. Furthermore, while the scalar potential  $Q$  is addressed with the surface integral in Eq. (2.48), the vector potential  $\mathbf{S}$  corresponds to a bulk displacement of the medium surrounding the sphere. Therefore, to compute the true effect of  $g_n$  on the displacement

of the sphere, integration over a volume enclosing the sphere is necessary, not just over the surface of the sphere.

### 2.3 Eulerian Description of Acoustic Radiation Force

Before proceeding, we briefly reconsider the use of Eulerian coordinates instead of Lagrangian coordinates to derive the radiation force as summarized by Lee and Wang [8, 9]. First, Eqs. (2.1) and (2.2) can be combined to obtain

$$\frac{\partial(\rho v_n)}{\partial t} = \frac{\partial \tilde{\sigma}_{nk}}{\partial \tilde{x}_k} - \frac{\partial(\rho v_n v_k)}{\partial \tilde{x}_k}, \quad (2.52)$$

where the term on the left-hand side is a rate of change of momentum within a fixed control volume and the terms on the right-hand side correspond the net exterior force on a control volume and the momentum inflow through the surface of the control volume, respectively [110]. For a time-harmonic quantity, the time average of its time derivative is zero. This gives

$$\frac{\partial S_{nk}}{\partial \tilde{x}_k} = 0, \quad (2.53)$$

where  $S_{nk}$  is referred to as the acoustic radiation stress tensor, first derived by Brillouin [38] and defined as

$$S_{nk} = \langle \tilde{\sigma}_{nk} \rangle - \langle \rho v_n v_k \rangle. \quad (2.54)$$

Then, integration of Eq. (2.53) over the space between the equilibrium surface  $\tilde{S}$  of the sphere and a much larger surface  $\tilde{S}_0$ , followed by use of the divergence theorem, yields

$$F_n = - \int_{\tilde{S}} (\langle \tilde{\sigma}_{nk} \rangle - \langle \rho v_n v_k \rangle) \tilde{n}_k d\tilde{S} = \int_{\tilde{S}_0} (\langle \tilde{\sigma}_{nk} \rangle - \langle \rho v_n v_k \rangle) \tilde{n}_k d\tilde{S}_0, \quad (2.55)$$

where  $\tilde{n}_k$  points away from the enclosed volume, meaning that it points inward on  $\tilde{S}$  and outward on  $\tilde{S}_0$ . Equation (2.55) can be simplified further by acknowledging that  $\rho v_n v_k$  contains third-order terms, and therefore  $\rho$  can be replaced with its equilibrium value  $\rho_0$  to obtain the following second-order expression for the force:

$$F_n = - \int_{\tilde{S}} (\langle \tilde{\sigma}_{nk} \rangle - \rho_0 \langle v_n v_k \rangle) \tilde{n}_k d\tilde{S} = \int_{\tilde{S}_0} (\langle \tilde{\sigma}_{nk} \rangle - \rho_0 \langle v_n v_k \rangle) \tilde{n}_k d\tilde{S}_0. \quad (2.56)$$

The idea of moving the surface of integration off the scatterer and out to an arbitrary distance, typically in the far field, is attributed to Westervelt [2, 3]. See, for example, Wang and Lee [105] for a review of work in which integration over  $\tilde{S}_0$  is performed in the far field to simplify the expressions for the scattered pressure and particle velocity fields.

What inhibits the use of the Eulerian formulation for our problem? It is a complete description of the force on the sphere, and it appears to be simpler than that described in previous sections because it does not require the removal of the irrotational part of the body force from  $\sigma_{nm}$ . However, while an analysis in Eulerian coordinates is effective for a sphere surrounded by a fluid medium (for which  $\tilde{\sigma}_{nk} = -P\delta_{nk}$ ), it becomes considerably more complicated when elasticity is involved. Of particular importance is how the Cauchy stress tensor is expressed in the case of nonlinear elasticity. From Eq. (2.5), the Cauchy stress tensor is written as

$$\tilde{\sigma}_{nk} = \frac{\rho}{\rho_0} \sigma_{nm} \frac{\partial \tilde{x}_k}{\partial x_m}. \quad (2.57)$$

Note that the Jacobian  $J$  (the determinant of the deformation gradient) can be written as  $J = \rho_0/\rho$ . Substitution of  $\rho/\rho_0 = 1/J$  and  $\tilde{x}_k = x_k + u_k$  yields the following second-order expression after simplifications:

$$\tilde{\sigma}_{nk} = \sigma_{nk} - \sigma_{nk} \frac{\partial u_l}{\partial x_l} + \sigma_{nm} \frac{\partial u_k}{\partial x_m}. \quad (2.58)$$

The second and third terms can ordinarily be handled without too much difficulty because only first-order components of the stress tensor and the displacement are required. However, the first term presents a problem because  $\sigma_{nk}$  contains another second-order component besides  $\sigma_{nk}^{(2)}$ : the first-order component  $\sigma_{nk}^{(1)}$  into which the second-order displacement  $u_n^{(2)}$  is substituted. Prior knowledge of  $u_n^{(2)}$  would obviate calculation of the radiation force altogether because displacement is what is measured experimentally, but it must be found numerically from Eqs. (2.21) and (2.22). In general, time-intensive numerical simulations (which will be addressed in Chapter 5) are required for this.

## 2.4 Radiation Force Due to Compressional Wave Fields

We now return to the Lagrangian description of radiation force and consider first  $F_n$ , the acoustic radiation force due to the displacement potential  $\varphi$  only. This is the sole contribution for a sphere in fluid, and it is expected to be the dominant contribution to acoustic radiation force on a sphere in soft tissue. The force  $F_n$  is written as the sum of the first two terms in Eq. (2.36) as

$$F_n = F_n^B + F_n^P. \quad (2.59)$$

The two contributions on the right-hand side are now discussed separately.

After substitution of Eq. (2.23) into Eq. (2.40),  $F_n^B$  can be written as

$$F_n^B = Kk^2 \int_S \left\langle \varphi \frac{\partial^2 \varphi}{\partial x_m \partial x_n} \right\rangle \frac{x_m}{R} dS. \quad (2.60)$$

Manipulation of the integrand gives

$$\begin{aligned} F_n^B &= \frac{Kk^2}{R} \int_S \left\langle \varphi \left[ x_m \frac{\partial^2 \varphi}{\partial x_m \partial x_n} \right] \right\rangle dS \\ &= \frac{Kk^2}{R} \int_S \left\langle \varphi \left[ \frac{\partial}{\partial x_n} \left( x_m \frac{\partial \varphi}{\partial x_m} \right) - \frac{\partial \varphi}{\partial x_m} \delta_{nm} \right] \right\rangle dS \\ &= \frac{Kk^2}{R} \int_S \left\langle \varphi \left[ \frac{\partial}{\partial x_n} \left( r \frac{\partial \varphi}{\partial r} \right) - \frac{\partial \varphi}{\partial x_n} \right] \right\rangle dS \\ &= \frac{Kk^2}{R} \int_S \left\langle \varphi \frac{\partial}{\partial x_n} \left( r \frac{\partial \varphi}{\partial r} - \varphi \right) \right\rangle dS. \end{aligned} \quad (2.61)$$

Next, it is necessary to substitute the expression for  $\varphi$  from Eq. (2.27) and time average. The result is

$$F_n^B = \frac{Kk^2}{4R} \int_S \left[ \psi^* \frac{\partial}{\partial x_n} \left( r \frac{\partial \psi}{\partial r} - \psi \right) \right] dS + \text{c.c.} \quad (2.62)$$

In the  $z$ -direction, this result becomes

$$F_z^B = \frac{Kk^2}{4R} \int_S \left[ \psi^* \frac{\partial}{\partial z} \left( r \frac{\partial \psi}{\partial r} - \psi \right) \right] dS + \text{c.c.} \quad (2.63)$$

Then,  $\partial/\partial z$  can be expressed in spherical coordinates as

$$\frac{\partial}{\partial z} = \cos \theta \frac{\partial}{\partial r} - \frac{\sin \theta}{r} \frac{\partial}{\partial \theta}. \quad (2.64)$$

The same can be done for  $x$  and  $y$ , but only the partial derivative in  $z$  is necessary, even for fields that are not axisymmetric. This is because the incident

field coefficients  $a_n^m$ , despite being defined about the  $z$ -axis, can be converted via a Wigner D-matrix transformation such that they are defined about the  $x$ -axis or  $y$ -axis instead. This manipulation is more convenient than deriving a different formula for each Cartesian direction, and it is briefly discussed at the end of this section and more thoroughly treated in Sec. 3.1.4.

For  $F_n^P$ , substitution of Eq. (2.51) into Eq. (2.47) gives

$$F_n^P = -\frac{Kk^2}{2R} \int_S \left\langle \left( \frac{\partial \varphi}{\partial x_m} \right)^2 - k^2 \varphi^2 \right\rangle x_n dS. \quad (2.65)$$

Then, substitution of  $\varphi$  from Eq. (2.27), time averaging, and replacement of  $x_n$  with  $z = R \cos \theta$  gives

$$F_z^P = -\frac{Kk^2}{4} \int_S \left( \frac{\partial \psi^*}{\partial x_m} \frac{\partial \psi}{\partial x_m} - k^2 \psi^* \psi \right) \cos \theta dS. \quad (2.66)$$

Note that, unlike in Eq. (2.63), no complex conjugate is added in Eq. (2.66). Both  $F_z^B$  and  $F_z^P$  are real quantities.

Finally, the total radiation force  $F_z$  can be calculated from the sum of Eq. (2.63) and Eq. (2.66). This is a laborious process; it is briefly outlined in Appendix B. The result for a non-axisymmetric incident field is [20]

$$F_z = i\pi Kk^2 \sum_{n=0}^N \sum_{m=-n}^n \frac{(n+m+1)!}{(2n+1)(2n+3)(n-m)!} \\ \times (A_n^* + A_{n+1} + 2A_n^* A_{n+1}) a_n^{m*} a_{n+1}^m + \text{c.c.}, \quad (2.67)$$

and the result for an axisymmetric incident field is

$$F_z = i\pi Kk^2 \sum_{n=0}^N \frac{n+1}{(2n+1)(2n+3)} (A_n^* + A_{n+1} + 2A_n^* A_{n+1}) a_n^* a_{n+1} + \text{c.c.}, \quad (2.68)$$

which follows from setting  $m = 0$  in Eq. (2.67). In both equations, the summation limit  $N$  is chosen such that the force has converged. Note that there is no explicit dependence on the sphere radius  $R$  in either equation, which further confirms Westervelt's reasoning that the surface of integration may be any surface containing the scatterer [2, 3].

As an alternative, it is often useful to expand the incident field in terms of normalized spherical harmonics  $Y_{nm}(\theta, \phi)$ ,

$$\psi_i = \sum_{n=0}^{\infty} \sum_{m=-n}^n \tilde{a}_n^m j_n(kr) Y_{nm}(\theta, \phi), \quad (2.69)$$

where

$$Y_{nm}(\theta, \phi) = \sqrt{\frac{(2n+1)(n-m)!}{4\pi(n+m)!}} P_n^m(\cos \theta) e^{im\phi}. \quad (2.70)$$

The normalization is such that the orthogonality integral assumes the form

$$\int_0^\pi \int_0^{2\pi} Y_{nm} Y_{n'm'}^* \sin \theta d\phi d\theta = \delta_{nn'} \delta_{mm'}. \quad (2.71)$$

The incident field coefficients are then related via the expression

$$\tilde{a}_n^m = \sqrt{\frac{4\pi(n+m)!}{(2n+1)(n-m)!}} a_n^m, \quad (2.72)$$

and the radiation force equations become

$$\begin{aligned} F_z = & i \frac{Kk^2}{4} \sum_{n=0}^N \sum_{m=-n}^n \sqrt{\frac{(n+m+1)(n-m+1)}{(2n+1)(2n+3)}} \\ & \times (\tilde{a}_n^m)^* \tilde{a}_{n+1}^m (A_n^* + A_{n+1} + 2A_n^* A_{n+1}) + \text{c.c.} \end{aligned} \quad (2.73)$$

for non-axisymmetric incident fields, and

$$\begin{aligned} F_z = & i \frac{Kk^2}{4} \sum_{n=0}^N \frac{n+1}{\sqrt{(2n+1)(2n+3)}} \\ & \times \tilde{a}_n^* \tilde{a}_{n+1} (A_n^* + A_{n+1} + 2A_n^* A_{n+1}) + \text{c.c.} \end{aligned} \quad (2.74)$$

for axisymmetric incident fields. The modified non-axisymmetric relation is especially convenient because it allows for more straightforward calculation of  $F_x$  and  $F_y$  through a Wigner D-matrix transformation of the incident field coefficients (Sec. 3.1.4). This results in coefficients  $[\tilde{a}_n^m]_x$  about the  $x$ -axis and  $[\tilde{a}_n^m]_y$  about the  $y$ -axis, which can be expressed in terms of  $\tilde{a}_n^m$  ( $\equiv [\tilde{a}_n^m]_z$ ) and used to find  $F_x$  and  $F_y$ , respectively:

$$F_x = \frac{i}{4} K k^2 \sum_{n=0}^N \sum_{m=-n}^n \sqrt{\frac{(n+m+1)(n-m+1)}{(2n+1)(2n+3)}} \times [\tilde{a}_n^m]_x^* [\tilde{a}_{n+1}^m]_x (A_n^* + A_{n+1} + 2A_n^* A_{n+1}) + \text{c.c.}, \quad (2.75)$$

$$F_y = \frac{i}{4} K k^2 \sum_{n=0}^N \sum_{m=-n}^n \sqrt{\frac{(n+m+1)(n-m+1)}{(2n+1)(2n+3)}} \times [\tilde{a}_n^m]_y^* [\tilde{a}_{n+1}^m]_y (A_n^* + A_{n+1} + 2A_n^* A_{n+1}) + \text{c.c.} \quad (2.76)$$

## 2.5 Comparison with Existing Theory

Classical results for radiation force on a sphere in fluid have all been obtained using Eulerian coordinates, whereas the result presented in the previous section was found using Lagrangian coordinates. Since there has been some controversy regarding radiation force predictions over the years [9, 27], it is useful to compare the theory in the previous section to other published results.

First, we consider results from Gor'kov for small spheres in liquid [7]. For sufficiently small spheres, two simplifications can be made. First, the field can be assumed to be axisymmetric, which allows for the use of Eq. (2.68).

Second, only scattered field coefficients for  $n = 0$  (monopole) and  $n = 1$  (dipole) in the expansion are significant; this yields

$$F_z = i\pi K k^2 \left[ \frac{1}{3}(A_0^* + A_1 + 2A_0^*A_1)a_0^*a_1 + \frac{2}{15}A_1^*a_1^*a_2 \right] + \text{c.c.} \quad (2.77)$$

To compare the above relation with the results obtained by Gor'kov, we first define the quantities

$$f_1 = \frac{K_s - K}{K_s}, \quad (2.78)$$

$$f_2 = \frac{2(\rho_s - \rho)}{2\rho_s + \rho}, \quad (2.79)$$

where  $K_s$  and  $\rho_s$  are the bulk modulus and density of the sphere, respectively, and  $K$  and  $\rho$  without subscripts denote the same quantities in the surrounding medium. Ignoring shear forces in both the sphere and the medium, we can determine the scattered field coefficients  $A_0$  and  $A_1$  for compressional waves from Eqs. (3.82) and (3.83). After the use of small-argument approximations for the spherical Bessel and Hankel functions, the coefficients become

$$A_0 = -i\frac{1}{3}(kR)^3 f_1 - \frac{1}{9}(kR)^6 f_2, \quad (2.80)$$

$$A_1 = i\frac{1}{6}(kR)^3 f_2 - \frac{1}{36}(kR)^6 f_2. \quad (2.81)$$

Next, because Gor'kov presents relations for the force due to both plane standing and plane traveling waves, we need to determine the incident field coefficients  $a_n$  for each case. For a plane traveling wave described by

$$\psi_i = \psi_0 e^{ikz}, \quad (2.82)$$

the incident field coefficients are [111]

$$a_n = i^n(2n + 1)\psi_0. \quad (2.83)$$

Substitution of Eqs. (2.80)–(2.83) into Eq. (2.77) yields, at leading order in  $kR$  [20],

$$F_z = \frac{2}{9}\pi K k^2 (kR)^6 |\psi_0|^2 \left( f_1^2 + \frac{3}{4}f_2^2 + f_1 f_2 \right), \quad (2.84)$$

which agrees with Eq. (10) of Gor'kov [7]. For a plane standing wave described by

$$\psi_i = \psi_0 \cos[k(z + z_0)], \quad (2.85)$$

representing a shift in the field by moving the sphere in the  $+z$ -direction by the quantity  $z_0$ , the incident field coefficients are

$$a_n = (2n + 1)\psi_0 \cos(kz_0 + n\pi/2). \quad (2.86)$$

Equivalently, this can be thought of as moving the standing wave profile  $\cos(kz)$  by  $z_0$  in the opposite direction. Substitution of Eqs. (2.80), (2.81), and (2.86) into Eq. (2.77) yields, at leading order in  $kR$  [20],

$$F_z = \pi K k^2 (kR)^3 \psi_0^2 \left( \frac{1}{3}f_1 + \frac{1}{2}f_2 \right) \sin(2kz_0), \quad (2.87)$$

which agrees with Eq. (13) of Gorkov [7]. The relation given by Eq. (2.68) is therefore verified for small spheres.

The relation given by Eq. (2.67) can also be shown to recover results for spheres of arbitrary size from Sapozhnikov and Bailey [10]. First, consider

their Eq. (16) for force due to an axisymmetric incident field:

$$F_z = \frac{2\pi}{\rho_0 c_l^2 k^2} \sum_n \frac{n+1}{(2n+1)(2n+3)} \text{Im}\{Q_n Q_{n+1}^* (A_n + A_{n+1}^* + 2A_n A_{n+1}^*)\}, \quad (2.88)$$

where  $Q_n$  are expansion coefficients for incident pressure instead of incident displacement potential and can be written as  $Q_n = \rho_0 \omega^2 a_n$ . Substituting this expression and noting that  $\text{Im}\{z\} = \text{Re}\{iz\}$  then gives

$$\begin{aligned} F_z &= \frac{2\pi \rho_0 \omega^4}{c_l^2 k^2} \sum_n \frac{n+1}{(2n+1)(2n+3)} \text{Re}\{i a_n a_{n+1}^* (A_n + A_{n+1}^* + 2A_n A_{n+1}^*)\} \\ &= 2\pi K k^2 \sum_n \frac{n+1}{(2n+1)(2n+3)} \text{Re}\{i a_n a_{n+1}^* (A_n + A_{n+1}^* + 2A_n A_{n+1}^*)\} \\ &= i\pi K k^2 \sum_{n=0}^N \frac{n+1}{(2n+1)(2n+3)} (A_n + A_{n+1}^* + 2A_n A_{n+1}^*) a_n a_{n+1}^* + \text{c.c.}, \end{aligned} \quad (2.89)$$

which is identical to Eq. (2.68). Next, consider their Eq. (48) for force due to a non-axisymmetric incident field:

$$F_z = -\frac{1}{4\pi^2 \rho_0 c_l^2 k^2} \text{Re} \left\{ \sum_n \Psi_n \sum_m B_{nm} H_{nm} H_{n+1,m}^* \right\}, \quad (2.90)$$

where

$$B_{nm} = \sqrt{\frac{(n+m+1)(n-m+1)}{(2n+1)(2n+3)}}, \quad (2.91)$$

$$\Psi_n = 2(A_n + A_{n+1} + 2A_n A_{n+1}^*), \quad (2.92)$$

and  $H_{nm}$  are expansion coefficients for incident pressure in terms of normalized spherical harmonics  $Y_{nm}$ . These can be written via  $a_n^m$  as

$$H_{nm} = \sqrt{\frac{4\pi(n+m)!}{(2n+1)(n-m)!}} \frac{\pi}{i^n} \rho_0 \omega^2 a_n^m. \quad (2.93)$$

Substituting these expressions gives

$$\begin{aligned}
F_z &= 2\pi K k^2 \operatorname{Re} \left\{ i \sum_n \sum_m \frac{(n+m+1)!}{(2n+1)(2n+3)(n-m)!} \right. \\
&\quad \left. \times (A_n + A_{n+1}^* + 2A_n A_{n+1}^*) a_n^m a_{n+1}^{m*} \right\} \\
&= i\pi K k^2 \sum_{n=0}^N \sum_{m=-n}^n \frac{(n+m+1)!}{(2n+1)(2n+3)(n-m)!} \\
&\quad \times (A_n + A_{n+1}^* + 2A_n A_{n+1}^*) a_n^m a_{n+1}^{m*} + \text{c.c.}, \tag{2.94}
\end{aligned}$$

which is identical to Eq. (2.67).

Finally, results can be compared graphically for a sphere of arbitrary size in liquid subject to plane traveling waves. Yosioka and Kawasima [4] first obtained results for a compressible sphere, but the comparison in this section will be for the more general case of an elastic sphere (i.e., including shear stiffness), the results for which were derived later by Hasegawa and Yosioka [5]. A plane traveling wave incident in the  $z$ -direction is described through displacement potential  $\varphi_i$  by

$$\varphi_i(z, t) = \varphi_0 e^{i(kz - \omega t)}. \tag{2.95}$$

The  $z$ -component of particle velocity and the pressure are then given by

$$v_i = \frac{\partial}{\partial z} \left( \frac{\partial \varphi_i}{\partial t} \right) = \omega k \varphi_i, \tag{2.96}$$

$$p_i = \rho_0 \frac{\partial^2 \varphi_i}{\partial t^2} = \rho_0 \omega^2 \varphi_i. \tag{2.97}$$

The time-averaged intensity is found to be

$$I_i = \frac{1}{2} \operatorname{Re}\{p_i v_i^*\} = \frac{1}{2} \rho_0 \omega^3 k |\varphi_0|^2, \tag{2.98}$$

	$\rho_0$ (kg/m <sup>3</sup> )	$c_l$ (m/s)	$c_t$ (m/s)
Water	1000	1500	—
Steel	7810	5945	3252
Stainless steel	7900	5240	2978
Brass	8100	3830	2050
Fused silica	2214	5950	3750

Table 2.1: Medium and scatterer properties for comparison with Hasegawa and Yosioka [5, 6].

from which the energy density is  $E_i = I_i/c_l$ . Following Hasegawa and Yosioka [5], we define the dimensionless acoustic radiation force function  $Y_p$  as the radiation force per unit cross section and unit mean energy density,

$$Y_p = \frac{\langle F \rangle}{\pi R^2 E_i}. \quad (2.99)$$

This is the quantity that will be plotted to compare most easily with results by Hasegawa and Yosioka [5, 6], and it will be used later in this dissertation as well as a convenient normalization, often with an additional subscript  $z$  or  $x$  to indicate direction.

We consider four different spheres embedded in water for comparison: steel, stainless steel (which is quite similar, but has shifted scattering resonances), brass, and fused silica. Properties of both water and the spheres are listed in Table 2.1, and results for each of the spheres are displayed in Fig. 2.1. In all four cases, both the plot and an examination of the underlying data suggest that the results agree to numerical precision. The peaks and minima in  $Y_p$  are of particular interest, as they indicate elastic scattering resonances unique

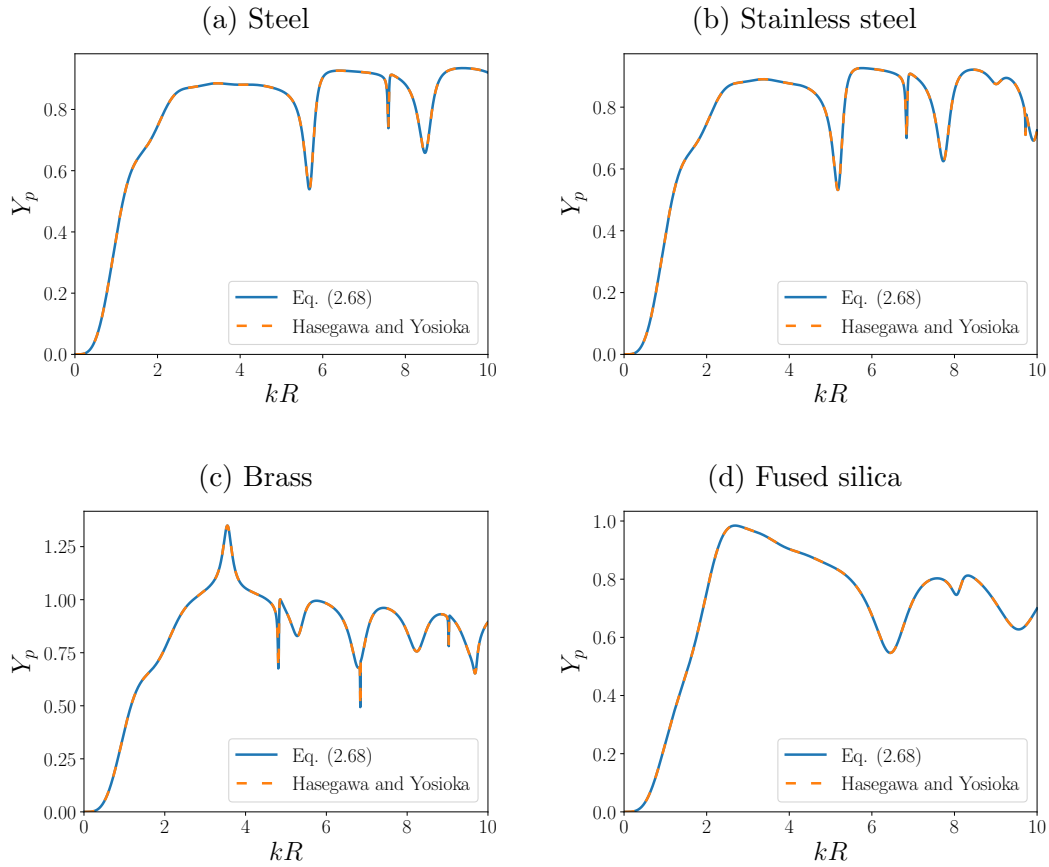


Figure 2.1: Comparison of Eq. (2.68) with results of Hasegawa and Yosioka [5] for the acoustic radiation force function  $Y_p$  versus dimensionless sphere size  $kR$  for various spheres in water. Note that the two curves, calculated with different equations, lie directly on top of each other.

to the material. Such resonances, which do not occur in King's theory for force on rigid spheres [1], will be discussed further in Sec. 3.4 and Chapter 4.

Since the equation for  $F_n$  is shown to be valid for the well-known case of a spherical scatterer in an ideal liquid medium, we must examine the effects of both shear elasticity and shear viscosity of the medium. As will be shown

in later chapters, these effects are important because even very small shear modulus and shear viscosity can introduce substantial changes in both the magnitude and direction of the radiation force compared to those in liquid. These effects are strongly dependent on the size of the scatterer.

## 2.6 Radiation Force Associated with the Scattered Shear Wave

If the medium is elastic, then  $G_n^B$  and  $G_n^P$  (the radiation force contributions due to the scattered shear wave field) must be computed as well. As with Eq. (2.59), the radiation force  $G_n$  due to the scattered shear wave field can be written as

$$G_n = G_n^B + G_n^P. \quad (2.100)$$

First, we find  $G_n^B$  from Eq. (2.41). Substitution of  $\sigma_{nm}^{lt}$  from Eq. (2.37) gives

$$G_n^B = Kk^2 \int_S \left\langle \varphi \frac{\partial u_m^t}{\partial x_n} \right\rangle \frac{x_m}{R} dS, \quad (2.101)$$

and manipulation of the integrand, which is comparable to that in Eq. (2.61), gives

$$\begin{aligned} G_n^B &= \frac{Kk^2}{R} \int_S \left\langle \varphi \left[ x_m \frac{\partial u_m^t}{\partial x_n} \right] \right\rangle dS \\ &= \frac{Kk^2}{R} \int_S \left\langle \varphi \left[ \frac{\partial}{\partial x_n} (x_m u_m^t) - u_m^t \delta_{nm} \right] \right\rangle dS \\ &= \frac{Kk^2}{R} \int_S \left\langle \varphi \left[ \frac{\partial}{\partial x_n} (r u_r^t) - u_n^t \right] \right\rangle dS. \end{aligned} \quad (2.102)$$

Time averaging yields

$$G_n^B = \frac{Kk^2}{4R} \int_S \left[ \psi^* \left( \frac{\partial}{\partial x_n} (r \tilde{u}_r^t) - \tilde{u}_n^t \right) \right] dS + \text{c.c.} \quad (2.103)$$

The tilde denotes that only the spatial part of  $u_n^t$  is retained in this equation.

In the  $z$ -direction, Eq. (2.103) becomes

$$G_z^B = \frac{Kk^2}{4R} \int_S \left[ \psi^* \left( \frac{\partial}{\partial z} (r\tilde{u}_r^t) - \tilde{u}_z^t \right) \right] dS + \text{c.c.}, \quad (2.104)$$

with  $\tilde{u}_z^t = \tilde{u}_r^t \cos \theta - \tilde{u}_\theta^t \sin \theta$  and, from Ying and Truell [109],

$$\tilde{u}_r^t = -\frac{1}{r} \Omega \Pi, \quad (2.105)$$

$$\tilde{u}_\theta^t = \frac{1}{r} \frac{\partial^2}{\partial r \partial \theta} (r \Pi), \quad (2.106)$$

where  $\Omega$  is a differential operator:

$$\Omega = \frac{1}{\sin \theta} \frac{\partial}{\partial \theta} \left( \sin \theta \frac{\partial}{\partial \theta} \right) + \frac{1}{\sin^2 \theta} \frac{\partial^2}{\partial \phi^2}. \quad (2.107)$$

As with  $F_z$ , the rest of the process is somewhat tedious, and it is outlined in Appendix B. The result for a non-axisymmetric incident field is [20]

$$\begin{aligned} G_z^B &= \pi K k^2 (\kappa R) \sum_{n=0}^N \frac{n(n+2)}{(2n+1)(2n+3)} \sum_{m=-n}^n \frac{(n+m+1)!}{(n-m)!} \\ &\quad \times \{ a_n^{m*} a_{n+1}^m B_{n+1} [j_n^*(kR) + A_n^* h_n^*(kR)] h_n(\kappa R) \\ &\quad - a_{n+1}^{m*} a_n^m B_n [j_{n+1}^*(kR) + A_{n+1}^* h_{n+1}^*(kR)] h_{n+1}(kR) \} + \text{c.c.}, \end{aligned} \quad (2.108)$$

and the result for an axisymmetric incident field is

$$\begin{aligned} G_z^B &= \pi K k^2 \sum_{n=1}^N \frac{(\kappa R) h_n(\kappa R)}{2n+1} [j_n(kR) + A_n^* h_n^*(kR)] a_n^* \\ &\quad \times \left[ \frac{n(n+1)(n+2)}{2n+3} B_{n+1} a_{n+1} - \frac{(n-1)n(n+1)}{2n-1} B_{n-1} a_{n-1} \right] + \text{c.c.} \end{aligned} \quad (2.109)$$

Note that in addition to the presence of the coefficients  $B_n$  for the scattered shear wave, there is another key difference between Eqs. (2.108) and (2.109) and Eqs. (2.67) and (2.68): the explicit presence of oscillatory functions depending on  $kR$  and  $\kappa R$  in Eqs. (2.108) and (2.109). In the force  $F_z$  due to compressional wave fields, these oscillatory terms are shown to balance one another (see Appendix B), resulting in an equation for the radiation force that is smoothly varying in  $kR$ .

In order to determine whether the same is true of the force  $G_z$ , it is necessary to find  $G_z^P$ . However, as discussed previously in Sec. 2.2, the body force  $g_n$  may not be analytically separable into irrotational and solenoidal parts, so the potential  $Q$  in Eq. (2.46) must be computed numerically. Since this potential is needed at the surface of a sphere of radius  $R$ , the domain is chosen to be a spherical shell with an inner radius slightly less than  $R$  and an outer radius slightly greater than  $R$ . The domain is then discretized with a triangular mesh (for axisymmetric fields, allowing for the reduction of the problem to two dimensions) or a tetrahedral mesh (for non-axisymmetric fields, requiring the problem to be formulated in three dimensions), and  $g_n$  is computed at each node in the mesh. Finally, a least-squares finite element method is used to solve for the potential at each node, and the potential is integrated over the surface of the sphere. This process is described by Tong et al. [112], and an overview of its implementation in the present work is discussed in Sec. 5.3.

Finally, once  $G_z^P$  has been found from the gradient part of  $g_n$ , there

remains the question of the effect due to the solenoidal part of  $g_n$ . From Eq. (2.46), the term  $\nabla \times \mathbf{S}$  causes a bulk deformation of the surrounding medium, which results in a displacement of the scatterer that is not due to a radiation force pushing the scatterer relative to the medium but rather a displacement of the medium itself. This effect must ultimately be determined by integrating over the volume surrounding the scatterer instead of just the surface of the scatterer, and it is briefly discussed in Sec. 5.4 but not treated as thoroughly due to the difficulty in calculating it.

## 2.7 Summary

The fundamental elastodynamic equations and the resulting expressions for acoustic radiation force presented in this chapter are important for understanding the results in the chapters to follow. The choice of Lagrangian coordinates instead of the usual Eulerian coordinates (as used for calculating the force in fluids) facilitates the incorporation of elasticity without requiring a full solution for the nonlinear contribution to the displacement, and the approximations discussed in Sec. 2.1 allow for a description of the problem that is analytically tractable. Furthermore, separating the radiation force into compressional wave and shear wave contributions  $F_n$  and  $G_n$  provides a means to decouple compressional and shear effects in analyzing the radiation force. Finally, the recovery of known results for acoustic radiation force in fluid obtained previously [5–7, 10] serves as a useful verification of this novel approach.

## Chapter 3

### Incident and Scattered Fields

In this chapter, the procedures for computing incident field coefficients ( $a_n$  for axisymmetric fields and  $a_n^m$  for non-axisymmetric fields) and scattered field coefficients in the surrounding medium ( $A_n$  for compressional waves and  $B_n$  for shear waves) are discussed. Incident field coefficients are discussed in Secs. 3.1 and 3.2, and scattered field coefficients are discussed in Secs. 3.3 and 3.4.

For incident field coefficients, the starting point is a description of the field in terms of its three-dimensional angular spectrum. The more traditional approach involves a two-dimensional angular spectrum that is propagated away from a source plane, a technique commonly referred to as Fourier acoustics [101]. Applications of this approach to focused sound beams often encountered in medical ultrasound applications have been developed by Sapozhnikov and Bailey [10]. The three-dimensional angular spectrum description is used in the present chapter because it lends itself to a convenient analytic expression for the coefficients of a focused incident field that is symmetric about the focal plane (Sec. 3.2.1), which facilitates the investigation of radiation force effects without complications related to a specific beam profile. Also, a

two-dimensional angular spectrum can be reformulated as a three-dimensional angular spectrum without great difficulty [102]. As shown with several examples, arbitrary incident fields may be represented by the three-dimensional angular spectrum.

The scattered field coefficients are examined for a variety of cases. Results for a rigid sphere versus a steel sphere and for a spherical void versus an air bubble are presented to demonstrate effects of scattering resonances. Also, various values for shear modulus in the surrounding medium are considered to investigate the effect of elasticity.

### **3.1 Incident Field Coefficients**

In this section, the procedure for finding the incident field coefficients is detailed. The most general case of a non-axisymmetric field is treated first, followed by a simplification for axisymmetric fields. Coefficients for an expansion about a point other than the origin are addressed next. Finally, a description of the coefficients about axes other than the  $z$ -axis (required for forces other than  $F_z$ ) is given.

#### **3.1.1 Non-axisymmetric Incident Field**

From Eq. (2.27), recall that a time-harmonic displacement potential that satisfies the Helmholtz equation can be written with spatial and temporal

dependence separated as

$$\varphi(\mathbf{r}, t) = \frac{1}{2} \psi(\mathbf{r}) e^{-i\omega t} + \text{c.c.}, \quad (3.1)$$

where particle displacement components are given by  $u_n = \partial\varphi/\partial x_n$ . The spatial component can be expanded as a superposition of plane waves via the relation

$$\psi(r, \theta, \phi) = \int e^{i\mathbf{k}\cdot\mathbf{r}} \Psi(\mathbf{k}) d\Omega_k = \int_0^\pi \int_0^{2\pi} e^{i\mathbf{k}\cdot\mathbf{r}} \Psi(\theta_k, \phi_k) \sin\theta_k d\phi_k d\theta_k, \quad (3.2)$$

where  $|\mathbf{k}| = k = \omega/c_l$  is the compressional wavenumber,  $\Psi$  is the angular spectrum of the field, and  $\theta_k, \phi_k$  are polar and azimuthal angles, respectively, indicating the direction of wave vector  $\mathbf{k}$ . Also recall that, from Eq. (2.29),  $\psi$  can be expanded in spherical coordinates with respect to spherical harmonics as

$$\psi(r, \theta, \phi) = \sum_{n=0}^{\infty} \sum_{m=-n}^n a_n^m j_n(kr) P_n^m(\cos\theta) e^{im\phi}, \quad (3.3)$$

and that the normalized spherical harmonics  $Y_{nm}(\theta, \phi)$  from Eq. (2.70) are

$$Y_{nm}(\theta, \phi) = \sqrt{\frac{(2n+1)(n-m)!}{4\pi(n+m)!}} P_n^m(\cos\theta) e^{im\phi}. \quad (3.4)$$

It is also useful to introduce the spherical harmonic expansion of a plane traveling wave [111]:

$$e^{ikz} = e^{ikr \cos\theta} = \sum_{n=0}^{\infty} (2n+1) i^n j_n(kr) P_n(\cos\theta). \quad (3.5)$$

Combining Eqs. (3.4) and (3.5) yields

$$e^{ikz} = e^{ikr \cos\theta} = \sum_{n=0}^{\infty} \sqrt{4\pi(2n+1)} i^n j_n(kr) Y_{n0}(\theta). \quad (3.6)$$

Any plane wave with wave vector  $\mathbf{k}$  forming angle  $\theta_k$  with the  $z$ -axis can be expanded with respect to spherical Bessel functions in the coordinate system  $(x', y', z')$  with the  $z'$ -axis aligned with  $\mathbf{k}$ . This allows us to rewrite Eq. (3.2) as

$$\psi(r, \theta, \phi) = \int_0^\pi \int_0^{2\pi} e^{ikz'} \Psi(\theta_k, \phi_k) \sin \theta_k d\phi_k d\theta_k. \quad (3.7)$$

Next, we employ a Wigner D-matrix transformation that allows us to rewrite a spherical harmonic expansion in a rotated coordinate system. Its importance in this section is that it allows us to rewrite the exponential  $e^{ikz'}$  in terms of the original  $(x, y, z)$  coordinate system. According to Wigner [113], under an arbitrary rotation from coordinate system  $(x, y, z)$  to  $(x', y', z')$  via the Euler angles  $(\alpha, \beta, \gamma)$ , spherical harmonics  $Y_{nm'}(\theta', \phi')$  in the rotated system can be expressed as a linear combination of spherical harmonics  $Y_{nm}(\theta, \phi)$  in the original coordinate system via the relation

$$Y_{nm'}(\theta', \phi') = \sum_{m=-n}^n D_{mm'}^n(\alpha, \beta, \gamma) Y_{nm}(\theta, \phi), \quad (3.8)$$

where the Wigner D-matrix is given by

$$D_{mm'}^n(\alpha, \beta, \gamma) = e^{-im\alpha} d_{mm'}^n(\beta) e^{-im'\gamma}. \quad (3.9)$$

The Wigner (small) d-matrix is given by, among other possible definitions [114],

$$\begin{aligned} d_{mm'}^n(\beta) &= (-1)^{m-m'} \sqrt{(n+m)!(n-m)!(n+m')!(n-m')!} \\ &\times \sum_s (-1)^s \frac{\left(\cos \frac{\beta}{2}\right)^{2n-2s-m+m'} \left(\sin \frac{\beta}{2}\right)^{2s+m-m'}}{s!(n-m-s)!(n+m'-s)!(m-m'+s)!}, \end{aligned} \quad (3.10)$$

where the summation limits are defined such that the factorials are non-negative. This particular definition is chosen so that  $d_{mm'}^n$  is real-valued, and it requires the  $z$ - $y$ - $z$  convention for Euler angle rotations: rotation about the  $z$ -axis by the angle  $\alpha$ , then rotation about the new  $y$ -axis by the angle  $\beta$ , and finally rotation about the newest  $z$ -axis by the angle  $\gamma$ .

The expression for the exponential  $e^{ikz'}$  in Eq. (3.6) is now substituted into Eq. (3.7), and the function  $Y_{n0}(\theta')$  is transformed into the original coordinate system using Eq. (3.8) with  $m' = 0$ ,  $\alpha = \phi_k$ , and  $\beta = \theta_k$  to obtain

$$Y_{n0}(\theta') = \sum_{m=-n}^n D_{m0}^n(\phi_k, \theta_k, \gamma) Y_{nm}(\theta, \phi) = \sum_{m=-n}^n e^{-im\phi_k} d_{m0}^n(\theta_k) Y_{nm}(\theta, \phi). \quad (3.11)$$

Substitution of Eq. (3.11) into Eq. (3.7) yields

$$\begin{aligned} \psi(r, \theta, \phi) &= \sum_{n=0}^{\infty} \sum_{m=-n}^n \sqrt{4\pi(2n+1)} i^n j_n(kr) Y_{nm}(\theta, \phi) \\ &\times \int_0^{\pi} \int_0^{2\pi} e^{-im\phi_k} d_{m0}^n(\theta_k) \Psi(\theta_k, \phi_k) \sin \theta_k d\phi_k d\theta_k, \end{aligned} \quad (3.12)$$

and substitution of Eq. (3.4) gives

$$\begin{aligned} \psi(r, \theta, \phi) &= \sum_{n=0}^{\infty} \sum_{m=-n}^n (2n+1) i^n j_n(kr) \sqrt{\frac{(n-m)!}{(n+m)!}} P_n^m(\cos \theta) e^{im\phi} \\ &\times \int_0^{\pi} \int_0^{2\pi} e^{-im\phi_k} d_{m0}^n(\theta_k) \Psi(\theta_k, \phi_k) \sin \theta_k d\phi_k d\theta_k. \end{aligned} \quad (3.13)$$

Finally, comparison with Eq. (3.3) yields the incident coefficients:

$$a_n^m = i^n (2n+1) \sqrt{\frac{(n-m)!}{(n+m)!}} \int_0^{\pi} \int_0^{2\pi} e^{-im\phi_k} d_{m0}^n(\theta_k) \Psi(\theta_k, \phi_k) \sin \theta_k d\phi_k d\theta_k. \quad (3.14)$$

The coefficients in Eq. (3.3) allow for the description of any incident field represented via  $\Psi(\theta_k, \phi_k)$  in  $k$ -space, and they can be used along with the scattering coefficients to calculate  $F_z$ , the acoustic radiation force in the  $z$ -direction, from Eq. (2.67) or Eq. (2.73). They are discussed for various focused beams in Sec. 3.2. Note that this is only one possible method of computing incident field coefficients for a spherical harmonic expansion. For example, Sapozhnikov and Bailey [10] use the more traditional approach based on the two-dimensional angular spectrum in their description of focused sound beams exerting radiation force on a sphere.

### 3.1.2 Axisymmetric Incident Field

In the case where  $\psi$  is axisymmetric, the function  $\Psi$  depends on polar angle  $\theta_k$  only, which gives

$$a_n^m = i^n (2n+1) \sqrt{\frac{(n-m)!}{(n+m)!}} \int_0^\pi \int_0^{2\pi} e^{-im\phi_k} d_{m0}^n(\theta_k) \Psi(\theta_k) \sin \theta_k d\phi_k d\theta_k. \quad (3.15)$$

Integrating over  $\phi_k$  eliminates all but the  $m = 0$  term to yield

$$a_n = i^n 2\pi (2n+1) \int_0^\pi d_{00}^n(\theta_k) \Psi(\theta_k) \sin \theta_k d\theta_k, \quad (3.16)$$

and since  $d_{00}^n(\beta) = P_n(\cos \beta)$ , the expression for  $a_n$  can finally be written as

$$a_n = i^n 2\pi (2n+1) \int_0^\pi P_n(\cos \theta_k) \Psi(\theta_k) \sin \theta_k d\theta_k. \quad (3.17)$$

These coefficients can then be used along with the scattering coefficients to calculate  $F_z$  from Eq. (2.68) or Eq. (2.74).

### 3.1.3 Off-Origin Field Expansion

Sections 3.1.1 and 3.1.2 describe the coefficients for an incident field defined about the origin. More specific to the purpose of calculating radiation force on a sphere, they apply when the sphere is centered at the same point about which  $\Psi(\theta_k, \phi_k)$  is defined. However, the sphere is not always centered at this point, so it is also useful to describe a transformation of the incident field coefficients that avoids the need to alter  $\Psi(\theta_k, \phi_k)$  itself. This transformation is especially useful for axisymmetric incident fields, so they will be considered here.

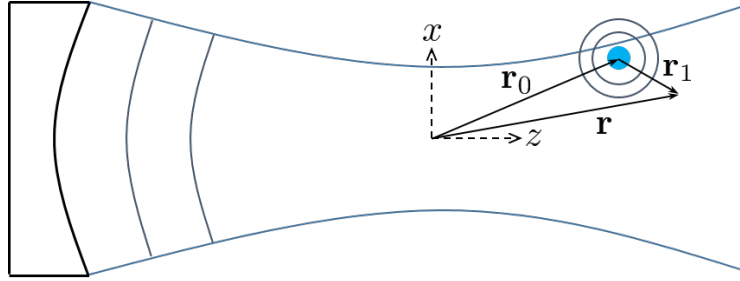


Figure 3.1: Diagram of a focused transducer (left) projecting a sound beam with a focus at the origin and the scatterer located away from the focus. Scattered waves are illustrated departing the scatterer.

Let the center of the sphere be located at  $\mathbf{r}_0 = (x_0, y_0, z_0)$  as in Fig. 3.1, and let the position vector relative to the new sphere center be  $\mathbf{r}_1$ . Then,  $\mathbf{r} = \mathbf{r}_0 + \mathbf{r}_1$  and

$$e^{i\mathbf{k}\cdot\mathbf{r}} = e^{i\mathbf{k}\cdot\mathbf{r}_0} e^{i\mathbf{k}\cdot\mathbf{r}_1} . \quad (3.18)$$

For an axisymmetric incident field,  $y_0$  can be set to zero without loss of gen-

erality. Since  $\mathbf{r}_0$  is fixed but  $\mathbf{r}_1$  varies, Eq. (3.2) becomes

$$\psi(\mathbf{r}_1) = \int_0^\pi \int_0^{2\pi} e^{i\mathbf{k}\cdot\mathbf{r}_1} e^{ik(x_0 \sin \theta_k \cos \phi_k + z_0 \cos \theta_k)} \Psi(\theta_k) \sin \theta_k d\phi_k d\theta_k. \quad (3.19)$$

Other than the removal of the dependence on  $\phi_k$ , the only difference between Eq. (3.19) and Eq. (3.2) is the second exponential in the integrand. Therefore, we can compare with Eq. (3.14) and write, by inspection,

$$a_n^m = i^n (2n+1) \sqrt{\frac{(n-m)!}{(n+m)!}} \int_0^\pi \int_0^{2\pi} e^{-im\phi_k} e^{ikx_0 \sin \theta_k \cos \phi_k} e^{ikz_0 \cos \theta_k} \times d_{m0}^n(\theta_k) \Psi(\theta_k) \sin \theta_k d\phi_k d\theta_k. \quad (3.20)$$

From the integral representation of a Bessel function given by

$$J_m(z) = \frac{e^{-im}}{2\pi} \int_0^{2\pi} e^{iz \cos \phi} e^{\pm im\phi} d\phi, \quad (3.21)$$

integration over  $\phi_k$  can be performed to obtain

$$a_n^m = i^n i^m 2\pi (2n+1) \sqrt{\frac{(n-m)!}{(n+m)!}} \times \int_0^\pi d_{m0}^n(\theta_k) J_m(kx_0 \sin \theta_k) e^{ikz_0 \cos \theta_k} \Psi(\theta_k) \sin \theta_k d\theta_k. \quad (3.22)$$

Note that the dependence on  $m$  has returned since the sphere has been moved off the symmetry axis. These coefficients can be used to find  $F_z$  from Eq. (2.67) or Eq. (2.73).

### 3.1.4 Incident Field Coefficients for Transverse Radiation Forces

For the acoustic radiation force components  $F_x$  and  $F_y$ , different incident field coefficients must be obtained. Since the coefficients  $\tilde{a}_n^m (\equiv [\tilde{a}_n^m]_z)$

pertain to an expansion about the  $z$ -axis to describe  $F_z$ , expansions about the  $x$ -axis and  $y$ -axis are necessary to describe  $F_x$  and  $F_y$ , respectively. To obtain these expansions, the Wigner D-matrix transformation is again quite useful. Combining a general spherical harmonic expansion, as in Eq. (2.69), with Eq. (3.8) gives

$$\begin{aligned}
\sum_{m'=-n}^n \tilde{a}_n^{m'} Y_{nm'}(\theta, \phi) &= \sum_{m'=-n}^n \tilde{a}_n^{m'} \sum_{m=-n}^n D_{mm'}^n(\alpha, \beta, \gamma) Y_{nm}(\theta, \phi) \\
&= \sum_{m=-n}^n Y_{nm}(\theta, \phi) \sum_{m'=-n}^n \tilde{a}_n^{m'} D_{mm'}^n(\alpha, \beta, \gamma) \\
&= \sum_{m=-n}^n \tilde{a}_n^m Y_{nm}(\theta, \phi), \tag{3.23}
\end{aligned}$$

where

$$\tilde{a}_n^m = \sum_{m'=-n}^n \tilde{a}_n^{m'} D_{mm'}^n(\alpha, \beta, \gamma). \tag{3.24}$$

Equivalently,  $\tilde{a}_n^{m'}$  can be written via an inverse transformation as

$$\tilde{a}_n^{m'} = \sum_{m=-n}^n \tilde{a}_n^m [D^{-1}(\alpha, \beta, \gamma)]_{m'm}^n = \sum_{m=-n}^n \tilde{a}_n^m D_{m'm}^n(-\gamma, -\beta, -\alpha). \tag{3.25}$$

The Euler angles  $(\alpha, \beta, \gamma)$  will have different values depending on whether  $z'$  is aligned with  $x$  or with  $y$ . For expansion about the  $x$ -axis—required for  $F_x$ —the Euler angles are  $(0, \pi/2, \pi/2)$ , and for expansion about the  $y$ -axis—required for  $F_y$ —the Euler angles are  $(-\pi/2, -\pi/2, 0)$ . The resulting coefficients for expansion about the  $x$ - and  $y$ -axes are, respectively,

$$[\tilde{a}_n^{m'}]_x = \sum_{m=-n}^n [\tilde{a}_n^m]_z D_{m'm}^n(-\pi/2, -\pi/2, 0), \tag{3.26}$$

$$[\tilde{a}_n^{m'}]_y = \sum_{m=-n}^n [\tilde{a}_n^m]_z D_{m'm}^n(0, \pi/2, \pi/2). \tag{3.27}$$

## 3.2 Modeling the Incident Beam

Incident field coefficients are computed here for several specific cases to illustrate the practicality of this method. The following cases are treated in this section: a “simple” focused beam in  $k$ -space (so-called because of its convenient mathematical definition), a focused Gaussian beam, and a focused circular transducer. While this section includes discussion of only traveling wave incident fields, standing waves are easily constructed by adding appropriate counter-propagating traveling waves.

### 3.2.1 Simple Focused Beam

The most simple description of an axisymmetric beam in  $k$ -space is

$$\Psi(\theta_k) = \begin{cases} \Psi_0, & 0 \leq \theta_k < \theta_0 \\ 0, & \theta_0 \leq \theta_k \leq \pi \end{cases}, \quad (3.28)$$

which corresponds to a beam with a focus at  $z = 0$ . Examples of this description are shown for frequency  $f = 1$  MHz and various values of  $\theta_0$  in Fig. 3.2. In Fig. 3.2(a) for  $\theta_0 = 5^\circ$ , the narrow confinement angle results in a beam that appears non-diffracting in the focal region. In Fig. 3.2(b) and (c), however, the beam is considerably narrower in the focal region, and as can be seen in Fig. 3.2(d), it appears to have a Bessel-like shape in the focal plane. Also, note that due to the idealized nature of the definition in Eq. (3.28), the focusing occurs at exactly  $z = 0$  and the axial profile shown in Fig. 3.2(e) is symmetric about  $z = 0$ .

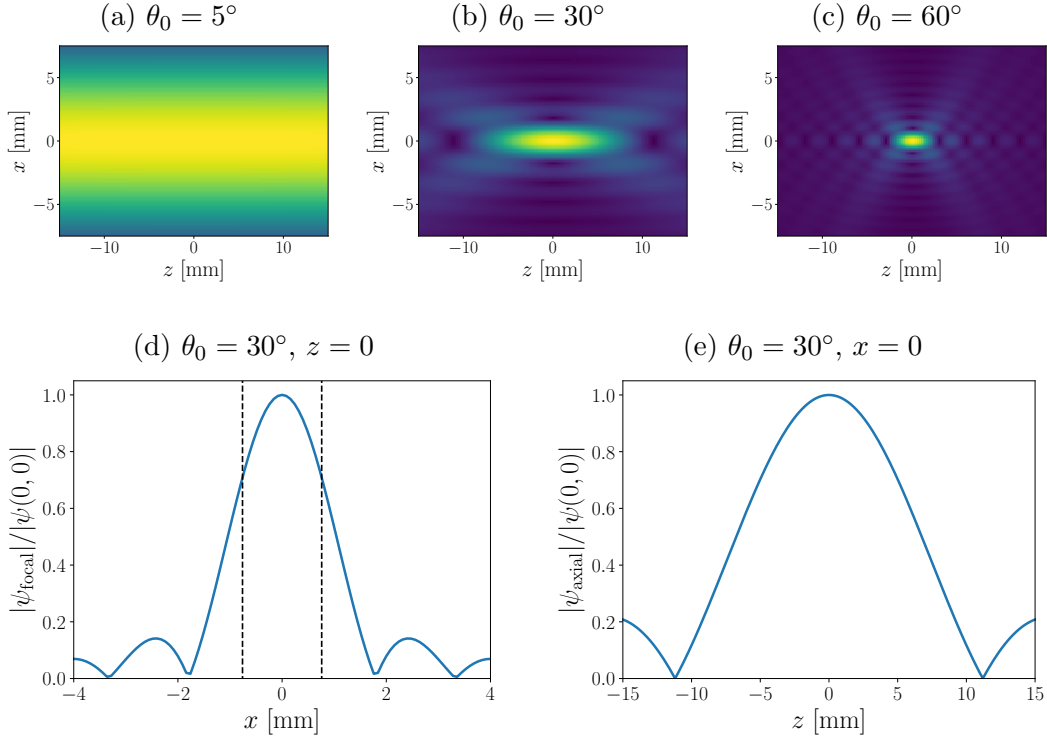


Figure 3.2: Beam amplitude profiles for  $\Psi(\theta_k)$  defined as in Eq. (3.28) for various confinement angles  $\theta_0$  at frequency  $f = 1$  MHz. For  $\theta_0 = 30^\circ$ , a focal profile (where dashed lines indicate the half-power beamwidth) is shown in (d) and an axial profile is shown in (e). The colors in (a), (b), and (c) correspond to the vertical axes in (d) and (e), with yellow equal to unity and dark blue equal to zero.

Substitution of Eq. (3.28) into Eq. (3.17) gives the expression

$$a_n = i^n 2\pi(2n+1)\Psi_0 \int_0^{\theta_0} P_n(\cos \theta_k) \sin \theta_k d\theta_k, \quad (3.29)$$

which can be evaluated with the following integral property of Legendre polynomials:

$$\left(n + \frac{1}{2}\right) \int_0^{\theta_0} P_n(\cos \theta_k) \sin \theta_k d\theta_k = \frac{1}{2} [P_{n-1}(\cos \theta_0) - P_{n+1}(\cos \theta_0)]. \quad (3.30)$$

Equation (3.29) then becomes

$$\begin{aligned} a_n &= i^n 4\pi\Psi_0 \left(n + \frac{1}{2}\right) \int_0^{\theta_0} P_n(\cos \theta_k) \sin \theta_k d\theta_k \\ &= i^n 2\pi\Psi_0 [P_{n-1}(\cos \theta_0) - P_{n+1}(\cos \theta_0)], \end{aligned} \quad (3.31)$$

which can be easily used along with scattering coefficients to compute the radiation force. Equation (3.28) can be substituted into Eq. (3.22) to obtain coefficients describing a non-axisymmetric field,

$$\begin{aligned} a_n^m &= i^n i^m 2\pi(2n+1)\Psi_0 \sqrt{\frac{(n-m)!}{(n+m)!}} \\ &\times \int_0^{\theta_0} d_{m0}^n(\theta_k) J_m(kx_0 \sin \theta_k) e^{ikz_0 \cos \theta_k} \sin \theta_k d\theta_k, \end{aligned} \quad (3.32)$$

but the integral cannot be evaluated analytically for arbitrary  $x_0$  and  $z_0$ , so it must be computed numerically.

In choosing the constant  $\Psi_0$  in Eq. (3.28), it is helpful to consider two possibilities. The first is to choose  $\Psi_0$  such that the amplitude of the potential field at the origin is equal to the value for a given plane wave. For a time-harmonic traveling plane wave with spatial dependence  $\psi(z) = \psi_0 e^{ikz}$

as described in Eq. (2.82), this can be accomplished by choosing the following normalization:

$$\Psi_0 = \psi_0 \left[ \int_0^{\theta_0} \int_0^{2\pi} \sin \theta_k d\phi_k d\theta_k \right]^{-1} = \frac{\psi_0}{2\pi(1 - \cos \theta_0)}. \quad (3.33)$$

This choice is useful when examining the effect of scatterer size on radiation force for a particular beam shape. However, its utility is diminished when comparing radiation force calculations between an incident plane wave and an incident sound beam. For this purpose, a different value of  $\Psi_0$  is chosen such that the power incident on a sphere of a given size is equal to the value for a plane wave. This second choice requires both the pressure and the particle velocity in the  $z = 0$  plane.

For an acoustic displacement potential described by Eq. (3.1), the pressure is

$$p(\mathbf{r}, t) = -\rho_0 \frac{\partial^2 \varphi}{\partial t^2} = \frac{1}{2} \rho_0 \omega^2 e^{-i\omega t} \psi(\mathbf{r}) + \text{c.c.}, \quad (3.34)$$

where  $\rho_0$  is the density of the medium, and the particle velocity is

$$\mathbf{v}(\mathbf{r}, t) = \nabla \frac{\partial \varphi}{\partial t} = -\frac{1}{2} i \omega e^{-i\omega t} \nabla \psi(\mathbf{r}) + \text{c.c.} \quad (3.35)$$

For a plane wave with spatial dependence given by Eq. (2.82), the pressure and particle velocity amplitudes are

$$\tilde{p}(z) = \rho_0 \omega^2 \psi_0 e^{ikz}, \quad (3.36)$$

$$\tilde{v}_z(z) = \omega k \psi_0 e^{ikz} = \frac{\omega^2}{c_l} \psi_0 e^{ikz}, \quad (3.37)$$

where

$$p(z, t) = \frac{1}{2} \tilde{p}(z) e^{-i\omega t} + \text{c.c.}, \quad (3.38)$$

$$v(z, t) = \frac{1}{2} \tilde{v}(z) e^{-i\omega t} + \text{c.c.} \quad (3.39)$$

Since the time-averaged intensity is given by

$$\mathbf{I} = \frac{1}{2} \text{Re} \{ \tilde{p} \tilde{\mathbf{v}}^* \}, \quad (3.40)$$

the power through a circular area of radius  $R$  contained in the plane wave described by Eqs. (3.36) and (3.37) is

$$W_{z,\text{plane}} = \pi R^2 \frac{\rho_0 \omega^4}{2c_l} |\psi_0|^2. \quad (3.41)$$

The pressure, particle velocity, and power over a circular area must also be calculated for the beam defined by  $\Psi(\theta_k)$ . Substitution into Eq. (3.2) gives the following result:

$$\psi(r, \theta) = 2\pi \Psi_0 \int_0^{\theta_0} e^{ikr \cos \theta \cos \theta_k} J_0(kr \sin \theta \sin \theta_k) \sin \theta_k d\theta_k, \quad (3.42)$$

which does not appear to be integrable analytically. Since the power incident on the cross-sectional area of a sphere is of interest, we need the value of  $\psi$  in the plane  $z = 0$  (i.e.,  $\theta = \pi/2$ ), which is

$$\psi\left(r, \frac{\pi}{2}\right) = 2\pi \Psi_0 \int_0^{\theta_0} J_0(kr \sin \theta_k) \sin \theta_k d\theta_k. \quad (3.43)$$

From this, the pressure amplitude is found to be

$$\begin{aligned} \tilde{p}\left(r, \frac{\pi}{2}\right) &= \rho_0 \omega^2 \psi\left(r, \frac{\pi}{2}\right) \\ &= 2\pi \Psi_0 \rho_0 \omega^2 \int_0^{\theta_0} J_0(kr \sin \theta_k) \sin \theta_k d\theta_k, \end{aligned} \quad (3.44)$$

and the particle velocity  $\tilde{v}_z$ , which is equivalent to  $-\tilde{v}_\theta$  for  $\theta = \pi/2$ , is

$$\begin{aligned}\tilde{v}_z\left(r, \frac{\pi}{2}\right) &= -i\omega \left. \frac{\partial\psi}{\partial z} \right|_{z=0} = \frac{i\omega}{r} \left. \frac{\partial\psi}{\partial\theta} \right|_{\theta=\frac{\pi}{2}} \\ &= 2\pi\Psi_0 \frac{\omega^2}{c_l} \int_0^{\theta_0} J_0(kr \sin\theta_k) \cos\theta_k \sin\theta_k d\theta_k.\end{aligned}\quad (3.45)$$

The power through the region occupied by the sphere is then found by integrating the  $z$ -component of Eq. (3.40) over a circular area of radius  $R$ . This result is

$$W_{z,\text{beam}} = \int_0^R 2\pi r I_z dr = \pi \int_0^R \text{Re} \left\{ \tilde{p}\left(r, \frac{\pi}{2}\right) \tilde{v}_z^*\left(r, \frac{\pi}{2}\right) \right\} r dr. \quad (3.46)$$

Equations (3.41) and (3.46) can be set equal to each other and reorganized such that  $\Psi_0$  for the focused beam is written in terms of  $\psi_0$  for the plane traveling wave, resulting in the same power incident on the sphere for either wave field. Equation (3.46) may also be used for two different types of focused beams to hold the incident power constant while varying the incident beam shape alone, isolating the effect of incident beam shape on the radiation force exerted on the sphere.

### 3.2.2 Focused Gaussian Beam

Expression of a focused Gaussian beam in terms of its angular spectrum lacks the analytic simplicity of Eq. (3.28), but it can still be accomplished numerically. The basic method requires the two-dimensional Fourier transform to obtain the angular spectrum of the incident field [101]. However, since our field description requires a three-dimensional angular spectrum, a few modi-

fications are made to map this angular spectrum onto a hemispherical cap in wavenumber space [102].

Consider a field  $\psi(x, y, 0)$ , where  $z = 0$  is the source plane. The two-dimensional angular spectrum can be found through

$$\Psi_2(k_x, k_y, 0) = \mathcal{F}_2\{\psi(x, y, 0)\}, \quad (3.47)$$

where  $\mathcal{F}_2$  represents a Fourier transform in two dimensions. The field at  $(x, y, z)$  can be found by propagating this angular spectrum in the  $z$ -direction and computing an inverse Fourier transform:

$$\psi(x, y, z) = \mathcal{F}_2^{-1}\{\Psi_2(k_x, k_y, 0)e^{ik_z z}\}, \quad (3.48)$$

where  $\mathcal{F}_2^{-1}$  represents an inverse Fourier transform in two dimensions. Equation (3.48) can easily be used to find the field at any point in space, but for the purpose of computing the incident field coefficients needed for the radiation force, a three-dimensional angular spectrum of the field is needed about the center of the spherical scatterer. From the convolution theorem, the above equation can be rewritten as

$$\begin{aligned} \psi(x, y, z) &= \psi(x, y, 0) ** \mathcal{F}_2^{-1}\{e^{ik_z z}\} \\ &= \psi(x, y, 0) ** \left[ -\frac{1}{2\pi} \frac{\partial}{\partial z} \left( \frac{e^{ikr}}{r} \right) \right] \\ &= -\frac{1}{2\pi} \int_{-\infty}^{\infty} \int_{-\infty}^{\infty} \psi(x_0, y_0, 0) \frac{\partial}{\partial z} \left( \frac{e^{ikR}}{R} \right) dx_0 dy_0, \end{aligned} \quad (3.49)$$

where  $**$  denotes a two-dimensional convolution and

$$R = \sqrt{(x - x_0)^2 + (y - y_0)^2 + (z - z_0)^2}. \quad (3.50)$$

Equation (3.49) can be rewritten via a three-dimensional integral as

$$\begin{aligned}\psi(x, y, z) &= -\frac{1}{2\pi} \int_{-\infty}^{\infty} \int_{-\infty}^{\infty} \int_{-\infty}^{\infty} \psi(x_0, y_0, z_0) \delta(z_0) \frac{\partial}{\partial z} \left( \frac{e^{ikR}}{R} \right) dx_0 dy_0 dz_0 \\ &= \frac{1}{2\pi} \int_{-\infty}^{\infty} \int_{-\infty}^{\infty} \int_{-\infty}^{\infty} \psi(x_0, y_0, z_0) \delta(z_0) \frac{\partial}{\partial z_0} \left( \frac{e^{ikR}}{R} \right) dx_0 dy_0 dz_0,\end{aligned}\tag{3.51}$$

where the minus sign is dropped because of the switch to differentiation in  $z_0$  instead of in  $z$ . The convolution theorem can be applied again to obtain

$$\begin{aligned}\psi(x, y, z) &= \frac{1}{2\pi} \mathcal{F}_3^{-1} \left\{ \mathcal{F}_3 \{ \psi(x_0, y_0, z_0) \delta(z_0) \} \mathcal{F}_3 \left\{ \frac{\partial}{\partial z_0} \left( \frac{e^{ikR}}{R} \right) \right\} \right\} \\ &= \frac{1}{2\pi} \mathcal{F}_3^{-1} \left\{ \mathcal{F}_2 \{ \psi(x_0, y_0, 0) \} \mathcal{F}_3 \left\{ \frac{\partial}{\partial z_0} \left( \frac{e^{ikR}}{R} \right) \right\} \right\},\end{aligned}\tag{3.52}$$

where  $\mathcal{F}_3$  and  $\mathcal{F}_3^{-1}$  represent Fourier and inverse Fourier transforms, respectively, in three dimensions. Equation (3.52) has the form needed for the computation of incident field coefficients since it is written as an inverse Fourier transform in three dimensions. Assuming that only propagating waves reach the scatterer—a reasonable assumption for practical applications—allows the second Fourier transform in brackets to be written as [102]

$$\mathcal{F}_3 \left\{ \frac{\partial}{\partial z_0} \left( \frac{e^{ikR}}{R} \right) \right\} = \frac{4\pi^2 k_z}{k} \delta(k_r - k).\tag{3.53}$$

So, for a scatterer located at a distance  $z$  from the source plane where the two-dimensional angular spectrum is  $\Psi_2(k_x, k_y, 0)$  (where  $k_x = k_r \sin \theta_k \cos \phi_k$  and  $k_y = k_r \sin \theta_k \sin \phi_k$ ), the function  $\Psi(\theta_k, \phi_k)$  in Eq. (3.2) is found to be

$$\Psi(\theta_k, \phi_k) = \frac{k^2}{4\pi^2} \cos \theta_k e^{ikz \cos \theta_k} \Psi_2(\theta_k, \phi_k),\tag{3.54}$$

and the same operations as mentioned in the previous sections apply.

In the paraxial approximation for  $ka \gg 1$  and small aperture angle, a focused Gaussian beam defined in the source plane in polar coordinates  $(\rho, z)$  can be described by the equation

$$\psi(\rho, 0) = \psi_0 e^{-\rho^2/a^2} e^{-ik\rho^2/2d}, \quad (3.55)$$

where  $a$  is the characteristic source radius and  $d$  is the focal distance. Equation (3.55) can be rewritten as

$$\psi(\rho, 0) = \psi_0 e^{-(1+ika^2/2d)\rho^2/a^2} = \psi_0 e^{-(1+iG)\rho^2/a^2} = \psi_0 e^{-\rho^2\tilde{a}^2}, \quad (3.56)$$

where  $G = ka^2/2d$  is the focusing gain [115] and  $\tilde{a}^2 = a^2/(1+iG)$ . The two-dimensional Fourier transform of Eq. (3.56) is

$$\Psi_2(\theta_k) = \pi\tilde{a}^2\psi_0 e^{-k^2\tilde{a}^2 \sin^2 \theta_k/4}. \quad (3.57)$$

Then, the incident coefficients for a sphere located at the focus can be found from the result in Eq. (3.17) and the transformation in Eq. (3.54):

$$a_n = \frac{i^n(2n+1)k^2\tilde{a}^2\psi_0}{2} \int_0^\pi P_n(\cos \theta_k) e^{ikd \cos \theta_k} e^{-k^2\tilde{a}^2 \sin^2 \theta_k/4} \sin \theta_k \cos \theta_k d\theta_k. \quad (3.58)$$

### 3.2.3 Focused Circular Transducer

The description of the field radiated by a focused circular transducer in terms of its angular spectrum also lacks the analytic simplicity of Eq. (3.28), but it can also still be obtained numerically through the same method described for the focused Gaussian beam. A focused circular transducer defined

in the source plane can be described approximately for directional radiation by the equation

$$\psi(\rho, 0) = \begin{cases} \psi_0 e^{-ik\rho^2/2d}, & 0 \leq \rho \leq a \\ 0, & \rho > a \end{cases}, \quad (3.59)$$

where  $a$  is now the exact radius of the transducer. The two-dimensional Fourier transform is

$$\Psi_2(\theta_k) = 2\pi\psi_0 \int_0^a e^{-ik\rho^2/2d} J_0(k \sin \theta_k \rho) \rho d\rho. \quad (3.60)$$

This integral can be computed analytically for  $\theta_k = 0$ , but in general it cannot be simplified. The incident coefficients for a sphere located at the focus can be found from the result in Eq. (3.17) and the transformation in Eq. (3.54):

$$a_n = i^n (2n + 1) k^2 \psi_0 \int_0^\pi \cos \theta_k e^{ik \cos \theta_k d} \left[ \int_0^a e^{ik\rho^2/2d} J_0(k \sin \theta_k \rho) \rho d\rho \right] d\theta_k. \quad (3.61)$$

Results for a focused Gaussian beam and a focused circular transducer are presented in Fig. 3.3. Note that  $z = 0$  corresponds to the plane of the geometric focus (absent diffraction effects); for both the Gaussian and the circular transducer, the source plane is  $z = -d$ . Both the Gaussian and the circular transducer focus early due to diffraction, and the circular transducer focuses still earlier because it requires a larger radius such that  $a_{\text{circ}}/\sqrt{2} = a_{\text{Gauss}}$  (and hence a larger gain) to achieve the same half-power beamwidth as a focused Gaussian. Recall from Fig. 3.2 that the simple beam focuses exactly at  $z = 0$  because of its  $k$ -space definition. The idealized nature of the Gaussian source also gives it a smoother spatial profile, whereas the abrupt cutoff of the

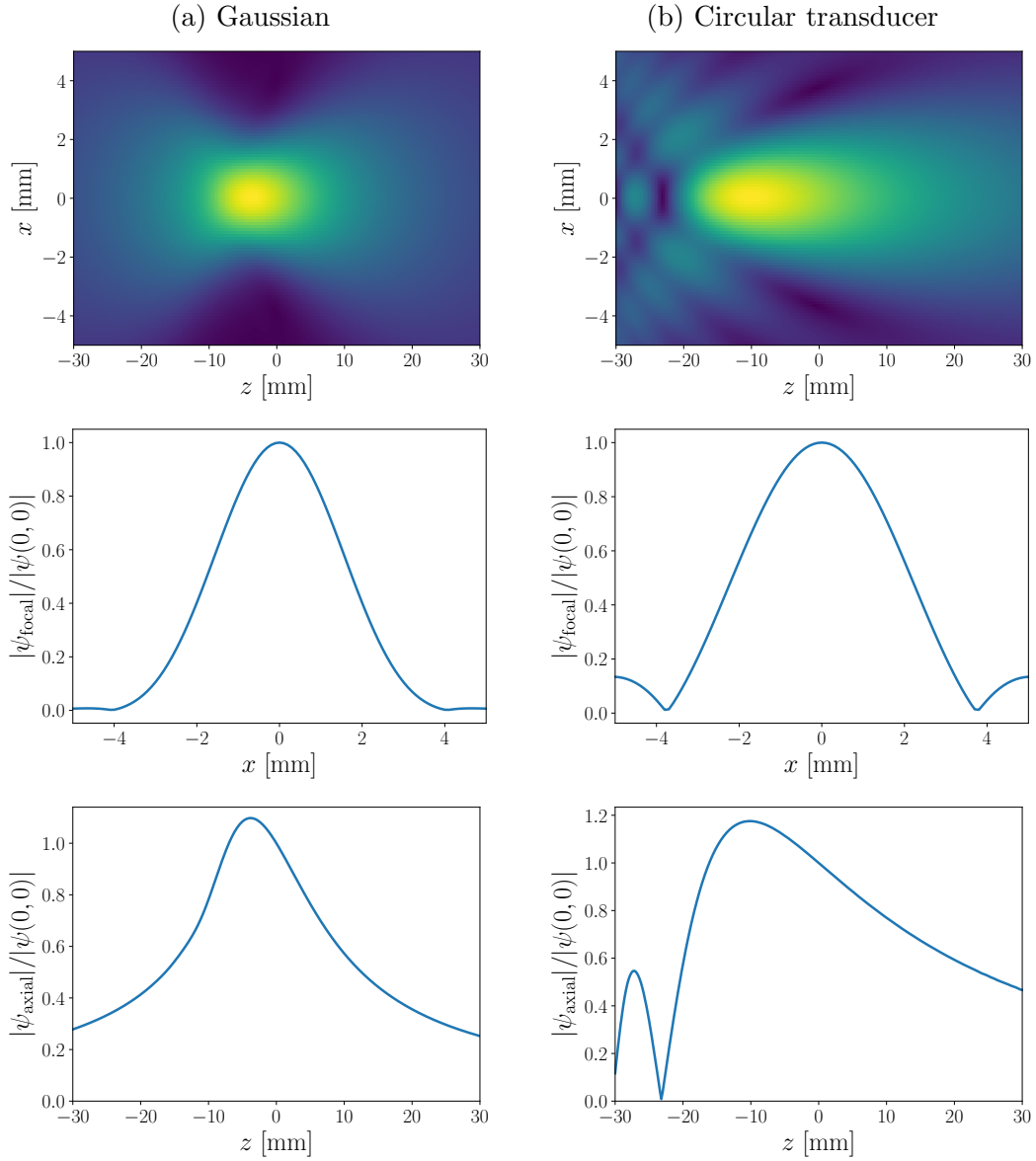


Figure 3.3: Plots of beam amplitude for a focused Gaussian beam and circular transducer with  $a = 1$  cm and  $d = 4$  cm ( $G = 5.2$ ) at  $f = 1$  MHz. The first row shows color plots of the beam amplitude in the  $z$ - $x$  plane, and the second and third rows show focal and axial profiles, respectively. The colors in the first row correspond to the vertical axes in the second and third rows, with yellow equal to the maximum value and dark blue equal to zero.

circular transducer and the abrupt cutoff in  $k$ -space for the simple beam both result in side lobes.

### 3.3 Elastic Scattering Coefficients

We now discuss the calculation of the elastic scattering coefficients. Several cases are treated in this section, all of which are related to the most general case of an elastic sphere embedded in an elastic medium. These cases have been previously discussed in several other works [109, 116], but they are included in this section both to consolidate them for the reader and to present them in the format and notation required for the radiation force equations presented in Sec. 2.1.2. Additionally, to the author’s knowledge, the limit of zero shear modulus in the medium surrounding the sphere—discussed at the end of Sec. 3.4.2—has not been addressed explicitly in the literature.

For an elastic sphere embedded in an elastic medium, boundary conditions at the surface of the sphere are continuity of normal and tangential displacement and continuity of normal and tangential stress:

$$u_n^i + u_n^s = u_n^t, \quad (3.62)$$

$$\sigma_{nr}^i + \sigma_{nr}^s = \sigma_{nr}^t, \quad (3.63)$$

where  $n$  refers to coordinate  $r$ ,  $\theta$ , or  $\phi$ . Normal and tangential displacements

and stresses are calculated via

$$u_r = \frac{\partial\psi}{\partial r} - \frac{1}{r}\Omega\Pi, \quad (3.64)$$

$$u_\theta = \frac{1}{r} \frac{\partial}{\partial\theta} \left[ \psi + \frac{\partial(r\Pi)}{\partial r} \right], \quad (3.65)$$

$$u_\phi = \frac{1}{r \sin\theta} \frac{\partial}{\partial\phi} \left[ \psi + \frac{\partial(r\Pi)}{\partial r} \right], \quad (3.66)$$

$$\sigma_{rr} = -\rho\omega^2 \left\{ \psi + \frac{2}{\kappa^2} \left[ \frac{2}{r} \frac{\partial\psi}{\partial r} + \frac{1}{r^2} \Omega\psi + \frac{\partial}{\partial r} \left( \frac{1}{r} \Omega\Pi \right) \right] \right\}, \quad (3.67)$$

$$\sigma_{\theta r} = \frac{2\rho\omega^2}{\kappa^2 r^2} \frac{\partial}{\partial\theta} \left[ r \frac{\partial\psi}{\partial r} - \psi - r \frac{\partial\Pi}{\partial r} - \left( 1 + \frac{1}{2} \kappa^2 r^2 \right) \Pi - \Omega\Pi \right], \quad (3.68)$$

$$\sigma_{\phi r} = \frac{2\rho\omega^2}{\kappa^2 r^2 \sin\theta} \frac{\partial}{\partial\phi} \left[ r \frac{\partial\psi}{\partial r} - \psi - r \frac{\partial\Pi}{\partial r} - \left( 1 + \frac{1}{2} \kappa^2 r^2 \right) \Pi - \Omega\Pi \right]. \quad (3.69)$$

From Eq. (2.107), recall that  $\Omega$  is the differential operator

$$\Omega = \frac{1}{\sin\theta} \frac{\partial}{\partial\theta} \left( \sin\theta \frac{\partial}{\partial\theta} \right) + \frac{1}{\sin^2\theta} \frac{\partial^2}{\partial\phi^2}. \quad (3.70)$$

Next, note that except for the angle derivative and the factor of  $1/\sin\theta$ , the relations for  $u_\phi$  and  $\sigma_{\phi r}$  are identical to those for  $u_\theta$  and  $\sigma_{\theta r}$ , respectively. The result is that for a spherical scatterer, boundary conditions for  $u_\phi$  and  $\sigma_{\phi r}$  will be equivalent to those for  $u_\theta$  and  $\sigma_{\theta r}$ , so they may therefore be ignored along with Eqs. (3.66) and (3.69) for  $u_\phi$  and  $\sigma_{\phi r}$ . Also, recall from Eqs. (2.29)–(2.33) that the potentials  $\psi$  and  $\Pi$  are defined as infinite sums of spherical wave functions, and note that spherical harmonics  $Y_n^m = P_n^m(\cos\theta)e^{im\phi}$  are eigenfunctions of the differential operator  $\Omega$ :

$$\Omega Y_n^m = -n(n+1)Y_n^m. \quad (3.71)$$

Equation (3.71) allows  $\Omega$  to be replaced with  $-n(n+1)$  Eqs. (3.64), (3.65), (3.67), and (3.68), removing all dependence on the index  $m$ . Therefore, the

scattering coefficients in the spherical harmonic expansions of  $\psi$  and  $\Pi$  will only depend on index  $n$ .

### 3.3.1 Elastic Sphere in Elastic Medium

In the most general case, potentials from Eqs. (2.29)–(2.33) are substituted into Eqs. (3.64)–(3.68) and then boundary conditions from Eqs. (3.62) and (3.63) are enforced. Continuity of radial displacement, tangential displacement, radial stress, and tangential stress yield the following four relations for the four coefficients  $A_n$ ,  $B_n$ ,  $C_n$ ,  $D_n$ :

$$\begin{aligned}
-nj_n(kR) + kRj_{n+1}(kR) &= A_n[nh_n(kR) - kRh_{n+1}] \\
&+ B_nn(n+1)h_n(\kappa R) \\
&- C_n[nj_n(k_tR) - k_tRj_{n+1}(k_tR)] \\
&- D_nn(n+1)j_n(\kappa_tR), \tag{3.72}
\end{aligned}$$

$$\begin{aligned}
-j_n(kR) &= A_nh_n(kR) \\
&+ B_n[(n+1)h_n(\kappa R) - \kappa Rh_{n+1}(\kappa R)] \\
&- C_nj_n(k_tR) \\
&- D_n[(n+1)j_n(\kappa_tR) - \kappa_tRj_{n+1}(\kappa_tR)], \tag{3.73}
\end{aligned}$$

$$\begin{aligned}
& -2n(n-1)j_n(kR) - 4kRj_{n+1}(kR) + (\kappa R)^2j_n(kR) \\
& = A_n[2n(n-1)h_n(kR) + 4kRh_{n+1}(kR) - (\kappa R)^2h_n(kR)] \\
& \quad + 2B_n(n+1)[(n-1)h_n(\kappa R) - \kappa Rh_{n+1}(\kappa R)] \\
& \quad - C_n \frac{\rho_t \kappa^2}{\rho \kappa_t^2} [2n(n-1)j_n(k_t R) + 4k_t R j_{n+1}(k_t R) - (\kappa_t R)^2 j_n(k_t R)] \\
& \quad - D_n \frac{\rho_t \kappa^2}{\rho \kappa_t^2} (n+1)[(n-1)j_n(\kappa_t R) - \kappa_t R j_{n+1}(\kappa_t R)], \tag{3.74} \\
& - (n-1)j_n(kR) + kRj_{n+1}(kR) \\
& = A_n[(n-1)h_n(kR) - kRh_{n+1}(kR)] \\
& \quad + B_n \left[ (n^2-1)h_n(\kappa R) - \frac{1}{2}(\kappa R)^2 h_n(\kappa R) + \kappa R h_{n+1}(\kappa R) \right] \\
& \quad - C_n \frac{\rho_t \kappa^2}{\rho \kappa_t^2} [(n-1)j_n(k_t R) - k_t R j_{n+1}(k_t R)] \\
& \quad - D_n \frac{\rho_t \kappa^2}{\rho \kappa_t^2} \left[ (n^2-1)j_n(\kappa_t R) - \frac{1}{2}(\kappa_t R)^2 j_n(\kappa_t R) + \kappa_t R j_{n+1}(\kappa_t R) \right], \tag{3.75}
\end{aligned}$$

respectively. These are the equations for the elastic scattering coefficients in their most general form, and they can be solved using Cramer's rule. For  $n = 0$ , both  $B_0$  and  $D_0$  are equal to zero and only Eq. (3.72) and Eq. (3.74) are needed to find  $A_0$  and  $C_0$ . For all other  $n$ , the system is solved for all four scattering coefficients.

### 3.3.2 Elastic Sphere in Fluid Medium

An elastic sphere in a fluid medium is now considered. In this case, continuity of tangential displacement is no longer enforced because the fluid can flow along the spherical interface. Also, since there is no scattered shear wave, the remaining equations are modified by setting all  $B_n$  to zero and taking

the limit  $\mu \rightarrow 0$ , and therefore  $\kappa$ , the shear wavenumber in the medium, becomes infinite [116]. The result corresponding to Eq. (3.72) is the same except for the lack of  $B_n$ , but Eqs. (3.74) and (3.75) must be further modified by noting that since  $\kappa \rightarrow \infty$ , only terms with  $\kappa^2$  will survive, since this is the largest order of  $\kappa$  present. This further reduces the number of terms in Eq. (3.74) and completely eliminates  $A_n$  from Eq. (3.75). The results are then, for continuity of radial displacement, radial stress, and tangential stress,

$$\begin{aligned}
-nj_n(kR) + kRj_{n+1}(kR) &= A_n[nh_n(kR) - kRh_{n+1}(kR)] \\
&\quad - C_n[nj_n(k_tR) - k_tRj_{n+1}(k_tR)] \\
&\quad - D_n n(n+1)j_n(\kappa_tR), \tag{3.76}
\end{aligned}$$

$$\begin{aligned}
-j_n(kR) &= A_n h_n(kR) \\
&\quad + C_n \frac{\rho_t}{\rho(\kappa_tR)^2} [2(n+2)k_tRj_{n+1}(k_tR) - (\kappa_tR)^2 j_n(k_tR)] \\
&\quad + D_n \frac{\rho_t}{\rho(\kappa_tR)^2} n [2(n+2)k_tRj_{n+1}(\kappa_tR) - (\kappa_tR)^2 j_n(\kappa_tR)], \tag{3.77}
\end{aligned}$$

$$\begin{aligned}
0 &= C_n [(n-1)j_n(k_tR) - k_tRh_{n+1}(k_tR)] \\
&\quad + D_n \left[ (n^2-1)h_n(\kappa_tR) - \frac{1}{2}(\kappa_tR)^2 h_n(\kappa_tR) + \kappa_tRh_{n+1}(\kappa_tR) \right], \tag{3.78}
\end{aligned}$$

respectively. Note that  $A_n$  does not appear in the last equation because the fluid medium does not support shear stresses, so the tangential stress due to the transmitted field in the scatterer must be zero at the sphere surface.

### 3.3.3 Fluid Sphere in Elastic Medium

Next, for a fluid sphere in an elastic medium, a similar set of operations can be performed. Again, continuity of tangential displacement no longer ap-

plies. The scattered shear wave is retained, but there is no transmitted shear wave into the scatterer, so the equations are modified by setting  $D_n$  to zero and taking the limit  $\mu_t \rightarrow 0$ , and therefore  $\kappa_t$ , the shear wavenumber in the scatterer, becomes infinite [116]. This again leaves Eq. (3.72) unaltered except for the absence of  $D_n$ , and Eqs. (3.74) and (3.75) are further modified by noting that all terms including  $\kappa_t$  in the denominator are eliminated. The results are then, for continuity of radial displacement, radial stress, and tangential stress,

$$\begin{aligned}
& -nj_n(kR) + kRj_{n+1}(kR) \\
& = A_n[nh_n(kR) - kRh_{n+1}(kR)] + B_nn(n+1)h_n(\kappa R) \\
& \quad - C_n[nj_n(k_tR) - k_tRj_{n+1}(k_tR)], \tag{3.79}
\end{aligned}$$

$$\begin{aligned}
& -2(n+2)kRj_{n+1}(kR) + (\kappa R)^2j_n(kR) \\
& = A_n[2(n+2)kRh_{n+1}(kR) - (\kappa R)^2h_n(kR)] \\
& \quad - B_nn[2(n+2)\kappa Rh_{n+1}(\kappa R) - (\kappa R)^2h_n(\kappa R)] \\
& \quad + C_n\frac{\rho_t}{\rho}(\kappa R)^2j_n(k_tR), \tag{3.80}
\end{aligned}$$

$$\begin{aligned}
& -(n-1)j_n(kR) + kRj_{n+1}(kR) \\
& = A_n[(n-1)h_n(kR) - kRh_{n+1}(kR)] \\
& \quad + B_n\left[(n^2-1)h_n(\kappa R) - \frac{1}{2}(\kappa R)^2h_n(\kappa R) + \kappa Rh_{n+1}(\kappa R)\right], \tag{3.81}
\end{aligned}$$

respectively. Note that  $C_n$  does not appear in the last equation because the fluid scatterer does not support shear stresses, so the tangential stress due to the scattered field must be opposite the tangential stress due to the incident field at the sphere surface.

### 3.3.4 Fluid Sphere in Fluid Medium

Results for a fluid sphere in a fluid medium can be obtained from either of the results in the previous two subsections by setting the other shear coefficients equal to zero and taking the corresponding shear wavenumber to infinity. The equation for continuity of tangential stress is also removed since neither the medium nor the scatterer can support shear waves. Either way, the only two equations that result are for  $A_n$  and  $C_n$ . For continuity of radial displacement and radial stress, the results are

$$\begin{aligned}
 -nj_n(kR) + kRj_{n+1}(kR) &= A_n[nh_n(kR) - kRh_{n+1}(kR)] \\
 &\quad - C_n[nj_n(k_tR) - k_tRj_{n+1}(k_tR)], \quad (3.82)
 \end{aligned}$$

$$-j_n(kR) = A_nh_n(kR) - C_n\frac{\rho_t}{\rho}j_n(k_tR), \quad (3.83)$$

respectively. In contrast with the previous systems of equations, these are relatively simple to solve without Cramer's rule.

### 3.3.5 Spherical Void or Rigid Sphere in Elastic Medium

To conclude the discussion of computing elastic scattering coefficients, two final cases are considered. The first is a spherical void in an elastic medium, and the second is a movable rigid sphere in an elastic medium.

For a spherical void, continuity of displacement is no longer enforced, and both the radial and tangential stresses at the surface of the sphere must be zero since the surface is free. This amounts to simply eliminating coefficients

$C_n$  and  $D_n$  from Eqs. (3.74) and (3.75) to obtain, respectively,

$$\begin{aligned}
& -2(n+2)kRj_{n+1}(kR) + (\kappa R)^2 j_n(kR) \\
& = A_n[2(n+2)kRh_{n+1}(kR) - (\kappa R)^2 h_n(kR)] \\
& \quad - B_n n[2(n+2)\kappa Rh_{n+1}(\kappa R) - (\kappa R)^2 h_n(\kappa R)], \tag{3.84}
\end{aligned}$$

$$\begin{aligned}
& -(n-1)j_n(kR) + kRj_{n+1}(kR) \\
& = A_n[(n-1)h_n(kR) - kRh_{n+1}(kR)] \\
& \quad + B_n \left[ (n^2-1)h_n(\kappa R) - \frac{1}{2}(\kappa R)^2 h_n(\kappa R) + \kappa Rh_{n+1}(\kappa R) \right]. \tag{3.85}
\end{aligned}$$

For a rigid sphere, continuity of stress is no longer enforced, leaving only continuity of radial and tangential displacements. If the sphere is not allowed to move, then the displacements are set to zero at the sphere surface. Then, Eqs. (3.72) and (3.73) become

$$-kRj_{n+1}(kR) = A_n kR h_{n+1}(kR) - B_n n \kappa R h_{n+1}(\kappa R), \tag{3.86}$$

$$-j_n(kR) = A_n h_n(kR) + B_n [(n+1)h_n(\kappa R) - \kappa R h_{n+1}(\kappa R)], \tag{3.87}$$

respectively. However, for a movable rigid sphere, another modification must be made. Suppose that the sphere is moving along the  $z$ -axis with displacement  $U_z$ . Conditions for  $u_r$  and  $u_\theta$  then become [116]

$$u_r^i + u_r^s = U_z \cos \theta = U_z P_1(\cos \theta), \tag{3.88}$$

$$u_\theta^i + u_\theta^s = -U_z \sin \theta = U_z \frac{dP_1(\cos \theta)}{d\theta}, \tag{3.89}$$

with  $U_z$  derived from the equation of motion,

$$M \frac{\partial^2 U_z}{\partial t^2} = \int_S (\sigma_{rr} \cos \theta - \sigma_{\theta r} \sin \theta) R^2 \sin \theta d\theta d\phi, \tag{3.90}$$

where  $M = (4/3)\pi R^3 \rho_t$  is the mass of the sphere. Since only  $P_1(\cos \theta)$  and  $dP_1(\cos \theta)/d\theta$  appear above, only the equations with  $n = 1$  must be modified. After solving Eq. (3.90) for  $U_z$  and substituting into Eqs. (3.88) and (3.89), we obtain Eq. (3.86) for continuity of radial displacement and

$$\begin{aligned}
 -\left(1 - \frac{\rho}{\rho_t}\right) j_1(kR) &= A_1 \left(1 - \frac{\rho}{\rho_t}\right) h_1(kR) \\
 &\quad - B_1 \left[ 2 \left(1 - \frac{\rho}{\rho_t}\right) h_1(\kappa R) - \kappa R h_2(\kappa R) \right] \quad (3.91)
 \end{aligned}$$

for continuity of tangential displacement. Note that this equation is identical to Eq. (3.87) for  $n = 1$  except for the coefficient  $(1 - \rho/\rho_t)$  multiplying  $j_1$  and  $h_1$ .

### 3.4 Discussion of Scattering Coefficients

Before proceeding with a discussion of radiation force computations in Chapter 4, consideration is given to the elastic scattering coefficients and scattered displacement fields for several different scatterers in soft tissue and fluid media. This is useful to facilitate understanding of later radiation force results, and as will be shown, it is necessary for the discussion of some non-intuitive results for limiting cases.

#### 3.4.1 Compressional Wave Scattering Coefficients

First, the lowest-order compressional scattering coefficients  $A_n$  in water are compared for hard elastic spheres and movable rigid spheres, then for gas bubbles and spherical voids. The elastic sphere is chosen to be steel, and the

	$\rho_0$ (kg/m <sup>3</sup> )	$c_l$ (m/s)	$c_t$ (m/s)
Water	1000	1500	—
Steel	7810	5945	3252
Rigid	7810	$\infty$	$\infty$
Air	1.21	343	—
Void	0	—	—

Table 3.1: Medium and scatterer properties for rigid/void comparisons

rigid sphere is chosen to have equivalent density to facilitate this comparison. The gas bubble is chosen to be filled with air at room temperature. Material parameters are provided in Table 3.1.

The comparison between a steel sphere and a rigid movable sphere is shown in Fig. 3.4. For smaller spheres, the lowest order scattering coefficients dominate and there is no discernible difference between the scattering coefficients in a steel sphere and a movable rigid sphere of the same density. However, for larger spheres, some differences can be observed as effects of elasticity become significant. Most notably, in Fig. 3.4(b), a null in  $A_1$  appears at  $kR \approx 7.6$ , and for Fig. 3.4(c), a null in  $A_2$  appears at  $kR \approx 5.7$ . Also, in Fig. 3.4(d), the  $A_3$  null at  $kR \approx 8.6$  disappears. These changes are consistent with the minima in the radiation force observed in Fig. 2.1(a). Note that the other nulls are not resonances due to sphere material properties but correspond instead with zeros of  $j'_n(kR)$ .

Similar phenomena can be seen in the coefficients for an air bubble and a spherical void, as shown in Fig. 3.5. As observed in Fig. 3.5(c), for smaller  $kR$ , the monopole scattering coefficient  $A_0$  differs near the Minnaert resonance

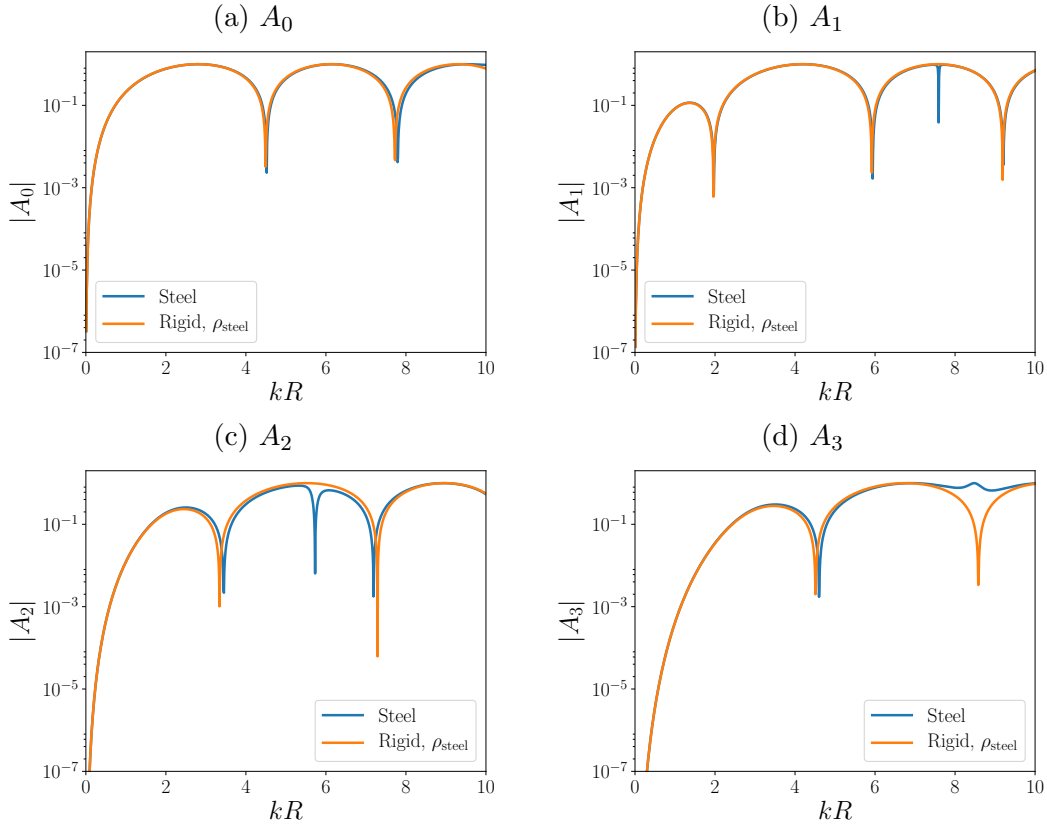


Figure 3.4: Compressional wave scattering coefficients for a steel sphere and a rigid movable sphere of equivalent density in water.

[117] for an air bubble of equilibrium radius  $R_0$ ,

$$f_0 = \frac{1}{2\pi R_0} \sqrt{\frac{3K_{\text{air}}}{\rho_{\text{host}}}}, \quad (3.92)$$

and the coefficients are identical otherwise. As shown in Fig. 3.5(a) and (b), other resonances appear for larger  $kR$ , but the scattering coefficients are again identical off the resonances. The Minnaert resonance will be of particular importance in future radiation force calculations for air bubbles in fluid and soft elastic media (Chapter 4).

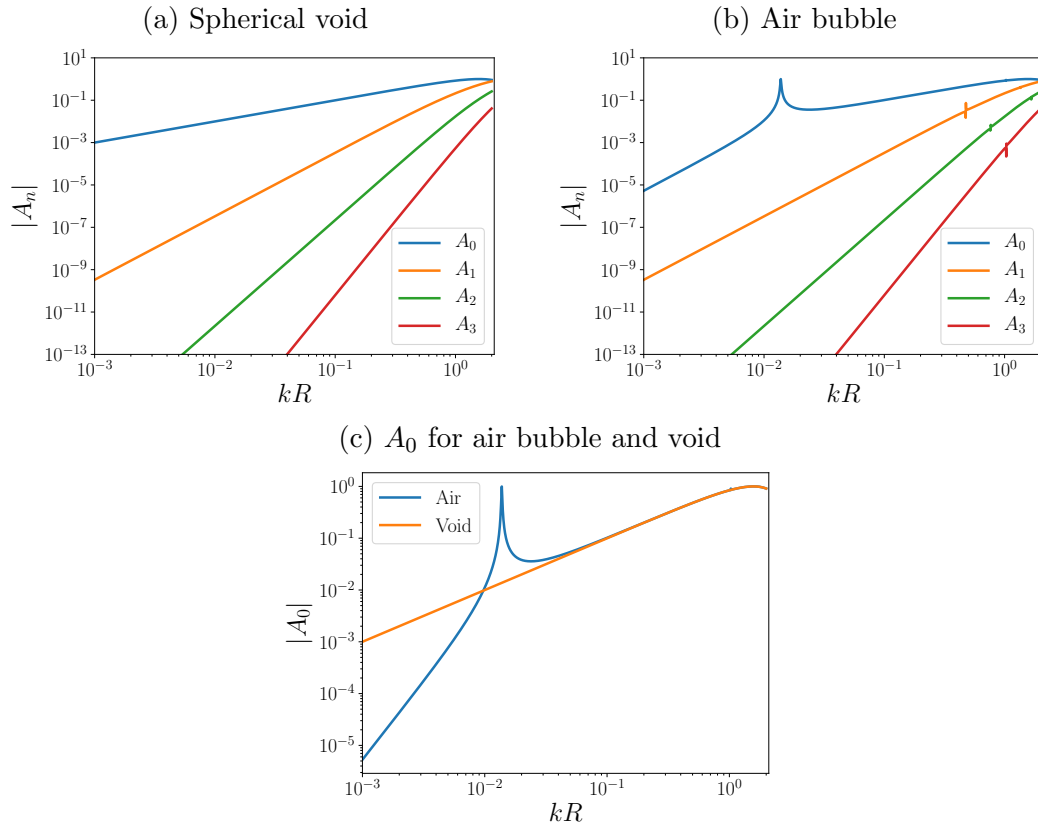


Figure 3.5: Compressional wave scattering coefficients for an air bubble and a spherical void in water.

A further comparison between the steel sphere and the air bubble is also useful. For small  $kR$ , note that from Fig. 3.4 for a steel sphere, the monopole and dipole scattering coefficients  $A_0$  and  $A_1$  are of the same order for the steel sphere, whereas from Fig. 3.5 for an air bubble, the monopole coefficient is much larger. This difference is due to the reaction force that the heavier and stiffer steel sphere exerts on the soft surrounding medium which is forced to move around it, whereas the lighter and softer air bubble exerts no such

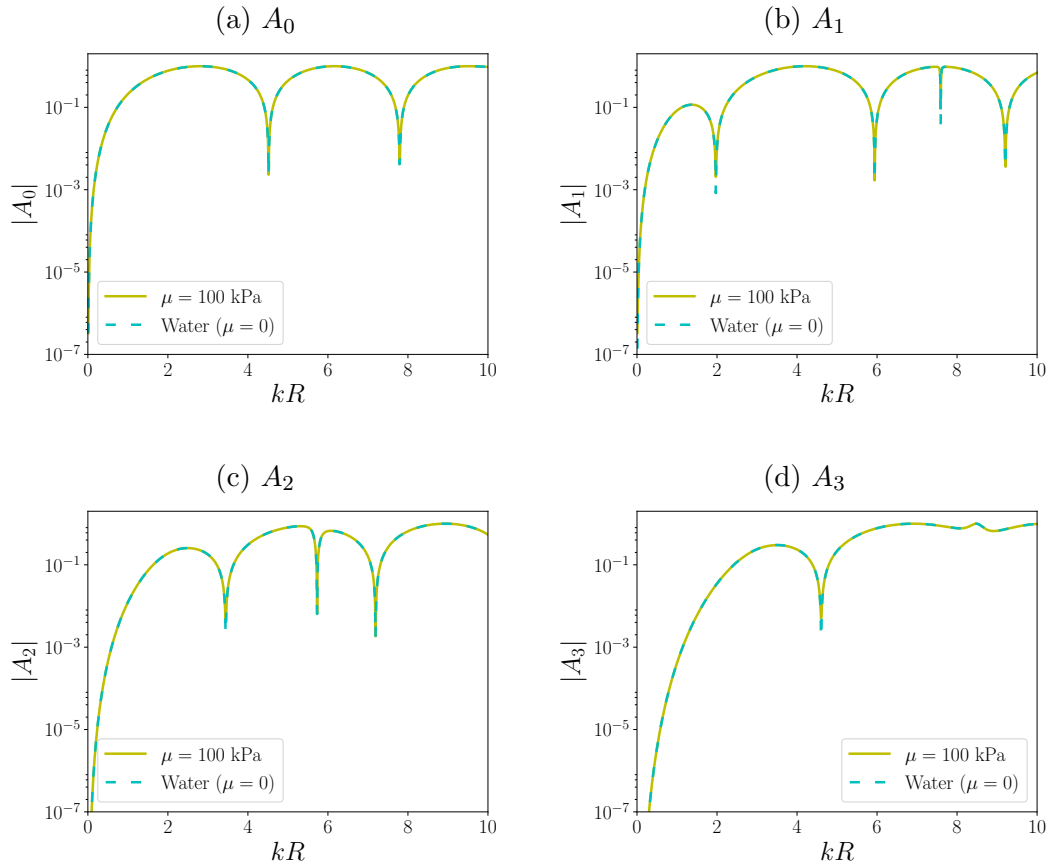


Figure 3.6: Compressional wave scattering coefficients in water and soft tissue ( $\mu = 100$  kPa) for a steel sphere.

reaction.

Considered next is the effect of nonzero shear modulus of the surrounding medium on the compressional wave scattering coefficients  $A_n$ . Recall from Sec. 2.1.1 that the shear modulus in the medium is very small compared to the bulk modulus, but note there are still clear effects on the scattering coefficients. For a hard elastic sphere, the coefficients corresponding to a medium with and

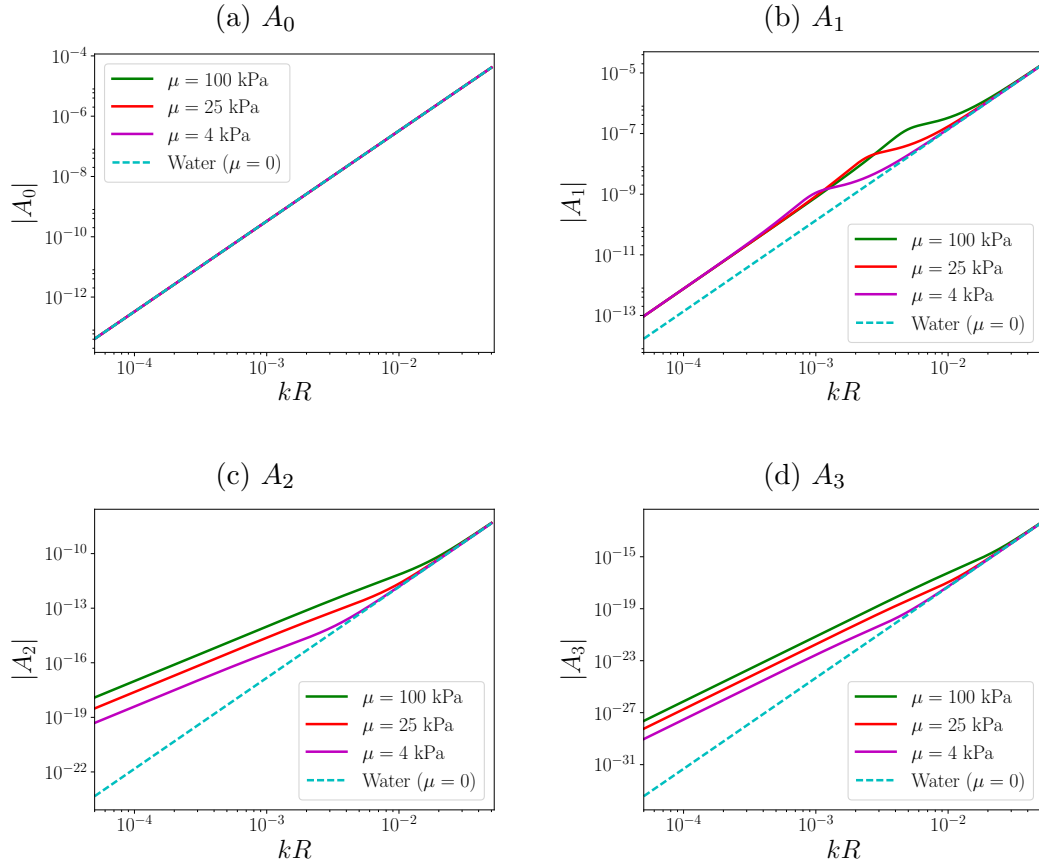


Figure 3.7: Compressional wave scattering coefficients in water and soft tissue for a steel sphere.

without shear are nearly identical for larger  $kR$ , resulting in an equivalent compressional contribution  $F_n$  to the radiation force (see Fig. 3.6). However, for smaller  $kR$ , differences can be observed for  $n > 0$  (see Fig. 3.7). In particular, the difference in the dipole scattering coefficients  $A_1$ —Fig. 3.7(b)—results in a substantial change in the radiation force components  $F_n$  (discussed in Chapter 4). While the coefficients  $A_2$  and  $A_3$ —Fig. 3.7(c) and (d), respectively—also

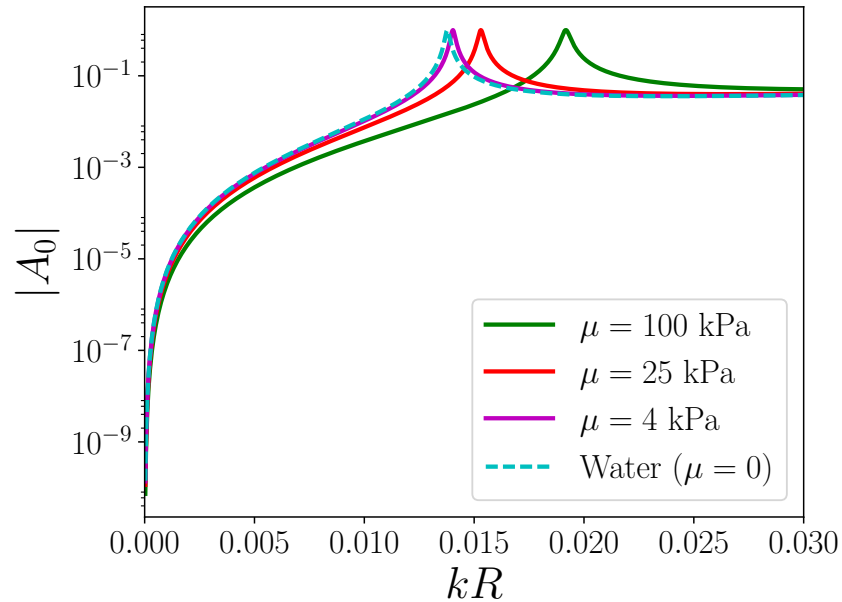


Figure 3.8: Monopole scattering coefficient magnitude for an air bubble in water and soft tissue-like media.

change substantially, their effect on  $F_n$  is much less because they are orders of magnitude smaller than  $A_1$ . Also note that the coefficients tend toward those for water with decreasing shear modulus, as expected.

For a gas bubble surrounded by a medium with and without shear modulus (see Fig. 3.8), the coefficients are nearly identical except at bubble resonances. Of greatest interest is the peak in  $A_0$  at the Minnaert resonance. The added shear stiffness in the medium results in an increase in the resonance frequency, which is written as [118]

$$f_0 = \frac{1}{2\pi R_0} \sqrt{\frac{3K_{\text{air}} + 4\mu_{\text{host}}}{\rho_{\text{host}}}}. \quad (3.93)$$

This shift in the resonance can be seen in Fig. 3.8, which shows a plot of the

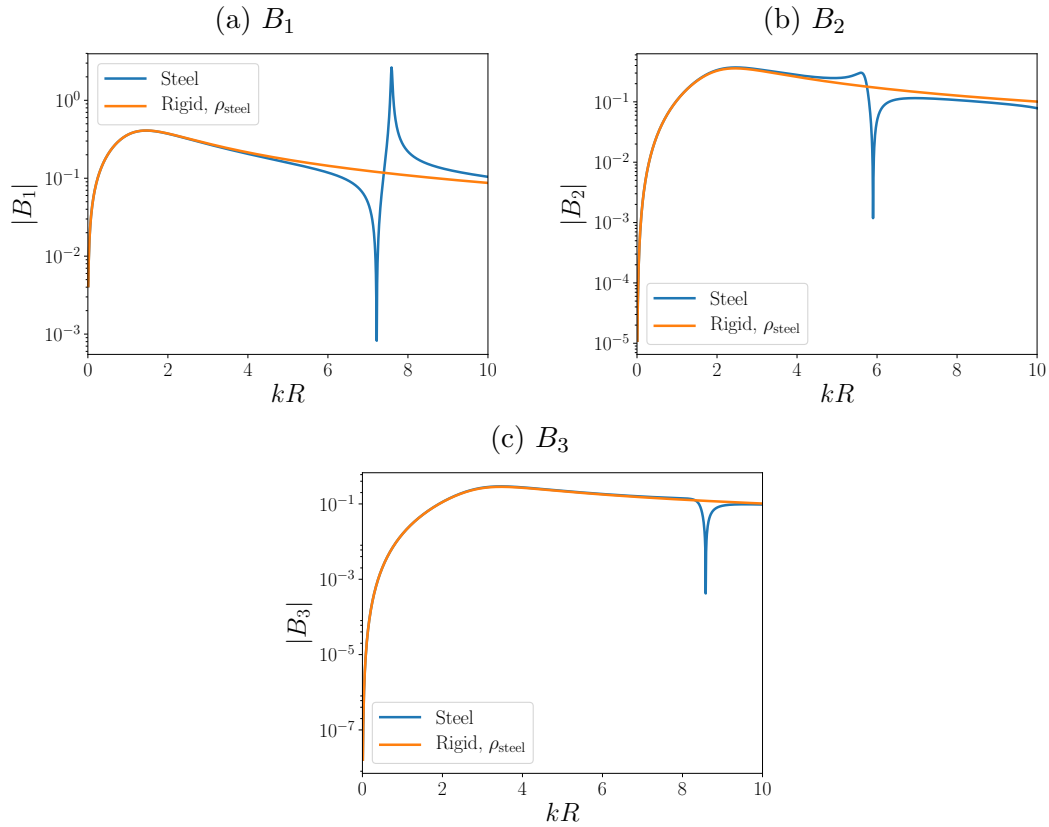


Figure 3.9: Scattering coefficients for the shear wave in a soft tissue-like medium ( $\mu = 4$  kPa) surrounding a steel sphere and a rigid movable sphere of equivalent density.

monopole scattering coefficient for small  $kR$ . The values of  $|A_0|$  are nearly indistinguishable for larger  $kR$ , and for other  $A_n$ , the values are nearly the same for any  $kR$ .

### 3.4.2 Shear Wave Scattering Coefficients

The coefficients  $B_n$  for the scattered shear wave are now considered. These coefficients are all equal to zero in the case of an inviscid fluid medium,

so they need only be examined for nonzero shear modulus. The comparison between a steel sphere and a rigid movable sphere embedded in a medium resembling soft tissue ( $\mu = 4$  kPa) is shown in Fig. 3.9. There is no discernible difference for  $kR < 1$ , but for larger spheres, scattering resonances become important. In Fig. 3.9(a), a null appears at  $kR \approx 7.2$  and a peak appears at  $kR \approx 7.6$  for  $B_1$ ; in (b), a null appears at  $kR \approx 5.9$  for  $B_2$ ; in (c), a null appears at  $kR \approx 8.6$  for  $B_3$ . As expected from scattering resonances, these peaks and nulls are at nearly the same values of  $kR$  as the peaks and nulls in  $A_n$  shown in the previous section.

Similar phenomena can be observed in the coefficients for an air bubble and a spherical void, as shown in Fig. 3.10. Unlike with  $A_n$ , no coefficients appear different for small  $kR$ , which is partly due to the lack of  $B_0$ , the monopole scattering coefficient for the shear wave. For larger  $kR$ , scattering resonances appear, but the coefficients are again equivalent away from these resonances.

Next, we consider a more continuous range of shear modulus in the surrounding medium. Results for air bubbles and hard elastic spheres of various sizes are presented in Fig. 3.11. For air bubbles in Fig. 3.11(a), (c), and (e), the coefficients steadily decrease as  $\mu \rightarrow 0$  except for some deviations that occur due to shifting resonances. This behavior is expected because an inviscid fluid medium does not support a scattered shear wave. However, this does not occur for a steel sphere, as seen in Fig. 3.11(b), (d), and (f). Instead, the coefficients tend toward a finite value as  $\mu \rightarrow 0$ . This paradox may be investigated by

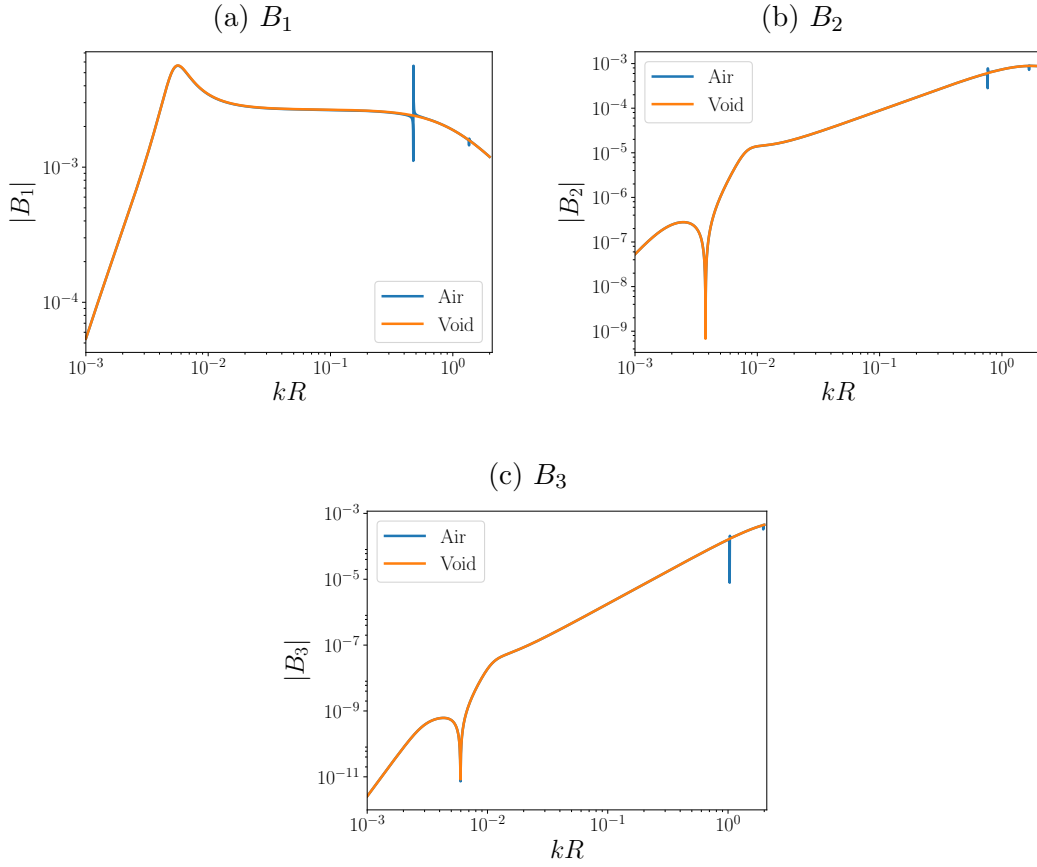


Figure 3.10: Scattering coefficients for the shear wave in a soft tissue-like medium ( $\mu = 4$  kPa) surrounding an air bubble and a spherical void.

considering the shear displacement components from Eqs. (2.24) and (2.28):

$$\tilde{u}_r^t = -\frac{1}{r} \left( \frac{\partial^2 \Pi}{\partial \theta^2} + \frac{\cos \theta}{\sin \theta} \frac{\partial \Pi}{\partial \theta} + \frac{1}{\sin^2 \theta} \frac{\partial^2 \Pi}{\partial \phi^2} \right), \quad (3.94)$$

$$\tilde{u}_\theta^t = \frac{1}{r} \left( \frac{\partial \Pi}{\partial \theta} + r \frac{\partial^2 \Pi}{\partial r \partial \theta} \right), \quad (3.95)$$

$$\tilde{u}_\phi^t = \frac{1}{r \sin \theta} \left( \frac{\partial \Pi}{\partial \phi} + r \frac{\partial^2 \Pi}{\partial r \partial \phi} \right). \quad (3.96)$$

The potential  $\Pi$  is represented by an infinite series, each term of which has

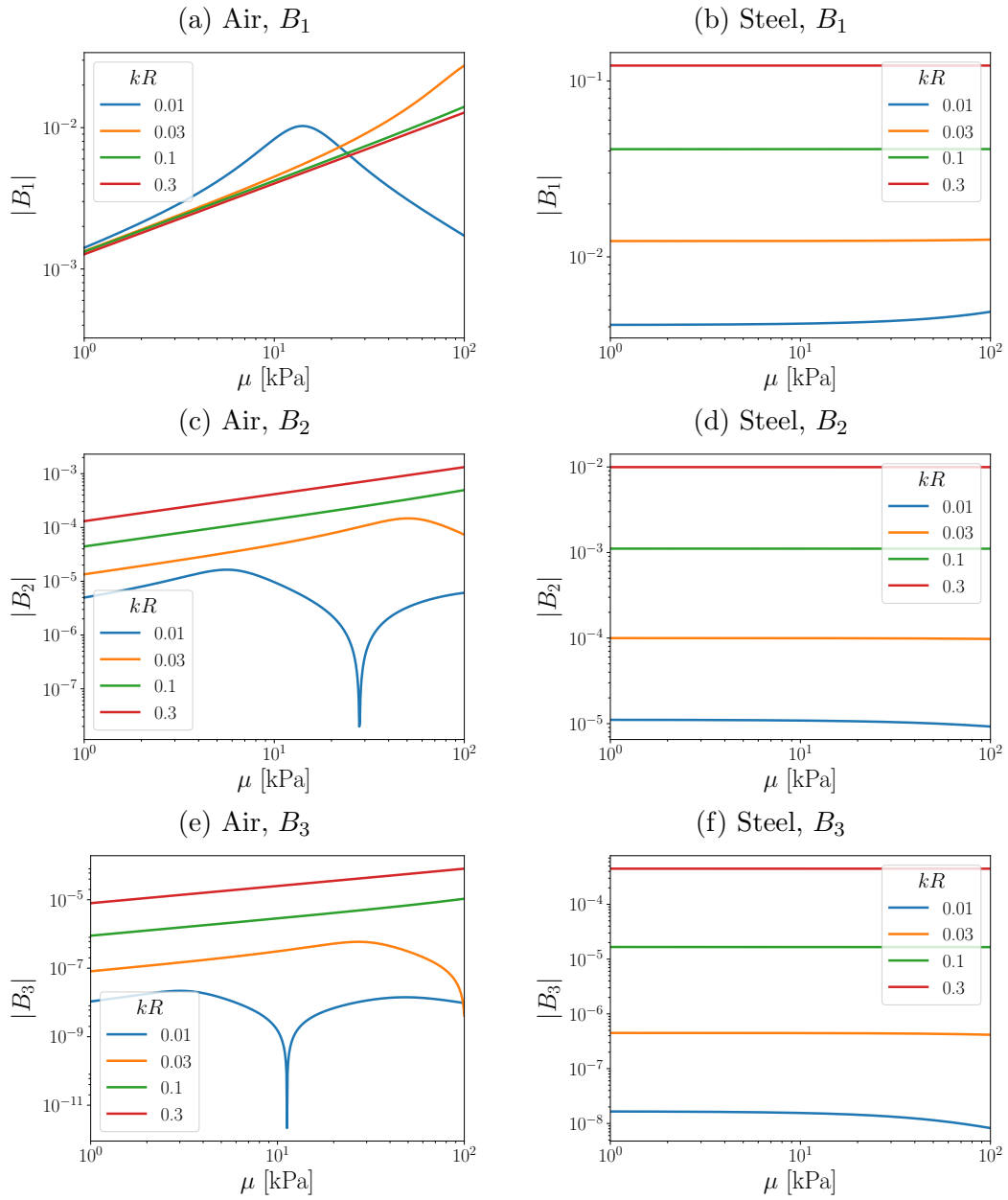


Figure 3.11: Scattering coefficients for the shear wave versus shear modulus for an air bubble (left column) and a steel sphere (right column).

the following form:

$$\Pi_n^m = B_n a_n^m h_n(\kappa r) P_n^m(\cos \theta) e^{im\phi} . \quad (3.97)$$

Taking care to calculate the  $\theta$  derivatives in a way that facilitates numerical computation [119], we can write Eqs. (3.94)–(3.96) for given  $n, m$  as

$$u_{n,r}^m = \frac{n(n+1)}{r} B_n a_n^m h_n(\kappa r) P_n^m(\cos \theta) e^{im\phi} , \quad (3.98)$$

$$u_{n,\theta}^m = -\frac{1}{2r} B_n a_n^m [(n+1)h_n(\kappa r) - \kappa r h_{n+1}(\kappa r)] \times [(n+m)(n-m+1)P_n^{m-1}(\cos \theta) - P_n^{m+1}(\cos \theta)] e^{im\phi} , \quad (3.99)$$

$$u_{n,\phi}^m = \frac{im}{r \sin \theta} B_n a_n^m [(n+1)h_n(\kappa r) - \kappa r h_{n+1}(\kappa r)] P_n^m(\cos \theta) e^{im\phi} . \quad (3.100)$$

Since  $\mu \rightarrow 0$  implies that  $\kappa \rightarrow \infty$ , it is necessary to know  $h_n(z)$  as  $z \rightarrow \infty$ , which may be determined from the asymptotic relation [120]

$$h_n(z) \sim \frac{i^{-n-1} e^{iz}}{z} \quad (3.101)$$

and which oscillates about zero and decays in magnitude. When Eq. (3.101) is substituted into Eq. (3.98), we can see that  $u_{n,r}^m \rightarrow 0$  for  $\mu \rightarrow 0$  as expected. However, when Eq. (3.101) is substituted into Eqs. (3.99) and (3.100), there is a term which oscillates about zero but *does not* approach zero in magnitude:

$$\kappa r h_{n+1}(\kappa r) \sim i^{-n-2} e^{i\kappa r} . \quad (3.102)$$

A contradiction seems to appear here: how can a shear wave persist in a medium with vanishing shear modulus? The reason for this peculiarity lies in the comparison with the results for an air bubble, where  $B_n \rightarrow 0$  as  $\mu \rightarrow 0$  in

the medium as expected. In the case of a fluid scatterer, continuity of tangential displacement is not enforced regardless of the properties of the medium, whereas in the case of an elastic scatterer, continuity of tangential displacement is still enforced even for infinitesimal shear modulus in the medium. It is the discrete nature of this no-slip condition that is responsible for this apparent discrepancy, and because of this, we cannot generally use the limit  $\mu \rightarrow 0$  as a check of the shear contribution to the radiation force. That is, the radiation force  $G_n$  due to shear wave fields will *not* necessarily approach zero as the shear modulus in the medium approaches zero.

### 3.5 Summary

The coefficients for the incident and scattered wave fields discussed in this chapter are important for producing the radiation force results in Chapters 4 and 5, especially for providing physical insight into certain radiation force effects. The incident field coefficients presented in Secs. 3.1 and 3.2 allow for the computation of the radiation force due to arbitrary incident fields, and while not commonly used in acoustics, the framework for rotating the coordinate system of a spherical harmonic expansion discussed in Sec. 3.1.4 is advantageous in that it avoids the need to use a separate force equation for each component of the force, instead requiring that the incident field coefficients simply be transformed. The scattered field coefficients presented in Secs. 3.3 and 3.4 aid in understanding several important radiation force effects related to increases in the magnitudes of the coefficients and shifting

resonances, and they help to illustrate that even a small change in the shear modulus in the surrounding medium can have substantial effects on the force.

## Chapter 4

# Radiation Force Due to Compressional Wave Fields

Presented in this chapter is a study of acoustic radiation force on a spherical scatterer due to compressional wave fields only. That is, the contribution  $G_n$  in Eq. (2.100) due to the scattered shear wave is ignored; only  $F_n$  in Eq. (2.59) due to the scattered compressional wave is considered. The radiation force is compared for various media, including soft tissue-like media, viscous liquid, and ideal liquid. Viscosity is introduced to model a viscoelastic host medium through a complex shear modulus  $\tilde{\mu}$  written as

$$\tilde{\mu} = \mu - i\omega\eta, \quad (4.1)$$

where  $\mu$  is the shear modulus and  $\eta$  is the shear viscosity. Bulk viscosity  $\zeta$  is ignored in this analysis due to practical difficulties in measuring it accurately [121, 122], so the bulk modulus is purely real ( $\tilde{K} = K$ ) and the complex

---

B. C. Treweek, Yu. A. Ilinskii, E. A. Zabolotskaya, and M. F. Hamilton, “Acoustic radiation force due to arbitrary incident fields on spherical particles in soft tissue,” *AIP Conf. Proc.*, vol. 1685, no. 1, p. 040008, 2015. The author of the present work implemented transformations of incident field coefficients  $a_n^m$  for a scatterer located off the beam axis and investigated direction reversals of the transverse force  $F_x$ .

	$\rho_0$ (kg/m <sup>3</sup> )	$c_l$ (m/s)	$c_t$ (m/s)	$\eta$ (Pa·s)
Water	1000	1500	—	—
Soft tissue	1000	1500	0–10	0–5
Stainless steel sphere	7900	5240	2978	—
Air bubble	1.21	343	—	—
Polystyrene sphere	1000	2400	1089	—
Aluminum sphere	2700	6374	3111	—

Table 4.1: Medium and spherical scatterer properties for radiation force comparisons.

compressional wave speed  $\tilde{c}_l$  is calculated via

$$\rho\tilde{c}_l^2 = \tilde{K} + \frac{4}{3}\tilde{\mu} = K + \frac{4}{3}\mu - i\frac{4}{3}\omega\eta. \quad (4.2)$$

The liquid used for comparison is water because soft tissue has similar acoustic properties. The shear wave speed  $c_t$  in the medium spans the range of values encountered in soft tissue [21], and shear viscosity spans a comparable range [89, 90, 123–125]. Four different spheres are examined: a stainless steel sphere (a representative hard scatterer), an aluminum sphere (another representative hard scatterer with different density and elastic moduli), an air bubble (a representative soft scatterer), and a polystyrene sphere (a solid scatterer with acoustic impedance much closer to that of the medium than the two metals considered). Properties of these media are listed in Table 4.1.

In all cases, the incident field is chosen to be time-harmonic with frequency  $f = 1$  MHz, and it is either a plane wave or a simple focused beam with confinement angle  $\theta_0 = 30^\circ$  as described in Sec. 3.2.1. A plane traveling wave is defined via Eq. (2.82) as  $\psi(z) = \psi_0 e^{ikz}$ , which yields the incident coefficients

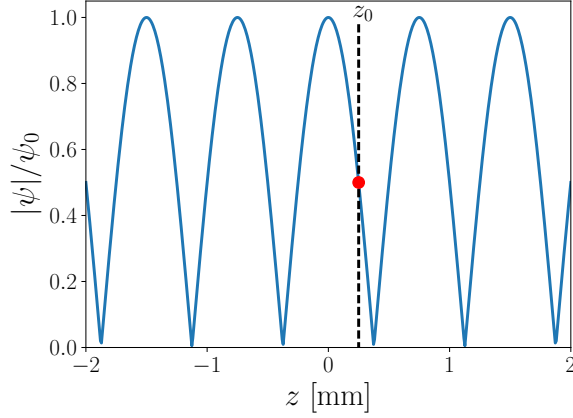


Figure 4.1: Axial profile of a plane standing wave at frequency  $f = 1$  MHz in a medium with compressional wave speed  $c_l = 1500$  m/s. The filled red circle marks an example sphere positioned at  $z = z_0$ .

described by Eq. (2.83):

$$a_n = \psi_0 i^n (2n + 1). \quad (4.3)$$

A plane standing wave is defined via two counter-propagating plane waves to yield  $\psi(z) = \frac{1}{2}\psi_0(e^{ikz} + e^{-ikz}) = \psi_0 \cos(kz)$ , and for a sphere moved to a position  $z = z_0$  as described in Sec. 3.1.3, this results in incident field coefficients described by Eq. (2.86):

$$a_n = \psi_0 (2n + 1) \cos(kz_0 + n\pi/2). \quad (4.4)$$

An axial profile for the plane standing wave amplitude is shown in Fig. 4.1, and we can refer to Fig. 3.2(d) and (e) for axial and focal profiles, respectively, of a simple focused beam.

While results are presented for nonzero shear viscosity in the surrounding medium, they are not extensively compared with results for viscous fluid

media obtained by others [11–16] because when the surrounding fluid is viscous, effects due to acoustic streaming must also be considered. The result is that additional terms are needed beyond those described in Eq. (2.36) and elaborated upon in the rest of Chapter 2. Also, the radiation force  $G_n$  associated with the scattered shear wave is necessary to provide a complete description even without streaming effects. Therefore, except for brief comments on qualitative similarities, results for nonzero shear viscosity are instead included as a comparison with results for nonzero shear modulus to demonstrate that in some cases, it may be difficult to ascertain whether an effect is due to the viscosity or the elasticity in the medium.

## 4.1 Numerical Convergence

First, it is important to briefly address the computational demands of calculating  $F_z$  using Eq. (2.67) or (2.68). Since the radiation force is written as an infinite sum, we must determine how many terms  $N$  are required for a solution to have converged. In practice, as few terms as possible should be used so that results can be computed quickly, but for a field described by an infinite sum of spherical wave functions in free space, more terms are needed to resolve the field as the distance from the origin increases. We may therefore expect the required value of  $N$  to increase as the scatterer size increases.

As shown in Figs. 4.2 and 4.3, this expectation is accurate. In these figures, plots show the ratio of  $F^N$  (the force computed for a given value of  $N$ ) to  $F^\infty$  (the force computed for a very large value of  $N$ ) versus  $kR$ , with

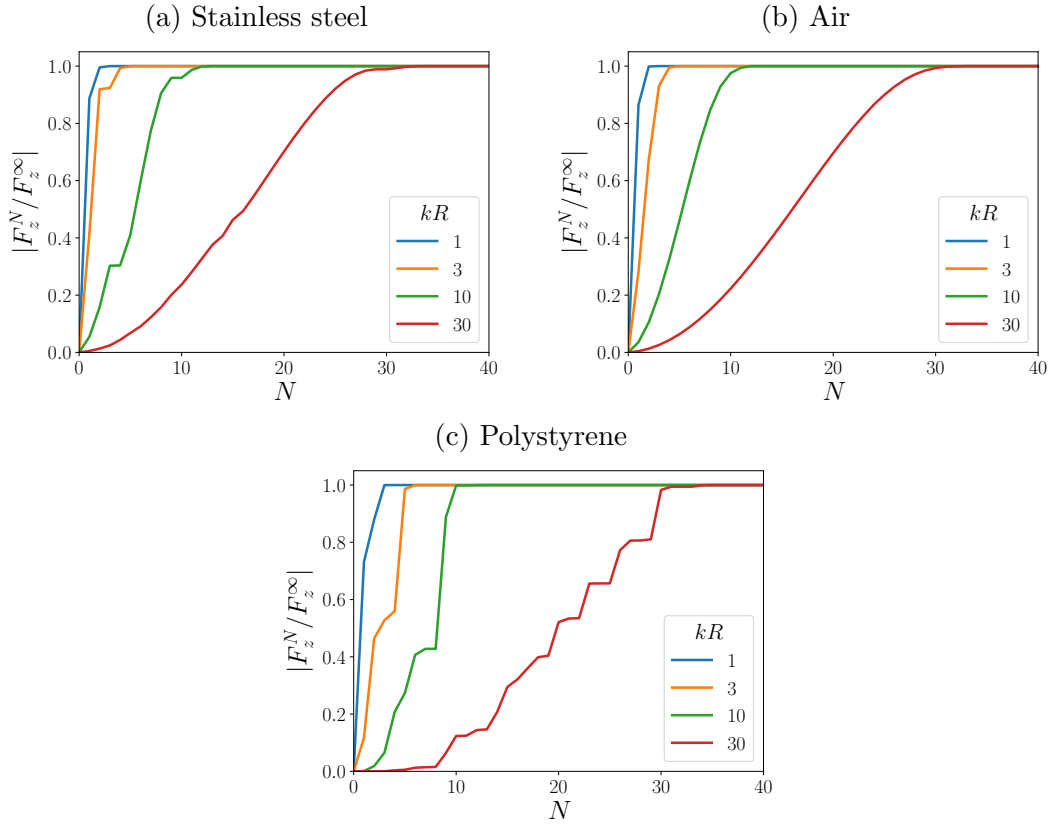


Figure 4.2: Number of terms  $N$  required for convergence of radiation force  $F_z$  given by Eq. (2.68) due to a traveling plane wave incident on spheres of various sizes  $kR$  in water.

convergence occurring when this ratio reaches unity. For a traveling plane wave, as shown in Fig. 4.2, sphere sizes up to  $kR = 3, 10,$  and  $30$  require approximately 5, 15, and 35 terms, respectively, with no strong dependence on the properties of the scatterer. Also, as shown in Fig. 4.3, the required value of  $N$  for a given scatterer size when the scatterer is moved off the axis of a simple focused beam is somewhat decreased for  $F_z$  and approximately the same for  $F_x$ . In experiments on radiation force due to ultrasound, scatterers are often

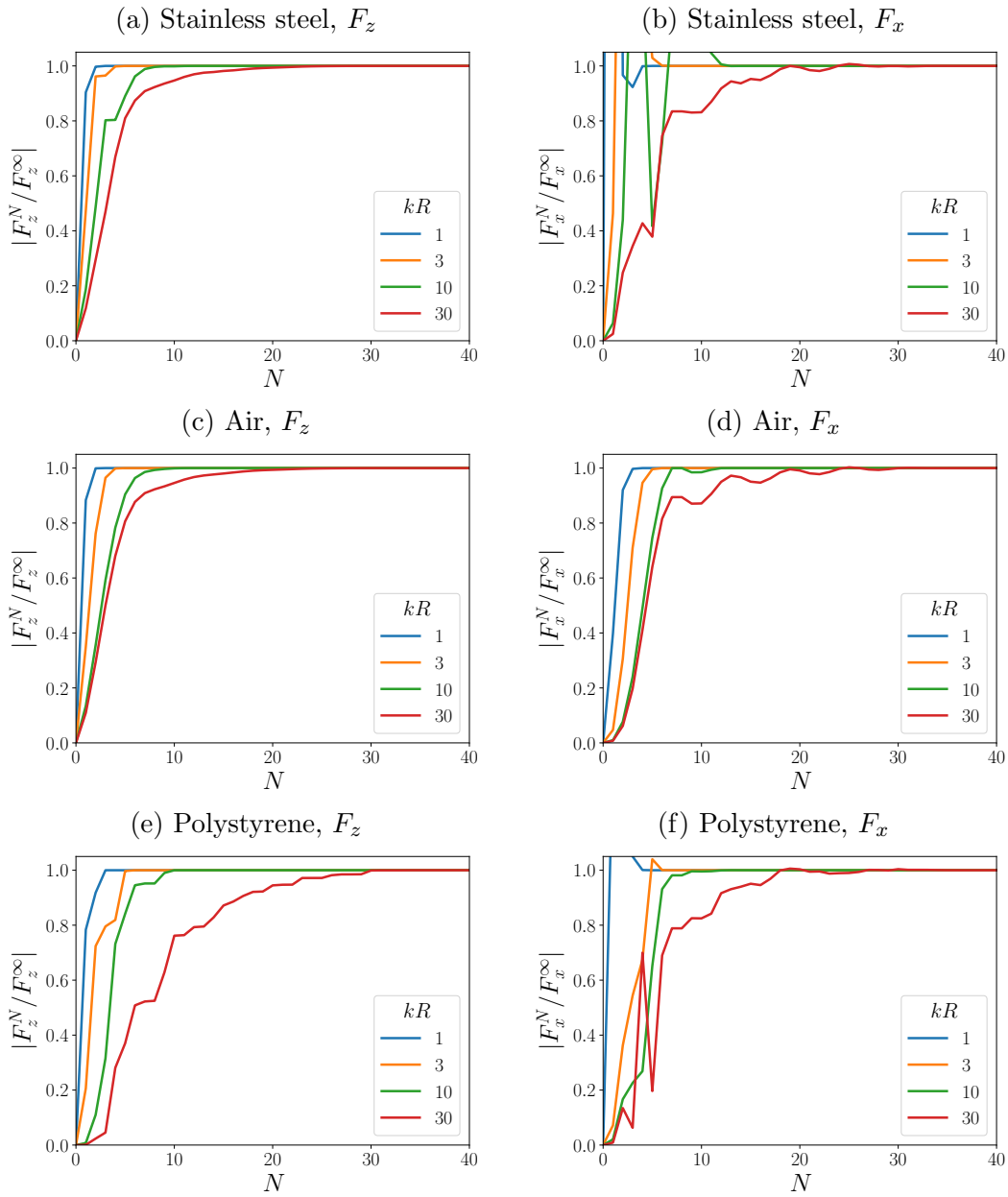


Figure 4.3: Terms required for convergence of axial ( $F_z$ ) and transverse ( $F_x$ ) radiation force due to a simple focused beam incident on spheres of various sizes  $kR$  in water. Both  $F_z$  and  $F_x$  are calculated using Eq. (2.67) with respective incident field coefficients. The sphere is located at  $(z_0, x_0) = (0, 0.5 \text{ mm})$ .

less than two wavelengths in diameter [89, 90], so it should be sufficient to use 10–15 terms in most practical cases.

## 4.2 Scatterer Position

We next examine the effect of varying the scatterer position within a sound field. In the cases considered, the incident field is either a plane standing wave or a beam. For a plane traveling wave, the time-averaged intensity has no spatial variation, and therefore a change in the scatterer position has no effect on the force. In order to focus on the effect of scatterer position, we choose only a few values for scatterer size and shear modulus or viscosity in the surrounding medium (i.e., water with either shear modulus or shear viscosity added).

### 4.2.1 Scatterer Located On Axis

Considered first is the variation of the position  $z = z_0$  of the scatterer along the axis of an incident plane standing wave. Scatterers in water are pushed toward either pressure nodes or pressure antinodes depending on the excitation frequency and their stiffness relative to the surrounding medium. Mathematically, this can be seen by considering the force on a small body of volume  $V$  due to a pressure gradient  $\nabla P$ , which is written as [126]

$$\mathbf{F} = -\langle V \nabla P \rangle . \tag{4.5}$$

For a plane standing wave described by  $p = p_0 \cos(kz) \sin(\omega t)$ , the above relation yields

$$F_z = \frac{2\pi k p_0^2 R^3}{3\rho_0 c_l^2} \sin(2kz) \quad (4.6)$$

for a rigid sphere (which underestimates results from King [1] by approximately 20%) and

$$F_z = \frac{\pi V_0 p_0^2}{2\gamma \lambda P_0} \frac{\sin(2kz)}{1 - \omega^2/\omega_0^2} \quad (4.7)$$

for a gas bubble, where  $V_0$  is the equilibrium bubble radius,  $\gamma$  is the ratio of specific heats in an ideal gas,  $\lambda$  is the wavelength,  $P_0$  is the equilibrium pressure in the bubble, and  $\omega_0$  is the resonance frequency of the bubble.

Plots of the radiation force on a stainless steel sphere subject to a plane standing wave in water are shown in Fig. 4.4. The stainless steel sphere is pushed toward a pressure node; for example, when the sphere is moved just to the right of  $z = 0.375$  mm, which is a pressure node (see Fig. 4.1), the force is negative, indicating that the sphere is pushed toward the node. This physical effect remains the same even with a nonzero shear modulus or shear viscosity. However, as seen in Fig. 4.4(a)–(d), there are noticeable differences in magnitude for small scatterers. As discussed in Sec. 3.4, this is primarily because of the dipole scattering coefficient  $A_1$ . For larger spheres ( $kR \gtrsim 0.1$ ), as shown in Fig. 4.4(e) and (f), the axial forces are nearly indistinguishable.

For a gas bubble, the effect is different. Since gas is much softer than a surrounding tissue-like (i.e., liquid-like) medium, the bubble is pushed toward pressure antinodes for frequencies below the bubble resonance and toward pressure nodes for frequencies above the bubble resonance [126], which

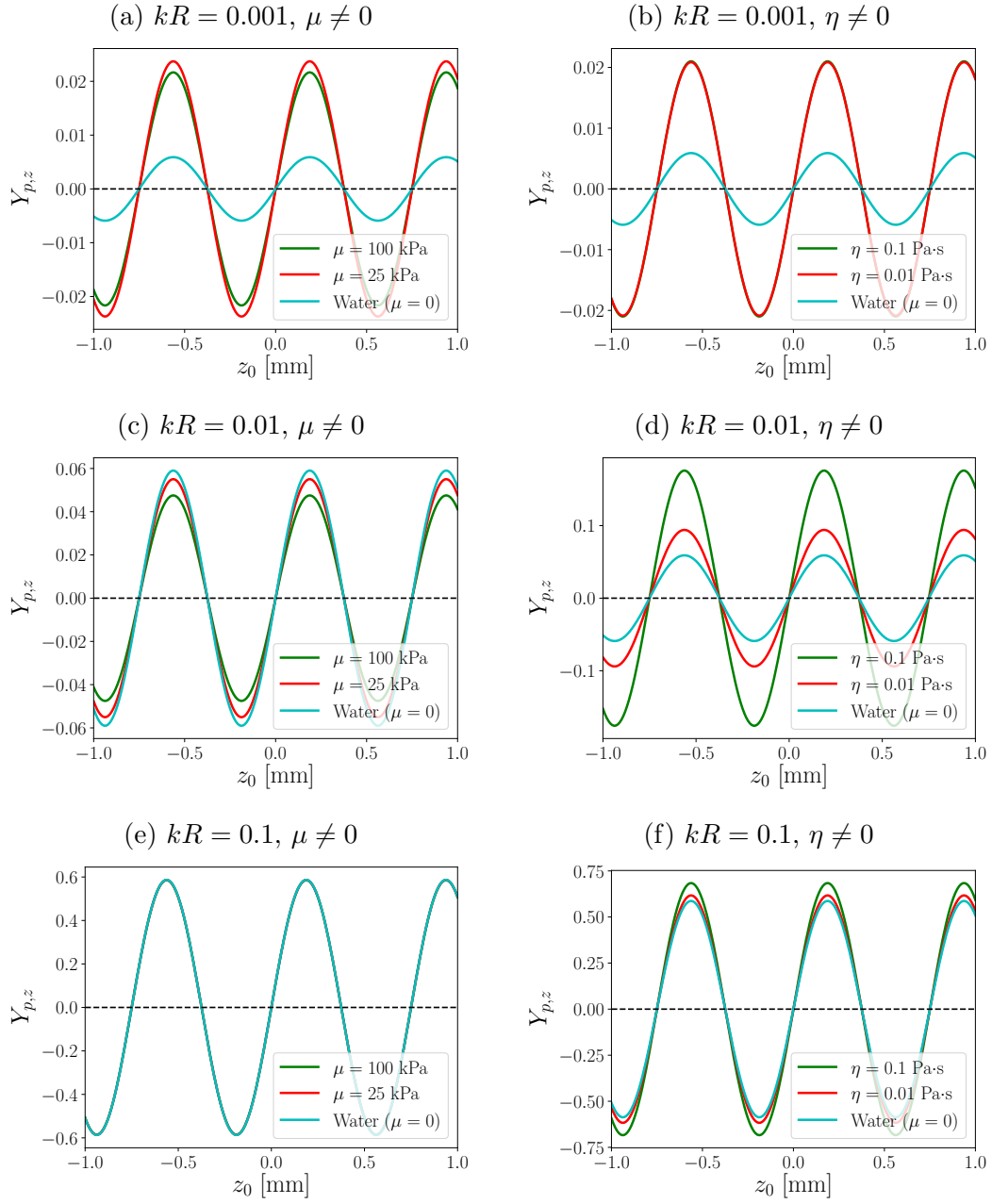


Figure 4.4: Acoustic radiation force function  $Y_{p,z}$  versus axial position  $z_0$  of a stainless steel sphere embedded in various media with a plane standing wave incident on the sphere. A dashed line is included at  $Y_{p,z} = 0$  for visual clarity.

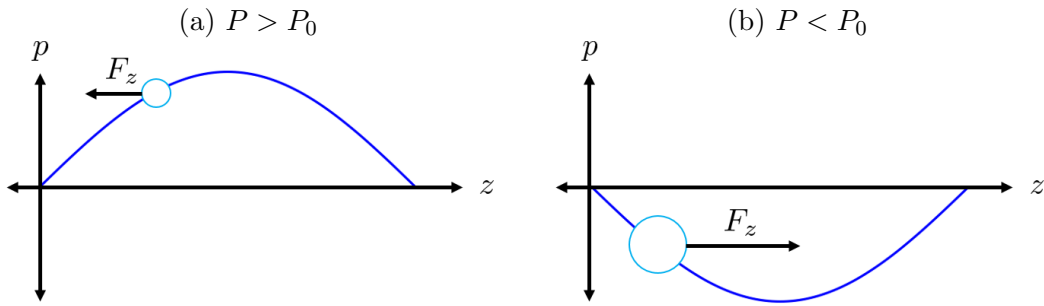


Figure 4.5: Force on a bubble in a standing wave at two different moments in the cycle.

corresponds to  $kR = 0.0138$  for an air bubble in water. This effect can be seen mathematically in Eq. (4.7) and physically in Fig. 4.5. For frequencies less than the bubble resonance, fluctuations in the pressure and the radius of the bubble are out of phase—the bubble is smaller when it is pushed away from an antinode, which results in a lower value of the force in Eq. (4.5), and the bubble is larger when it is pushed toward the antinode, which results in a larger value of the force and hence an average force toward the antinode per cycle. The effect reverses for frequencies above the bubble resonance. As discussed in Sec. 3.4, the important consideration in determining differences between various media is therefore the shift in the resonance frequency of the bubble with increasing shear stiffness in the surrounding medium.

Figure 4.6 shows results for radiation force on an air bubble in media with nonzero shear modulus or viscosity. In Fig. 4.6(a), the bubble is pushed toward pressure antinodes for all three choices of surrounding medium. That is, when the bubble is moved just to the right of a pressure antinode (e.g.,  $z = 0$ ), the force is to the left (negative), and vice versa for a bubble moved

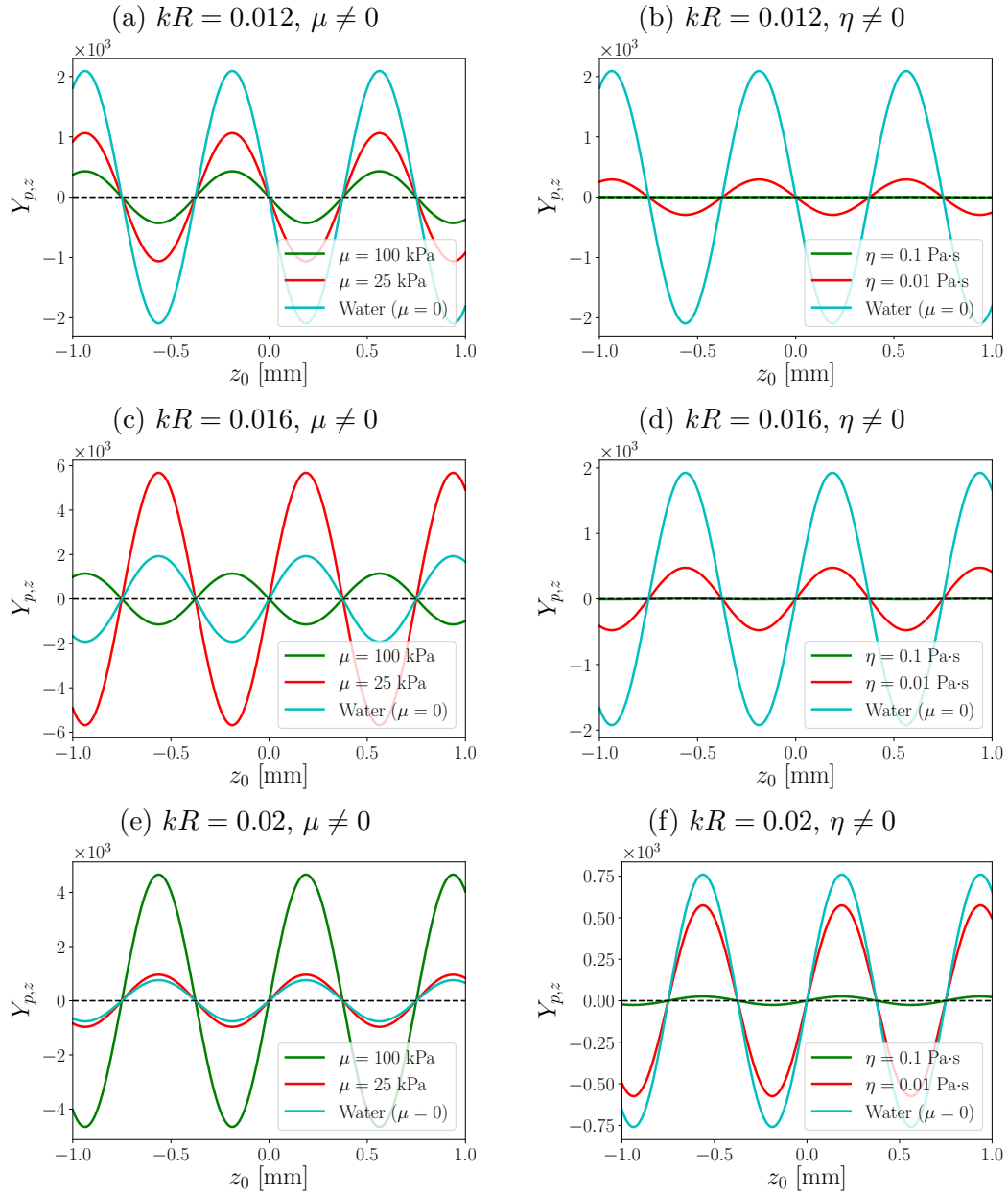


Figure 4.6: Acoustic radiation force function  $Y_{p,z}$  versus axial position  $z_0$  of an air bubble embedded in various media with a plane standing wave incident on the bubble. A dashed line is included at  $Y_{p,z} = 0$  for visual clarity.

just to the left. In Fig. 4.6(c), the direction of the force has reversed in water and the softer tissue-like medium; in these media, this larger bubble has a resonance below the excitation frequency, whereas in the stiffest medium, the bubble resonance is still above the excitation frequency. In Fig. 4.6(e), the direction has reversed in all three media. In Fig. 4.6(b), (d), and (f), which show results for nonzero shear viscosity, the direction of the force is the same in all three media. There is still a reversal in the direction above the bubble resonance—i.e., Fig. 4.6(b) and (d) are out of phase—but shear viscosity does not have a strong effect on where this resonance occurs. The only difference in radiation force among the various media is the diminished magnitude of the force, which is expected when loss is involved, especially in the neighborhood of a resonance.

Next, we consider a simple focused beam. Results for an aluminum sphere that is small compared to a compressional wavelength in the medium are shown in Fig. 4.7. (Note that in this figure as well as several others, a logarithmic  $y$ -axis is used in order to better show results on a single plot.  $Y_p > 0$  is indicated with solid lines,  $Y_p < 0$  with dashed lines.) In Fig. 4.7(a) and (b) showing results very small spheres in elastic media, it is observed that the direction of the force is not necessarily the same as the propagation direction. Instead, the direction depends on the axial position of the sphere within the sound beam—from Fig. 3.2(e), recall that  $z_0 = 0$  indicates that the sphere is precisely at the beam focus—and the point at which the direction reverses is dependent on the shear modulus in the surrounding medium. In Fig. 4.7(c)–(f)

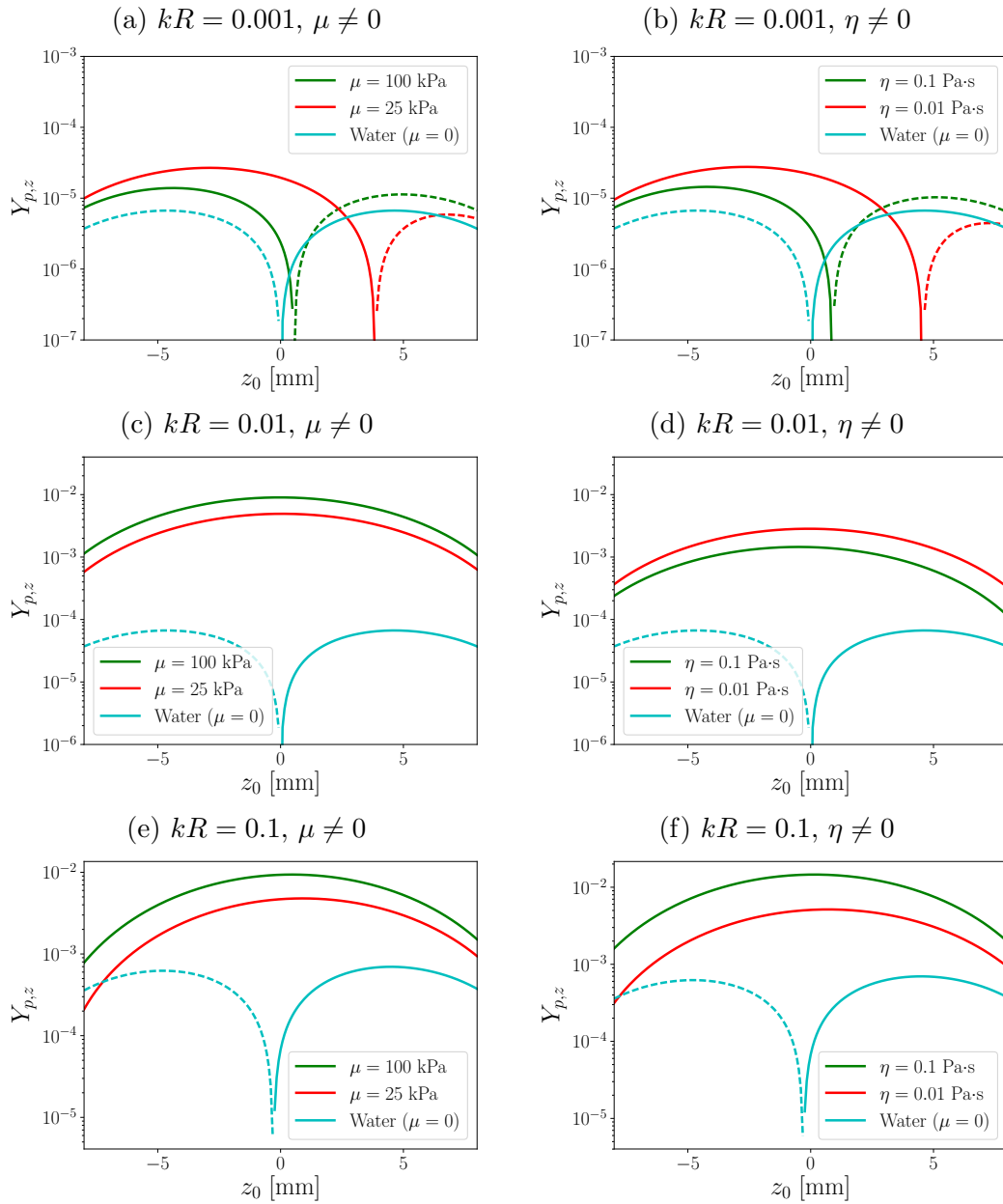


Figure 4.7: Acoustic radiation force function  $Y_{p,z}$  versus axial position  $z_0$  of an aluminum sphere embedded in various media with a simple focused beam incident on the sphere. Solid lines indicate  $Y_{p,z} > 0$  and dashed lines indicate  $Y_{p,z} < 0$ .

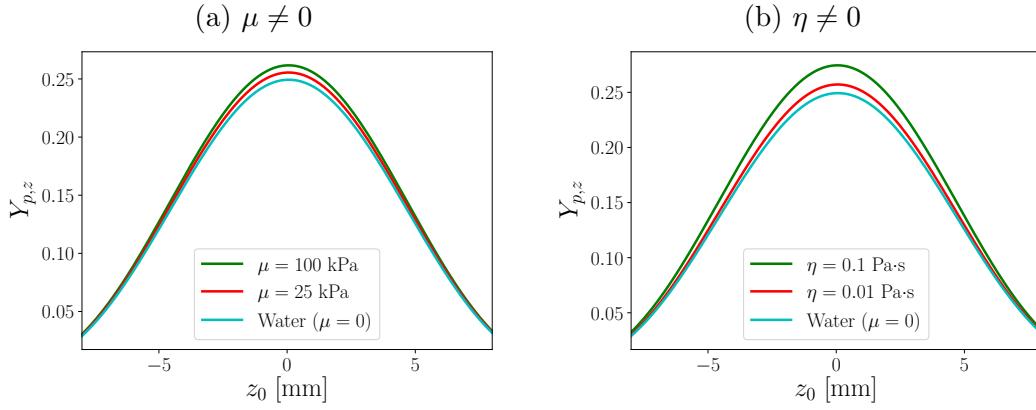


Figure 4.8: Acoustic radiation force function  $Y_{p,z}$  versus axial position  $z_0$  of an aluminum sphere ( $kR = 1$ ) embedded in various media with a simple focused beam incident on the sphere.

showing results for larger spheres that are still small relative to a compressional wavelength, the force direction coincides with the propagation direction when the sphere is embedded in a medium with nonzero shear modulus, but the force still depends on axial position for a sphere in water. The magnitude of the force is substantially increased when the medium has nonzero shear modulus—or, in qualitative agreement with existing literature, nonzero shear viscosity [12, 15, 16]—but it is considerably lower than the magnitude of the force due to plane standing wave incidence. For even larger spheres approaching the order of a compressional wavelength, as shown in Fig. 4.8, the sphere is pushed in the propagation direction regardless of the medium, and the magnitude of the radiation force is similar in all media.

For an air bubble, as shown in Fig. 4.9, the effect again depends on the bubble resonance. As expected, the most important effect is the significant

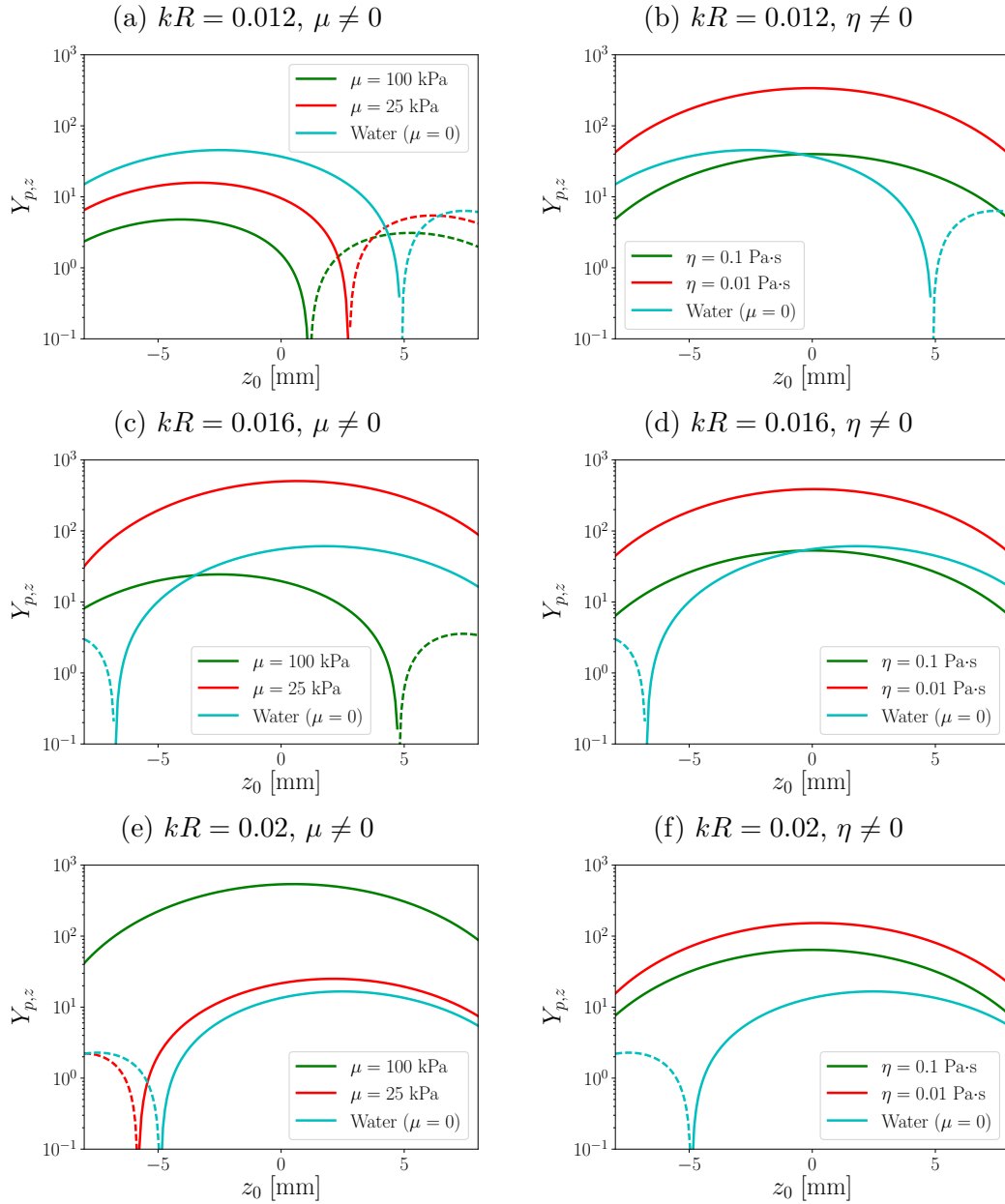


Figure 4.9: Acoustic radiation force function  $Y_{p,z}$  versus axial position  $z_0$  of an air bubble embedded in various media with a simple focused beam incident on the sphere. Solid lines indicate  $Y_{p,z} > 0$  and dashed lines indicate  $Y_{p,z} < 0$ .

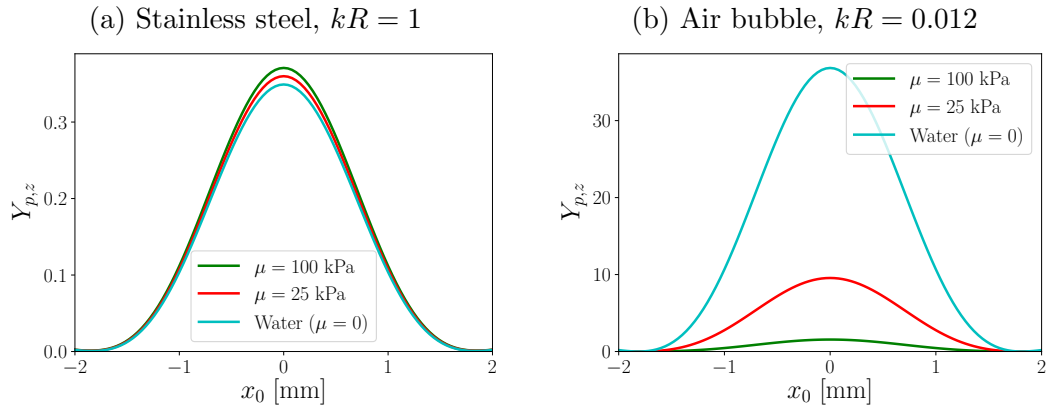


Figure 4.10: Acoustic radiation force function  $Y_{p,z}$  versus transverse position  $x_0$  of a stainless steel sphere and a gas bubble embedded in various media with a simple focused beam incident on the sphere. Compare with Fig. 3.2(d), which shows that the first null is approximately 2 mm from the axis in the focal plane.

increase in the magnitude of the force for frequencies near resonance. For frequencies below resonance, as shown in Fig. 4.9(a) and (b), the direction of the force reverses at a point in front of the beam focus ( $z > 0$ ). For frequencies above resonance, as shown in Fig. 4.9(c)–(f), the direction reverses at a point behind the beam focus ( $z < 0$ ). However, as the magnitude of the force in the neighborhood of the direction reversal is low, it may be difficult to observe a precise location for the direction reversal in practice. For nonzero shear viscosity, the resonance is not prominent and the force is positive regardless of axial position of the scatterer.

### 4.2.2 Scatterer Located Off Axis

For examination of the radiation force on a scatterer located at position  $x_0$  off the propagation axis, a field with transverse variation as shown in Fig. 3.2 is necessary. Therefore, plane waves are no longer used in this section, only simple focused beams. Also, only the transverse direction of the force is examined in depth here because the force in the axial direction generally behaves as expected. As shown in Fig. 4.10, force in the axial direction follows results in the previous section, but its magnitude is decreased as the sphere is moved off the beam axis.

Results for a steel sphere are presented in Fig. 4.11. Depending on sphere size and shear modulus in the medium, the sphere may be pushed either toward the beam axis or away from it. For the smaller spheres in Fig. 4.11(a) and (c), the direction of the force may differ. Smaller spheres in tissue-like media are pushed toward the beam axis, whereas smaller spheres in water are pushed (albeit much more weakly) toward a point off the beam axis but still within the main lobe of the beam. When sphere size increases to  $kR = 0.1$  in Fig. 4.11(e), the force in the transverse direction is nearly equivalent in both water and tissue-like media. For nonzero shear viscosity in Fig. 4.11(b), (d), and (f), the effect is more consistent across sphere size: viscosity causes the sphere to be pushed toward the beam axis.

For a different metal sphere with different elastic properties, the effects may differ. As seen in Fig. 4.12 for aluminum, for instance, the sphere is consistently pushed away from the beam axis in water, but it may be pushed

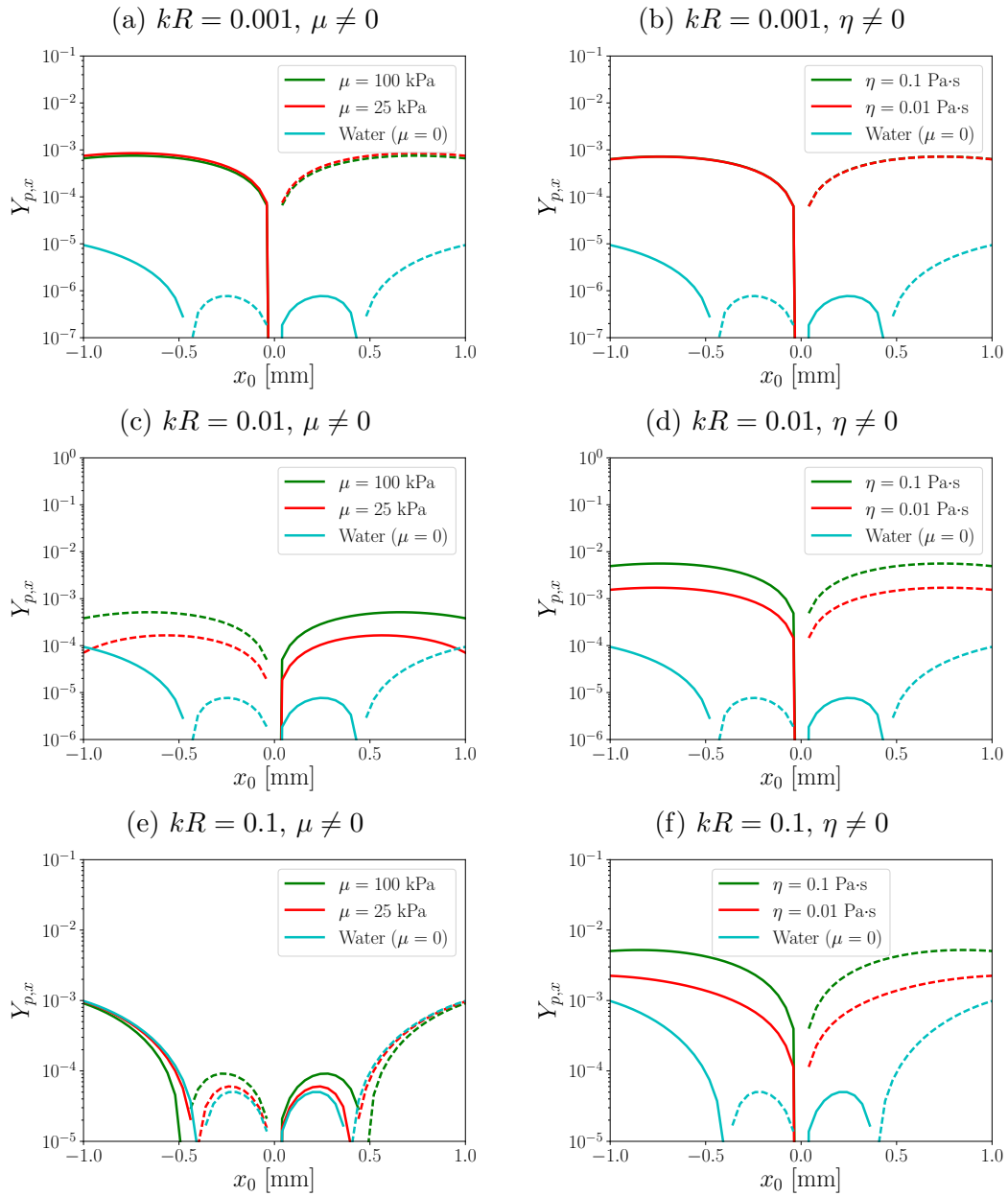


Figure 4.11: Acoustic radiation force function  $Y_{p,x}$  versus transverse position  $x_0$  of a stainless steel sphere embedded in various media with a simple focused beam incident on the sphere. Solid lines indicate  $Y_{p,x} > 0$  and dashed lines indicate  $Y_{p,x} < 0$ .

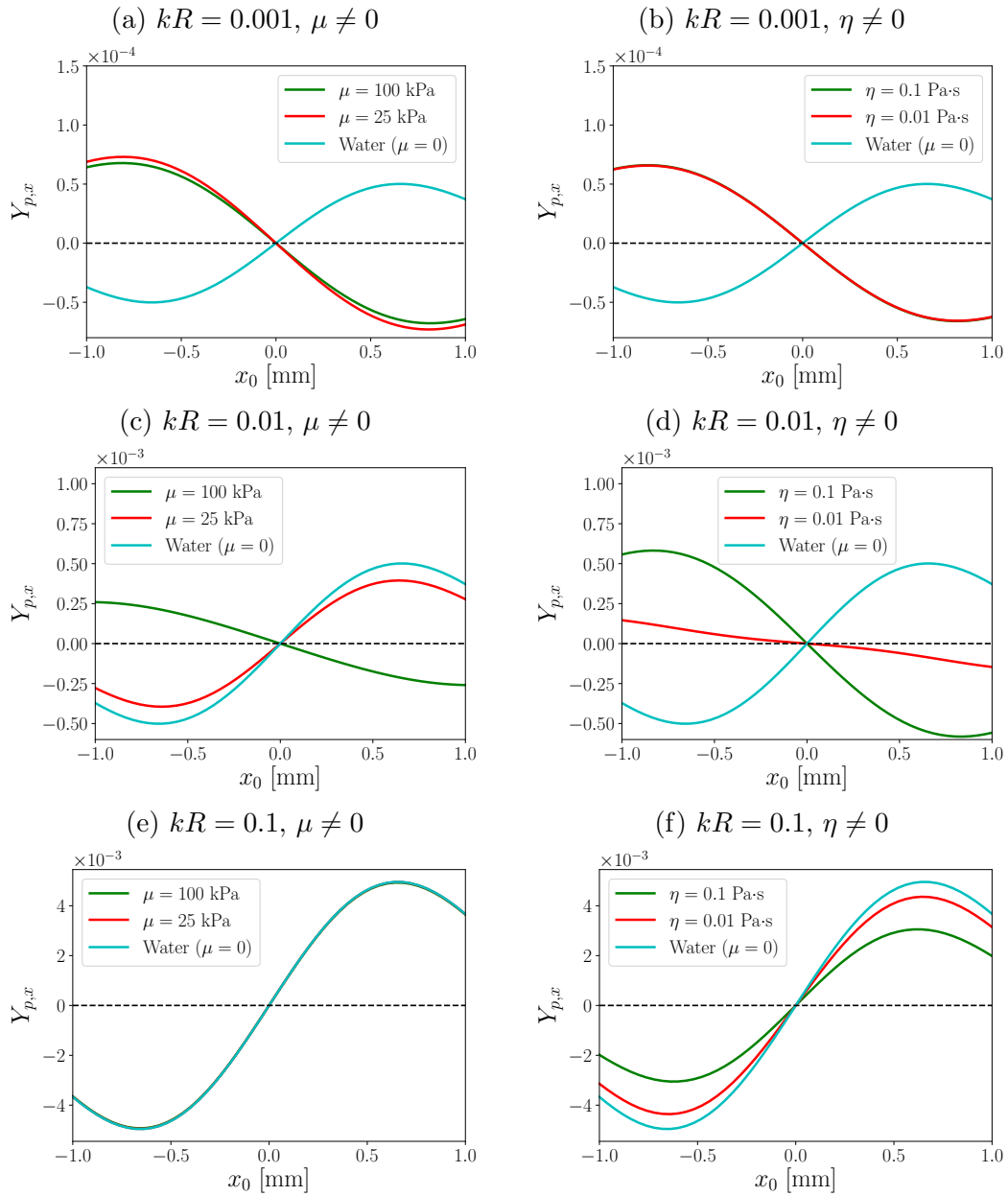


Figure 4.12: Acoustic radiation force function  $Y_{p,x}$  versus transverse position  $x_0$  of an aluminum sphere embedded in various media with a simple focused beam incident on the sphere. A dashed line is included at  $Y_{p,x} = 0$  for visual clarity.

in either direction depending on its size and the shear modulus or viscosity in the surrounding medium. Furthermore, unlike for the stainless steel sphere, the effect of shear viscosity in the medium is less distinct from the effect of shear modulus. Such observations will be further developed in following sections.

Results for an air bubble are presented in Fig. 4.13. Again, the bubble resonance is clearly responsible for the observed effects. As in the standing wave (recall Fig. 4.6), the bubble is pushed toward the beam axis (i.e., the pressure antinodes) for frequencies below the shifted resonance, and it is pushed away from the beam axis for frequencies above the shifted resonance. In Fig. 4.13(a), the three solid curves for  $x_0 < 0$  indicate a positive force in the  $x$ -direction, and the three dashed curves for  $x_0 > 0$  indicate a negative force in the  $x$ -direction. In Fig. 4.13(c), two of the pairs of solid and dashed curves have switched, indicating that the bubble is pushed away from the beam axis for the two softer media and toward the beam axis in the stiffest medium. Finally, in Fig. 4.13(e), the bubble is pushed away from the beam axis in all three media. When shear viscosity is included in Fig. 4.13(b), (d), and (f), there is a clear effect on the magnitude. A direction reversal occurs as well, but it always appears to occur at the bubble resonance in water regardless of the viscosity.

### 4.3 Scatterer Size

We now consider a more continuous range of scatterer size. In this section, functional dependence on  $kR$  is investigated by fixing the frequency of the incident field and varying the radius of the scatterer. (In an experiment, it

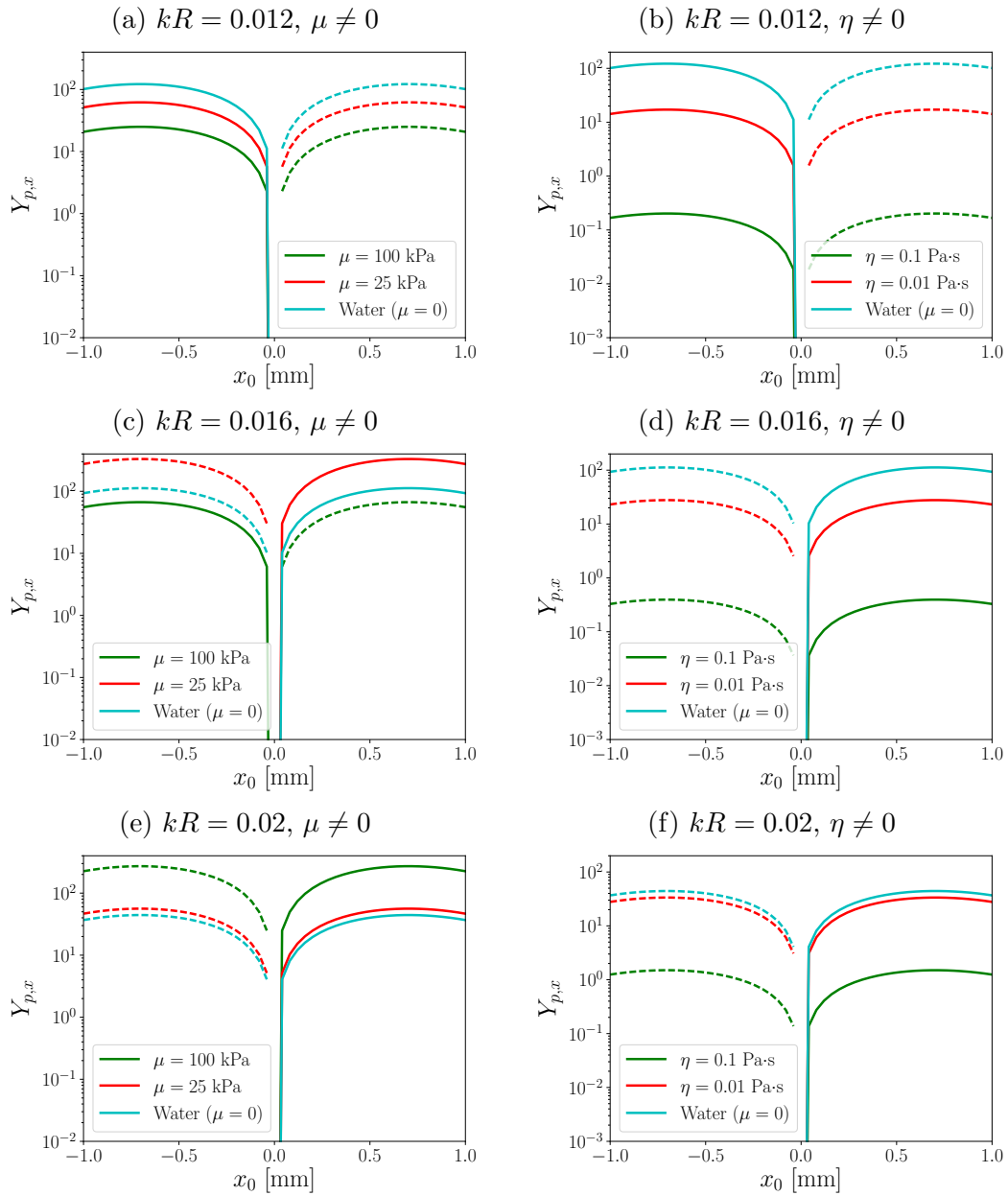


Figure 4.13: Acoustic radiation force function  $Y_{p,x}$  versus transverse position  $x_0$  of an air bubble embedded in various media with a simple focused beam incident on the bubble. Solid lines indicate  $Y_{p,x} > 0$  and dashed lines indicate  $Y_{p,x} < 0$ .

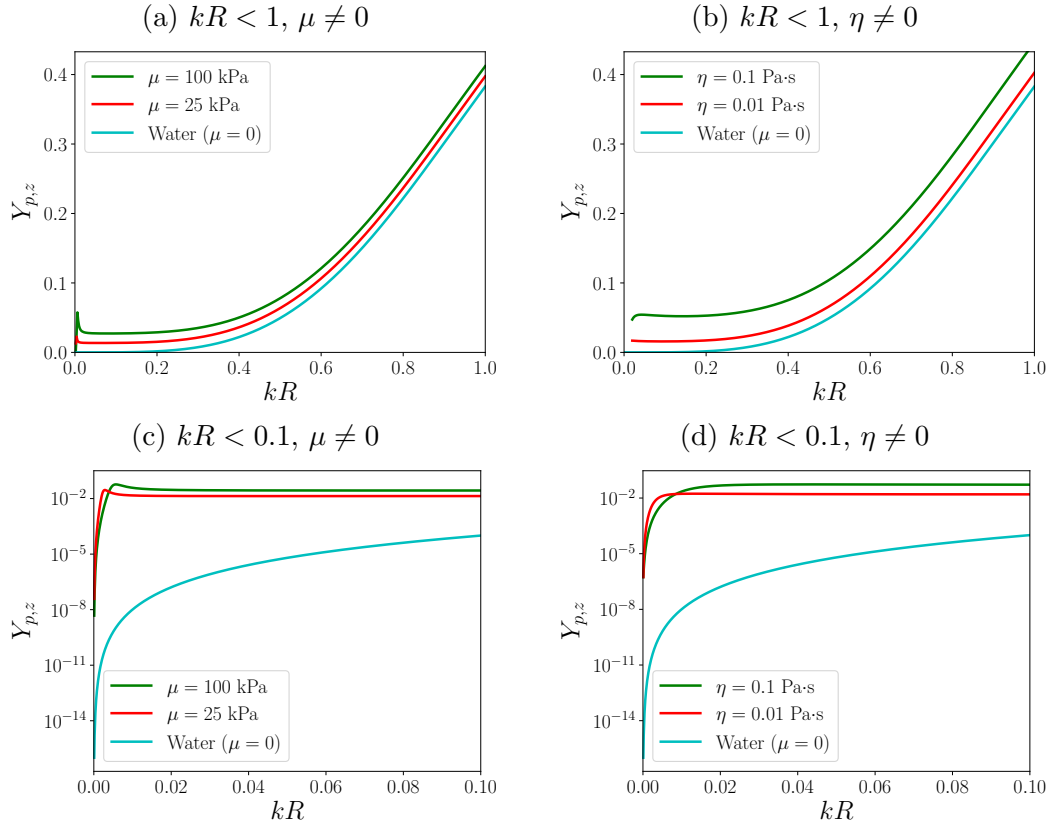


Figure 4.14: Acoustic radiation force function  $Y_{p,z}$  versus scatterer size  $kR$  of a stainless steel sphere embedded in various media with a plane traveling wave incident on the sphere.

may be easier to sweep the frequency of the incident wave, but the effect is the same for theoretical purposes.) In order to emphasize the effect of scatterer size, the shear modulus and shear viscosity in the surrounding medium are again set to specific values, and the scatterer is either at the origin or at a location off the axis of a simple focused beam.

Results for axial force on a stainless steel sphere in a plane traveling

wave are presented in Fig. 4.14. For the larger spheres in Fig. 4.14(a) and (b), the difference between liquid and soft tissue-like or viscous liquid media is relatively small, but for smaller spheres in Fig. 4.14(c) and (d), the dipole scattering coefficient (discussed in Sec. 3.4.1) initially causes a rapid increase in the radiation force with increasing  $kR$ . Larger values for either shear modulus or shear viscosity produce a more pronounced effect, and the effect is more abrupt for shear modulus than for shear viscosity due to loss. Again, the increase in the magnitude of the radiation force due to viscosity in the surrounding medium is corroborated by other works [12, 15, 16]. Other metals (e.g., aluminum) tend to exhibit similar properties.

The transverse force associated with a sphere off axis in a traveling wave beam is shown in Fig. 4.15. In this case the sphere is centered at  $x_0 = 0.5$  mm in the focal plane, so a positive force (solid line) indicates that it is pushed away from the beam axis and a negative force (dashed line) indicates that it is pushed toward the beam axis. Since the differences are negligible for  $kR = O(1)$ , only results for smaller  $kR$  are shown. For a stainless steel sphere in Fig. 4.15(a) and (b), the sphere is pushed in the same direction (toward the beam axis) regardless of scatterer size for nonzero shear viscosity, but for nonzero shear modulus there is a narrow range of  $kR$  for which the direction is reversed. For an aluminum sphere in Fig. 4.15(c) and (d), however, there is a similar reversal in direction for both nonzero shear modulus and nonzero shear viscosity: very small scatterers are pushed toward the beam axis, whereas larger scatterers are pushed away.

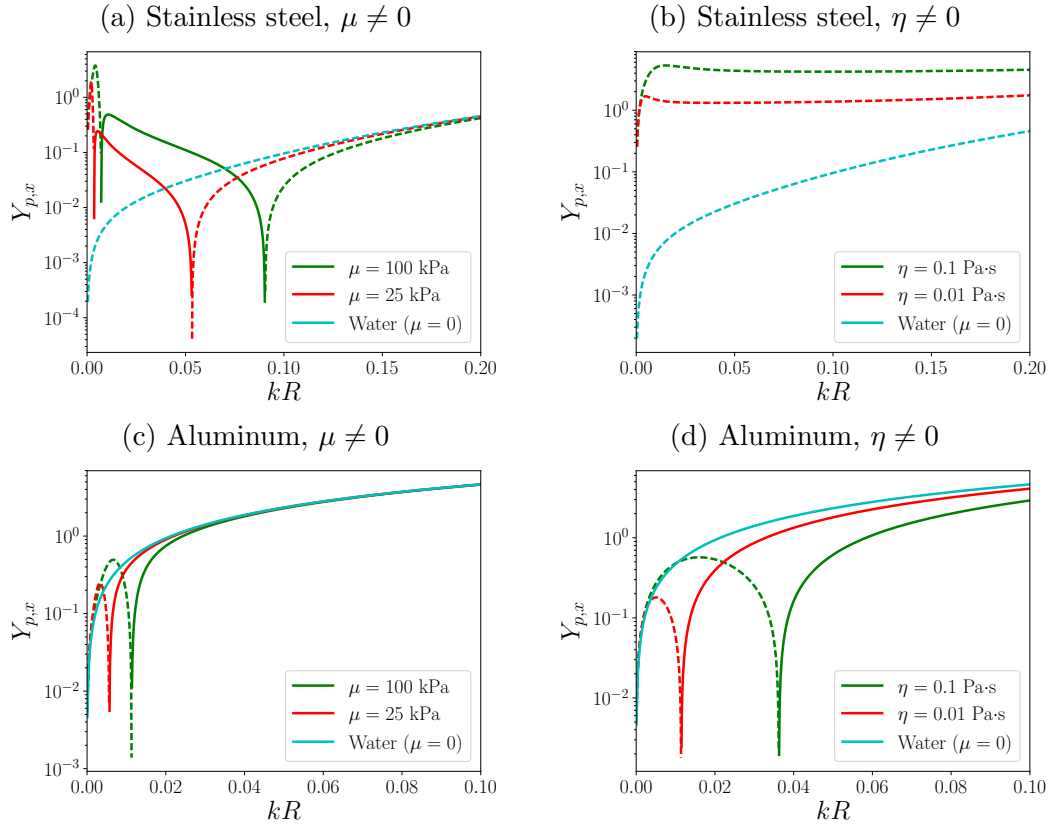


Figure 4.15: Acoustic radiation force function  $Y_{p,x}$  versus scatterer size  $kR$  of a stainless steel sphere and an aluminum sphere embedded in various media with a simple focused beam incident on the sphere, located at  $x_0 = 0.5$  mm in the focal plane. Solid lines indicate  $Y_{p,x} > 0$  and dashed lines indicate  $Y_{p,x} < 0$ .

For an air bubble in a traveling plane wave, as shown in Fig. 4.16(a) and (b), the axial force is nearly indistinguishable for larger bubbles regardless of shear properties in the medium. For smaller bubbles, however, the differences are substantial. The resonance frequency shift is clearly visible for nonzero shear modulus in Fig. 4.16(c) and the resonance peak is characteristically broadened for nonzero shear viscosity in Fig. 4.16(d). When the bubble is

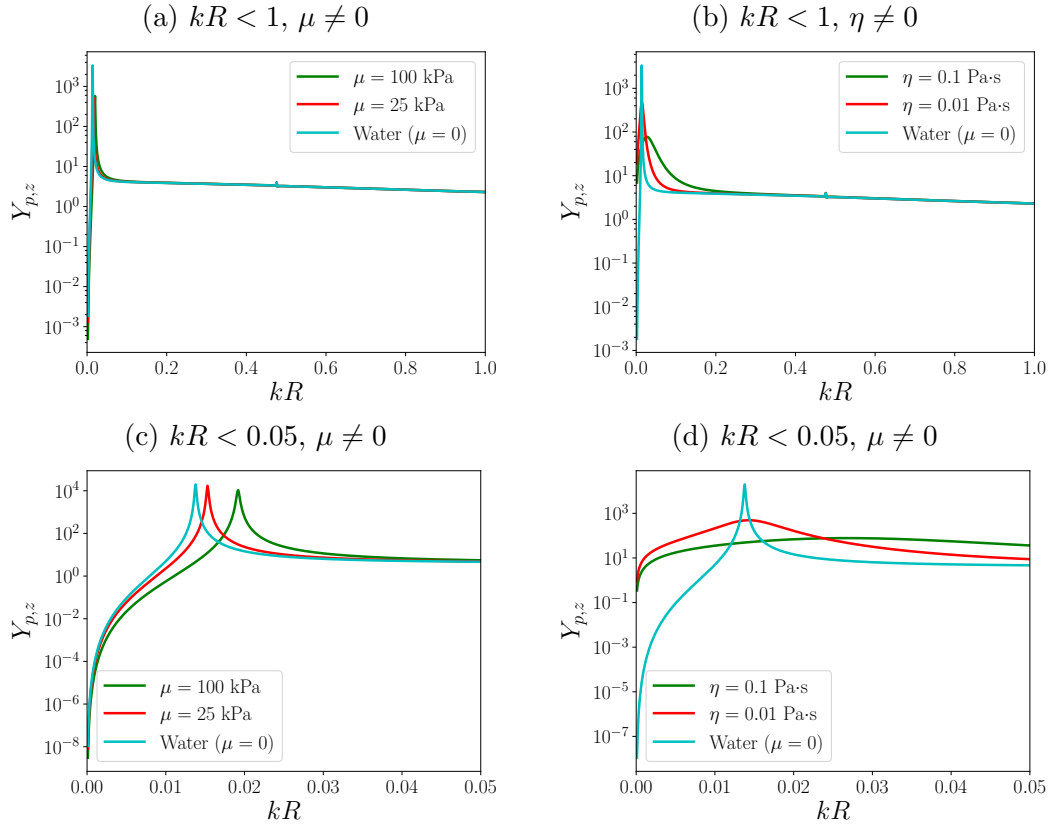


Figure 4.16: Acoustic radiation force function  $Y_{p,z}$  versus scatterer size  $kR$  of an air bubble embedded in various media with a plane traveling wave incident on the bubble.

moved off the axis of a traveling wave beam, as shown in Fig. 4.17, we can see the effect of the resonance in greater detail. Clearly, for frequencies below resonance, the bubble is pushed toward the beam axis, and for frequencies below resonance, the bubble is pushed away from it. As shown in Fig. 4.17(a), the resonance frequency shifts for nonzero shear modulus, and as shown in Fig. (b), the shift is negligible for nonzero shear viscosity in the surrounding medium. Also, according to the zoomed in plots Fig. 4.17(c) and (d), a peak

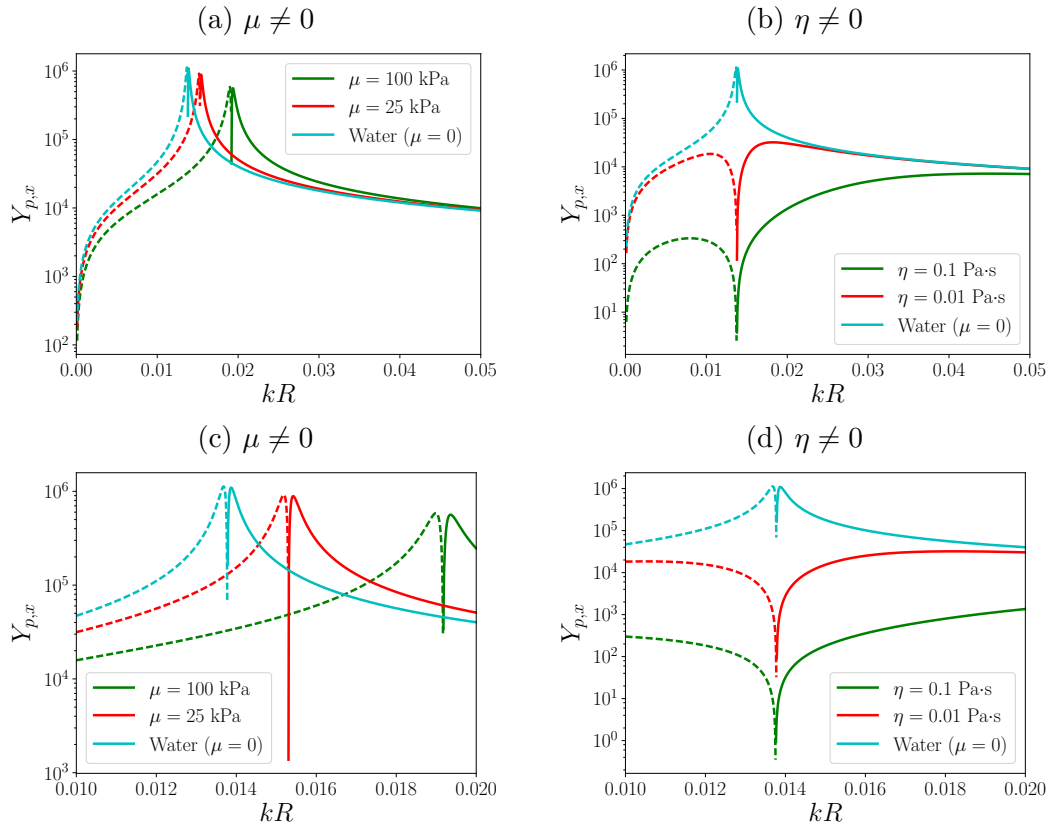


Figure 4.17: Acoustic radiation force function  $Y_{p,x}$  versus scatterer size  $kR$  of an air bubble embedded in various media with a simple focused beam incident on the sphere, located at  $x_0 = 0.5$  mm in the focal plane. Solid lines indicate  $Y_{p,x} > 0$  and dashed lines indicate  $Y_{p,x} < 0$ .

clearly occurs before the direction reversal at  $kR = 0.0137$  in all inviscid media, but in viscous liquid there is a smoother transition between positive and negative force without a resonance peak because of damping. A final observation worth noting is that the magnitude of the transverse force appears to be greater than the magnitude of the axial force, making it potentially easier to measure in practice with appropriate placement of imaging transducers.

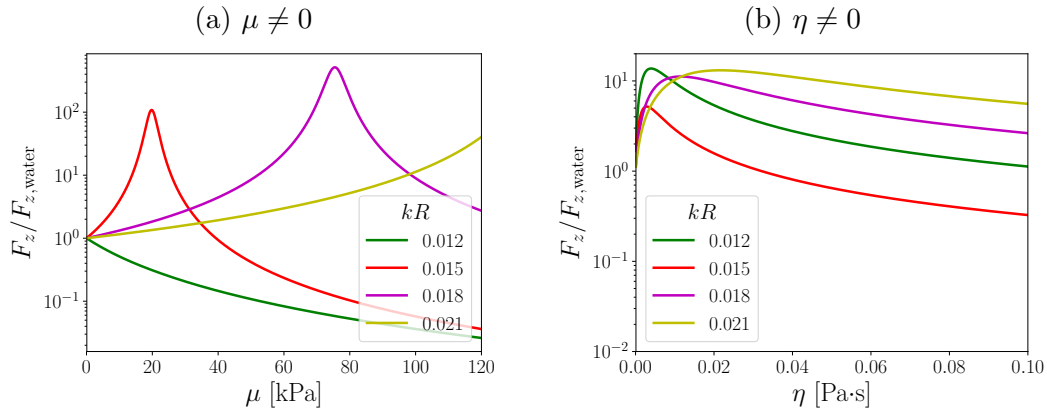


Figure 4.18: Ratio of axial radiation force in various media to that in inviscid water for air bubbles of various sizes located at  $(z_0, x_0) = (0.2 \text{ mm}, 0.5 \text{ mm})$  off the focus of a beam incident on the bubble.

#### 4.4 Elasticity in Surrounding Medium

Finally, we consider a more continuous range of shear modulus and shear viscosity in the surrounding medium. For this analysis, a simple focused beam incident on the sphere is used, the scatterer is located off the beam axis at  $(z_0, x_0) = (0.2 \text{ mm}, 0.5 \text{ mm})$ , and the ratio of force in soft tissue or viscous liquid to that in inviscid water is presented.

Results for axial and transverse force on air bubbles are shown in Figs. 4.18 and 4.19, respectively. These figures simply offer another perspective on previous discussions. Nonzero shear modulus causes a shift in the resonance frequency, causing an increase in the axial force, as shown in Fig. 4.18(a), or a reversal in direction of the transverse force, as shown in Fig. 4.19(a). Nonzero shear viscosity broadens the resonance, which causes a decrease of the force near resonance and an increase in the force off the resonance, as shown in

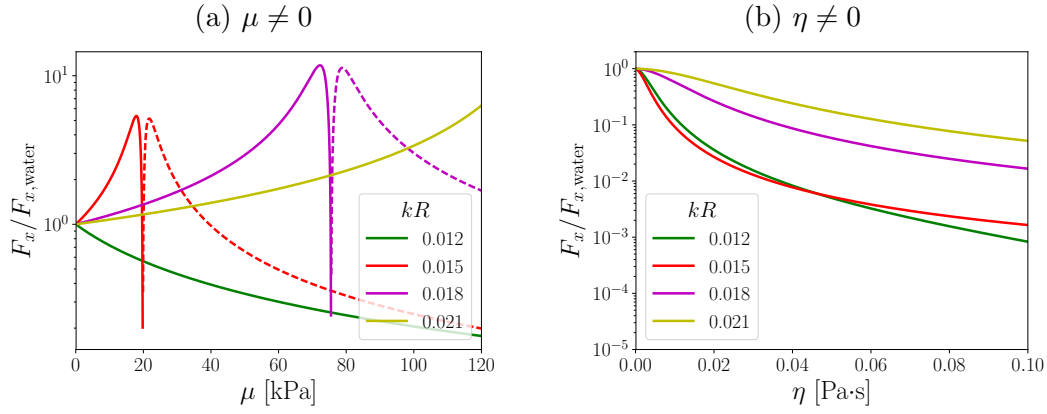


Figure 4.19: Ratio of transverse radiation force in various media to that in inviscid water versus shear modulus  $\mu$  or shear viscosity  $\eta$  for air bubbles of various sizes located at  $(z_0, x_0) = (0.2 \text{ mm}, 0.5 \text{ mm})$  off the focus of a beam incident on the bubble. A solid line indicates a positive ratio and a dashed line indicates a negative ratio.

Figs. 4.18(b) and 4.19(b).

Results for axial and transverse force on aluminum spheres are shown in Figs. 4.20 and 4.21, respectively. Both nonzero shear modulus and nonzero shear viscosity cause an increase in the axial force on the sphere until  $kR \simeq 1$ , where it levels out to unity as shown in Fig. 4.20(c) and (d), with the greatest increase occurring at different values of  $\mu$  or  $\eta$  at different values for smaller spheres as shown in Fig. 4.20(a) and (b). In Fig. 4.21(a) and (b), the transverse force exhibits direction reversals for smaller spheres at shear modulus or viscosity values that appear to approximately coincide with maxima in the axial radiation force. Also, as shown in Fig. 4.21(c) and (d), the transverse force is nearly indistinguishable between water and soft tissue-like or viscous liquid media for all but the very smallest spheres.

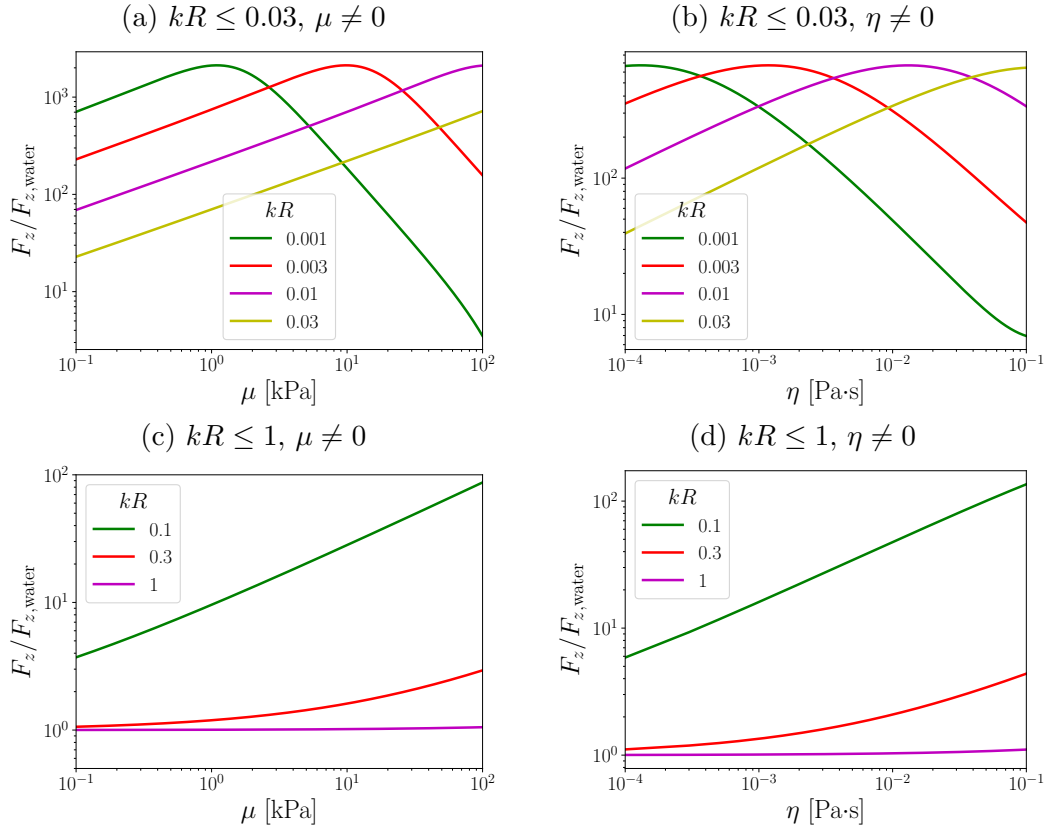


Figure 4.20: Ratio of axial radiation force in various media to that in inviscid water for aluminum spheres of various sizes located at  $(z_0, x_0) = (0.2 \text{ mm}, 0.5 \text{ mm})$  off the focus of a beam incident on the sphere.

A final look at the transverse radiation force on small scatterers in a focused sound beam is presented in Fig. 4.22, which shows color plots of the aforementioned force ratio versus both scatterer size and shear modulus or shear viscosity. In these plots, red regions indicate that the forces are in the same direction, and blue regions indicate that the forces are in the opposite direction. Because direction reversals would be easier to observe in practice than changes in magnitude of the force, these plots suggest regions in pa-

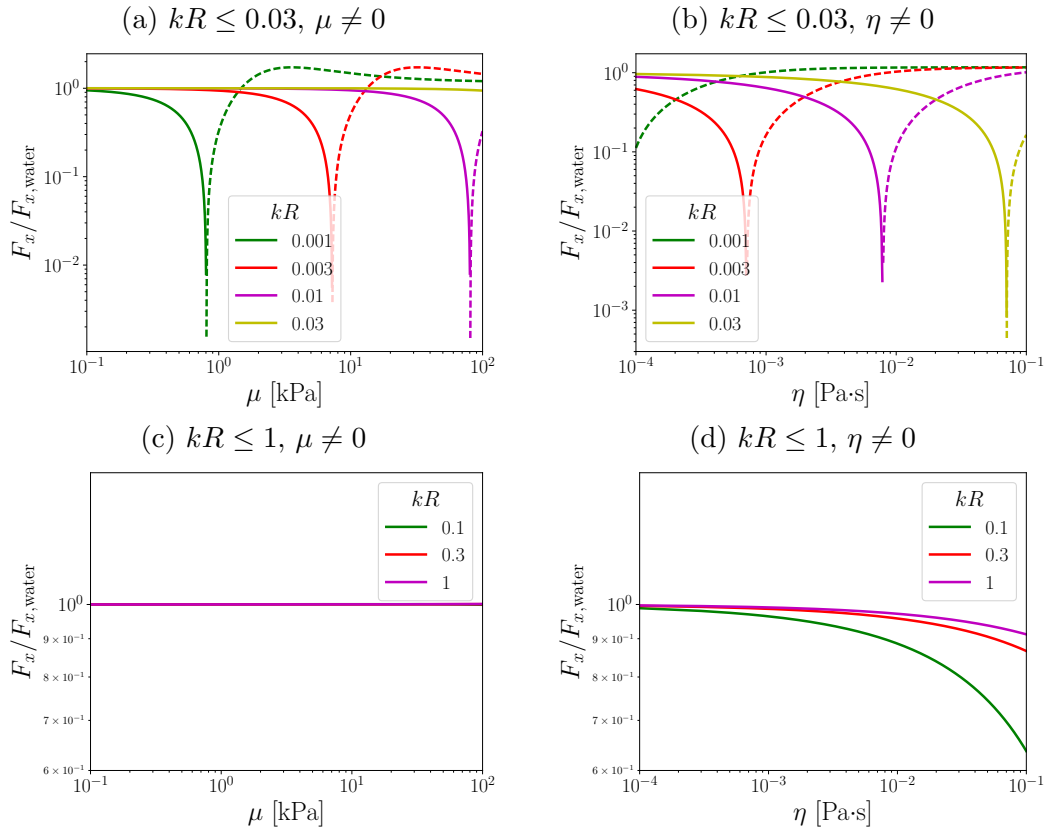


Figure 4.21: Ratio of transverse radiation force in various media to that in inviscid water versus shear modulus  $\mu$  or shear viscosity  $\eta$  for aluminum spheres of various sizes located at  $(z_0, x_0) = (0.2 \text{ mm}, 0.5 \text{ mm})$  off the focus of a beam incident on the sphere. A solid line indicates a positive ratio and a dashed line indicates a negative ratio.

parameter space that may provide useful information about the medium. For aluminum spheres in Fig. 4.22(a) and (b), the effects of nonzero shear modulus and nonzero shear viscosity are difficult to distinguish. Either property can cause a reversal in the direction of the force, so determining which is responsible for this change may require additional rheological tests. For air bubbles

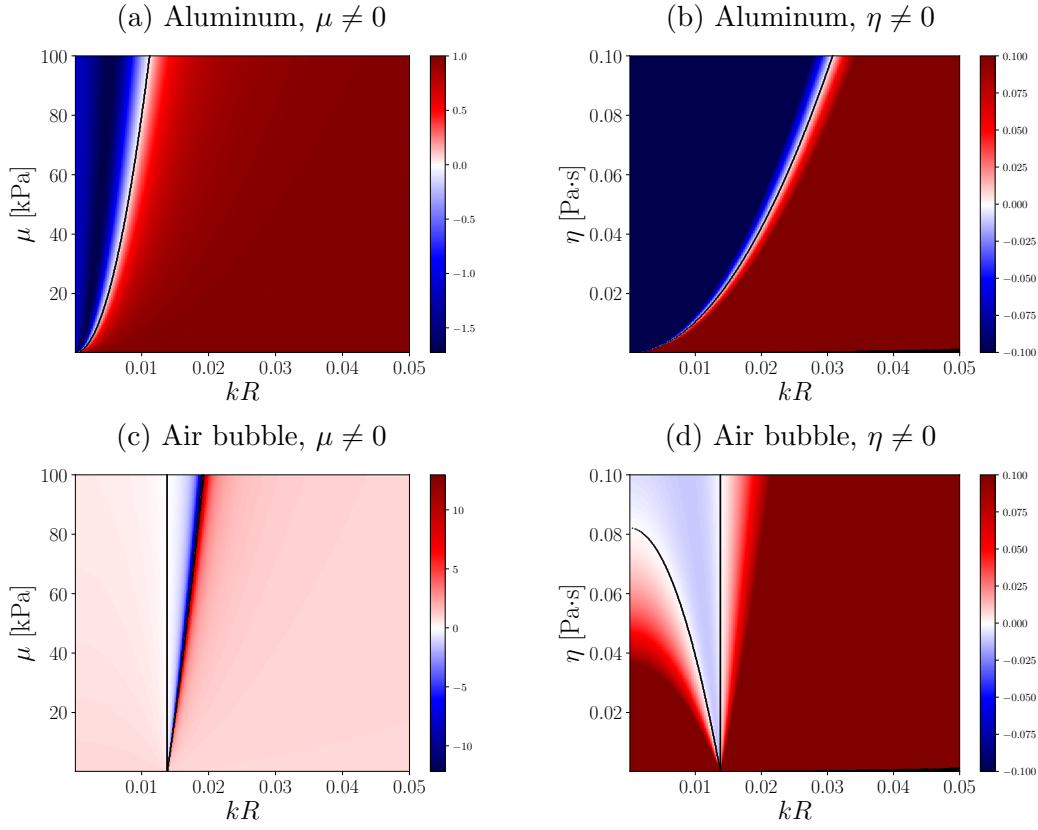


Figure 4.22: Ratio of transverse radiation force in various media to that in inviscid water versus scatterer size  $kR$  and shear modulus  $\mu$  or shear viscosity  $\eta$  for air bubbles and aluminum spheres in a simple focused beam, located at  $(z_0, x_0) = (0, 0.5 \text{ mm})$ . Black lines have been added as visual aids to identify direction reversals [127].

in Fig. 4.22(c) and (d), there is a narrow range of bubble size that causes a reversal in the force direction, and this range is different for nonzero shear modulus and nonzero shear viscosity. This result suggests that if a range of bubble sizes is introduced in a soft tissue to be examined, it may be possible to determine the tissue properties based on which bubble sizes are pushed in

opposite directions. However, the narrowness of the range and possible challenges associated with transducer placement may still make this phenomenon difficult to investigate in practice.

## 4.5 Summary

The radiation force results discussed in this chapter cover a variety of variables: size, position, and mechanical properties of the spherical scatterer, and both elasticity and viscosity in the surrounding medium. By determining sets of parameters where the force is especially sensitive to a change in the elasticity in the medium, we can develop experiments to test the practical utility of this theory. The results presented here suggest that small scatterers, though subject to a correspondingly smaller radiation force, are especially worth investigating as they exhibit the most different behavior between liquid and soft elastic media. Nonzero shear modulus and nonzero shear viscosity in the surrounding medium often produce similar effects, but there are some instances where they differ enough that these effects may be examined separately.

For viscosity, previous results showed a large increase in the radiation force on small, rigid scatterers [12, 15, 16], and this effect is qualitatively corroborated by the results shown in this chapter. However, direction reversal of the force due to a traveling plane wave was also observed [12], but this effect is not observed from our force. There are several reasons for this. First, the approximation we made to the stress tensor removed all terms that would have included explicit dependence on shear viscosity; by leaving only  $\sigma_{nm}^B$ , which

only has elastic constant  $B = -K$  as its coefficient in a fluid, we have removed any term that could have been important as regards shear viscosity in a fluid. Second, in neglecting effects due to absorption, we have ignored acoustic streaming, which seems to be important when the sphere radius is smaller than the viscous wave penetration depth  $\delta$  as defined in Eq. (1.9).

Finally, while several of the results presented in this chapter may be useful, an important point must be reemphasized here: these results only include effects due to the scattered compressional wave field and the accompanying scattering coefficients  $A_n$ . Although the coefficients  $A_n$  do exhibit dependence on the shear modulus of the medium surrounding the sphere, the scattered shear wave field itself (along with the accompanying scattering coefficients  $B_n$ ) must also be considered. This discussion is the subject of Chapter 5, though  $G_n$  is not examined as extensively as  $F_n$  in this chapter due to the difficulty in obtaining analytical—and even semi-analytical or numerical—results.

## Chapter 5

# Acoustic Radiation Force Associated with the Scattered Shear Wave

In this chapter, consideration is given to the radiation force  $G_n$  on a spherical scatterer due to the scattered shear wave field in a soft elastic medium. Viscous liquid media have been examined by others [11, 12, 15–19, 128], and these studies have revealed some non-intuitive results due to the viscous boundary layer and acoustic streaming. However, surrounding media with nonzero shear moduli have not been considered despite their relevance to soft tissue. The purpose of this chapter is to examine the force term  $G_n$  in greater detail and compare it to the force  $F_n$  due to the scattered compressional wave field.

All numerical comparisons making use of the full expression  $G_n = G_n^B + G_n^P$  in Eq. (2.100) for the contribution associated with the scattered shear wave are limited in this chapter to the  $z$ -component of the radiation force. The quantity  $G_n^B$  is the component of the radiation force due to direct integration of the stress tensor over the surface of the scatterer, and the quantity  $G_n^P$  is the reaction force due to the body force  $g_n$  in Eq. (2.46) associated with shear stress in the surrounding medium. The limitation to the  $z$ -component of the force

is necessary due to the heavy computational burden resulting from the large discrepancy between shear wave speed and compressional wave speed in soft tissue-like media, which requires body forces and particle displacements to be very finely discretized. Therefore, the problem considered here is the axisymmetric case, which allows for discretization in two dimensions instead of three to numerically compute  $G_z^P$ . Additionally, we will see that analytic approximations for  $G_n^P$ , which would allow for easy calculation of the  $x$ -component of the force, are unsatisfactory for the types of scatterers that would be useful as targets in soft tissue. That is, an analytic approximation for  $G_n^P$  appears to be possible only for scatterers so acoustically similar to the surrounding medium that they would be almost acoustically transparent.

Furthermore, in order to obtain a full solution of the time-averaged second-order equations of motion, the shear wave speed in the medium is increased by a factor of ten from what has been considered previously (100 m/s instead of 10 m/s). This increase in the shear wave speed is also necessary to reduce the discretization and thus facilitate computation.

In Sec. 5.1, the term  $G_n^B$ , which has been calculated analytically in Sec. 2.6, is examined in comparison with the force  $F_n$  due to the scattered compressional wave to determine whether effects due to the scattered shear wave field are likely to present a significant correction to  $F_n$ . Next, in Sec. 5.2, an approximation to the body force  $g_n$  in Eq. (2.44) due to shear wave fields is proposed such that an analytical result for  $G_n^P$  might be obtained. The validity of this approximation is examined for several different scatterer materials. In

Sec. 5.3, a least-squares finite element method (FEM) is presented to compute  $G_z^P$  numerically for axisymmetric incident fields, which is added to the analytic calculations for  $G_z^B$  and  $F_z$  to provide the net contribution  $F_z + G_z$  to the radiation force on the sphere. Finally, in Sec. 5.4, a full FEM solution based on the time-averaged second-order equations of motion is obtained with the FEniCS open-source computing platform to include effects related to the deformation of the surrounding medium. That is, in the full FEM solution, the displacement of the sphere is due to  $F_z$ ,  $G_z$ , and the solenoidal component of  $g_n$  written as  $\nabla \times \mathbf{S}$  from Eq. (2.46); this final computation is important to determine whether the solenoidal component of  $g_n$  also has a significant effect on the predicted sphere displacement.

## 5.1 Comparison of $F_n$ and $G_n^B$

Since  $G_n^B$  can easily be determined analytically from Eq. (2.108) for non-axisymmetric fields or from Eq. (2.109) for axisymmetric fields, it is useful to consider in order to estimate the magnitude of  $G_n$  relative to  $F_n$ . While a large value of  $G_n^B$  may not strictly correspond to a large value of  $G_n$  compared with  $F_n$  since  $G_n^P$  is unknown, this comparison is an appropriate first step because  $G_n^B$  and  $G_n^P$  may be expected to be of the same order, since  $F_n^B$  and  $F_n^P$  are observed to be the same order in Fig. 5.2.

The ratio of force terms  $G_n^B/F_n$  for various spheres in different soft tissue-like media is presented in Fig. 5.1. In these plots, a simple focused beam with confinement angle  $\theta_0 = 30^\circ$  is used, and the sphere is located off

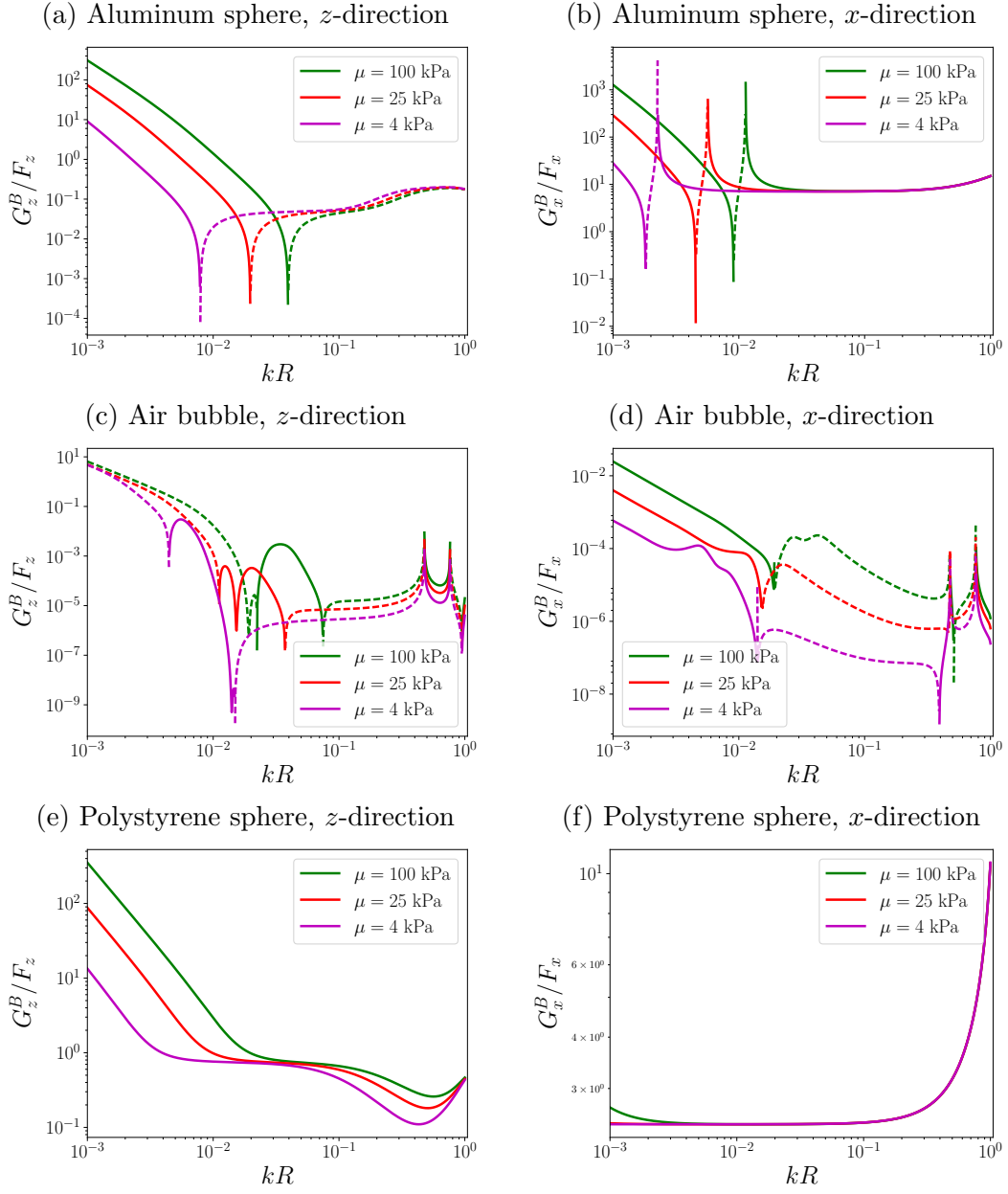


Figure 5.1: Ratio of force terms  $G_n^B/F_n$  for various spheres embedded in soft tissue-like media subject to a simple focused beam with confinement angle  $\theta_0 = 30^\circ$  located off the beam axis at  $(z_0, x_0) = (0, 0.5 \text{ mm})$ . A positive ratio is indicated with solid lines, and a negative ratio is indicated with dashed lines.

the beam axis at  $(z_0, x_0) = (0, 0.5 \text{ mm})$ . A positive  $G_n^B/F_n$  ratio is indicated with solid lines, and a negative ratio is indicated with dashed lines.

The ratio  $G_n^B/F_n$  is shown for an aluminum sphere in Fig. 5.1(a) and (b). For the axial direction shown in Fig. 5.1(a), it is clear that  $G_z^B$  is large compared with  $F_z$  for small spheres ( $kR \lesssim 0.01$ ) but levels off to approximately  $-0.1$  as the sphere size increases. However, for the transverse direction shown in Fig. 5.1(b),  $|G_x^B|$  is an order of magnitude greater than  $|F_x|$  for nearly all sphere sizes, with several reversals in direction, suggesting that shear effects may be especially important for the transverse force on a hard sphere in a soft tissue-like medium.

The ratio  $G_n^B/F_n$  for an air bubble is shown in Fig. 5.1(c) and (d). For the force in the axial direction shown in Fig. 5.1(c),  $G_z^B$  is small compared with  $F_z$  for  $kR \gtrsim 0.005$ , and for the force in the transverse direction shown in Fig. 5.1(d),  $G_x^B$  is always small in comparison with  $F_x$ . Because  $G_n^B$  and  $G_n^P$  may be expected to be of the same order as is often the case with  $F_n^B$  and  $F_n^P$ , this suggests that for most bubble sizes of interest, especially those near the resonance  $kR = 0.0137$  in water, the correction  $G_n$  associated with the scattered shear wave may not be too large compared with  $F_n$  for very soft scatterers in soft tissue-like media.

Finally, the ratio  $G_n^B/F_n$  for a polystyrene sphere is shown in Fig. 5.1(e) and (f). For both the axial and the transverse directions of the force,  $G_n^B$  appears to be of the same order as  $F_n$ . This suggests that  $G_n$  may be of the same order as  $F_n$  and must be considered for such scatterers. From the three

comparisons in Fig. 5.1, it therefore appears to be necessary to consider  $G_n$ .

## 5.2 Approximation of $G_n^P$

Since the previous section suggests a significant effect due to  $G_n$  for several scatterer properties and sizes, it is necessary to find a way to calculate  $G_n^P$ . Ideally, this could be done analytically, which would considerably ease computational requirements for determining the radiation force on a sphere in a soft elastic medium.

First, it is useful to consider a special property of  $F_n$  and examine whether it may apply to  $G_n$  as well. Specifically,  $F_n$  is the same for any surface of integration chosen to enclose the sphere. Though  $F_n^B$  and  $F_n^P$  both oscillate with  $kr$  outside the sphere—as shown in Appendix B by Eqs. (B.9) and (B.17)—the sum  $F_n^B + F_n^P$  has no explicit dependence on  $kr$ . We thus consider whether this feature could help predict  $F_n$  just from  $F_n^B$ , and if so, whether this could be applied to  $G_n^B$ .

As can be seen in Fig. 5.2, there are several issues that prevent this. First, depending on the type of scatterer,  $F_z^B$  and  $F_z^P$  have different relative importance depending on  $kR$ . For example, in Fig. 5.2(a) for the stainless steel sphere,  $F_z^B$  is greater than the total force  $F_z$  at  $kr = kR$ , whereas for the air bubble in Fig. 5.2(b),  $F_z^P$  makes up the entirety of the force at the bubble radius. Second, even for the same scatterer type, the relative importance of  $F_z^B$  and  $F_z^P$  at  $kr = kR$  may be different. In Fig. 5.2(a) for a small stainless steel sphere,  $F_z^B$  appears to be nearly equivalent to  $F_z$ , whereas for a larger

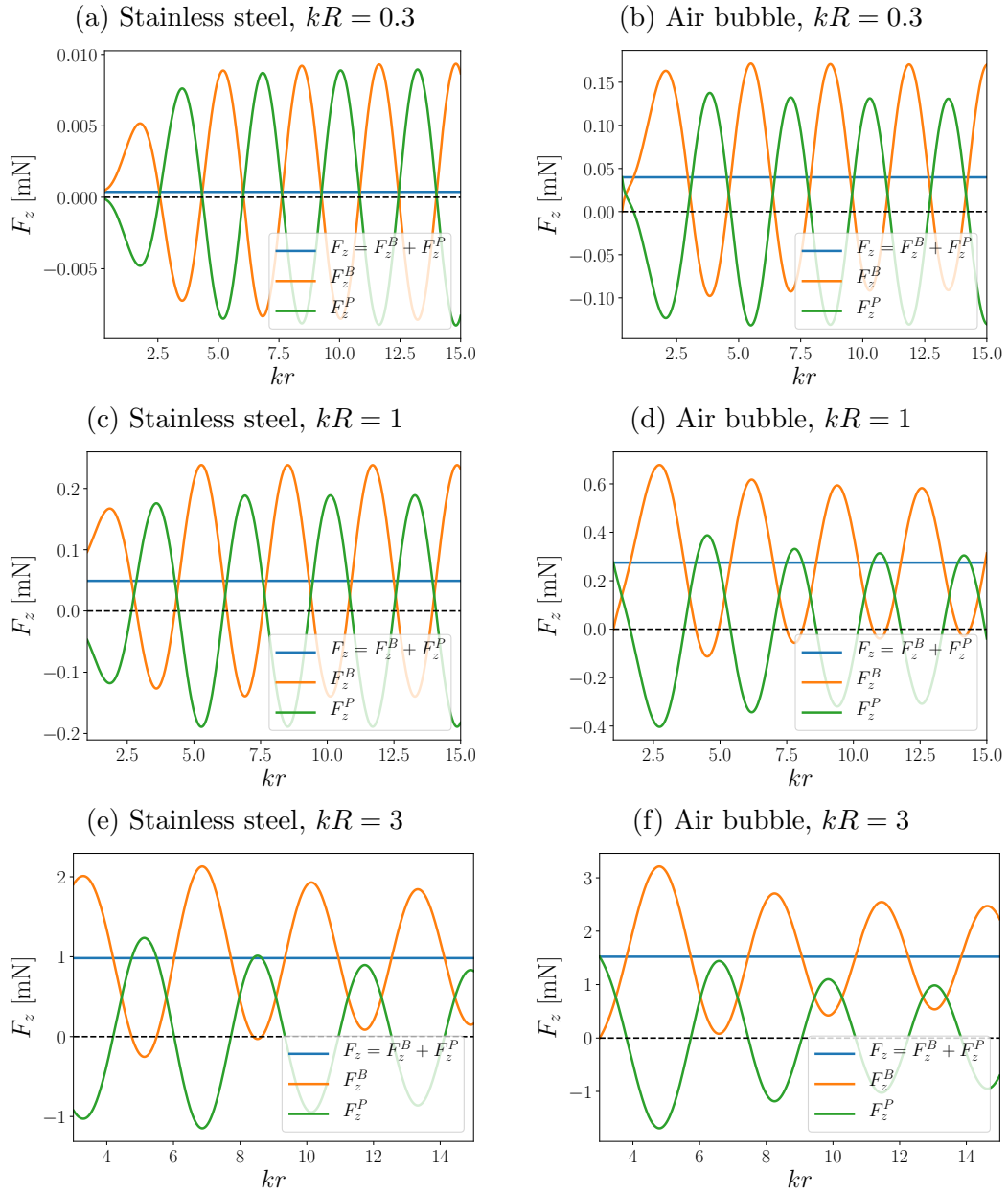


Figure 5.2: Plots of the two force terms  $F_z^B$  and  $F_z^P$  due to compressional wave fields for a traveling plane wave incident on various spheres in a soft tissue-like medium ( $\mu = 100$  kPa). A dashed line is included at  $F_z = 0$  for visual clarity.

sphere in Fig. 5.2(c) or (e),  $F_z^P$  represents a large correction. Finally, while at large  $kr$  the value of  $F_z^B$  appears to oscillate about  $F_z$  and  $F_z^P$  appears to oscillate about zero, especially in Fig. 5.2(d)–(f), this may not be the case for  $G_z^B$  and  $G_z^P$  because the body force  $g_n$  in Eq. (2.46) cannot be written purely as a gradient, whereas  $f_n$  in Eqs. (2.50) and (2.51) can. So, the behavior of  $F_z^B$  and  $F_z^P$  for  $kr \gg 1$  may not generalize to  $G_z^B$  and  $G_z^P$ .

Since it does not appear to be possible to draw rigorous conclusions about  $G_n$  from  $G_n^B$  alone, we therefore proceed by determining whether there are any scenarios for which  $G_n^P$  can be found analytically. To begin, recall several relations for the shear field from Secs. 2.1–2.2. First, from Eq. (2.24), we have the shear wave field  $u_n^t$  in terms of the potential  $\Theta$  written in vector notation as

$$\mathbf{u}^t = \nabla \times \nabla \times (\mathbf{r}\Theta). \quad (5.1)$$

Next, from Eq. (2.37),  $\sigma_{nm}^{lt}$  can be written as

$$\sigma_{nm}^{lt} = Kk^2\varphi \frac{\partial u_m^t}{\partial x_n}, \quad (5.2)$$

where  $\varphi$  is the displacement potential for the compressional wave field  $u_n^l$ .

Finally,  $\sigma_{nm}^{lt}$  can be used to find  $g_n$  from Eq. (2.44):

$$g_n = \frac{\partial \sigma_{nm}^{lt}}{\partial x_m}. \quad (5.3)$$

Substitution of Eq. (5.1) into Eq. (5.2) and then the result into Eq. (5.3) gives, after some manipulation,

$$g_n = Kk^2 \frac{\partial \varphi}{\partial x_m} \left( 3 \frac{\partial^2 \Theta}{\partial x_m \partial x_n} + \kappa^2 \Theta \delta_{nm} + r \frac{\partial^3 \Theta}{\partial r \partial x_m \partial x_n} + \kappa^2 r \frac{\partial \Theta}{\partial r} \right). \quad (5.4)$$

Now recall from Eq. (2.46) that we seek a scalar potential  $Q$  and a vector potential  $\mathbf{S}$  such that

$$\mathbf{g} = \nabla Q + \nabla \times \mathbf{S}. \quad (5.5)$$

In deriving Eq. (5.5), one obtains the following integral expressions for the potentials  $Q$  and  $\mathbf{S}$  [129]:

$$Q(\mathbf{r}) = -\frac{1}{4\pi} \int_V \frac{\nabla' \cdot \mathbf{g}(\mathbf{r}')}{|\mathbf{r} - \mathbf{r}'|} dV' + \frac{1}{4\pi} \int_S \hat{\mathbf{n}}' \cdot \frac{\mathbf{g}(\mathbf{r}')}{|\mathbf{r} - \mathbf{r}'|} dS', \quad (5.6)$$

$$\mathbf{S}(\mathbf{r}) = \frac{1}{4\pi} \int_V \frac{\nabla' \times \mathbf{g}(\mathbf{r}')}{|\mathbf{r} - \mathbf{r}'|} dV' - \frac{1}{4\pi} \int_S \hat{\mathbf{n}}' \times \frac{\mathbf{g}(\mathbf{r}')}{|\mathbf{r} - \mathbf{r}'|} dS', \quad (5.7)$$

where  $V$  is a volume enclosing the position  $\mathbf{r}$  with surface  $S$ ,  $\hat{\mathbf{n}}'$  represents the unit vector normal to  $S$ , and  $\nabla'$  represents either divergence or curl in the primed coordinate system.

While it is tempting to directly evaluate the integrals presented in Eqs. (5.6) and (5.7), we encounter several practical difficulties with the volume integrals. In their existing form, both volume integrals have a singularity at  $\mathbf{r}' = \mathbf{r}$  since  $\mathbf{g}(\mathbf{r}')$  is neither divergence-free nor curl-free at that point. The volume integrals must therefore be transformed to remove the singularity. This can be accomplished with the change of variables  $\mathbf{r}_0 = \mathbf{r} - \mathbf{r}'$ , after which the volume integrals in Eqs. (5.6) and (5.7) become

$$\int_V \frac{\nabla_0 \cdot \mathbf{g}(\mathbf{r} - \mathbf{r}_0)}{r_0} dV_0 = \int_V \nabla_0 \cdot \mathbf{g}(\mathbf{r} - \mathbf{r}_0) r_0 \sin \theta_0 d\phi_0 d\theta_0 dr_0, \quad (5.8)$$

$$\int_V \frac{\nabla_0 \times \mathbf{g}(\mathbf{r} - \mathbf{r}_0)}{r_0} dV_0 = \int_V \nabla_0 \times \mathbf{g}(\mathbf{r} - \mathbf{r}_0) r_0 \sin \theta_0 d\phi_0 d\theta_0 dr_0, \quad (5.9)$$

where  $\nabla_0$  represents either divergence or curl in the transformed coordinate system. The point  $r_0 = 0$  is no longer a problem after this transformation, but

the new expression for the body force requires

$$r' = \sqrt{r^2 + r_0^2 - 2rr_0 [\cos \theta \cos \theta_0 + \sin \theta \sin \theta_0 \cos (\phi - \phi_0)]}, \quad (5.10)$$

$$\theta' = \arccos \left( \frac{r \cos \theta - r_0 \cos \theta_0}{r'} \right), \quad (5.11)$$

$$\phi' = \arctan \left( \frac{r \sin \theta \sin \phi - r_0 \sin \theta_0 \sin \phi_0}{r \sin \theta \cos \phi - r_0 \sin \theta_0 \cos \phi_0} \right), \quad (5.12)$$

resulting in a substantially more complicated expression for  $g_n$  even before the divergence and curl are calculated. Also, since the potential  $Q$  is sought at radius  $R$  on the surface of the sphere and  $g_n$  is both singular at the origin and rapidly varying with  $r$ , the region of integration must be a thin spherical shell with inner radius slightly less than  $R$  and outer radius slightly greater than  $R$ , which is difficult to express in the transformed  $(r_0, \theta_0, \phi_0)$  coordinates. With the further complication that  $g_n$  is itself expressed in terms of products of infinite sums of spherical Bessel or Hankel functions and associated Legendre functions, this transformation clearly makes the volume integrals intractable from an analytical standpoint. A sufficiently clever numerical integration should be possible, but another method discussed in Sec. 5.3.1 is used instead for its simplicity.

To attempt further progress in analyzing the effect of  $g_n$  without an analytic expression for  $Q$ , we will consider a possible approximation whereby  $g_n$  can be written entirely as a gradient:

$$g_n \approx \frac{\partial Q}{\partial x_n}. \quad (5.13)$$

Recalling Eq. (2.48), we can find the force term  $G_n^P$  by integrating  $Q$  over the

surface of the sphere,

$$G_n^P = - \int_S \langle Q \rangle \frac{x_n}{R} dS, \quad (5.14)$$

in a similar manner as for the other three force terms  $F_n^B$ ,  $F_n^P$ , and  $G_n^B$ . Like the body force  $g_n$ , the potential  $Q$  is complicated even with the approximation in Eq. (5.13). However, unlike the integrals in Eqs. (5.6) and (5.7), the integral in Eq. (5.14) can be calculated numerically by truncating the infinite series expressions in  $Q$ .

To reorganize  $g_n$  into a form that permits the use of the approximation in Eq. (5.13), we can separate each term on the right-hand side of Eq. (5.4) into two parts, a gradient and a remainder. The result of this procedure is

$$g_n = g_n^{(1)} + g_n^{(2)} + g_n^{(3)} + g_n^{(4)}, \quad (5.15)$$

where

$$\frac{g_n^{(1)}}{Kk^2} = 3 \frac{\partial \varphi}{\partial x_m} \frac{\partial^2 \Theta}{\partial x_m \partial x_n} = \frac{\partial}{\partial x_n} \left( 3 \frac{\partial \varphi}{\partial x_m} \frac{\partial \Theta}{\partial x_m} \right) - 3 \frac{\partial^2 \varphi}{\partial x_n \partial x_m} \frac{\partial \Theta}{\partial x_m}, \quad (5.16)$$

$$\frac{g_n^{(2)}}{Kk^2} = \kappa^2 \frac{\partial \varphi}{\partial x_n} \Theta = \frac{\partial}{\partial x_n} (\kappa^2 \varphi \Theta) - \kappa^2 \varphi \frac{\partial \Theta}{\partial x_n}, \quad (5.17)$$

$$\begin{aligned} \frac{g_n^{(3)}}{Kk^2} = r \frac{\partial \varphi}{\partial x_m} \frac{\partial^3 \Theta}{\partial r \partial x_m \partial x_n} = \frac{\partial}{\partial x_n} \left( r \frac{\partial \varphi}{\partial x_m} \frac{\partial^2 \Theta}{\partial r \partial x_m} \right) \\ - \frac{\partial \varphi}{\partial x_m} \frac{\partial^2 \Theta}{\partial x_m \partial x_n} - r \frac{\partial^2 \varphi}{\partial x_m \partial x_n} \frac{\partial^2 \Theta}{\partial r \partial x_m}, \end{aligned} \quad (5.18)$$

$$\frac{g_n^{(4)}}{Kk^2} = \kappa^2 r \frac{\partial \varphi}{\partial r} \frac{\partial \Theta}{\partial x_n} = \frac{\partial}{\partial x_n} \left( \kappa^2 r \frac{\partial \varphi}{\partial r} \Theta \right) - \kappa^2 \frac{\partial \varphi}{\partial x_n} \Theta - \kappa^2 r \frac{\partial^2 \varphi}{\partial r \partial x_n} \Theta. \quad (5.19)$$

There are now four terms that are explicitly gradients, appearing first on the right-hand side of each expression. If some combination of these terms

comprises the dominant contribution to  $g_n$ —that is, if the other terms are small comparison—then  $g_n$  may be written as a gradient of these terms. Combining Eqs. (5.16)–(5.19) yields

$$g_n = g_n^Q + g_n^S, \quad (5.20)$$

where

$$\frac{g_n^Q}{Kk^2} = \frac{\partial}{\partial x_n} \left( 2 \frac{\partial \varphi}{\partial x_m} \frac{\partial \Theta}{\partial x_m} + r \frac{\partial \varphi}{\partial x_m} \frac{\partial^2 \Theta}{\partial r \partial x_m} + \kappa^2 r \frac{\partial \varphi}{\partial r} \Theta \right), \quad (5.21)$$

$$\frac{g_n^S}{Kk^2} = -2 \frac{\partial^2 \varphi}{\partial x_n \partial x_m} \frac{\partial \Theta}{\partial x_m} - r \frac{\partial^2 \varphi}{\partial x_m \partial x_n} \frac{\partial^2 \Theta}{\partial r \partial x_m} - \kappa^2 r \frac{\partial^2 \varphi}{\partial r \partial x_n} \Theta. \quad (5.22)$$

Since the right-hand side of Eq. (5.21) is exclusively the gradient of a scalar function, we will investigate parameter ranges for which  $g_n^Q$  is much larger than  $g_n^S$  so that Eq. (5.13) may be used.

Results for various scatterers are shown in Fig. 5.3. The plots show the ratio  $|g_n^S|/|g_n^Q|$  as a function of  $kR$  and  $\theta$ . A small value of  $|g_n^S|/|g_n^Q|$  (indicating that  $g_n^S$  may be discarded) is visualized with blue shading, whereas a large ratio is visualized with red shading. (Note that in order to better visualize parameter regions with large values, the plot is saturated at a ratio of 5.) This ratio should be small for all  $\theta$  in order for the approximation given by Eq. (5.13) to be valid for a given scatterer size. Also, depending on the direction of radiation force sought, a low ratio is more important for some values of  $\theta$  than for others. For example, if force in the  $z$ -direction is to be calculated, then the accuracy of the approximation is more important for  $\theta \rightarrow 0$  and  $\theta \rightarrow \pi$  because  $x_n = R \cos \theta$  appears in the integration of the potential from Eq. (5.14).

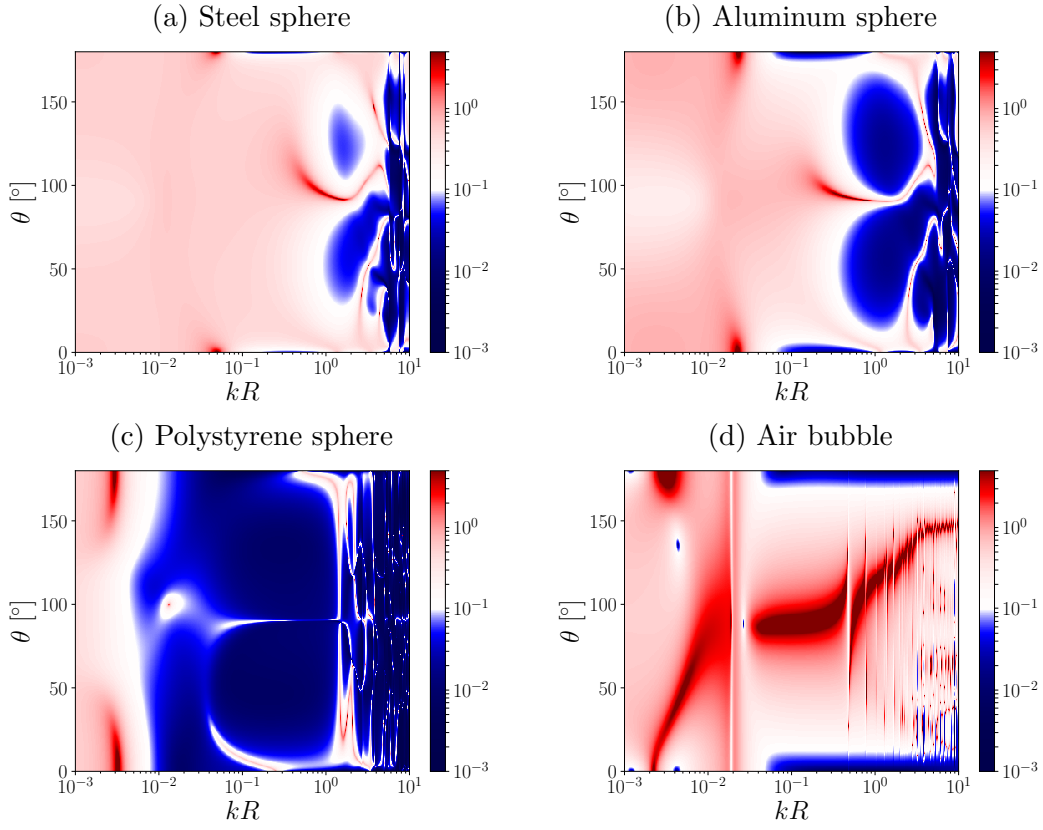


Figure 5.3: Ratio of terms  $|g_n^S|/|g_n^Q|$  in Eqs. (5.21)–(5.22) for various spheres in a soft tissue-like medium ( $\mu = 100$  kPa) subject to a simple focused beam with confinement angle  $\theta_0 = 30^\circ$ . Small ratio is indicated with blue shading, large ratio with red shading.

Unfortunately, it appears to be difficult to meet the criterion of a small  $|g_n^S|/|g_n^Q|$  ratio. Results for the steel sphere, the aluminum sphere, and the air bubble in Fig. 5.3(a), (b), and (d), respectively, all show large regions where the ratio may not be small. For steel and aluminum spheres, the ratio is almost always large for  $kR < 1$ , as indicated by the red regions on the left of Fig. 5.3(a) and (b). For air bubbles, the ratio is small only for  $kR > 0.1$  at

angles near zero and  $\pi$ , as indicated by the blue regions at the top and bottom of Fig. 5.3(d). Even for the polystyrene sphere in Fig. 5.3(c), for which there are large regions where the ratio may be small, the features near  $\theta = 0$  and  $\theta = \pi$  for  $0.05 \lesssim kR \lesssim 1$  are problematic for this approximation.

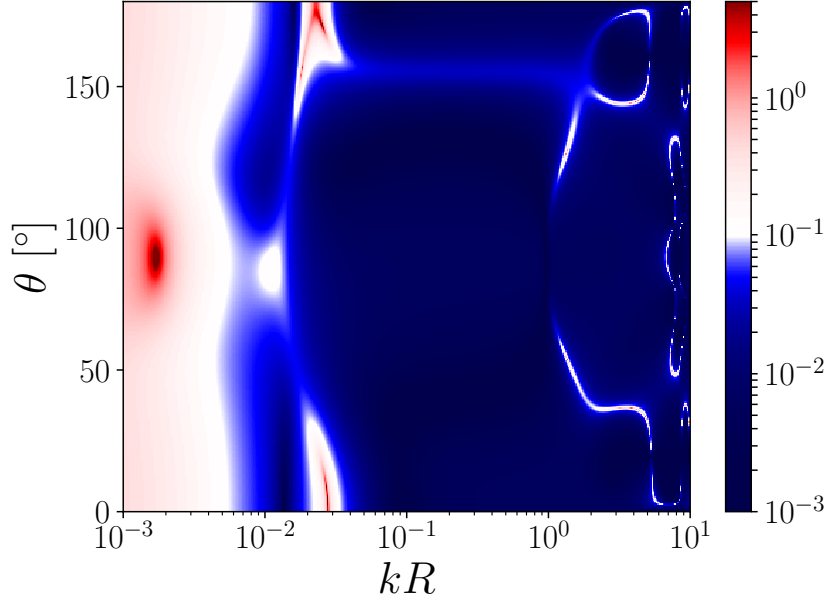


Figure 5.4: Ratio of terms  $|g_n^S|/|g_n^Q|$  in Eqs. (5.21)–(5.22) for a spherical mass of castor oil in a soft tissue-like medium ( $\mu = 100$  kPa) subject to a simple focused beam with confinement angle  $\theta_0 = 30^\circ$ . Small ratio is indicated with blue shading, large ratio with red shading.

What sphere materials may actually allow for this approximation? Consider castor oil, which has density  $950$  kg/m<sup>3</sup> and sound speed  $1540$  m/s, making it very acoustically similar to water and therefore, likewise, a surrounding soft tissue-like medium. A plot of the ratio  $|g_n^S|/|g_n^Q|$  for castor oil embedded in a soft tissue-like medium ( $\mu = 100$  kPa) is shown in Fig. 5.4. In the

case of castor oil, there appears to be a range  $0.05 \lesssim kR \lesssim 1$  where  $|g_n^S|$  is sufficiently small for all angles, which would allow for the approximation  $g_n \approx \partial Q / \partial x_n$ . However, it is necessary to consider the acoustic impedance of castor oil relative to the surrounding water-like medium:  $Z_{\text{oil}} = 1.463$  MRayl versus  $Z_{\text{water}} = 1.5$  MRayl. These values differ by only 2.5%, which makes castor oil a poor choice for a spherical scatterer whose displacement is to be measured in soft tissue. It would not only result in a minimal radiation force due to the weak scattering interaction, but would also be very difficult to image for the same reason.

While the approximation  $g_n \approx \partial Q / \partial x_n$  in Eq. (5.13) is tempting to explore due to the dramatic analytical simplification that would be possible, it does not appear to be valid for the types of scatterers that would be useful in practice. Therefore, it is necessary to pursue a numerical method of determining  $Q$  and the radiation force on the scatterer that results.

### 5.3 Numerical Solution for $G_z^P$

In this section, a numerical technique is used to perform a Helmholtz decomposition of the body force  $g_n$ . The choice is a least-squares finite element method (FEM) to find  $Q$  by minimizing the following energy functional:

$$F(Q) = \frac{1}{2} \int_T |\nabla Q - \mathbf{g}|^2 dV, \quad (5.23)$$

where  $T$  refers to the triangulation or the tetrahedralization (for two- or three-dimensional discretizations for axisymmetric or non-axisymmetric fields inci-

dent on the sphere, respectively) describing the domain. This method is described in detail for three-dimensional vector fields by Tong et al. [112] and for two-dimensional vector fields by Polthier and Preuß [130, 131]; the basics will be summarized here. Once the scalar potential  $Q$  is found, it must be integrated per Eq. (5.14) to find the force term  $G_n^P$ , completing the computation of the radiation force per Eq. (2.36).

### 5.3.1 Description of Numerical Helmholtz Decomposition

First, it is necessary to discretize the domain. Depending on whether the problem requires two dimensions or three dimensions, a triangulation and a tetrahedralization are used in two and three dimensions, respectively; both are given the label  $T$ . A given triangular or tetrahedral element with index  $j$  within the discretized domain is then given the label  $T_j$ . Two function spaces must then be defined. The first function space is a space of piecewise-linear potential fields and allows us to define a field  $\Phi(\mathbf{x})$  as

$$\Phi(\mathbf{x}) = \sum_i \phi_i(\mathbf{x})\Phi_i, \quad (5.24)$$

where  $\Phi_i$  is the value of the field at the node with index  $i$  (which is located at position  $\mathbf{x}_i$ ) and  $\phi_i(\mathbf{x})$  is a piecewise-linear shape function equal to unity at  $\mathbf{x}_i$  and equal to zero at every other node in the domain. The second function space is a space of piecewise-constant vector fields which allows for the definition of a vector field  $\Psi(\mathbf{x})$  as

$$\Psi(\mathbf{x}) = \sum_j \psi_j(\mathbf{x})\Psi_j, \quad (5.25)$$

where  $\Psi_j$  is the value of the field in a given tetrahedron or triangle  $T_j$  and  $\psi_j(\mathbf{x})$  is a basis function that is equal to unity inside  $T_j$  and equal to zero everywhere else. These two function spaces are necessary because the gradient of a potential defined in the first function space gives a vector field defined in the second function space [112].

Next, to find a piecewise-linear function  $Q$  such that  $\nabla Q$  is equal to the irrotational part of  $\mathbf{g}$ , it is necessary to minimize the following quadratic functional defined in Eq. (5.23) as first specified by Polthier and Preuß [131]. The integral is minimized if the quantity  $\partial F/\partial Q_i$  is equal to zero for each node  $i$ , which gives the following expressions:

$$\forall i, \quad \int_T \nabla \phi_i \cdot \nabla Q \, dV = \int_T \nabla \phi_i \cdot \mathbf{g} \, dV. \quad (5.26)$$

The solution of this system of linear equations then gives the value of  $Q$  at each node, which must be numerically integrated over the surface of the sphere to compute  $G_n^P$ .

An artificial two-dimensional field with a source at  $(-1/2, -3/4)$ , a sink at  $(-1/2, 0)$ , and two rotations centered at  $(-1/4, -1/2)$  and  $(1/2, 0)$  is shown in Fig. 5.5, and color plots are shown in Fig. 5.6 for the reference potential (used to synthesize the irrotational field) and the potential computed from numerical Helmholtz decomposition. The vector components due to the sources/sinks are specified by the relation

$$\mathbf{u}^l = -\nabla \Phi, \quad \Phi = \Phi_0 e^{-r^2}, \quad (5.27)$$

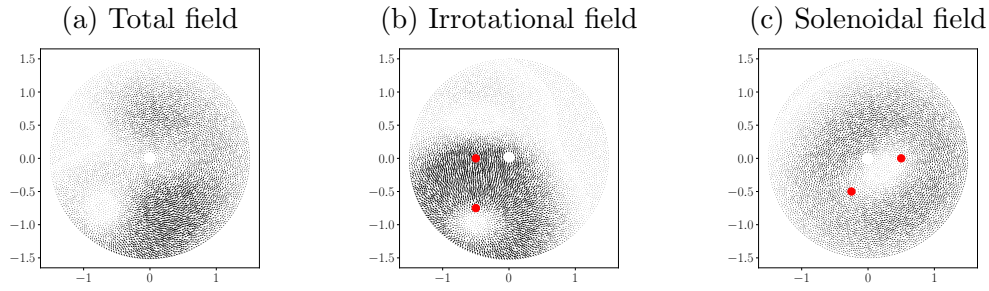


Figure 5.5: Synthesized test field comprised of irrotational and solenoidal parts. Red dots mark a source of strength 0.9 at  $(-1/2, -3/4)$ , a sink of strength 0.5 at  $(-1/2, 0)$ , and two rotations of strength 0.7 and 1 centered at  $(-1/4, -1/2)$  and  $(1/2, 0)$ , respectively. Note that the deviation between the red dots and *apparent* centers of source, sink, and rotation is due to their being spatially near each other and of different strengths.

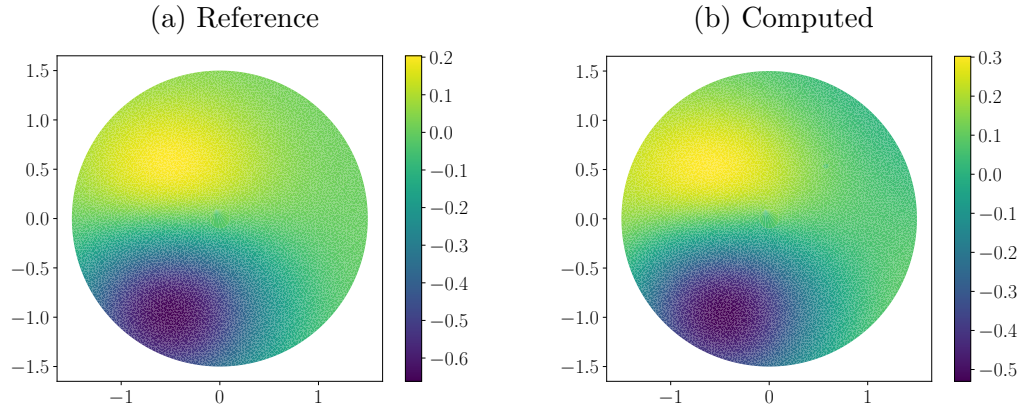


Figure 5.6: Irrotational potential for synthesized test field in Fig. 5.5 (left) and computed from numerical Helmholtz decomposition (right).

where  $\Phi_0$  is the strength of the source or sink (for positive or negative  $\Phi_0$ , respectively) and  $r$  denotes the distance from the source or sink. The rotations are specified by the relation

$$\mathbf{u}^t = A_0 e^{-r^2} (-y\mathbf{e}_x + x\mathbf{e}_y), \quad (5.28)$$

where  $A_0$  denotes the strength of the rotation and  $(x, y)$  denotes the coordinates of the field point relative to the rotation center. The recovered potential is nearly indistinguishable from the reference potential except for a small static offset, as can be seen by the different numbers on the color bar in Fig. 5.6. Although the offset may be larger depending on the field, this offset does not alter the integral of the potential  $Q$  per Eq. (5.14). That is, since  $x_n = z = R \cos \theta$  at the surface of integration and  $\cos \theta$  varies from  $-1$  to  $1$ , any static offset in  $Q$  cancels out in Eq. (5.14), and since computation of this integral is ultimately the goal of this technique, such an offset need not cause concern here.

Note that the hole at the center of the domain in Figs. 5.5 and 5.6 is included for this field because it is necessary for our particular problem. The shear body force  $g_n$  becomes infinite at the origin because it contains spherical Hankel functions that are proportional to  $1/r$  as  $r \rightarrow 0$ , so the domain must not include the origin. The choice to limit the domain in this way is further explained in Sec. 5.4.1.

### 5.3.2 Results for $G_z^P$

There are several important considerations for computing the force term  $G_z^P$  using the method described in Sec. 5.3.1. First, in order to properly resolve the field, a sufficiently fine mesh is necessary. Whereas the example in Figs. 5.5 and 5.6 only has a few slowly-varying features, the body force  $g_n$  due to shear wave fields is spatially oscillatory with a characteristic wavelength equal to that for shear waves in the medium. The mesh must therefore be chosen to

have a characteristic length of at most one tenth the shear wavelength in the medium, a guideline often used in acoustic scattering problems [132]. Second, since the incident field is purely compressional, the size of the scatterer relative to a compressional wavelength is important. For example, recall from Sec. 3.4 that a scatterer that is small compared to a compressional wavelength will cause much less scattering than a larger scatterer. Since the shear wave speed in soft tissue tends to be below 10 m/s compared with a compressional wave speed of 1500 m/s, the result is a characteristic length scale for the mesh that is much smaller than the overall domain. Therefore, the domain is chosen to extend only slightly inside and slightly outside the surface of the sphere (no more than a few shear wavelengths) so that the problem remains numerically tractable. (Section 5.4.1 includes more detail on this point.)

Radiation force results for various spheres embedded in soft tissue-like media due to a simple focused beam incident on the sphere ( $\theta_0 = 30^\circ$ ) are shown in Fig. 5.7. In all plots, solid lines represent  $F_z + G_z$ , whereas dashed lines represent  $F_z$  only. Again, the effect of shear modulus in the medium on  $F_z$  alone is not necessarily very large, but including  $G_z$  causes a substantial change in the force. For the steel sphere in Fig. 5.7(a),  $F_z$  has a significant effect for small scatterers by itself (due to the dipole scattering coefficient), but  $G_z$  amplifies this effect and increases the force on larger scatterers as well. Results for the aluminum sphere in Fig. 5.7(b) are similar. For the polystyrene sphere in Fig. 5.7(c), the change appears to be of the same order as the change due in  $F_z$  alone due to shear modulus. Finally, for the air bubble in Fig. 5.7(d), the

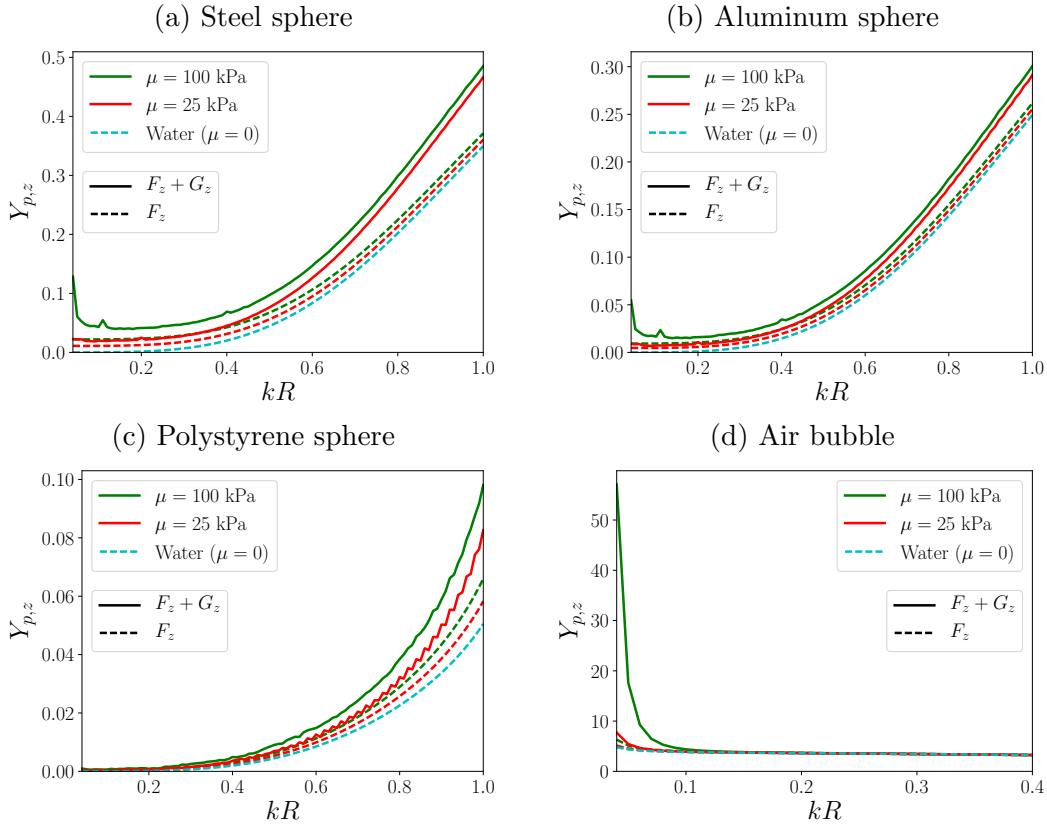


Figure 5.7: Acoustic radiation force function  $Y_{p,z}$  on various spheres embedded in soft tissue-like media due to a simple focused beam with confinement angle  $\theta_0 = 30^\circ$ . Solid lines indicate that both  $F_z$  and  $G_z$  force terms are included, whereas dashed lines show only  $F_z$ .

Minnaert resonance is again the most prominent effect, but it too is amplified by the addition of  $G_z$ .

Having computed  $G_z^P$ , which includes the effect of the potential  $Q$  in the body force  $g_n$ , we can now calculate the force  $F_z^{\text{total}} = F_z^B + F_z^P + G_z^B + G_z^P$  on the sphere, from which the displacement of the sphere in a given soft tissue-like medium can be predicted. However, there is another component of the body

force  $g_n$  that must be considered in order to calculate the true displacement of the sphere: the solenoidal term  $\nabla \times \mathbf{S}$ . The solenoidal term results in a bulk deformation of the medium, which results in an additional contribution to the sphere displacement beyond that due to the radiation force. The comparison of the displacement predicted from  $F_z^{\text{total}}$  and the true displacement of the sphere is the subject of the next section.

#### 5.4 Full Solution for $u_n^{(2)}$ with Finite Element Method

In this section, the full FEM solution for the nonlinear displacement component  $u_n^{(2)}$  is detailed. This is done to assess the accuracy of the predicted displacement due to the force  $F_z^{\text{total}}$  numerically computed in the previous section.

We begin with the full elastodynamic equation, which is obtained by combining Eqs. (2.3), (2.9), and (2.10). After some manipulation, first-order equations for the linear displacement  $u_n^{(1)}$  and the nonlinear displacement  $u_n^{(2)}$  can be written as

$$\rho_0 \frac{\partial^2 u_n^{(1)}}{\partial t^2} - \frac{\partial \sigma_{nm}^{(1)}}{\partial x_m} \Big|_{u_n^{(1)}} = 0, \quad (5.29)$$

$$\rho_0 \frac{\partial^2 u_n^{(2)}}{\partial t^2} - \frac{\partial \sigma_{nm}^{(1)}}{\partial x_m} \Big|_{u_n^{(2)}} = \frac{\partial \sigma_{nm}^{(2)}}{\partial x_m} \Big|_{u_n^{(1)}}. \quad (5.30)$$

The linear displacement field in Eq. (5.29) has already been found through Eqs. (2.19)–(2.20) and the associated potentials and scattered field coefficients. The result is then substituted into the right-hand side of Eq. (5.30), which

becomes, after some simplification,

$$\rho_0 \frac{\partial^2 u_n^{(2)}}{\partial t^2} - \mu \frac{\partial^2 u_n^{(2)}}{\partial x_m^2} - \left( K + \frac{\mu}{3} \right) \frac{\partial^2 u_m^{(2)}}{\partial x_n \partial x_m} = \left. \frac{\partial \sigma_{nm}^{(2)}}{\partial x_m} \right|_{u_n^{(1)}}. \quad (5.31)$$

Since  $u_n^{(1)}$  oscillates about zero with angular frequency  $\omega$ ,  $u_n^{(2)}$  is expected to be oscillatory, but with a nonzero time average. Therefore, time averaging Eq. (5.31) eliminates the time derivative and yields

$$-\mu \frac{\partial^2 U_n}{\partial x_m^2} - \left( K + \frac{\mu}{3} \right) \frac{\partial^2 U_m}{\partial x_n \partial x_m} = \frac{\partial \Sigma_{nm}}{\partial x_m}, \quad (5.32)$$

where

$$U_n = \langle u_n^{(2)} \rangle, \quad (5.33)$$

$$\Sigma_{nm} = \left\langle \frac{\partial \sigma_{nm}^{(2)}}{\partial x_m} \right\rangle. \quad (5.34)$$

Equation (5.32) represents an elastostatic equation that may then be solved via FEM.

#### 5.4.1 Weak Form and Simplifications

The problem represented by Eq. (5.32) is continuous, and once boundary conditions and forcing functions are specified, it is referred to as the differential “strong form” because it is satisfied everywhere within the domain of interest. However, since Eq. (5.32) is not known to have an exact analytic solution, especially considering the complexity of the right-hand side (to be described later in this subsection), it is useful to determine a corresponding integral “weak form” to proceed [133]. The “weak form” is so called because

Eq. (5.32) is no longer required to hold everywhere within the domain of interest; it is only satisfied in a weighted average manner.

We first form a dot product of Eq. (5.32) with the arbitrary vector test function  $W_n$  and integrate over the volume  $V$  of the domain to get

$$-\mu \int_V W_n \frac{\partial^2 U_n}{\partial x_m^2} dV - \left(K + \frac{\mu}{3}\right) \int_V W_n \frac{\partial^2 U_m}{\partial x_n \partial x_m} dV = \int_V W_n \frac{\partial \Sigma_{nm}}{\partial x_m} dV. \quad (5.35)$$

Next, we integrate by parts and use the divergence theorem to obtain, for the first integral on the left-hand side,

$$-\int_V W_n \frac{\partial^2 U_n}{\partial x_m^2} dV = -\int_S \frac{\partial U_n}{\partial x_m} W_n n_m dS + \int_V \frac{\partial U_n}{\partial x_m} \frac{\partial W_n}{\partial x_m} dV, \quad (5.36)$$

and, for the second integral on the left-hand side,

$$-\int_V W_n \frac{\partial^2 U_m}{\partial x_n \partial x_m} dV = -\int_S \frac{\partial U_m}{\partial x_m} W_n n_m dS + \int_V \frac{\partial U_m}{\partial x_m} \frac{\partial W_n}{\partial x_n} dV. \quad (5.37)$$

Finally, we note that for an infinite domain, the displacement  $U_n$  must tend toward zero. Therefore, assuming a sufficiently large domain, we set  $U_n = 0$  at the boundary, which necessarily requires  $W_n = 0$  as well. This allows us to eliminate the surface integrals above to obtain the following weak form:

$$\mu \int_V \frac{\partial U_n}{\partial x_m} \frac{\partial W_n}{\partial x_m} dV + \left(K + \frac{\mu}{3}\right) \int_V \frac{\partial U_m}{\partial x_m} \frac{\partial W_n}{\partial x_n} dV = \int_V W_n \frac{\partial \Sigma_{nm}}{\partial x_m} dV. \quad (5.38)$$

Note that this weak form is symmetric. That is, exchanging  $U_n$  and  $W_n$  with each other gives an equivalent relation. Therefore, after discretization, the result will be a symmetric matrix system, making the weak form especially well-suited to this problem.

While in principle the weak form in Eq. (5.38) may be solved numerically for any discretized domain, several simplifications are needed for the problem to be tractable in practice. First, for the same reason as in Sec. 5.3.2, we consider axisymmetric incident fields and restrict the problem again here to two dimensions. In spherical coordinates, the differential volume element is  $dV = r^2 \sin \theta d\phi d\theta dr$ , and for an axisymmetric problem with no  $\phi$ -dependence, we can integrate over  $\phi$  to obtain  $dV = 2\pi r^2 \sin \theta d\theta dr$ . The weak form is then

$$\mu \int_A \frac{\partial U_n}{\partial x_m} \frac{\partial W_n}{\partial x_m} x dA + \left( K + \frac{\mu}{3} \right) \int_A \frac{\partial U_m}{\partial x_m} \frac{\partial W_n}{\partial x_n} x dA = \int_A W_n \frac{\partial \Sigma_{nm}}{\partial x_m} x dA, \quad (5.39)$$

where  $x = r \sin \theta$  is the distance from the symmetry axis and  $dA = r dr d\theta$  is the differential area element. The weak form represented by Eq. (5.39) will ultimately be represented by a matrix equation when the domain is discretized, from which the sphere displacement—as well as the displacement at every other point in the discretized domain—will be determined.

Next, as in Sec. 5.3.2, a very fine mesh is needed to accurately discretize the body force  $g_n$  in the domain. However, where the problem could previously be restricted to a small region including the surface of the sphere, the same restriction is not possible when computing the full solution. A much larger domain is therefore required, which leads to an enormous number of nodes in the discretization. For example, consider a sphere of dimensionless size  $kR = 1$  embedded in a soft tissue-like medium with shear wave speed  $c_t = 10$  m/s, and consider a domain that extends only one compressional wavelength outside the sphere. In the axisymmetric case, for which the domain is a plane with a

semicircle as a boundary, such a problem contains approximately 6.3 million nodes. As is shown later in this section, a boundary at one compressional wavelength from the sphere is too close, affecting the computed displacement of the sphere; for a boundary at ten compressional wavelengths (which is still too close), the number of nodes increases to approximately 500 million, and for a boundary at 50 wavelengths (which appears to be sufficient for several of the cases treated later), the number of nodes increases to approximately 12 billion. Furthermore, as  $c_t = 10$  m/s is a reasonable upper bound for soft tissue, these values represent the best-case scenario; for lower, more typical shear wave speeds, the number of nodes increases even further. In addition to being challenging to solve numerically, this problem is even difficult to set up because the nonlinear body force represented by  $\langle g_n \rangle = \partial \Sigma_{nm} / \partial x_m$  is distributed continuously throughout the medium and must therefore be calculated at each one of the nodes.

For the above reasons, several approximations are required to reduce the computational burden. First, the shear wave speed in the medium is increased to 100 m/s. This choice allows for a coarser mesh while keeping the shear wave speed in the medium less than one tenth of the compressional wave speed, which still ensures that  $\mu/K \ll 1$  and is thus consistent with the approximations to the body force discussed in Sec. 2.1.1.

Second, the body force  $g_n$  due to shear wave fields is only computed over a limited portion of the domain. That is, for large enough  $kr$  outside the sphere,  $g_n$  is assumed to be negligible to the sphere displacement and is set to

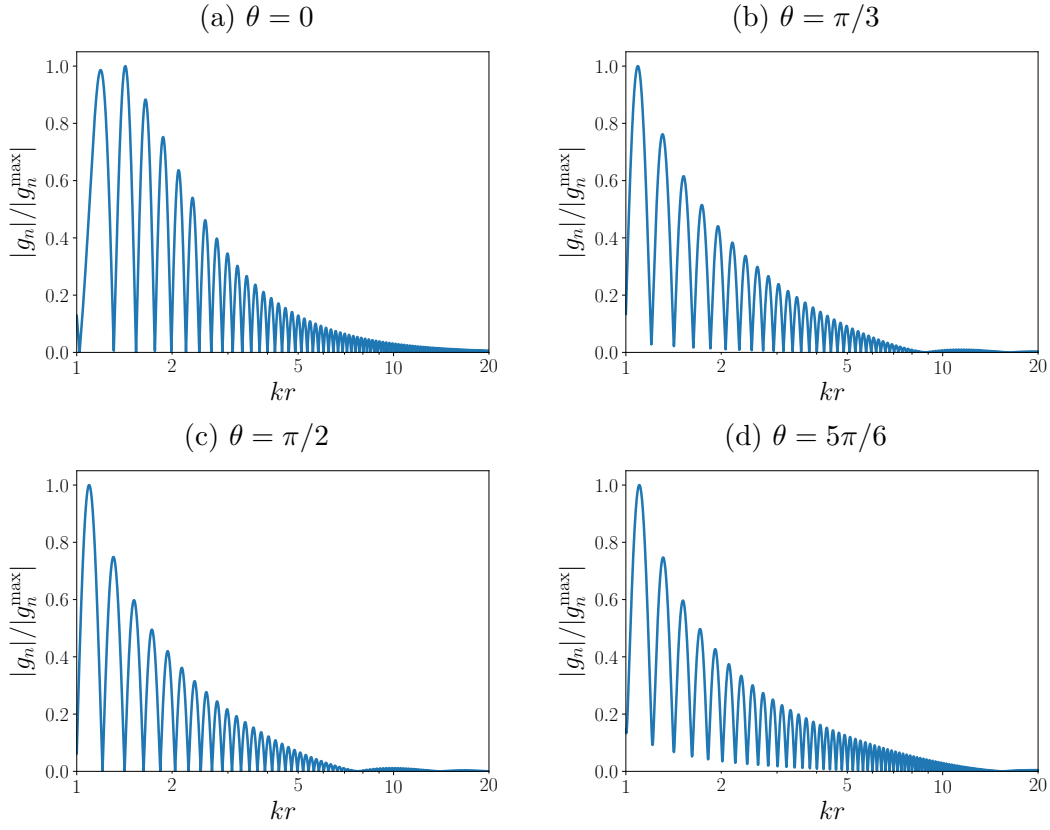


Figure 5.8: Plots of the body force  $g_n$  due to shear wave fields versus  $kr$  at various angles outside a steel scatterer ( $kR = 1$ ) in a soft tissue-like medium with shear wave speed  $c_t = 100$  m/s. The incident field is a simple focused beam with confinement angle  $\theta_0 = 30^\circ$ . Note the logarithmic  $x$ -axis so that oscillatory properties of  $g_n$  may be seen for  $kr$  just outside the sphere.

zero. For instance, Fig. 5.8 shows plots of  $g_n$  versus position  $kr$  outside a steel sphere ( $kR = 1$ ) at four different angles when the incident field is a simple focused beam ( $\theta_0 = 30^\circ$ ). The rapid decay in the magnitude of  $g_n$  suggests that  $g_n$  may be ignored for large enough values of  $kr$ , so we choose to compute it out to only  $kr \approx 20$ . Furthermore, since the effect of  $g_n$  on the sphere

displacement is separate from the effect of  $f_n$ , which is already captured by the full solution  $F_n$  for the radiation force due to compressional wave fields, we need only consider the magnitude of  $g_n$  relative to itself when determining what should be retained and what may be discarded.

Finally, for  $g_n$  defined only within a given source region as described in the previous paragraph, the displacement induced away from the source diminishes with distance from the source. As this distance becomes greater, effects due to rapid variations in  $g_n$  are expected to smooth out, resulting in less need for a very fine mesh outside the region in which  $g_n$  is computed. Therefore, we allow a smooth transition in the characteristic length of the mesh from one tenth of the shear wavelength to half of the shear wavelength at the edge of the domain.

#### 5.4.2 Displacement Results

We first consider how large the domain must be for the solution for the displacement of the sphere to converge. In Fig. 5.9, computed displacement is shown for a steel sphere ( $kR = 1$ ) embedded in a soft elastic medium with shear wave speed  $c_t = 100$  m/s subject to a simple focused beam ( $\theta_0 = 30^\circ$ ). Clearly, a domain that only includes one or two wavelengths outside the scatterer is not sufficient for the displacement to converge, indicating that the zero boundary condition at the edge of the domain is affecting the problem. It is not until approximately 40 wavelengths outside the scatterer that the computed displacement appears to level off. Given the approximations mentioned

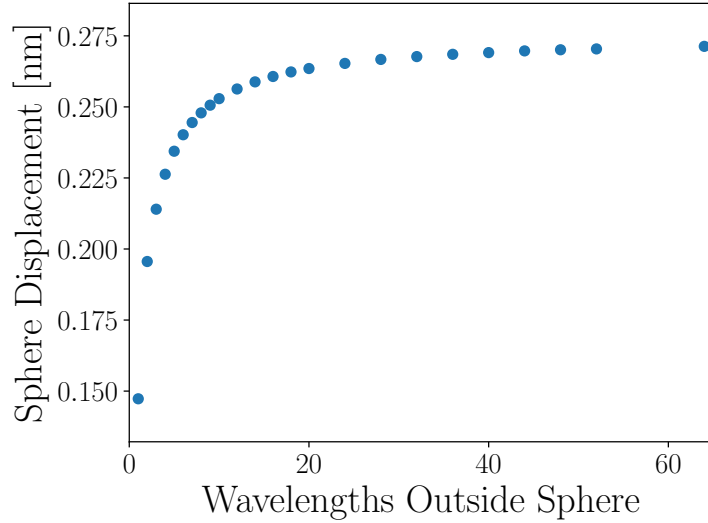


Figure 5.9: Displacement of a steel sphere ( $kR = 1$ ) versus domain size in a soft tissue-like medium with shear wave speed  $c_t = 100$  m/s. The incident field is a simple focused beam with confinement angle  $\theta_0 = 30^\circ$ .

at the end of Sec. 5.4.1, the number of nodes in the mesh when the domain extends 64 wavelengths outside the scatterer—the value ultimately chosen to ensure convergence—is approximately 8.3 million. As previously discussed, this number of nodes would increase massively for a soft elastic medium with  $c_t = 10$  m/s and a sufficiently fine mesh.

Finally, we compare the FEM computation for the displacement of the steel sphere with predictions from  $F_z$  given by Eq. (2.68) and from  $F_z + G_z$  given by the sum of Eqs. (2.68), (2.109), and (2.48). The sphere displacement  $d$  predicted from a static radiation force  $F$ —which is chosen to be either  $F_z$  or  $F_z + G_z$  depending on the comparison of interest—is calculated from the

relation [91]

$$d = \frac{F}{6\pi\mu R}. \quad (5.40)$$

This relation, which is comparable to the result due to Stokes for the velocity of a sphere in a viscous liquid, does not include the displacement expected due to the bulk deformation of the medium caused by the solenoidal component of  $g_n$ , so we expect discrepancies in the displacement computed from the full FEM computation and from  $F_z + G_z$  to reflect the significance of the curl term.

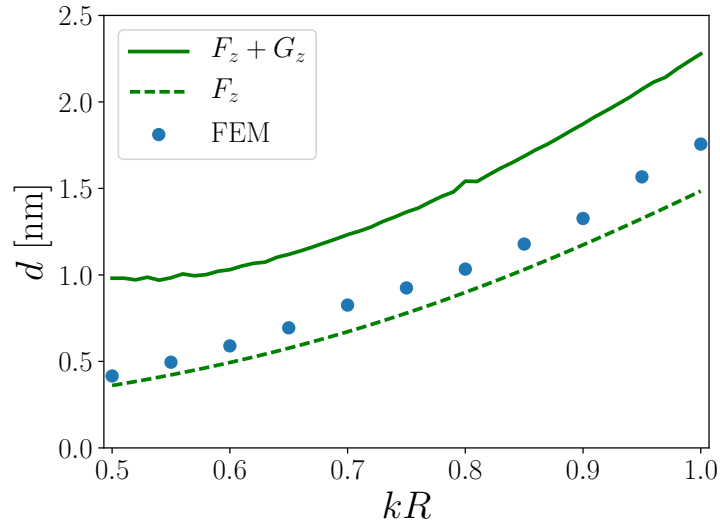


Figure 5.10: FEM calculation of the displacement (blue dots) of a steel sphere embedded in a soft tissue-like medium ( $c_t = 100$  m/s) due to the body force  $f_n + g_n$ . The incident field is a simple focused beam with confinement angle  $\theta_0 = 30^\circ$ .

Figure 5.10 shows the comparison of FEM computations for the displacement of a steel sphere versus corresponding predictions for  $F_z$  and  $F_z + G_z$ . The surrounding medium is again a soft elastic medium with  $c_t = 100$  m/s,

and the incident field is a simple focused beam ( $\theta_0 = 30^\circ$ ), with the sphere located at the focus. The displacement predicted from  $F_z + G_z$  as computed in Sec. 5.3.2 does not match the full FEM result, so it appears that the solenoidal component  $\nabla \times \mathbf{S}$  in  $g_n$  decreases the displacement relative to the expected value based on  $F_z + G_z$  (solid green curve). However, including  $g_n$  still increases the displacement from what would be expected from  $F_z$  alone. For instance, the displacement computed from FEM for a steel sphere of size  $kR = 1$  exceeds that predicted using  $F_z$  alone by approximately 20%, so even for larger scatterers where  $F_z$  is not too different for ideal fluid and soft tissue-like media, the radiation force in a fluid is not sufficient to predict the sphere displacement; shear effects must also be considered.

It is also important to note that due to the increase in the shear wave speed in the surrounding medium by an order of magnitude,  $g_n$  has been changed in such a way that might either increase or decrease the solenoidal component  $\nabla \times \mathbf{S}$  relative to the irrotational component  $\nabla Q$ . This may alter the effect of the curl term from what would occur in a tissue-like medium with more realistic parameters, but this cannot be conclusively determined without more computational power. At any rate, the sphere displacements predicted from  $F_z$  and  $F_z + G_z$  may be reasonably considered to bound the true displacement of the sphere.

## 5.5 Summary

Due to analytical and numerical challenges, the results presented in this chapter are necessarily less comprehensive than those presented in Chapter 4. Nonetheless, they serve as an important step toward further understanding of acoustic radiation force in a soft elastic medium.

The analysis presented in Sec. 5.1 for the radiation force due to the scattered compressional field does not appear to be applicable to the radiation force associated with the scattered shear wave, and the approximation  $g_n \approx \partial Q / \partial x_m$  presented in Sec. 5.2, while tempting, appears to be valid only for scatterers very acoustically similar to a surrounding soft tissue-like medium, which severely limits its effectiveness in practice. However, the numerical results for Helmholtz decomposition presented in Sec. 5.3, though currently limited in their application to axisymmetric fields and the  $z$ -direction of the radiation force  $F_z + G_z$ , correspond to a significant correction to the force even for larger scatterers. This is in contrast with the results in Chapter 4, where  $F_z$  appeared noticeably different for water and soft tissue-like media only for small scatterers (steel, aluminum, or polystyrene spheres) or frequencies near resonance (air bubbles). Finally, FEM results in Sec. 5.4 suggest that the solenoidal component  $\nabla \times \mathbf{S}$  in  $g_n$  may further alter the displacement of the sphere.

The main result of this chapter is that despite the large difference in bulk modulus and shear modulus in soft tissue-like media, effects due to the scattered shear wave must be considered for radiation force calculations to be

accurate. However, considerable work remains to be done in fully simulating the displacement of a sphere in an elastic medium with mechanical properties more representative of those in soft tissue.

## Chapter 6

### Conclusions and Future Work

The primary purpose of this dissertation was to improve the theoretical understanding of acoustic radiation force due to scattering from a sphere with arbitrary material properties embedded in a soft elastic medium. This phenomenon may have important applications in the assessment of soft tissue health, but since existing literature pertaining to radiation force on scatterers is limited to surrounding media comprised of fluid, whether ideal [1–10] or viscous [3, 11–16] or heat-conducting [14, 17–19], it is important to consider an extension of existing theory that applies to the more general case of soft elastic media surrounding the scatterer.

After a brief discussion in Chapter 1 of historical developments in acoustic radiation force and descriptions of several existing clinical applications of radiation force to soft tissue elastography, in Chapter 2 the fundamental equations of elastodynamics and the theoretical framework for acoustic radiation force on an elastic sphere in a soft elastic medium were derived. The choice of Lagrangian coordinates, instead of the more conventional Eulerian coordinates used for fluid media surrounding the scatterer, was found to facilitate the incorporation of elasticity without requiring a full solution for the nonlinear

portion of the displacement field. Several approximations were made to arrive at an analytically tractable problem. It was shown the force can be separated into contributions from the compressional wave field and the shear wave field, labeled  $F_n$  and  $G_n$ , respectively, to decouple these two contributions. To support this approach, it was demonstrated that the result for  $F_n$  in the limit of zero shear modulus in the surrounding medium recovers previously obtained results for a fluid surrounding the sphere [5–7, 10].

In Chapter 3, the incident and scattered wave fields were presented in greater mathematical detail. A three-dimensional angular spectrum description was used to find the incident field coefficients instead of the more traditional two-dimensional angular spectrum method [101] because it permits a convenient description of a focused sound beam in spherical coordinates. With radiation from a focused Gaussian source and a focused circular piston being presented as examples, it was also shown to be relatively straightforward to transform between one method and the other [102]. The Wigner D-matrix was then introduced to determine the radiation force in directions other than the propagation direction of the beam merely by transforming the incident field coefficients [113]. The scattered field coefficients were examined to better understand effects such as dipole scattering and shifts in resonance frequencies on the radiation force.

In Chapter 4, the radiation force due to the incident and scattered compressional waves alone acting on an elastic sphere in a soft elastic medium was presented in greater depth. The radiation force  $G_n$  in Eq. (2.100) due to the

scattered shear wave was ignored in this chapter because only the force  $F_n$  due to the scattered compressional wave is known analytically from Eqs. (2.67) and (2.68). Nonetheless, a variety of variables were examined to determine their effect on the radiation force: size, position, and mechanical properties of the spherical scatterer, and both elasticity and viscosity in the surrounding medium. The results suggest that small scatterers may be especially worth investigating due to their different behavior in liquid and in soft tissue-like media. For hard scatterers like steel or aluminum, small scatterers were observed to experience much greater axial radiation force in soft tissue-like media than in liquid. For soft scatterers like an air bubble, the shift in the Minnaert resonance frequency caused by the addition of shear stiffness to the surrounding medium was seen to correspond to dramatic changes in both magnitude and direction of the radiation force.

In Chapter 5, the radiation force  $G_n = G_n^B + G_n^P$  on a spherical scatterer due to the scattered shear wave was considered. From Eqs. (2.108) and (2.109) for nonaxisymmetric and axisymmetric incident fields, respectively, an analytical expression was obtained for  $G_n^B$ , the component of radiation force due to direct integration of the stress tensor  $\sigma_{nm}^{lt}$  over the surface of the sphere. However, since no analytical expression was found for  $G_n^P$ , the component of radiation force that arises from the reaction force in the medium due to the body force  $g_n = \partial\sigma_{nm}^{lt}/\partial x_m$ , several approximations were examined. The approximations were found not to be fruitful for problems of practical interest—one property relating  $F_n^B$  and  $F_n^P$  did not appear to be applicable to  $G_n^B$  and  $G_n^P$ ,

and it was found that the approximation  $g_n \approx \partial Q / \partial x_n$  might only apply for scatterers very acoustically similar to the surrounding soft tissue-like medium. Therefore, numerical methods were required to calculate the potential  $Q$  in the relation  $\mathbf{g} = \nabla Q + \nabla \times \mathbf{S}$ , which then permits calculation of  $G_n^P$ . Using these methods,  $G_z$  was computed and added to  $F_z$  to calculate the total radiation force on the scatterer, and it was found that  $G_z$  could contribute significantly to the radiation force even for larger scatterers. While  $F_z + G_z$  includes both the direct integration of the stress tensor over the surface of the sphere and the irrotational potentials  $P$  and  $Q$  corresponding to the reaction force in the medium, it was also necessary to determine the additional static displacement of the surrounding medium due to the solenoidal component  $\nabla \times \mathbf{S}$  in  $g_n$ . The obtained FEM results suggest that this solenoidal component may further alter the displacement of the sphere, somewhat counteracting  $G_z$  for the particular set of parameters considered in Sec. 5.4 but still resulting in a significant deviation from  $F_z$  alone (approximately 20% for  $kR = 1$ ).

There are several questions that warrant further investigation in order to better apply the analysis presented in this dissertation. The first avenue for further inquiry is experimental in nature. Several groups have had some success determining the shear stiffness of gel phantoms and *ex vivo* tissues by examining the transient displacement of an embedded spherical scatterer in response to acoustic radiation force [89, 90, 92, 93], but as described in this dissertation, the actual radiation force from a given time-harmonic incident field is still difficult to ascertain analytically. It would be especially useful to

examine the radiation force on spherical scatterers with a variety of different sizes and elastic properties in actual gel phantoms to test some of the predictions made in Chapters 4 and 5, especially those relating to resonance shifts and direction reversals of the radiation force.

The second, and likely more challenging, avenue for further inquiry is numerical in nature. Numerical calculation of the effect of the scattered shear wave field was necessarily simplified in this work. As described in Chapter 5, the enormous difference in characteristic length scales for compressional waves (around 1500 m/s) and shear waves (up to 10 m/s) in soft tissue presents significant numerical challenges because of how finely the domain must be discretized to accurately capture effects due to the shear wave. Therefore, numerical calculations of both the radiation force on the sphere and the resulting static displacement of the sphere were restricted to the special case of axisymmetric incident fields, which allowed the problem to be formulated in two dimensions instead of three. The shear wave speed was also increased by a factor of ten from the approximate upper limit found in soft tissue in order to make discretization more tractable. However, it is necessary to determine whether the computations in Chapter 5 for the sphere displacement in a medium with increased shear wave speed are indicative of similar effects for the lower shear wave speeds corresponding to actual soft tissue. It is also necessary to determine whether the effects suggested by the observations in Chapter 4 such as resonance shifts and direction reversals of the force when the sphere is moved off the axis of a focused beam might still apply when the

full effect of the scattered shear wave is included. A sufficiently large domain with physical properties representative of actual soft tissue might contain billions of nodes even for the two-dimensional axisymmetric formulation of the problem, so much more powerful computational infrastructure will be required to address this problem further.

## Appendices

# Appendix A

## Mathematical Conventions

For simplification due to symmetry, the target scatterer in the liquid or tissue medium is assumed to be a sphere. Much of the analysis is therefore performed in spherical coordinates. Cartesian coordinates  $(x, y, z)$  are expressed through spherical coordinates  $(r, \theta, \phi)$  via the transformations

$$\begin{aligned}x &= r \sin \theta \cos \phi, \\y &= r \sin \theta \sin \phi, \\z &= r \cos \theta,\end{aligned}\tag{A.1}$$

where  $r$  represents the radial distance,  $\theta$  the polar angle, and  $\phi$  the azimuthal angle. The Cartesian differentials are expressed as

$$\begin{aligned}dx &= \sin \theta \cos \phi dr + r \cos \theta \cos \phi d\theta - r \sin \theta \sin \phi d\phi, \\dy &= \sin \theta \sin \phi dr + r \cos \theta \sin \phi d\theta + r \sin \theta \cos \phi d\phi, \\dz &= \cos \theta dr - r \sin \theta d\theta,\end{aligned}\tag{A.2}$$

and the spherical differentials are written as

$$\begin{aligned}dr &= \sin \theta \cos \phi dx + \sin \theta \sin \phi dy + \cos \theta dz, \\r d\theta &= \cos \theta \cos \phi dx + \cos \theta \sin \phi dy - \sin \theta dz, \\r \sin \theta d\phi &= -\sin \phi dx + \cos \phi dy.\end{aligned}\tag{A.3}$$

In spherical coordinates, the differential area element on a spherical surface is  $dS = R^2 \sin \theta d\theta d\phi$  and the different volume element is  $dV = dR dS$ . The

derivative  $\partial/\partial z$  is also important for the computation of  $F_z$ , and it can be calculated from Eqs. (A.1)–(A.3):

$$\frac{\partial}{\partial z} = \cos\theta \frac{\partial}{\partial r} - \frac{\sin\theta}{r} \frac{\partial}{\partial\theta}. \quad (\text{A.4})$$

Descriptions of vectors and differential operators are also needed in spherical coordinates. A vector  $\mathbf{A}$  can be represented in spherical coordinates as

$$\mathbf{A} = A_r(r, \theta, \phi)\mathbf{e}_r + A_\theta(r, \theta, \phi)\mathbf{e}_\theta + A_\phi(r, \theta, \phi)\mathbf{e}_\phi, \quad (\text{A.5})$$

and a scalar function  $\psi$  is simply written as

$$\psi = \psi(r, \theta, \phi). \quad (\text{A.6})$$

The gradient, divergence, curl, scalar Laplacian, and vector Laplacian are written as

$$\nabla\psi = \frac{\partial\psi}{\partial r}\mathbf{e}_r + \frac{1}{r}\frac{\partial\psi}{\partial\theta}\mathbf{e}_\theta + \frac{1}{r\sin\theta}\frac{\partial\psi}{\partial\phi}\mathbf{e}_\phi, \quad (\text{A.7})$$

$$\nabla \cdot \mathbf{A} = \frac{1}{r^2}\frac{\partial}{\partial r}(r^2 A_r) + \frac{1}{r\sin\theta}\frac{\partial}{\partial\theta}(\sin\theta A_\theta) + \frac{1}{r\sin\theta}\frac{\partial A_\phi}{\partial\phi}, \quad (\text{A.8})$$

$$\begin{aligned} \nabla \times \mathbf{A} &= \frac{1}{r\sin\theta} \left[ \frac{\partial(\sin\theta A_\phi)}{\partial\theta} - \frac{\partial A_\theta}{\partial\phi} \right] \mathbf{e}_r \\ &+ \left[ \frac{1}{r\sin\theta}\frac{\partial A_r}{\partial\phi} - \frac{1}{r}\frac{\partial(r A_\phi)}{\partial r} \right] \mathbf{e}_\theta \\ &+ \left[ \frac{1}{r}\frac{\partial(r A_\theta)}{\partial r} - \frac{1}{r}\frac{\partial A_r}{\partial\theta} \right] \mathbf{e}_\phi, \end{aligned} \quad (\text{A.9})$$

$$\nabla^2\psi = \frac{1}{r^2}\frac{\partial}{\partial r}\left(r^2\frac{\partial\psi}{\partial r}\right) + \frac{1}{r^2\sin\theta}\frac{\partial}{\partial\theta}\left(\sin\theta\frac{\partial\psi}{\partial\theta}\right) + \frac{1}{r^2\sin^2\theta}\frac{\partial^2\psi}{\partial\phi^2}, \quad (\text{A.10})$$

$$\nabla^2\mathbf{A} = \nabla(\nabla \cdot \mathbf{A}) - \nabla \times (\nabla \times \mathbf{A}). \quad (\text{A.11})$$

It is often convenient to use Einstein notation (i.e., the summation convention) to express vector equations more compactly. In this scheme, a repeated index in a term indicates summation over all values of the index. In Cartesian coordinates, common vector operations are expressed as follows:

$$\mathbf{u} \cdot \mathbf{v} = u_1v_1 + u_2v_2 + u_3v_3 = \sum_{i=1}^3 u_iv_i \equiv u_iv_i, \quad (\text{A.12})$$

$$\nabla \cdot \mathbf{u} = \frac{\partial u_1}{\partial x_1} + \frac{\partial u_2}{\partial x_2} + \frac{\partial u_3}{\partial x_3} = \sum_{i=1}^3 \frac{\partial u_i}{\partial x_i} \equiv \frac{\partial u_i}{\partial x_i}, \quad (\text{A.13})$$

$$\begin{aligned} \mathbf{u} \times \mathbf{v} &= (u_2v_3 - u_3v_2)\mathbf{e}_1 - (u_1v_3 - u_3v_1)\mathbf{e}_2 + (u_1v_2 - u_2v_1)\mathbf{e}_3 \\ &= \sum_{j=1}^3 \sum_{k=1}^3 u_jv_k \epsilon_{ijk} \mathbf{e}_i \equiv u_jv_k \epsilon_{ijk} \mathbf{e}_i, \end{aligned} \quad (\text{A.14})$$

$$\begin{aligned} \nabla \times \mathbf{u} &= \left( \frac{\partial u_2}{\partial x_3} - \frac{\partial u_3}{\partial x_2} \right) \mathbf{e}_1 - \left( \frac{\partial u_1}{\partial x_3} - \frac{\partial u_3}{\partial x_1} \right) \mathbf{e}_2 + \left( \frac{\partial u_1}{\partial x_2} - \frac{\partial u_2}{\partial x_1} \right) \mathbf{e}_3 \\ &= \sum_{j=1}^3 \sum_{k=1}^3 \frac{\partial u_j}{\partial x_k} \epsilon_{ijk} \mathbf{e}_i \equiv \frac{\partial u_j}{\partial x_k} \epsilon_{ijk} \mathbf{e}_i, \end{aligned} \quad (\text{A.15})$$

where  $\delta_{il}$  is the Kronecker delta, equal to 1 for  $i = l$  and zero otherwise, and  $\epsilon_{ijk}$  is the Levi-Civita symbol, equal to 1 if  $(i, j, k)$  is an even permutation of  $(1, 2, 3)$ , equal to  $-1$  if  $(i, j, k)$  is an odd permutation of  $(1, 2, 3)$ , and equal to zero if an index is repeated. These compact relations are especially useful in equations for elastodynamics, which can otherwise appear unwieldy if the summation symbol is retained.

## Appendix B

### Acoustic Radiation Force Integrals

#### B.1 Radiation Force Due to Compressional Wave Fields

Recall, from Eq. (2.63),

$$F_z^B = \frac{Kk^2}{4R} \int_S \left[ \psi^* \frac{\partial}{\partial z} \left( r \frac{\partial \psi}{\partial r} - \psi \right) \right] dS + \text{c.c.} \quad (\text{B.1})$$

For compactness, define

$$L_n(kr) = j_n(kr) + A_n h_n(kr). \quad (\text{B.2})$$

Substitution into Eq. (B.1) and rewriting  $\partial/\partial z$  in terms of spherical coordinates from Eq. (A.4) yields

$$F_z^B = \frac{Kk^2}{4} \sum_{n,n',m} a_n^{m*} a_{n'}^m \left[ I_{n,n',m}^{(1)} + I_{n,n',m}^{(2)} \right] + \text{c.c.}, \quad (\text{B.3})$$

where  $I_{n,n',m}^{(1)}$  and  $I_{n,n',m}^{(2)}$  are written as

$$I_{n,n',m}^{(1)} = \frac{1}{R} \int_S L_n^*(kr) \frac{\partial}{\partial r} \left[ r \frac{\partial L_{n'}(kr)}{\partial r} - L_{n'}(kr) \right] \times P_n^m(\cos \theta) P_{n'}^m(\cos \theta) \cos \theta dS, \quad (\text{B.4})$$

$$I_{n,n',m}^{(2)} = \frac{1}{R^2} \int_S L_n^*(kr) \frac{\partial}{\partial r} \left[ r \frac{\partial L_{n'}(kr)}{\partial r} - L_{n'}(kr) \right] \times P_n^m(\cos \theta) \frac{dP_{n'}^m(\cos \theta)}{d(\cos \theta)} \sin^2 \theta dS. \quad (\text{B.5})$$

The rest of the process used to determine  $F_z^B$  is cumbersome and will only be summarized here. A function  $F_{n'}(kr)$  is introduced to be equal to the term in square brackets in Eqs. (B.4) and (B.5), and a function  $G_{n'}(kr) = r\partial[F_{n'}(kr)]/\partial r$  is defined for further compactness. Recurrence relations [134] are then used to calculate the derivative  $P'_{n'}(\cos\theta)$ , after which orthogonality of Legendre polynomials is employed to obtain simplified expressions for  $I_{n,n',m}$ . It is found that  $I_{n,n',m} = I_{n,n',m}^{(1)} + I_{n,n',m}^{(2)} \neq 0$  only for  $n' = n \pm 1$ , where

$$I_{n,n+1,m} = \frac{4\pi(n+m+1)(n+m)!}{(2n+1)(2n+3)(n-m)!} L_n^*(kR) [G_{n+1}(kR) + (n+2)F_{n+1}(kR)] , \quad (\text{B.6})$$

$$I_{n,n-1,m} = \frac{4\pi(n-m)(n+m)!}{(2n-1)(2n+1)(n-m)!} L_n^*(kR) [G_{n-1}(kR) - (n-1)F_{n-1}(kR)] . \quad (\text{B.7})$$

Now define a two-index version of  $L_n$ :

$$\begin{aligned} L_{n'}^{(n)}(kR) &= j_{n'}(kR) + A_n h_{n'}(kR) , \\ L_{n'}^{(n)*}(kR) &= j_{n'}^*(kR) + A_n^* h_{n'}^*(kR) . \end{aligned} \quad (\text{B.8})$$

Then, the expressions can be substituted into Eq. (B.3) and reorganized as

$$F_z^B = Kk^2 \sum_{n=0}^N \sum_{m=-n}^n (I_{n,n+1,m} + I_{n+1,n,m}^*) (a_n^m)^* a_{n+1}^m + \text{c.c.} , \quad (\text{B.9})$$

where

$$\begin{aligned} I_{n,n+1,m} &= \frac{(n+m+1)(n+m)!}{(2n+1)^2(2n+3)(n-m)!} (kR)^2 L_n^{(n)*}(kR) \\ &\quad \times \left[ n L_{n-1}^{(n+1)}(kR) - (n+1) L_{n+1}^{(n+1)}(kR) \right] , \end{aligned} \quad (\text{B.10})$$

$$\begin{aligned} I_{n+1,n,m}^* &= - \frac{(n+m+1)(n+m)!}{(2n+1)(2n+3)^2(n-m)!} (kR)^2 L_{n+1}^{(n+1)}(kR) \\ &\quad \times \left[ (n+1) L_n^{(n)*}(kR) - (n+2) L_{n+2}^{(n)*}(kR) \right] . \end{aligned} \quad (\text{B.11})$$

Next, from Eq. (2.66),

$$F_z^P = -\frac{Kk^2}{4} \int_S \left[ \frac{\partial \psi^*}{\partial x_m} \frac{\partial \psi}{\partial x_m} - k^2 \psi^* \psi \right] \cos \theta \, dS. \quad (\text{B.12})$$

Substitution of Eq. (B.2) gives

$$F_z^P = -\frac{Kk^2}{4} \sum_{n,n',m} a_n^{m*} a_{n'}^m I_{n,n',m}^P, \quad (\text{B.13})$$

where

$$\begin{aligned} I_{n,n',m}^P &= \int_S \nabla [L_n^*(kr) P_n^m(\cos \theta) e^{-im\phi}] \cdot \nabla [L_{n'}(kr) P_{n'}^m(\cos \theta) e^{im\phi}] \cos \theta \, dS \\ &\quad - k^2 \int_S L_n^*(kr) L_{n'}(kr) P_n^m(\cos \theta) P_{n'}^m(\cos \theta) \cos \theta \, dS. \end{aligned} \quad (\text{B.14})$$

Again, the rest of the process is laborious, so it will be summarized here. We proceed with a gradient formula [135],

$$\begin{aligned} \mathbf{\Gamma} \equiv \nabla [f(r) Y_{nm}(\theta, \phi)] &= -\sqrt{\frac{n+1}{2n+1}} \left( \frac{df}{dr} - n \frac{f}{r} \right) \mathbf{T}_{nm}^{n+1} \\ &\quad + \sqrt{\frac{n}{2n+1}} \left[ \frac{df}{dr} + (n+1) \frac{f}{r} \right] \mathbf{T}_{nm}^{n-1}, \end{aligned} \quad (\text{B.15})$$

where  $\mathbf{T}_{nm}^l$  are vector spherical harmonics [114]. We can then find the scalar product of vector spherical harmonics in terms of Wigner  $6j$  symbols and Clebsch-Gordan coefficients [114]. Finally, substitution of recurrence relations for spherical Bessel functions [134], use of orthogonality relations, and use of

the two-index notation for  $L_n$  lead to

$$\begin{aligned}
I_{n,n+1,m}^P &= \frac{4\pi(n+m+1)(n+m)!}{(2n+1)^2(2n+3)^2(n-m)!} (kR)^2 \\
&\times \left[ (2n+1)(n+2)L_{n+1}^{(n)*}(kR)L_{n+2}^{(n+1)}(kR) \right. \\
&\quad - L_{n+1}^{(n)*}(kR)L_n^{(n+1)}(kR) \\
&\quad + n(2n+3)L_{n-1}^{(n)*}(kR)L_n^{(n+1)}(kR) \\
&\quad \left. - (2n+1)(2n+3)L_n^{(n)*}(kR)L_{n+1}^{(n+1)}(kR) \right]. \quad (\text{B.16})
\end{aligned}$$

Note that  $I_{n,n-1,m}$  is also nonzero, but it is omitted here because it can be expressed through recurrence relations as  $(I_{n,n+1,m}^P)^*$ , which allows for

$$F_z^P = -Kk^2 \sum_{n=0}^N \sum_{m=-n}^n I_{n,n+1,m}^P (a_n^m)^* a_{n+1}^m + \text{c.c.} . \quad (\text{B.17})$$

Now that  $F_z^B$  and  $F_z^P$  have been obtained separately, they can be added together to produce  $F_z$ . Adding Eqs. (B.9) and (B.17) and subsequently manipulating them produces

$$\begin{aligned}
F_z &= i\pi Kk^2 \sum_{n=0}^N \sum_{m=-n}^n \frac{(n+m+1)(n+m)!}{(2n+1)(2n+3)(n-m)!} \\
&\quad \times (A_n^* + A_{n+1} + 2A_n^* A_{n+1}) (a_n^m)^* a_{n+1}^m + \text{c.c.} , \quad (\text{B.18})
\end{aligned}$$

which is the same as Eq. (2.67).

## B.2 Radiation Force Associated with the Scattered Shear Wave

From Eq. (2.104), recall

$$G_z^B = \frac{Kk^2}{4R} \int_S \left[ \psi^* \left( \frac{\partial}{\partial z} (r\tilde{u}_r) - \tilde{u}_z \right) \right] dS + \text{c.c.} . \quad (\text{B.19})$$

Then, from Eq. (A.4) for  $\partial/\partial z$  and Eqs. (3.98)–(3.100) for a given  $\tilde{u}_n^m$ , obtain

$$\begin{aligned} \frac{\partial(r\tilde{u}_{n,r}^m)}{\partial z} - \tilde{u}_{n,z}^m &= \frac{\kappa}{2n+1} [(n+m)(n^2-1)h_{n-1}(\kappa r)P_{n-1}^m(\cos\theta) \\ &\quad - n(n+2)(n-m+1)h_{n+1}(\kappa r)P_{n+1}^m(\cos\theta)] a_n^m B_n e^{im\phi}. \end{aligned} \quad (\text{B.20})$$

Substitution of Eq. (B.20) into the integrand of Eq. (B.19) gives

$$G_z^B = \frac{\pi K k^2}{2R} \int_S \sum_{n,n'} J_{n,n',m} dS + \text{c.c.}, \quad (\text{B.21})$$

where

$$\begin{aligned} J_{n,n',m} &= \frac{\kappa}{2n'+1} (a_n^m)^* a_{n'}^m L_n^*(kR) B_{n'} P_n^m(\cos\theta) \\ &\quad \times [(n'+m)(n'^2-1)h_{n'-1}(\kappa R)P_{n'-1}^m(\cos\theta) \\ &\quad - n'(n'+2)(n'-m+1)h_{n'+1}(\kappa R)P_{n'+1}^m(\cos\theta)]. \end{aligned} \quad (\text{B.22})$$

Note that  $e^{i(m-m')\phi}$  is not included because integration over  $\phi$  requires that  $m' = m$ . From orthogonality of Legendre polynomials, integration over  $\theta$  eliminates all terms but  $n' = n \pm 1$ , resulting in

$$\begin{aligned} \int_0^\pi \sum_{n,n'} J_{n,n+1,m} \cos\theta d\theta &= \sum_{n=1}^N \frac{2\kappa n(n+2)(n+m+1)!}{(2n+3)(2n+1)(n-m)!} \\ &\quad \times [(a_n^m)^* a_{n+1}^m L_n^*(kR) B_{n+1} h_n(\kappa R) \\ &\quad - (a_{n+1}^m)^* a_n^m L_{n+1}^*(kR) B_n h_{n+1}(\kappa R)]. \end{aligned} \quad (\text{B.23})$$

Finally, we recover Eq. (2.108) and obtain

$$\begin{aligned} G_z^B &= \pi K k^2 (\kappa R) \sum_{n=0}^N \frac{n(n+2)}{(2n+1)(2n+3)} \sum_{m=-n}^n \frac{(n+m+1)!}{(n-m)!} \\ &\quad \times \{ a_n^{m*} a_{n+1}^m B_{n+1} [j_n^*(kR) + A_n^* h_n^*(kR)] h_n(\kappa R) \\ &\quad - a_{n+1}^{m*} a_n^m B_n [j_{n+1}^*(kR) + A_{n+1}^* h_{n+1}^*(kR)] h_{n+1}(\kappa R) \} + \text{c.c.} \end{aligned} \quad (\text{B.24})$$

## Bibliography

- [1] L. V. King, “On the acoustic radiation pressure on spheres,” *Proc. R. Soc. Lond. A*, vol. 147, no. 861, pp. 212–240, 1934.
- [2] P. J. Westervelt, “The theory of steady forces caused by sound waves,” *J. Acoust. Soc. Am.*, vol. 23, no. 4, pp. 312–315, 1951.
- [3] P. J. Westervelt, “Acoustic radiation pressure,” *J. Acoust. Soc. Am.*, vol. 29, no. 1, pp. 26–29, 1957.
- [4] K. Yosioka and Y. Kawasima, “Acoustic radiation pressure on a compressible sphere,” *Acustica*, vol. 5, no. 3, pp. 167–173, 1955.
- [5] T. Hasegawa and K. Yosioka, “Acoustic radiation force on a solid elastic sphere,” *J. Acoust. Soc. Am.*, vol. 46, no. 5, pp. 1139–1143, 1969.
- [6] T. Hasegawa and K. Yosioka, “Acoustic radiation force on fused silica spheres, and intensity determination,” *J. Acoust. Soc. Am.*, vol. 58, no. 3, pp. 581–585, 1975.
- [7] L. P. Gor’kov, “On the forces acting on a small particle in an acoustical field in an ideal fluid,” *Sov. Phys. Doklady*, vol. 6, no. 9, pp. 773–775, 1962.

- [8] C. P. Lee and T. G. Wang, “Acoustic radiation force on a bubble,” *J. Acoust. Soc. Am.*, vol. 93, no. 3, pp. 1637–1640, 1993.
- [9] C. P. Lee and T. G. Wang, “Acoustic radiation pressure,” *J. Acoust. Soc. Am.*, vol. 94, no. 2, pp. 1099–1109, 1993.
- [10] O. A. Sapozhnikov and M. R. Bailey, “Radiation force of an arbitrary acoustic beam on an elastic sphere in a fluid,” *J. Acoust. Soc. Am.*, vol. 133, no. 2, pp. 661–676, 2013.
- [11] A. A. Doinikov, “Acoustic radiation pressure on a compressible sphere in a viscous fluid,” *J. Fluid. Mech.*, vol. 267, pp. 1–22, 1994.
- [12] A. A. Doinikov, “Acoustic radiation pressure on a rigid sphere in a viscous fluid,” *Proc. R. Soc. Lond. A*, vol. 447, no. 1931, pp. 447–466, 1994.
- [13] A. A. Doinikov, “Radiation force due to a spherical sound field on a rigid sphere in a viscous fluid,” *J. Acoust. Soc. Am.*, vol. 96, no. 5, pp. 3100–3105, 1994.
- [14] A. A. Doinikov, “Theory of acoustic radiation pressure for actual fluids,” *Phys. Rev. E*, vol. 54, no. 6, pp. 6297–6303, 1996.
- [15] S. D. Danilov and M. A. Mironov, “Mean force on a small sphere in a sound field in a viscous fluid,” *J. Acoust. Soc. Am.*, vol. 107, no. 1, pp. 143–153, 2000.

- [16] M. Settnes and H. Bruus, “Forces acting on a small particle in an acoustical field in a viscous fluid,” *Phys. Rev. E*, vol. 85, no. 1, pp. 016327:1–12, 2012.
- [17] A. A. Doinikov, “Acoustic radiation force on a spherical particle in a viscous heat-conducting fluid. I. General formula,” *J. Acoust. Soc. Am.*, vol. 101, no. 2, pp. 713–721, 1997.
- [18] A. A. Doinikov, “Acoustic radiation force on a spherical particle in a viscous heat-conducting fluid. II. Force on a rigid sphere,” *J. Acoust. Soc. Am.*, vol. 101, no. 2, pp. 722–730, 1997.
- [19] A. A. Doinikov, “Acoustic radiation force on a spherical particle in a viscous heat-conducting fluid. III. Force on a liquid drop,” *J. Acoust. Soc. Am.*, vol. 101, no. 2, pp. 731–740, 1997.
- [20] Yu. A. Ilinskii, E. A. Zabolotskaya, B. C. Treweek, and M. F. Hamilton, “Acoustic radiation force on an elastic sphere in a soft elastic medium,” *J. Acoust. Soc. Am.*, vol. 144, no. 2, pp. 568–576, 2018.
- [21] S. Catheline, J.-L. Gennisson, and M. Fink, “Measurement of elastic nonlinearity of soft solid with transient elastography,” *J. Acoust. Soc. Am.*, vol. 114, no. 6, pp. 3087–3091, 2003.
- [22] J. Ophir, S. K. Alam, B. S. Garra, F. Kallel, E. E. Konofagou, T. Krouskop, C. R. B. Merritt, R. Righetti, R. Souchon, S. Srinivasan, and T. Vargh-

- ese, “Elastography: imaging the elastic properties of soft tissues with ultrasound,” *J. Med. Ultrasonics*, vol. 29, pp. 155–171, 2002.
- [23] A. P. Sarvazyan, O. V. Rudenko, S. D. Swanson, J. B. Fowlkes, and S. Y. Emelianov, “Shear wave elasticity imaging: A new ultrasonic technology of medical diagnostics,” *Ultrasound Med. Biol.*, vol. 24, no. 9, pp. 1419–1435, 1998.
- [24] K. R. Nightingale, M. S. Soo, R. W. Nightingale, and G. E. Trahey, “Acoustic radiation force impulse imaging: In vivo demonstration of clinical feasibility,” *Ultrasound Med. Biol.*, vol. 28, no. 2, pp. 227–235, 2002.
- [25] J. Bercoff, M. Tanter, and M. Fink, “Supersonic shear imaging: A new technique for soft tissue elasticity mapping,” *IEEE Trans. Ultrason. Ferroelectr. Freq. Control*, vol. 51, no. 4, pp. 396–409, 2004.
- [26] T. Heidarzadeh, *A History of Physical Theories of Comets, from Aristotle to Whipple*. Netherlands: Springer, pp. 159–164, 2008.
- [27] R. T. Beyer, “Radiation pressure—the history of a mislabeled tensor,” *J. Acoust. Soc. Am.*, vol. 63, no. 4, pp. 1025–1030, 1978.
- [28] J. C. Maxwell, *A Treatise on Electricity and Magnetism*. Oxford: Clarendon, 1874.
- [29] P. Lebedev, “Investigations on the pressure forces of light,” *Annalen der Physik*, vol. 6, pp. 433–458, 1901.

- [30] E. F. Nichols and G. F. Hull, “The pressure due to radiation,” *Astrophys. J.*, vol. 17, no. 5, pp. 315–351, 1903.
- [31] A. Ashkin, J. M. Dziedzic, J. E. Bjorkholm, and S. Chu, “Observation of a single-beam gradient force optical trap for dielectric particles,” *Opt. Lett.*, vol. 11, no. 5, pp. 288–290, 1986.
- [32] A. Ashkin and J. M. Dziedzic, “Optical trapping and manipulation of viruses and bacteria,” *Science*, vol. 235, no. 4795, pp. 1517–1520, 1987.
- [33] A. Ashkin, J. M. Dziedzic, and T. Yamane, “Optical trapping and manipulation of single cells using infrared laser beams,” *Nature*, vol. 330, pp. 769–771, 1987.
- [34] J. W. Strutt, “On the pressure of vibrations,” *Phil. Mag.*, vol. 3, no. 15, pp. 338–346, 1902.
- [35] J. W. Strutt, “On the momentum pressure of gaseous vibrations, and on the connexion with the virial theorem,” *Phil. Mag.*, vol. 10, no. 57, pp. 364–374, 1905.
- [36] P. Langevin (from P. Biquard), “Ultrasonic waves,” *Rev. Acoust.*, vol. 1, pp. 93–109, 1932.
- [37] P. Langevin (from P. Biquard), “Ultrasonic waves (II),” *Rev. Acoust.*, vol. 1, pp. 315–335, 1932.

- [38] L. Brillouin, *Tensors in Mechanics and Elasticity*. New York: Academic Press, pp. 380–384, 1964.
- [39] A. Kundt and O. Lehmann, “Ueber longitudinale schwinungen und klangfiguren in cylindrischen flussigkeitssaulen,” *Ann. Phys.*, vol. 153, pp. 1–12, 1874.
- [40] E. Klein, “Absolute sound intensity in liquids by spherical torsion pendula,” *J. Acoust. Soc. Am.*, vol. 9, no. 4, pp. 312–320, 1938.
- [41] I. Rudnick, “Measurements of the acoustic radiation pressure on a sphere in a standing wave field,” *J. Acoust. Soc. Am.*, vol. 62, no. 1, pp. 20–22, 1977.
- [42] E. Leung, N. Jacobi, and T. Wang, “Acoustic radiation force on a rigid sphere in a resonance chamber,” *J. Acoust. Soc. Am.*, vol. 70, no. 6, pp. 1762–1767, 1981.
- [43] L. A. Crum and A. I. Eller, “Motion of bubbles in a stationary sound field,” *J. Acoust. Soc. Am.*, vol. 48, no. 1B, pp. 181–189, 1970.
- [44] L. A. Crum, “Acoustic force on a liquid droplet in an acoustic stationary wave,” *J. Acoust. Soc. Am.*, vol. 50, no. 1B, pp. 157–163, 1971.
- [45] T. Hasegawa, “Comparison of two solutions for acoustic radiation pressure on a sphere,” *J. Acoust. Soc. Am.*, vol. 61, no. 6, pp. 1445–1448, 1977.

- [46] T. Hasegawa, “Acoustic radiation force on a sphere in a quasistationary wave field—theory,” *J. Acoust. Soc. Am.*, vol. 65, no. 1, pp. 32–40, 1979.
- [47] T. Hasegawa, “Acoustic radiation force on a sphere in a quasistationary wave field—experiment,” *J. Acoust. Soc. Am.*, vol. 65, no. 1, pp. 41–44, 1979.
- [48] T. Hasegawa and Y. Watanabe, “Acoustic radiation pressure on an absorbing sphere,” *J. Acoust. Soc. Am.*, vol. 63, no. 6, pp. 1733–1737, 1978.
- [49] T. Hasegawa, M. Ochi, and K. Matsuzawa, “Acoustic radiation force on a solid elastic sphere in a spherical wave field,” *J. Acoust. Soc. Am.*, vol. 69, no. 4, pp. 937–942, 1981.
- [50] J. Wu and G. Du, “Acoustic radiation force on a small compressible sphere in a focused beam,” *J. Acoust. Soc. Am.*, vol. 87, no. 3, pp. 997–1003, 1990.
- [51] X. Chen and R. E. Apfel, “Radiation force on a spherical object in an axisymmetric wave field and its application to the calibration of high-frequency transducers,” *J. Acoust. Soc. Am.*, vol. 99, no. 2, pp. 713–724, 1996.
- [52] P. L. Marston, “Axial radiation force of a Bessel beam on a sphere and direction reversal of the force,” *J. Acoust. Soc. Am.*, vol. 120, no. 6, pp. 3518–3524, 2006.

- [53] P. L. Marston, “Radiation force of a helicoidal bessel beam on a sphere,” *J. Acoust. Soc. Am.*, vol. 125, no. 6, pp. 3539–3547, 2009.
- [54] F. G. Mitri, “Negative axial radiation force on a fluid and elastic spheres illuminated by a high-order Bessel beam of progressive waves,” *J. Phys. A: Math. Theor.*, vol. 42, no. 24, 2009.
- [55] F. G. Mitri and G. T. Silva, “Off-axial acoustic scattering of a high-order Bessel vortex beam by a rigid sphere,” *Wave Motion*, vol. 48, pp. 392–400, 2011.
- [56] G. T. Silva, “Off-axis scattering of an ultrasound Bessel beam by a sphere,” *IEEE Trans. Ultrason. Ferroelectr. Freq. Control*, vol. 58, no. 2, pp. 298–304, 2011.
- [57] L. D. Landau and E. M. Lifshitz, *Fluid Mechanics*, vol. 6 of *Course of Theoretical Physics*. Oxford: Pergamon Press, 2nd ed., p. 84, 1987.
- [58] J. H. Cantrell, Jr., “Acoustic-radiation stress in solids. I. Theory,” *Phys. Rev. B*, vol. 30, no. 6, pp. 3214–3220, 1984.
- [59] B.-T. Chu, “Relationship between Boussinesq and Cauchy radiation stresses in solids,” *Phys. Rev. B*, vol. 35, no. 2, pp. 870–871, 1987.
- [60] W. T. Yost and J. H. Cantrell, Jr., “Acoustic radiation stress in solids. II. Experiment,” *Phys. Rev. B*, vol. 30, no. 6, pp. 3221–3229, 1984.

- [61] A. P. Sarvazyan, O. V. Rudenko, and W. L. Nyborg, “Biomedical applications of radiation force of ultrasound: Historical roots and physical basis,” *Ultrasound Med. Biol.*, vol. 36, no. 9, pp. 1379–1394, 2010.
- [62] J. Hultström, O. Manneberg, K. Dopf, H. M. Hertz, H. Brismar, and M. Wiklund, “Proliferation and viability of adherent cells manipulated by standing-wave ultrasound in a microfluidic chip,” *Ultrasound Med. Biol.*, vol. 33, no. 1, pp. 145–151, 2007.
- [63] H. M. Hertz, “Standing wave acoustic trap for nonintrusive positioning of microparticles,” *J. Appl. Phys.*, vol. 78, no. 8, pp. 4845–4849, 1995.
- [64] L. Schmid, D. A. Weitz, and T. Franke, “Sorting drops and cells with acoustics: Acoustic microfluidic fluorescence-activated cell sorter,” *Lab Chip*, vol. 14, pp. 3710–3718, 2014.
- [65] A. Shah, N. R. Owen, W. Lu, B. W. Cunitz, P. J. Kaczkowski, J. D. Harper, M. R. Bailey, and L. A. Crum, “Novel ultrasound method to reposition kidney stones,” *Urol. Res.*, vol. 38, pp. 491–495, 2010.
- [66] P. A. Dayton, A. Klibanov, G. Brandenburger, and K. Ferrara, “Acoustic radiation force *in vivo*: A mechanism to assist targeting of microbubbles,” *Ultrasound Med. Biol.*, vol. 25, no. 8, pp. 1195–1201, 1999.
- [67] P. A. Dayton, S. Zhao, S. H. Bloch, P. Schumann, K. Penrose, T. O. Matsunaga, R. Zutshi, A. Doinikov, and K. W. Ferrara, “Application of

- ultrasound to selectively localize nanodroplets for targeted imaging and therapy,” *Mol. Imaging*, vol. 5, no. 3, pp. 160–174, 2006.
- [68] W. L. M. Nyborg, “Acoustic streaming,” in *Physical Acoustics* (W. P. Mason, ed.), vol. IIB, ch. 11, pp. 265–331, New York: Academic Press, 1965.
- [69] G. R. Torr, “The acoustic radiation force,” *Am. J. Phys.*, vol. 52, no. 5, pp. 402–408, 1984.
- [70] K. J. Parker, “Ultrasonic attenuation and absorption in liver tissue,” *Ultrasound Med. Biol.*, vol. 9, no. 4, pp. 363–369, 1983.
- [71] M. L. Palmeri, M. H. Wang, J. J. Dahl, K. D. Frinkley, and K. R. Nightingale, “Quantifying hepatic shear modulus *in vivo* using acoustic radiation force,” *Ultrasound Med. Biol.*, vol. 34, no. 4, pp. 546–558, 2008.
- [72] K. R. Nightingale, M. L. Palmeri, R. W. Nightingale, and G. E. Trahey, “On the feasibility of remote palpation using acoustic radiation force,” *J. Acoust. Soc. Am.*, vol. 110, no. 1, pp. 625–634, 2001.
- [73] K. Nightingale, “Acoustic radiation force impulse (ARFI) imaging: a review,” *Curr. Med. Imaging Rev.*, vol. 7, no. 4, pp. 328–339, 2011.
- [74] J. Bercoff, M. Tanter, M. Muller, and M. Fink, “The role of viscosity in the impulse diffraction field of elastic waves induced by the acoustic ra-

- diation force,” *IEEE Trans. Ultrason. Ferroelectr. Freq. Control*, vol. 51, no. 11, pp. 1523–1536, 2004.
- [75] J.-L. Gennisson, M. Rénier, S. Catheline, C. Barrière, J. Bercoff, M. Tanter, and M. Fink, “Acoustoelasticity in soft solids: Assessment of the nonlinear shear modulus with the acoustic radiation force,” *J. Acoust. Soc. Am.*, vol. 122, no. 6, pp. 3211–3219, 2007.
- [76] M. Tanter, J. Bercoff, A. Athanasiou, T. Deffieux, J.-L. Gennisson, G. Montaldo, M. Muller, A. Tardivon, and M. Fink, “Quantitative assessment of breast lesion viscoelasticity: Initial clinical results using supersonic shear imaging,” *Ultrasound Med. Biol.*, vol. 34, no. 9, pp. 1373–1386, 2008.
- [77] A. Athanasiou, A. Tardivon, M. Tanter, B. Sigal-Zafrani, J. Bercoff, T. Deffieux, J.-L. Gennisson, M. Fink, and S. Neuenschwander, “Breast lesions: Quantitative elastography with supersonic shear imaging—preliminary results,” *Radiology*, vol. 256, no. 1, pp. 297–303, 2010.
- [78] J.-L. Gennisson, T. Deffieux, E. Macé, G. Montaldo, M. Fink, and M. Tanter, “Viscoelastic and anisotropic mechanical properties of *in vivo* muscle tissue assessed by supersonic shear imaging,” *Ultrasound Med. Biol.*, vol. 36, no. 5, pp. 789–801, 2010.
- [79] K. Arda, N. Ciledag, E. Aktas, B. K. Aribas, and K. Köse, “Quantitative assessment of normal soft-tissue elasticity using shear-wave ultrasound elastography,” *Am. J. Roentgenol.*, vol. 197, no. 3, pp. 532–536, 2011.

- [80] K. S. S. Bhatia, C. S. L. Tong, C. C. M. Cho, E. H. Y. Yuen, Y. Y. P. Lee, and A. T. Anuja, “Shear wave elastography of thyroid nodules in routine clinical practice: preliminary observations and utility for detecting malignancy,” *Eur. Radiol.*, vol. 22, no. 11, pp. 2397–2406, 2012.
- [81] E. Bavu, J.-L. Gennisson, M. Couade, J. Bercoff, V. Mallet, M. Fink, A. Badel, A. Vallet-Pichard, B. Nalpas, M. Tanter, and S. Pol, “Noninvasive *in vivo* liver fibrosis evaluation using supersonic shear imaging: A clinical study on 113 hepatitis C virus patients,” *Ultrasound Med. Biol.*, vol. 37, no. 9, pp. 1361–1373, 2011.
- [82] C. Cassinotto, B. Lapuyade, A. Mouries, J.-B. Hiriart, J. Vergniol, D. Gaye, C. Castain, B. L. Bail, F. Chermak, J. Foucher, F. Laurent, M. Montaudon, and V. D. Ledinghen, “Non-invasive assessment of liver fibrosis with impulse elastography: Comparison of supersonic shear imaging with ARFI and FibroScan,” *J. Hepatol.*, vol. 61, no. 3, pp. 550–557, 2014.
- [83] J. Bercoff, M. Pernot, M. Tanter, and M. Fink, “Monitoring thermally-induced lesions with supersonic shear imaging,” *Ultrason. Imaging*, vol. 26, no. 2, pp. 71–84, 2004.
- [84] E. E. Konofagou and K. Hynynen, “Localized harmonic motion imaging: Theory, simulations, and experiments,” *Ultrasound Med. Biol.*, vol. 29, no. 10, pp. 1405–1413, 2003.
- [85] E. E. Konofagou, C. Maleke, and J. Vappou, “Harmonic motion imaging for tumor imaging and treatment monitoring,” in *Soft Tissue Biome-*

*chanical Modeling for Computer Assisted Surgery* (Y. Payan, ed.), ch. 11, pp. 257–280, Springer, 2012.

- [86] V. Suomi, D. Edwards, and R. O. Cleveland, “Optical quantification of harmonic acoustic radiation force excitation in a tissue-mimicking phantom,” *Ultrasound Med. Biol.*, vol. 41, no. 12, pp. 3216–3232, 2015.
- [87] V. Suomi, Y. Han, E. E. Konofagou, and R. O. Cleveland, “The effect of temperature dependent tissue parameters on acoustic radiation force induced displacements,” *Phys. Med. Biol.*, vol. 61, no. 20, p. 7427, 2016.
- [88] V. Suomi, *The feasibility of ultrasound elastography in monitoring high-intensity focused ultrasound therapy*. PhD thesis, University of Oxford, St. Hilda’s College, 2016.
- [89] A. B. Karpouk, S. R. Aglyamov, Yu. A. Ilinskii, E. A. Zabolotskaya, and S. Y. Emelianov, “Assessment of shear modulus of tissue using ultrasound radiation force acting on a spherical acoustic inhomogeneity,” *IEEE Trans. Ultrason. Ferroelectr. Freq. Control*, vol. 56, no. 11, pp. 2380–2387, 2009.
- [90] S. R. Aglyamov, A. B. Karpouk, Yu. A. Ilinskii, E. A. Zabolotskaya, and S. Y. Emelianov, “Motion of a solid sphere in a viscoelastic medium in response to applied acoustic radiation force: Theoretical analysis and experimental verification,” *J. Acoust. Soc. Am.*, vol. 122, no. 4, pp. 1927–1936, 2007.

- [91] Yu. A. Ilinskii, G. D. Meegan, E. A. Zabolotskaya, and S. Y. Emelianov, “Gas bubble and solid sphere motion in elastic media in response to acoustic radiation force,” *J. Acoust. Soc. Am.*, vol. 117, no. 4, pp. 2338–2346, 2005.
- [92] S. Yoon, S. Aglyamov, A. Karpiouk, and S. Emelianov, “A high pulse repetition frequency ultrasound system for the *ex vivo* measurement of mechanical properties of crystalline lenses with laser-induced microbubbles interrogated by acoustic radiation force,” *Phys. Med. Biol.*, vol. 57, no. 15, pp. 4871–4884, 2012.
- [93] S. Yoon, S. Aglyamov, A. Karpiouk, and S. Emelianov, “The mechanical properties of *ex vivo* bovine and porcine crystalline lenses: Age-related changes and location-dependent variations,” *Ultrasound Med. Biol.*, vol. 39, no. 6, pp. 1120–1127, 2013.
- [94] P. A. Dayton, J. S. Allen, and K. W. Ferrara, “The magnitude of radiation force on ultrasound contrast agents,” *J. Acoust. Soc. Am.*, vol. 112, no. 5, pp. 2183–2192, 2002.
- [95] A. L. Klibanov, “Microbubble contrast agents: Targeted ultrasound imaging and ultrasound-assisted drug-delivery applications,” *Invest. Radiol.*, vol. 41, no. 3, pp. 354–362, 2006.
- [96] K. Ferrara, R. Pollard, and M. Borden, “Ultrasound microbubble contrast agents: Fundamentals and application to gene and drug delivery,” *Ann. Rev. Biomed. Eng.*, vol. 9, no. 1, pp. 415–447, 2007.

- [97] F. Burbank and N. Forcier, “Tissue marking clip for stereotactic breast biopsy: initial placement accuracy, long-term stability, and usefulness as a guide for wire localization,” *Radiology*, vol. 205, no. 2, pp. 407–415, 1997.
- [98] N. Dash, S. H. Chafin, R. R. Johnson, and F. M. Contractor, “Usefulness of tissue marker clips in patients undergoing neoadjuvant chemotherapy for breast cancer,” *Am. J. Roentgenol.*, vol. 173, no. 4, pp. 911–917, 1999.
- [99] F. R. Margolin, L. Kaufman, S. R. Denny, R. P. Jacobs, and J. D. Schrupf, “Metallic marker placement after stereotactic core biopsy of breast calcifications: Comparison of two different clips and deployment techniques,” *Am. J. Roentgenol.*, vol. 181, no. 6, pp. 1685–1690, 2003.
- [100] J. L. Oh, G. Nguyen, G. J. Whitman, K. K. H. T.-K. Yu, W. A. Woodward, W. Tereffe, E. A. Strom, G. H. Perkins, and T. A. Buchholz, “Placement of radiopaque clips for tumor localization in patients undergoing neoadjuvant chemotherapy and breast conversion therapy,” *Cancer*, vol. 110, no. 11, pp. 2420–2427, 2007.
- [101] E. G. Williams, *Fourier Acoustics*. London: Academic Press, pp. 31–34, 1999.
- [102] S. S. Kou, C. J. R. Sheppard, and J. Lin, “Calculation of the volumetric diffracted field with three-dimensional convolution: The three-dimensional angular spectrum method,” *Opt. Lett.*, vol. 38, no. 24, pp. 5296–5298, 2013.

- [103] Yu. A. Ilinskii, E. A. Zabolotskaya, and M. F. Hamilton, “Acoustic radiation force on a sphere in tissue,” *AIP Conf. Proc.*, vol. 1474, pp. 255–258, 2012.
- [104] Yu. A. Ilinskii, E. A. Zabolotskaya, and M. F. Hamilton, “Acoustic radiation force on a sphere without restriction to axisymmetric fields,” *Proc. Meet. Acoust.*, vol. 19, no. 1, p. 045004, 2013.
- [105] T. G. Wang and C. P. Lee, “Radiation pressure and acoustic levitation,” in *Nonlinear Acoustics* (M. F. Hamilton and D. T. Blackstock, eds.), ch. 6, pp. 177–206, New York: Acoustical Society of America, 2008.
- [106] A. C. Eringen and E. S. Suhubi, *Elastodynamics*, vol. 1. New York: Academic Press, pp. 22–34, 1974.
- [107] L. D. Landau and E. M. Lifshitz, *Theory of Elasticity*, vol. 7 of *Course of Theoretical Physics*. Oxford: Pergamon Press, 3rd ed., pp. 106–107, 1986.
- [108] M. F. Hamilton, Yu. A. Ilinskii, and E. A. Zabolotskaya, “Separation of compressibility and shear deformation in the elastic energy density,” *J. Acoust. Soc. Am.*, vol. 116, no. 1, pp. 41–44, 2004.
- [109] C. F. Ying and R. Truell, “Scattering of a plane longitudinal wave by a spherical obstacle in an isotropically elastic solid,” *J. Appl. Phys.*, vol. 27, no. 9, pp. 1086–1097, 1956.

- [110] D. T. Blackstock, *Fundamentals of Physical Acoustics*. New York: Wiley-Interscience, pp. 69–77, 2000.
- [111] G. N. Watson, *A Treatise on the Theory of Bessel Functions*. Cambridge, England: Cambridge University Press, 2nd ed., pp. vi+804, 1944. Reprinted in 1995.
- [112] Y. Tong, S. Lombeyda, A. N. Hirani, and M. Desbrun, “Discrete multiscale vector field decomposition,” *ACM Trans. Graph.*, vol. 22, no. 3, pp. 445–452, 2003.
- [113] E. P. Wigner, *Group Theory and its Application to the Quantum Mechanics of Atomic Spectra*. New York: Academic Press, pp. 75–76, 1959.
- [114] D. A. Varshalovich, A. N. Moskalev, and V. K. Khersonskii, *Quantum Theory of Angular Momentum*. Singapore: World Scientific, pp. 72–169 and 196–234, 1989.
- [115] M. F. Hamilton, Yu. A. Ilinskii, and E. A. Zabolotskaya, “Dispersion,” in *Nonlinear Acoustics* (M. F. Hamilton and D. T. Blackstock, eds.), ch. 5, pp. 151–176, New York: Acoustical Society of America, 2008.
- [116] Y.-H. Pao and C. C. Mow, “Scattering of plane compressional waves by a spherical obstacle,” *J. Appl. Phys.*, vol. 34, no. 3, pp. 493–499, 1963.
- [117] M. Minnaert, “On musical air-bubbles and the sounds of running water,” *Phil. Mag.*, vol. 16, no. 104, pp. 235–248, 1933.

- [118] V. N. Alekseev and S. A. Rybak, “Gas bubble oscillations in elastic media,” *Acoust. Phys.*, vol. 45, no. 5, pp. 535–540, 1999.
- [119] W. Bosch, “On the computation of derivatives of Legendre functions,” *Phys. Chem. Earth (A)*, vol. 25, no. 9–11, pp. 655–659, 2000.
- [120] “*NIST Digital Library of Mathematical Functions.*” <http://dlmf.nist.gov/10.52.ii>, Release 1.0.20 of 2018-09-15. F. W. J. Olver, A. B. Olde Daalhuis, D. W. Lozier, B. I. Schneider, R. F. Boisvert, C. W. Clark, B. R. Miller and B. V. Saunders, eds.
- [121] M. S. Cramer, “Numerical estimates for the bulk viscosity of ideal gases,” *Phys. Fluids*, vol. 24, no. 6, 2012.
- [122] R. E. Graves and B. M. Argrow, “Bulk viscosity: past to present,” *J. Thermophys. Heat Transfer*, vol. 13, no. 3, pp. 337–342, 1999.
- [123] H. H. Oestreicher, “Field and impedance of an oscillating sphere in a viscoelastic medium with an application to biophysics,” *J. Acoust. Soc. Am.*, vol. 23, no. 6, pp. 707–714, 1951.
- [124] E. L. Madsen, H. J. Sathoff, and J. A. Zagzebski, “Ultrasonic shear wave properties of soft tissues and tissuelike materials,” *J. Acoust. Soc. Am.*, vol. 74, no. 5, pp. 1346–1355, 1983.
- [125] S. Catheline, J.-L. Gennisson, G. Delon, M. Fink, R. Sinkus, S. Abouelkaram, and J. Culioli, “Measurement of viscoelastic properties of homoge-

- neous soft solid using transient elastography: An inverse problem approach,” *J. Acoust. Soc. Am.*, vol. 116, no. 6, pp. 3734–3741, 2004.
- [126] T. G. Leighton, A. J. Walton, and M. J. W. Pickworth, “Primary Bjerknes forces,” *Eur. J. Phys.*, vol. 11, no. 1, pp. 47–50, 1990.
- [127] B. C. Treweek, Yu. A. Ilinskii, E. A. Zabolotskaya, and M. F. Hamilton, “Acoustic radiation force due to arbitrary incident fields on spherical particles in soft tissue,” *AIP Conf. Proc.*, vol. 1685, no. 1, p. 040008, 2015.
- [128] A. N. Guz and A. P. Zhuk, “Motion of solid particles in a liquid under the action of an acoustic field: The mechanism of radiation pressure,” *Int. Appl. Mech.*, vol. 40, no. 3, pp. 246–265, 2004.
- [129] P. M. Morse and H. Feshbach, *Methods of Theoretical Physics*. New York: McGraw-Hill, pp. 52–54, 1953.
- [130] K. Polthier and E. Preuß, “Variational approach to vector field decomposition,” in *Data Visualization 2000* (W. C. de Leeuw and R. van Liere, eds.), ch. 15, pp. 147–155, New York: Springer-Verlag/Wien, 2000.
- [131] K. Polthier and E. Preuß, “Identifying vector field singularities using a discrete hodge decomposition,” in *Visualization and Mathematics III* (H.-C. Hege and K. Polthier, eds.), ch. 6, pp. 113–134, Berlin: Springer-Verlag, 2003.

- [132] F. Ihlenburg, *Finite Element Analysis of Acoustic Scattering*, vol. 132 of *Applied Mathematical Sciences*. New York: Springer, p. 116, 1998.
- [133] O. C. Zienkiewicz, R. L. Taylor, and J. Z. Zhu, *The Finite Element Method: its Basis and Fundamentals (Seventh Edition)*. Oxford: Butterworth-Heinemann, seventh edition ed., pp. 211–255, 2013.
- [134] M. Abramowitz and I. A. Stegun, *Handbook of Mathematical Functions with Formulas, Graphs, and Mathematical Tables*. New York: Dover Publications, 1964.
- [135] M. E. Rose, *Elementary Theory of Angular Momentum*. New York: Wiley, p. 124, 1957.

## Vita

Benjamin Charles Treweek was born on April 19, 1989 in Washington, D.C. An avid practitioner of sports (running, climbing, basketball, soccer), music (guitar, piano, karaoke), and less useful diversions (chess puzzles, impersonations and quotes, computer and video games), he attended Thomas Jefferson High School for Science and Technology (Alexandria, Virginia)—arguably the nerdiest public high school in the United States—graduating in 2007. He then attended the University of Michigan (Ann Arbor, Michigan), graduating in 2011 with a B.S. in Physics and a B.S. in Music through the College of Literature, Science, and the Arts, and earning Highest Distinction and Phi Beta Kappa honors. He lived in San Francisco, California for the next two years, deliberating about how to proceed with his life while tutoring high school students in physics and math, working as a solutions architect in big data analytics, and playing guitar in a Mongolian rock band. In August 2013, he moved to Austin, Texas to begin his Ph.D. at The University of Texas at Austin.

Permanent address: btreweek [at] gmail [dot] com

This dissertation was typeset with  $\text{\LaTeX}^\dagger$  by the author.

---

<sup>†</sup> $\text{\LaTeX}$  is a document preparation system developed by Leslie Lamport as a special version of Donald Knuth's  $\text{\TeX}$  Program.